# SIMULATIONS OF THE MARTIAN DUST CYCLE WITH A GENERAL CIRCULATION MODEL

Thesis by

Shabari Basu

In Partial Fulfillment of the Requirements for the

degree of

Doctor of Philosophy


CALIFORNIA INSTITUTE OF TECHNOLOGY

Pasadena, California

2005

(Defended September 21st, 2005)

ACKNOWLEDGEMENTS

I must begin by thanking my supervisors, Professor Mark Richardson (Caltech), John Wilson (Geophysical Fluid Dynamics Laboratory), Professor Andy Ingersoll (Caltech) for their help and support over the past few years and, in particular, for reading my papers and my thesis with such dedication. I have also received valuable advice and support from many people in the department and elsewhere. I would like to especially thank Professor Yuk Yung who has been my academic advisor since I arrived at Caltech and has given me excellent professional guidance throughout these years. I would also like to extend special thanks to Dr. Claire Newman, Dr. Michael Mischna (Jet Propulsion Laboratory) and Professor Tapio Schneider for valuable discussions, guidance, and collaborations.

And finally, I would like to thank my parents, Mr. Bishan Basu and Mrs. Malabika Basu, and Sayanti and Raktim, for their love and support.

## ABSTRACT

The Martian seasonal dust cycle is examined with a General Circulation Model (GCM) that treats dust as a radiatively and dynamically interactive trace species. Dust injection is parameterized as being due to convective processes (such as dust devils) and model-resolved wind stresses. Multi-year Viking and Mars Global Surveyor mission air temperature data sets are used to quantitatively assess the quality of simulations. Varying the three free parameters for the two dust injection schemes (rate parameters for the two schemes and a threshold for wind-stress lifting), we find that northern spring and summer temperatures, which are observed to repeat very closely each year, can be reproduced by the model if the background dust haze is supplied by convective lifting. To obtain spontaneous and variable dust storms, dust injection due to high threshold and high rate stress lifting must be added. The convective scheme is found unable to generate a dust storm but is a good candidate for background dust (in agreement with imaging observations e.g., dust devils). Combining the convective scheme and high-threshold stress lifting, we obtain a "best fit" multi-year simulation, which includes simulation of both a realistic thermal state in northern spring and summer and, for the first time, the spontaneous generation of inter-annually-variable global dust storms. Our results support the idea that variable and spontaneous global dust storm behavior can emerge from a periodically forced system (the only forcing being the diurnal and seasonal cycles) when the dust injection mechanism involves an activation threshold. The general circulation model is also used to evaluate changes to the circulation and dust transport in the Martian atmosphere for simulations with a finite supply of dust on the surface. The focus is on changes to atmospheric temperatures and dust-related surface features, as these may potentially be verified by observations. In this work, the use of a finite surface dust supply increases the amount of inter-annual variability the system is capable of producing. This is due to a new set of initial conditions, in the form of available surface dust, being present at the beginning of each storm season.

TABLE OF CONTENTS

Chapter 1: Introduction....10
1.1 Introduction....10
1.2 Research: Global modeling of the Martian dust cycle and the dust storms ...13
1.3 The seasonal cycle of the Background dust haze....17
1.4 The Generation of spontaneous and variable global dust storms....21
1.5 Experiments with Prognostic surface dust deposits. ....25
Chapter 2:Simulation of the Martian Dust Cycle with the GFDL Mars GCM.....29
2.1 Introduction....30
2.2 Observations....34
2.3 The Model....36
2.3.1 Convective ("Dust Devil") Parameterization....38
2.3.2 Stress Lifting Parameterization....43
2.4 Fitting the Annual Cycles of Air Temperature and Dust....49
2.4.1 The Dust Devil Source....50
2.4.2 The Model-Resolved Wind Stress Source....53
2.4.3 Summary of Dust Source Results....56
2.5 Characteristics of the "Best Fit" Model Annual Cycle....60
2.5.1 Meridional and Vertical Distribution of Air Temperature....62
2.5.2 Spatial Pattern of Dust Devil Lifting and Dust Devil Predictions....71
2.5.3 Prediction of Local and Regional Dust Storm Activity....75
2.6. Spatial Distribution of Net Dust Lifting and Deposition ....77
2.7 Summary and Conclusions....80
Chapter3: Simulation of Spontaneous and Variable Global Dust Storms ....84
3.1. Introduction....84
3.2. Model Description....92
3.3. Exploration of Model Behavior as Wind Stress Lifting Parameters Vary .....93
3.4. Simulated Global Dust Storms.... 100
3.4.1.1 Evolution.... 105
3.4.1.2 Dust and Air Temperature Distributions .... 109
3.4.2.1 A regional Dust Storm initiated by a Northern Hemisphere Storm..... 126
3.4.2.2 Dust and air temperature distribution for Chryse type storms.... 142
3.5. Global Dust Storm Initiation.... 144
3.6. The Dust Storm "Switch-Off" Problem .... 156
3.7. Net Dust Transport by Global Dust Storms.... 161
3.8. Inter-annual Variability of Global Dust Storms at this and Other States.... 163
3.9. Summary.... 165
Chapter 4: Simulating Dust Activity with Evolving Surface Dust.... 168
4.1 Introduction:.... 169
4.1.1 The impact of finite dust sources on the seasonal cycle of dust.... 171
4.1.2 The impact of finite dust sources on the evolution of .... 171
4.1.3 The impact of using non-uniform initial finite dust distributions.... 174
4.1.4 The impact of finite dust sources when the stress threshold is varied..... 175

4.2: Description of Method ..... 177
4.2.1 The Model: ..... 177
4.2.2 Initializing the Finite surface dust distribution ..... 178
4.2.2.1 Uniform surface dust ..... 178
4.2.2.2 Non-uniform surface dust based on albedo ..... 179
4.3: The Experiments ..... 179
4.3.1 The impact of finite dust sources on the seasonal cycle of dust ..... 179
4.3.2 The effect of finite dust sources on the inter-annual variability & storms 182
4.3.2.1 The effect of initializing with insufficient surface dust ..... 184
4.3.2.2 The effect of initializing with sufficient surface dust ..... 188
4.3.2.3 A particularly significant simulation ..... 190
4.3.3 The impact of using non-uniform initial finite dust distributions ..... 202
4.3.4 The impact of finite dust sources when the stress threshold is varied ..... 216
4.3.3.1 Increasing stress threshold with dust depletion ..... 219
4.3.3.2 Decreasing stress threshold with dust depletion ..... 227
4.4 Conclusions ..... 231
4.5 Future Work ..... 231
Chapter 5: Conclusions ..... 233
Chapter 6: Future Work ..... 239
6.1 High resolution simulations of the Martian dust cycle and global storms- ... 240
6.2 Interaction of the water cycle and the clouds with the dust ..... 240
6.3 Interaction of the polar caps with the dust cycle ..... 241
6.4 Incorporating variable stress threshold scheme for Mars ..... 241
6.5 Improving the current Mars GCM with better schemes ..... 241

# LIST OF FIGURES

Chapter 1
1. Global mean mid-level air temperatures ..... 17
2. Simulation of spontaneous storms in a GCM simulation ..... 23

Chapter2
1. Seasonal variation of midlevel air temperatures ..... 35
2. Relation between DDL rates and various model variables ..... 40
3. Single time step from the sequence shown in previous figure..... 42
4. Stress lifting scheme formulation ..... 46
5. Diurnal mean surface stresses ..... 48
6. Atmospheric temperatures predicted by model..... 51
7. Seasonal cycle of air temperatures due to stress lifting ..... 54
8. Spatial distribution of dust injection predicted by stress lifting..... 55
9. Globally averaged injection and fall out rates ..... 57
10. Phase space of parameters explored ..... 61
11. Comparison of simulated vs observed zonal mean t-15 ..... 64
12. Cross sections of thermal structure for Ls=90..... 65
13. Cross sections of thermal structure for Ls=180..... 66
14. Cross sections of thermal structure for Ls=270..... 67
15. Cross sections of thermal structure for Ls=360..... 68
16. Diurnal mean injection by dust devils ..... 71
17. Spatial distribution of simulated and observed storms ..... 75
18. Annually integrated net erosion depth..... 78

Chapter3
1. Globally averaged temperature for various threshold..... 94
2. Phase space of parameters explored ..... 97
3. Initiation vs peak opacity for dust storms..... 101
4. Zonal mean T-15 and dust opacity evolution..... 103
5. T-15 temperatures for high resolution simulation..... 104
6. Evolution of early Hellas storm ..... 105
7. Evolution of late Hellas storm ..... 106
8. Synthetic ITRM data from GCM compared with observations..... 110
9. Diurnal variation of T-15 during Viking missions..... 112
10. Surface Pressure tides ..... 113
11. Evolution of equatorial dust opacity and T-15 ..... 114
12. Comparison of cross sections of MGCM vs TES data ..... 115
13. Temperature and dust cross section from MGCM at Ls=295 ..... 117
14. Cross section of evolution of early Hellas storm ..... 119
15. Cross section of evolution of storm starting at Ls=200 ..... 120
16. Cross section of storm starting at Ls=219 ..... 121
17. Dust evolution for late Hellas storm..... 122
18. Vertical profile of zonally averaged temperatures at Ls=280..... 124

19. Vertical profile of dust at Ls=280 ..... 125

20. V-shaped Chryse storm ..... 126
21. Evolution of Chryse type of storm ..... 128
22. Surface Pressure variance showing wave activity ..... 129
23. Spatial map of rms temperatures ..... 132
24. Spatial map of rms surface pressure ..... 133
25. Spatial map of rms velocity field ..... 134
26. Evolution of Arcadia storm ..... 135
27. Spatial variation of eddy fields at Ls=241 ..... 136
28. Transient wave activity in Northern Hemisphere ..... 137
29. Traveling waves, T rms amplitudes ..... 139
30. Traveling waves, Surface pressure rms amplitudes ..... 140
31. Traveling waves, V- rms amplitudes ..... 141
32. Vertical profiles of dust and temperature comparisons with TES ..... 142
33. Vertical profile of evolving Chryse storm ..... 143
34. Vertical profile of second Chryse storm ..... 144
35. Spatial map of stresses ..... 146
36. Variation of stresses in Hellas basin ..... 147
37. Mean and variance of stresses in Hellas basin ..... 149
38. Geographic distribution of maximum stresses ..... 159
39. Net annual deposition predicted by GCM ..... 162

Chapter 4

1. Seasonal cycle of dust with finite surface dust ..... 180
2. Dust cycle and lifting sites due to initial dust=0.1gm/cm2 ..... 185
3. Dust cycle and lifting sites due to initial dust=0.8gm/cm2 ..... 187
4. Dust cycle and lifting rates due to initial dust=2.0 gm/cm2 ..... 189
5. Dust Cycle and lifting rates due to initial dust=3.0 gm/cm2 ..... 192
6. Dust cover as a function of season for lon=48, lat=-45 ..... 197
7. Dust cover as a function of season for lon=54, lat=-40 ..... 198
8. Dust cover as a function of season for lon=48, lat=-40 ..... 199
9. Dust cover as a function of season for lon=54, lat=-20 ..... 199
10. Dust cover as a function of season for lon=78, lat=-15 ..... 200
11. Comparison of GCM dust distribution with TES data ..... 204
12. Dust cycle and lifting sites for prescribed dust ..... 207
13. Similar plots as Figure 12 with various thresholds ..... 209
14. Albedo maps from TES observations ..... 212
15. Difference in dust distribution before and after a storm ..... 215
16. Erosion Potential for dust storms ..... 218
17. Dust cycle for variable stress lifting as a function of surface dust ..... 220
18. Storm in Isidis region ..... 222
19. Cross over storms for variable threshold scheme ..... 223
20. Similar storms as Figure 19 but for different initializations ..... 225
21. Decreasing threshold with dust depletion ..... 227

22. Similar to Figure 21 but for different initialization.....

LIST OF TABLES

Chapter 1
1. Simulation series for infinite surface dust case ..... 24
2. Simulation series for finite surface dust case ..... 27

# Chapter 1

# Introduction

## 1.1 Introduction

Dust is a major moderator of Martian climate, playing a role in some ways similar to that of water in the terrestrial atmosphere [Zurek et al., 1992]. During large dust storms, the visible optical depth of the global atmosphere can exceed unity, obscuring surface features, while global mean air temperatures at mid-levels can increase by tens of Kelvins [Briggs et al., 1979; Martin and Kieffer, 1979; James and Zurek, 1993; Zurek and James, 1992; Martin and Richardson, 1993; Smith et al., 2000, 2001a, b, 2002; Cantor et al., 2001; Liu et al., 2002], with minimum opacities during late northern spring, and maximum no-dust storm opacities in mid southern spring. It is during southern spring and summer that large dust storms typically occur. This correlation makes it tempting to suggest that the seasonal cycle of dust simply corresponds to slow fall out following large dust storms, however, while the size and timing of major dust storms in southern spring and summer vary dramatically, northern spring and summer opacities and temperatures are vastly more repeatable. This indicates that the northern spring and summer atmosphere is essentially insensitive to dust storm activity that occurs during the previous southern spring and summer, and that a non-dust storm mechanism is of dominant importance for determining the seasonal cycle of dustiness.

Dust lifting on Mars has been observed in several forms: as dust devils (boundary layer convective vortices) with horizontal scales of meters to about half a kilometer; within plumes that appear similar to examples of terrestrial dust lifting by strong mean wind stresses; and as dust storms, where it is difficult to definitively identify the dust lifting mechanism, but is usually ascribed to a combination of large scale and self induced wind stresses [e.g., Kahn et al., 1992]. Dust devils appear to be active over a very broad region of the planet, based on orbiter imaging of the structures themselves and of the tracks they leave on the surface [Balme et al., 2003; Cantor et al., 2002; Fisher et al., 2003]. Non global dust storms, termed local and regional events depending on scale, occur frequently on Mars. An exhaustive catalog of storm events was compiled by Cantor et al. [2001] from a portion of the Martian year in 1999. Storms were observed to be associated with edges of the seasonal ice caps that wax and wane

across the Martian surface [Siili et al., 1997; Toigo et al., 2002]. There have also been observations in association with large slopes in topography and in forms that suggest association with the fronts of low pressure cyclones [Cantor et al., 2001; Wang et al., 2003].

Very large dust storms that grow to encompass the entire planet are rare and variable. These storms are often called "global dust storms" or "planet encircling storms". The limited baseline of observations suggests that they recur every three years or so [Martin and Zurek, 1993]. When they do recur, there is variability in the exact season of initiation (the 2001 storm began at the southern spring equinox, while the 1977 b storm began just after southern summer solstice) and in the magnitude of the events. This "quazi-randomness" of global dust storm behavior is one of the major unknowns of the current climate system. Our lack of understanding of how and why these storms are triggerred, combined with their major impact on climate, generates significant uncertainty in predicting how climate on Mars may have differed in the past.

The full dust cycle on Mars likely involves both the atmospheric branch and slower redistribution of dust on the surface, including feedback on the climate through varying surface albedo. The first quantitative evidence for this has recently been found. Air temperature observations from the Viking and Mars Global Survey orbiter shows a high degree of repeatability in northern spring and summer that corresponds with the cycle of dust opacity. However, in the spring and summer following the 2001 global dust storm, observations showed that global-mean night-time temperatures were distinctively (~5K) cooler [Liu et al., 2003]. Smith et al., [2003] subsequently found that the coolness of daytime air temperatures correlates directly with the relative coolness of the daytime ground temperatures, compared to previous years, and that the ultimate cause is elevated global-mean albedo. It would seem that dust falling out following the storm, does so in a spatially uniform-manner. Where it falls on previously dust-free, dark surfaces, it brightens them, while dust fall-out on a dusty surface does not change the albedo. As a result, Mars brightens and cools slightly after the storm, at least until the dust is swept from the dark regions back into the major dust deposits. These observations provide unique quantitative insight into what is likely a major climatic memory site (the surface dust distribution) and information on how that memory site interacts with and modifies the climate. Many complex terrestrial climatic systems, such as El

Nino, develop because of the interaction between the atmosphere and slower responding memory sites, such as the upper ocean.

Development of a prognostic understanding of the Martian dust cycle, as we would need in order to make statements about how Mars' climate may have differed in the past, requires that we address several critical questions about the dynamics of the global dust cycle:

1. What processes control the seasonal cycle of the global "background haze" of dust?

2. What processes are responsible for the initiation of dust storms, and for the spectrum of sizes of dust storms that occur on Mars?

3. What processes are responsible for the variability in size and season of initiation of global storms on Mars?

4. How does the coupled (surface plus atmosphere) cycle of dust on Mars operate, and is it a cycle?

5. How do changes in the surface distribution of dust affect the dust cycle; via changes in the dust source distribution, and via surface radiative heating changes that force changes in the circulation and atmospheric transport?

There are other critical questions for the Martian dust cycle involving the microphysics and micrometeorology of dust injection and coupling of the dust cycle with the water cycle through cloud processes. We do not investigate these here for two main reasons: First, it is impossible to do everything (and in any case, doing everything may not even be the most effective means of gaining insight). It is important to realize that the level of the field is such that basic questions about the global dust cycle remain open that need to be addressed before we can make even basic statements about how much more detail in modeling of microphysical and micrometeorological processes is needed. We cannot say yet we have failed to simulate the global cycles with simple global models, as only three pioneering efforts have yet been undertaken [Murphy et al., 1995; Newman et al., 2002 ab, Pankine and Ingersoll, 2002]. Second, we know that work on micro-scale processes is ongoing in other research projects, both within the wider group with which we are affiliated [Toigo et al., 2003] and outside [e.g.,

Balme et al. 2003]. As these efforts develop, there is a natural interchange of ideas. The kind of low-resolution, global study proposed here provides a "systems level" approach that is a vital complement to these high-resolution "mechanisms" approaches.

In this research we undertake experiments to address the large-scale questions (above) using a Martian General Circulation Model (GCM). Understanding of the Martian climate (as with that of the Earth) requires careful use of both data and models. Global models of the Martian atmosphere and climate have become increasingly "skillful" over the past decade or so, and when used in conjunction with observations, yield insight into how the atmosphere and climate work that simply would not be attainable from the data alone. Our work will build upon that of Murphy et al., [1990,1993,1995], who used two and three dimensional global models to examine the dynamics of the global dust storms using prescribed dust sources. More recently, while working with the Oxford Mars GCM, Dr. Claire Newman, undertook a comprehensive study of the Martian dust cycle using prognostic dust lifting schemes [Newman et al., 2002 ab]. That work demonstrated that variable dust related phenomena (dust storms on various scales, etc.) could emerge from the natural steady forcing of the model by diurnal and seasonal cycles. It also defined the two-process dust injection formalism that we follow, with dust injected by sub-grid scales convective processes and resolved wind stresses. However, the questions outlined above remain open following the Newman et al., [2002 ab] work. The model was not able to obtain global storms in any realistic way (while "global" dust events were simulated, it should be made very clear that they corresponded to wholly unrealistic dust injection scenarios), and the year – to –year variability in dust activity was muted compared with observations). The model did not modify the surface distribution of dust. Finally, as it was never a major goal of that project, spacecraft thermal data were not used to quantify the validity of the modeled seasonal dust cycle. We propose to pick-up where the Newman et al., 2002 ab work left off, by modeling surface dust deposits, and the use of observed air temperature data.

**1.2 Research: Global modeling of the Martian dust cycle and the dust storms**

We examine the behavior of dust in a Martian General Circulation model with the goal of developing a self-consistent and realistic dust cycle and of understanding the required components of this cycle. The philosophy of approach is to start with the simplest model that

includes processes of suspected importance, examine emergent behavior, and only improve model processes where results suggest we have to. We have used this approach before in studying the Martian Water cycle with the same GCM [Richardson and Wilson, 2002; Richardson et al., 2002]. The thesis will be broken into three parts:

1. Examination of the seasonal cycle of background dust and air temperatures.

2. Simulation of the inter-annually variable, spontaneous global dust storms.

3. Simulation of interactions between surface dust deposits, the climate/circulation, and atmospheric dust.

The Geophysical Fluid Dynamics Laboratory (GFDL) Mars GCM is used in this project. This model has been extensively used over the past few years and validated against available spacecraft data [Wilson and Hamilton, 1996; Wilson and Richardson, 2000; Fenton and Richardson, 2001; Richardson and Wilson, 2002; Richardson et al., 2002; Wang et al., 2003]. The model integrates the primitive equations on a discretized grid and includes a significant number of Mars-specific parameterizations. These include a CO2 cycle with prognostic variations in surface pressure and seasonal ice caps [Mischna et al., 2003]; a water cycle, which includes atmospheric transport; simple cloud microphysics; water ice seasonal caps [Richardson and Wilson, 2002; Richardson et al., 2003]; and radiative heating sue to solar and thermal infrared interactions with dust and CO2 gas [Wilson and Hamilton, 1996].

The dust cycle components are included in the model. Dust is transported in the atmosphere by the model resolved winds and sub-grid scale diffusion, and falls under the influence of gravity (we currently carry two particle sizes of radii: 1.6 and 2.5 microns). Dust is injected using a scheme that represents the net effect of dust devils and one that represents resolved wind stress driver lifting:

The convective or dust devil injection scheme uses the model-predicted sensible heat flux and convective boundary layer (PBL) height to predict dust devil activity and then generate injection rates by multiplying this value by a rate coefficient (injection rate=rate constant*sensible heat flux*fn (PBL depth). This formulation comes from a thermodynamics theory of dust devils [Renno et al., 1998] and was used by Newman et al., 2002 ab. The rate

coefficient is a tunable, though spatially and temporally constant, free parameter. This free parameter must capture the unknown transfer function between the vigor of an individual dust devil responding to a local sensible heat flux and local PBL top height, and an ensemble of dust devils responding to average values of heat flux and PBL height over the model grid scale (tens to hundreds of thousands of square kilometers). It also captures the unknown relationship between the intensity of Martian dust devils, the number of dust devils developing per unit area for a given intensity, and the injection capacity of dust devils.

The resolved wind stress injection scheme uses the surface stresses predicted by the model PBL scheme to generate dust injection fluxes. The injection is proportional to the frictional velocity cubed above a given stress threshold and is zero below that value [e.g., Shao, 2001]. More complex schemes that smooth the step function into a sharp ramp to represent the effects of gusts are possible [Newman et al., 2002 a], and will be used if our results suggest they must. They are not used initially in the spirit of making the model as complex as necessary to generate realistic dust cycle behavior, but not more so. A Monin Obukhov scheme is used to predict stresses from the stability of the lowest level and the winds at the center of the lowest level. This level is defined in sigma coordinates, but is typically centered between 150 and 250 m above the surface. PBL parameterizations are a perennial cause of concern in large-scale models, as they attempt to represent still poorly understood turbulent motions on scales much smaller than the model grid. It is therefore easy to criticize any given PBL scheme. Modeled wind interactions with the surface, insofar as wind direction is concerned, has been tested with for the GFDL Mars GCM (as used in this study) by comparison with observed bright and dark streaks on Mars [Fenton and Richardson, 2001]. These results, however, do not validate the stress magnitudes. Alternative PBL schemes are readily available, and it is easy to change the vertical structure of the model (i.e., thickness of the lowest level) such that sensitivity of key results to model structure and the PBL scheme can be checked by reconfiguring the model. The wind stress scheme has two tunable parameters: rate coefficient and the stress threshold. While it is possible to take wind tunnel results [White, 1979; Greeley et al., 1992] for both the threshold and injection rates, there would seem to us to be problems in doing so for the same area based reasons discussed above: what transfer function is applicable that maps a homogenous wind tunnel experiment over areas of meters to tens of meters square to a very heterogeneous wind and surface environment on the model grid scale? The GCM actually

does predict stresses above the threshold derived by wind tests, and the example situation shown in Figure 2 shows uses a threshold closed to the observed. This may be a coincidence of the particular PBL scheme used, however, it would not wise to over-interpret this result. Model errors in prediction of the stress magnitude and experimental errors regarding the cohesion of dust and the role of sand saltation are also folded into this tunable parameter. In effect, the use of the tunable rate and threshold parameters reflects an honest statement of ignorance. From terrestrial experience [e.g., Shao, 2001] we can be fairly certain the wind stress lifting will go roughly as the frictional velocity cubed above some threshold, but defending a specific value of the threshold or rate parameter would be extremely hard. As such, we turn the experiment around: what values of these parameters are needed in the model to yield realistic results (e.g., good seasonal cycle, variable global dust storms, etc.)?

The three free parameters in the combined convective and wind stress dust lifting scheme provide a means of examining the model response and resulting state as by changing dust forcing. Our results suggest that the dust devil and stress lifting free parameters are separable and that the dust devil parameter may only be allowed to take a very limited range of values if the model is to remain in agreement with observed air temperatures.

Dust optical depth is calculated for each grid box. In fact, the advected quantity is not the dust mass or mixing ratio, but the visible optical depth per unit pressure drop across the box using a visible-to-infrared optical depth ratio of 1.5. A single scattering albedo of 0.92 is used. Ideally, a full spectrum of dust would be used, and coupled to generate prognostic particle radiative properties in the visible and infra-red, that would then be used in full scattering and absorbing radiative transfer scheme. While it is always possible to improve the model radiation code, the ability of the current model to fit the observations, as given in the references above suggests that the model will be a more than valuable tool for examining the dust cycle. Philosophically, we would rather use the model in as simplified a manner as possible and have it demonstrate that we require more complex processes and parameterizations than to make assumptions that overly complicate and slow the model, expending time in such a way that detracts from using the model to investigate scientific questions. In any case, we can demonstrate that the model in its current form can generate spontaneous, inter-annually variable global dust storms, something that already represents a significant advance in the state of the field and provides

some confidence (or evidence) that something useful can be learned from the current model. As with the PBL scheme issues, sensitivity to the specific representation of dust radiative heating can and will be tested in example cases.

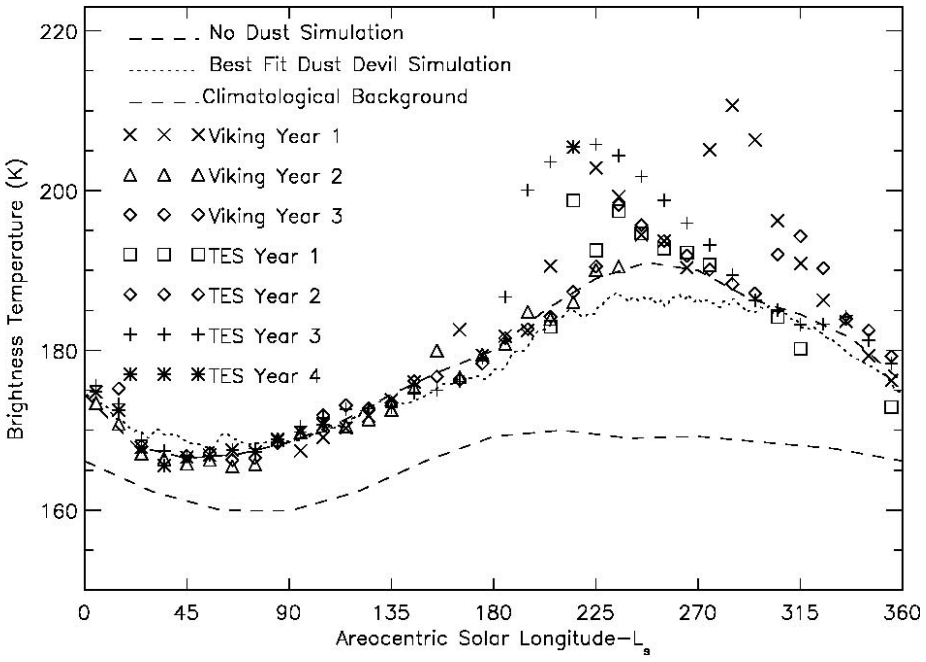


**Figure 1:** Global mean, mid-level air temperatures [Liu et al., 2003] show the seasonal cycle to repeat closely each year during northern spring and early summer (Ls=0-140), based on 7 years of spacecraft thermal infra-ed data. In the absence of dust, the atmosphere at ~ 25 km would be about 15 K cooler than observed. The climatology of air temperatures provides a powerful constraint on the seasonal dust cycle. During southern spring and summer (Ls=180-320), the impact of large dust storms is evident as peaks and bumps in the air temperature record. The 2001 global dust storm is evident as the rounded peak, beginning just after Ls=180. An example 'fit' using the GCM with only dust devils lifting is also shown in the figure.

### 1.3 The seasonal cycle of the Background dust haze

The seasonal cycle of mid-level air temperatures observed by the Viking Landers and by the Mars Global Surveyor Orbiter is shown in Figure 1 [Liu et al., 2003]. The cycle shows a minimum in northern spring, when temperatures are highly repeatable, and a maximum during southern spring and summer. The prominent peaks and spikes in southern spring and summer season are dust storms of various sizes. Also on this figure are curves corresponding to a dust free model atmosphere, one simulated with a uniform optical depth. Dust is clearly needed in

the atmosphere, as without it, air temperatures are cold by about 15K. This has long been recognized, and all current Mars GCMs include a representation of dust radiative heating.

The major question we ask here is: What mixture of processes, and specifically which injection mechanism, controls this background cycle? Currently, most GCM's use prescribed dust distributions that are redesigned to give the best fit to the annual air temperature cycle [Forget et al., 1999]. While this is an excellent way to maintain maximum model validity when investigating other problems in Martian climate and atmospheric dynamics, it obviously is of limited utility for investigation of the Martian dust cycle itself. The GFDL and Oxford Mars GCM's have generated published seasonal cycle results with interactive (transported and radiatively active) dust. However, the former used a very simplified scheme that was not the main focus of the study, while the latter, although using the more complex dual injection scheme to be used in this study, did not focus on identifying which of the following lifting processes were important for controlling the annual cycle or on constraining the problem with the use of sir temperature data.

The dual injection dust scheme described above presents three free parameters, which we intend to sweep in a non-random manner to search for realistic climatic states. These parameters are the rate constants for convective and resolved wind-stress lifting and the stress threshold for resolved wind stress lifting. Since the model is known to come into steady state after less than one year, we carry each simulation for 3-10 years, using the second and third of the years as our results for any given simulation (two valid years are generated for each simulation as a minimal check for inter-annual variability). Each simulation of this kind takes about three days to complete on our computer system, and multiple simulations can be run at the same time without interfering or slowing. We initially examine convective and wind stress lifting separately using zonal mean, mid-level air temperatures [Figure 1] as a broad-brush quality check (a necessary, but not sufficient validity criteria, if you like).

Examination of convective lifting is straight forward, as there is one tunable parameter- only a handful of runs are required to find the range at which any kind of fit can be found, and a few more to place the upper and lower limits. The scheme input quantities (PBL height and sensible heat flux) are in accord with expectations [Haberle et al., 1993]. They also show that the scheme can fit the air temperature seasonal cycle "shape" [Figure 1], which is not all that

surprising given the success of a much simpler scheme included previously in the GFDL model [Richardson and Wilson, 2002]. Once a good fit has been found with the convective scheme by comparison with average air temperatures [Figure 1], the quality of the fit can be assessed in greater detail by comparison with air temperature data as a function of latitude and season, and by comparison with cross sections (latitude and height), and latitude vs. local time plots of temperature for different seasons. The latitudinal, local time, and vertical distribution of temperature provides constraints on the spatial pattern of heating and the response of the circulation to this heating, which are not provided by the global integrated data shown in Figure 1. Good fits to the seasonal curve and other data will be used to predict the location and relative intensity of dust devil activity, which can be used to test the model against dust devil distribution observations. The same output will also be used to examine the relationship between where the model predicts dust devil lifting is active and where dust is actually lifted out of the lower level into the rest of the atmosphere. Results with the previous dust scheme in the GFDL model suggests that the atmosphere pulls dust from limited geographical regions, such that regions of strong dust devil lifting may not correspond with the most important regions for net atmospheric dust injection.

The stress lifting scheme has two free parameters, and thus in principal a "mixing line' of injection rate coefficients and thresholds may be obtained that agrees in some sense with the observations. With the extra degree of freedom, more test simulations will be needed for wind stress lifting. A pattern of a few thresholds and injection rates yielding a few tens of runs is tested out. The major test criteria will be seasonal air temperature cycle shape- while it seems clear that a temperature fit can be obtained at some season with some injection value, it is not clear that the entire shape can be fit. It is also not clear how the shape fit will vary with stress threshold which will be tested. It is important to determine if the stress lifting can fit the seasonal cycle by itself, as a regional study of dust-devil tracks by Balme et al., [2003] has been used to argue that dust devils are several orders of magnitude too ineffective to maintain the background dust. Additional data can be used to constrain the wind stress simulations. The same meridional, local time, and vertical distributions of temperature mentioned above for convective lifting will be applied. In addition, the stress scheme simulations will present predictions of discrete dust lifting events: local and regional dust storms. These events will be cataloged and put into a format that can be compared with the observational data base

collected and collated by Cantor et al., 2001. These data on the number and nature of dust lifting events provides a powerful constraint on the wind stress scheme. As the threshold is lowered, the geographical distribution and occurrence frequency of localized lifting events increases. If the threshold is too high or too low, the model is in significant disagreement with the data on the number of storm events (and hence proven wrong). From Viking Lander observations, we know that dust is not continuously lifted into the atmosphere by wind stresses [e.g. Zurek et al., 1992; Moore, 1984], and so gauging the model in this way seems reasonable. Correlation of model lifting events with camera observations and model dynamical processes (e.g., cap edge freezes and low pressure cyclones, etc.) holds promise for qualitatively validating the GCM and supporting conceptual models of dust lifting, as has begun by Newman et al., 2002 ab, studies.

Depending on the results of the isolated tests, we undertake simulations with both schemes active. We address how well the schemes work together, including the degree to which there is feedback between the convective injection scheme and stress lifting (e.g., by stabilizing the environment, does dust devil activity inhibit or reduce stress lifting?). A goal of these simulations will be to find a combined scheme state(s) that allows a good fit to the data. The convective processes, which are found to dominate the background haze maintenance (as we are inclined to believe, from our simulations), are explored in the range of freedom the wind stress parameters have such that they do not damage the observational fit afforded by the convective scheme. This is important for studies of global dust storms that aspire to use the "base state" generated in this portion of the study. The major scientific result that is obtainable from this first part of the dust cycle project is a statement about the relative roles of dust lifting and resolved wind stress lifting in maintaining the background dust haze. Such a result would have important implications for our understanding of how mean climate on Mars might vary with changes in the pattern of solar forcing (from obliquity, eccentricity, and argument of perihelion changes).

A final series of simulations in this part assess the impact of the chosen PBL and radiation scheme parameters. A limited number of simulations using the model with higher vertical resolution will be undertaken. The main impact is on the wind stresses, but this can be accounted for by retuning of the stress threshold and injection rate. The heat flux and the PBL

top do not change a great deal, and hence there is not much change in the convective dust injection. The Hadley Cell Unified Model radiation code has been added to the GCM, which allows a much more detailed simulation if dust radiative heating rates. In combination with the use of more dust particle sizes, we also undertake a few simulations to study the impact of improved radiative properties. We do not use this scheme as standard as it slows down the model.

**1.4 The Generation of spontaneous and variable global dust storms**

The generation of spontaneous, quasi-variable global dust storms in a GCM has been a major technical goal for over a decade. By quasi-variable, we mean matching critical observation that while global dust storms only occur in southern spring and summer, they do so intermittently (once every two or three years in Mars years) at different times in this seasonal window in different years and forming global storms of different sizes (thickness and uniformity of dust coverage). While the prognostic model of Newman et al., 2002b was able to generate a "global storm", there was no significant year-to year variability in activity, the background state from which it evolved was highly unrealistic, and the simulation predicted major dust storm activity in northern summer, in contrast to observations. Our model can generate global storms from a base state that appear realistic, and more importantly do so in some years and not in others [Figure 2]. This is an important prerequisite, as it provides a basis for investigating such dust storms in the model with confidence that we will actually have something to study.

The first part of the thesis maps out the behavior of the dust cycle within the range of dust lifting parameters allowed while still fitting the seasonal temperature cycle. We are able to eliminate the convective injection scheme rate parameter as a free variable. Hence the convective parameter is thrown into the mix to generate a three dimensional parameter volume to be searched. The key factor for dust storm lifting are the wind stress parameters (there is no observational indication or suggestion from our modeling that dust devils are involved in the initiation of major storms). For a given convective injection rate fit to the seasonal cycle, variations in the stress threshold and stress lifting rate will move the model between states with no dust storms (rate too low and/or threshold too high) and states with excessive and regular dust lifting (rate too high and /threshold too low). We systematically map the behavioral regimes of the model. One important question is: how small is the range of

parameters that yield inter-annually variable global dust storms? If it is very small, the question of why Mars sits at such a "special" place in parameter space will be raised. We find in our simplistic system (with a relative low resolution, lack of small scale circulation, uniform stress threshold conditions all over the planet and other simplifications) that the same kind of climate is simulated year after year and thus to capture any kind of transience in the system, the range of parameters has to be fairly narrow. This is the range that gives us simulations with inter-annually variable dust storms. Whether real Mars is finely tuned or not is still under speculation. Pankine and Ingersoll [Pankine & Ingersoll, 2002] hypothesize that the negative feedback between the stress thresholds and the amount of dust on the surface is what keeps the system so finely balanced. When dust is depleted the threshold becomes higher, thus disabling new storms from developing. In the meantime, depleted sites are replenished by dust devils and dust fall out in the absence of big storms, and the threshold becomes lower. Thus conditions are again conducive for a big global storm.

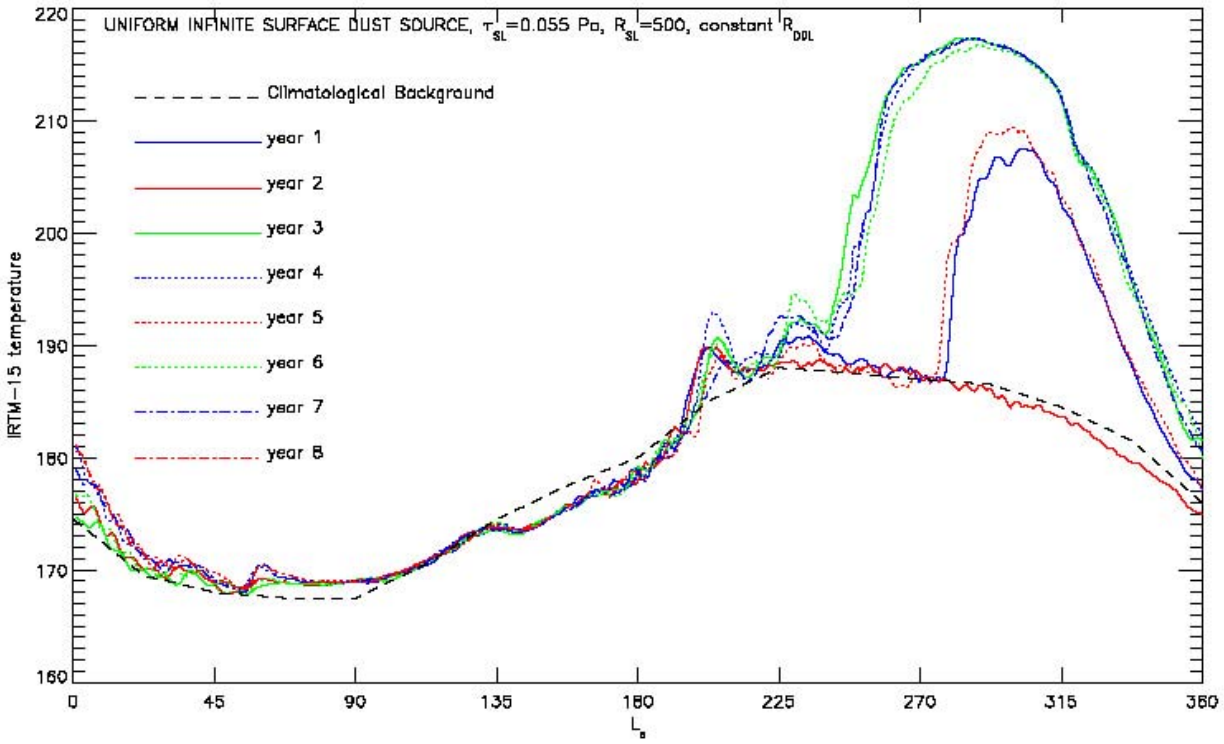


**Figure 2:** Simulation of spontaneous, quasi-variable global dust storms in a single, multi-year annual simulation with the Mars GCM. The storms are indicated by the dramatic rise in temperatures in late southern spring and summer (Ls=225-300). Note that there is no drift in storm activity: years without storms are interspersed with years with global storm activity.

For cases in which quasi-variable global storms occur, we thoroughly examine the nature of storm development (e.g., from synoptic meteorology point of view, how do storms grow? What dynamical systems are involved in triggering the storms?). We examine the importance of radiative feedback by comparing the model circulation at the same season in different years from the same run. A major question revolves around dust storm shut off. What causes the lifting mechanisms to run down as the storm reaches global extent? Is there a radiative negative feedback mechanism or is source expiration required? Where do the storms start and are the predictions consistent with observations? The storms are examined in detail in comparison with observations available from Martian global dust storms (for initiation and growth this is limited to the two storms of 1977 and the global storm of 2001). The zonal

mean temperature structure and the local time variation of temperature (the thermal tide) are used to check on the quality of the simulated storms.

The complete sequence of global dust storm simulations is shown in Table 2. The first line item totals simulations required developing the stress lifting parameter sweep designed to identify the different regimes of Martian dust storm activity. The second line totals follow-up decadal simulations designed to develop a longer baseline for simulations that appear realistic. In all cases, we have chosen to examine the situation in which the supply of dust at all locations is effectively infinite. This is done to isolate the range of dust storm behavior that can emerge naturally from the model's internal atmospheric variability. Global storms resulting from this work correspond to an emergent state switching behavior in a periodically forced, short-memory system (as a consequence of internal variability near a state-switching threshold). A wholly separate mechanism involving interactions between the short (sub-annual) memory atmosphere and the long (multi-annual) memory surface dust deposits may also be important, but these experiments are deferred to the next section of the project so as not to confuse mechanisms.

| **Simulation** | **Number of simulations** | **Computational time (days)** |
|---|---|---|
| **Stress-parameter sweep** | **100(X 5 year simulations)** | **500** |
| **Extended simulations** | **5 (X 10-year simulations)** | **150** |
| **PBL/Radiation sensitivity** | **10(X 5 year simulation)** | **50** |

**Table 1**: Simulation series, number of run per series, and computational time for part two of the project (global dust storms). Many simulations run concurrently or in parallel.

**1.5 Experiments with Prognostic surface dust deposits.**

Changes in the surface dust distribution of dust as a result of dust storms has been observed from orbit [Christensen, 1988; Smith et al., 2004] and has been suggested as an important part of inter-annual variability of global dust storms [Haberle et al., 1986]. The observations of air and surface temperatures following the 2001 global dust storm, described in more detail in the introduction, provide the first direct evidence for climactic coupling between changes in surface dust and the atmosphere [Smith et al., 2004]. In this component of the project, we have four goals, to examine the impact of finite dust sources on (1) the seasonal cycle of background dust; (2) on the evolution of dust storms and the pattern of global dust storm inter-annual variability; (3) on the global dust storm characteristics with surface dust dependent threshold parameterizations; and (4) to examine the response of circulation to changes in the surface dust distribution (and hence albedo and surface temperature) following the 2001 global dust storm.

The surface dust deposits are introduced into the model as two dimensional surface budgets (one for each dust size used) in a manner analogous to the way the GCM currently tracks the surface budgets of water and CO2 ice in the seasonal caps (i.e., we will update on every time step a value of dust in $g/cm^2$ for every grid point). Dust is added to the surface in response to fluxes from the lowest atmospheric level predicted by sedimentation scheme. Dust is removed from the surface so as to provide the injection amounts predicted by the lifting schemes. If a surface element is exhausted, dust is not injected into the atmosphere, regardless of the injection rates required by the lifting scheme. In some cases we will couple the surface albedo using the surface dust abundance, the map of underlying albedo from MGS map, and results of surface scattering models. The implementation is simple, but care must be taken to ensure that total dust mass is conserved.

The annual cycle experiments in part one of the projects assumed dust was available for lifting at all locations on the planet. The albedo and thermal inertia data suggest that large dust deposits only exist in limited areas and that in other parts of the planet, dust is very thin or not present. We describe a spatial pattern of surface dust deposits based on albedo and thermal inertia observations [Christensen, 1988; Mellon et al., 2001]. Since the spatial pattern of convective lifting varies over the year as the sub solar point moves in latitude, it is interesting

to investigate if coherence with the limited availability of dust may modify the seasonal cycle of dust injection and hence air temperatures from that examined in part one. Elucidating the magnitude of the spatial dust distribution effect (if any) is the primary goal- changes in the behavior of the cycle and comparison with observations is also examined.

The second and third goals of this part of the project are addressed in longer baseline simulations. We begin with globally uniform but finite volume dust deposits and rerun some of the "good fit" experiments from part two. The impact of dust exhaustion on the evolution of global dust storms is observed. The infinite source simulation does not spin down until southern autumn. We wish to address whether source exhaustion is an important/necessary part of dust storm switch off. Beyond the dynamics of individual storms, we examine whether it is possible for extended simulations to come into equilibrium with exhausted dust. Preferable areas for dust lifting will exhaust at some point, and it is an open question as to whether the model can re-supply these regions (through fall out of the background dust) and if so, on what timescales.

The evolution of global dust storms is examined with a surface dust dependent stress threshold parameterization. When the dust is depleted below a certain amount, the threshold is adjusted such that new lifting centers are activated and there is more inter-annual variability in the system.

We investigate how exhaustible dust affects the ability of the model to generate 'realistic' seasonal cycles with variable dust storms. Failing that, we hope to have isolated problems for future work that have prevented us from attaining this good simulation.

The final experiment sequence involve running a "best case" background cycle simulation for pre- and post-2001 global dust storm patterns of albedo and thermal inertia. The model surface fields are adjusted so as to match the observed surface temperatures before and after the storm. We examine the changes in air temperature and circulation to these imposed changes in the surface thermal properties. The air temperatures can be constrained against observations from Thermal Emission Spectrometer (TES). The circulation vigor is important not only for dust transport, but also for the water cycle. Quantification of the impact on the circulation is an important stand-alone task.

| Simulation | Number of simulations | Computational time (days) |
|---|---|---|
| Background dust cycle | 10 (X5 year simulations) | 50 |
| Dust storms | 30 (X 10 year simulations) | 300 |
| Response of circulation to albedo | 5 (X2 year simulation) | 10 |

**Table 2:** Simulation series, number of runs per series, and computation time for part three of project (interactive surface dust deposits).

The work done in this project moves us towards a greater understanding of the Martian dust cycle. This cycle is a critical component of the Martian climate system, and that in many ways is least well understood. Significant improvements in understanding would have a direct impact not only on the quality and accuracy of current climate models for Mars, but also on the representation of dust processes in the models that seek to understand conditions on Mars in the past. Mars related major paleo-climate problems include the formation of polar-layered deposits, which are stacked layers of dust and water ice. These layers may contain a record of the Martian climate, but the mechanisms of deposition and dependence of layer dust content upon the behavior of dust in the climate system are unknown. Dustiness is also a major concern for Mars spacecraft, and this good model of the Martian dust cycle will have a direct practical benefit.

## 1.5 Conclusions and Further work

This thesis presented results from the Geophysical Fluid Dynamics Models of the Martian Atmosphere capable of radiatively active dust transport, which was developed for the purpose of simulating the observed dust cycle (including dust storms), and thus of improving the realism of the simulated atmospheric circulation and climate. In concluding it is therefore appropriate to begin with summary of how the dust transport scheme was constructed before proceeding to a discussion of how a successful the model was in producing realistic dust cycles and storm events and a realistic atmospheric response. Section 6 outlines future work which

could be performed to further investigate dust transport on Mars using this model and which could remove some remaining deficiencies of the present simulations.

## Chapter 2:

# Simulation of the Martian Dust Cycle with the GFDL Mars GCM

**Abstract**

The Martian seasonal dust cycle is examined with a General Circulation Model (GCM) that treats dust as a radiatively and dynamically interactive trace species. Dust injection is parameterized as being due to convective processes (such as dust devils) and model-resolved wind stresses. Size-dependent dust settling, transport by large-scale winds and sub-grid scale diffusion, and radiative heating in the visible and infrared due to the predicted dust distribution are treated. Multi-year Viking and Mars Global Surveyor air temperature data sets are used to quantitatively assess the quality of simulations. Varying the three free parameters for the two dust injection schemes (rate parameters for the two schemes and a threshold for wind-stress lifting), we find that northern spring and summer temperatures, which are observed to repeat very closely each year, can be reproduced by the model if the background dust haze is supplied by either convective lifting or by stress lifting with a very low threshold and a low injection rate. In order for either of these cases to yield dust storms, and specifically spontaneous and variable global storms, dust injection due to high threshold, high rate stress lifting must be added. The convective scheme is found unable to generate a dust storm (not to be confused with perennial high-opacity background haze) from which we conclude that dust devils do not initiate dust storms (in agreement with imaging observations). In order to supply the background haze, wide-spread and on-going lifting is required by the model. Imaging data provides a viable candidate mechanism for this lifting if it is convective, in the form of dust devils. However, local storms and other observed, non-convective lifting systems appear insufficiently frequent and widespread to satisfy the role demanded by the model. The high repeatability of northern spring and summer temperatures precludes slow fall-out of dust following global dust storms as important for maintaining the background haze. Further quantitative studies of dust lifting observations are needed to determine with confidence the nature of small-scale dust lifting. However, on the basis of the model results and inferences from thermal and imaging data, we suggest that the seasonal cycle of background dust haze on

Mars is maintained by the action of convective processes, and specifically dust devils. Combining the convective scheme and high-threshold stress lifting, we obtain a "best fit" multi-year simulation, which includes simulation of both a realistic thermal state in northern spring and summer and, for the first time, the spontaneous generation of inter-annually-variable global dust storms. This simulation predicts latitudinal and vertical distributions of air temperature that compare well with observations, and produces a variety of spontaneous local-to-global dust storms whose spatial and seasonal distribution compare reasonably well with orbiter camera observations. The model predicts a spatial distribution of convective dust lifting, including a pronounced peak in the Amazonis region, where numerous dust devils have been observed. The annually integrated net dust erosion/deposition is predicted using the full dust cycle, yielding net erosion rates one-to-two orders-of-magnitude lower than if deposition is neglected.

**2.1 Introduction**

Atmospheric dust is a very important component of the Martian climate system. The suspended mineral aerosol interacts with both visible and infrared radiation, and through this interaction, modifies atmospheric heating rates [Gierasch and Goody, 1968; Kahn et al., 1992]. A rich potential for feedback exists due to the non-linear relationship between the dust distribution, heating rates, and the atmospheric circulation that transports dust. The most dramatic example of such feedback is the Martian global dust storm, which over a matter of weeks can completely enshroud the planet with haze [Leovy et al., 1972; Briggs et al., 1979; Martin and Richardson, 1993; Smith et al., 2002]. Of likely equal or greater importance for the mean climate of Mars is the control of the perpetual, but seasonally varying, "background" haze of dust. Models suggest that this haze produces at minimum roughly 5-10K of warming in mid-level air temperatures compared to a clear atmosphere. The means by which this haze is maintained is unknown, but it now seems unlikely that it is maintained by slow fall-out of dust following global dust storms: the high degree of repeatability of air temperatures in northern spring and summer [Richardson, 1998; Clancy et al., 2000; Liu et al., 2003; Smith, 2004] contrasts sharply with the inter-annual variability of global storms.

The seasonal cycle of dust has been observed in a number of ways. Air temperatures have been measured from orbit discontinuously since 1971 [Hanel et al., 1972; Martin, 1981;

Conrath et al., 2000; Liu et al., 2003; Smith, 2004]. These data provide a powerful and highly quantitative constraint on the dust cycle, but one that is convolved with the seasonal cycle of insolation. Dust opacities have been directly measured from these same orbital platforms [Martin, 1986; Fenton et al., 1997; Smith et al., 2001; Liu et al., 2003; Smith, 2004] and for more limited periods from the ground [Colburn et al., 1989. See also Toigo and Richardson, 2000; Smith and Lemmon, 1999]. Germane to the issue of dust injection to support this annual cycle of haze is orbiter imaging of dust storms and dust devils. Local and regional dust storms have been observed from the Viking Orbiter camera [Briggs et al., 1979], and most recently from the Mars Global Surveyor (MGS) Mars Orbiter Camera (MOC) [Cantor et al., 2001]. The coverage and resolution of MOC is such that the catalog of local and regional storms provided by Cantor et al. [2001] now provides a good climatology for a limited portion of one year. Dust devils have been observed in Viking Orbiter images [Thomas and Gierasch, 1985], Mars Pathfinder meteorological and imaging data [Murphy and Nelli, 2002; Metzger et al., 1999; Ferri et al., 2003], and MOC images [Malin and Edgett, 2001; Cantor et al., 2002; Fisher et al., 2002].

Dust is included in all modern numerical models of the Martian atmosphere, but usually as a prescribed opacity. This opacity is either held constant over the course of a given simulation [Haberle et al., 1993; Haberle et al., 2003], or prescribed to vary as a fixed function of season [Forget et al., 1999]. Such approaches are valuable as they allow the dust to be controlled as a free parameter when investigating a variety of atmospheric phenomena. However, these approaches are obviously very limiting when it comes to examining the dust cycle itself. Interactive dust experiments, which involve the coupling between the modeled winds, the dust distribution, and the calculation of atmospheric radiative heating rates were first undertaken in General Circulation Models (GCM) in the mid-1990's [Murphy et al., 1995; Wilson, 1997]. These studies were directly focused on the simulation of forced global dust storms and resulting polar warming phenomena – prescribed surface sources of dust were used to trigger the storms. Annual and inter-annual GCM simulations described by Fenton and Richardson [2001], Richardson and Wilson [2002], and Richardson et al. [2002] used interactive dust with an injection scheme based on surface-atmosphere temperature differences to simulate the seasonal cycle of non-dust storm opacities and air temperature, performing well in comparison with observations [Richardson and Wilson, 2002]. However, simulation of large dust storms

has remained the key focus of GCM dust studies to the present time. Most recently, Newman et al. [2002ab] implemented a set of interactive dust injection parameterizations, allowing interactions between the circulation, radiative environment, and dust injection to be examined for the first time. Critically, this allowed dust injection and dust storms to be generated as prognostic, "emergent" features of each simulation (in contrast to the "forced" nature of previous studies). The Newman et al. [2002b] simulations generated storms similar to the 1999 "flushing storm" event observed by MGS [Cantor et al., 2001; Smith et al., 2001; Liu et al., 2003], likely due to the mechanism described by Wang et al. [2003].

In future papers describing our studies, the dynamics of global dust storms and their inter-annual variability will be a major focus. However, in order to generate meaningful simulations of global dust storms, we believe it is crucial to properly simulate the "background" state from which these storms are spawned. The reason for this, as described further in a companion paper [Basu et al., paper in preparation, 2004, hereafter B04], is that the background dustiness of the atmosphere strongly mediates the response of the atmospheric circulation to a given amount of injected dust, as would be expected as a possible outcome for such a complex non-linear system. This means that one could develop major storms too easily, or with too great a difficulty if the background state of the model is incorrectly (unrealistically) defined. Conversely, generation of a global dust storm in southern summer is meaningless if as a natural consequence of the required dust injection parameters, the model generates global dust storms in northern summer, which is inconsistent with observations [Newman et al., 2002b].

Aside from its control of dust storm genesis, the seasonally varying haze is a critical component of climate on Mars – moderating mean air temperatures and the corresponding circulation. Attaining understanding of the mechanisms controlling this cycle is critical if we are to examine how Martian climate may have differed in the past when forced by different patterns of insolation (such as associated with changes in obliquity [Kieffer and Zent, 1992]). Despite its direct and indirect importance, relatively little effort has been expended directly studying the "background" seasonal cycle of dust and hence air temperatures without prescription. This paper focuses on this cycle.

This study takes advantage of dust injection parameterizations inspired by those developed and used by Newman et al. [2002a]. These schemes focus on two injection mechanisms: lifting by

convective processes (based on a thermodynamic theory of dust devils), and lifting directly related to the model resolved winds. These schemes are still quite primitive in the sense that their scale dependence has not been exhaustively studied. As such, we see this work as a first explorative step. In this light, we use only three free parameters to control the schemes, with the hope that the scale dependence is folded into these constants. As described in Section 3, these free parameters are injection rate coefficients applied to convective and wind-stress lifting, and a stress-threshold for wind-stress lifting. We have extensively explored the phase-space of these free parameters, simultaneously targeting a realistic background (non-dust storm) climate and generation of realistic global dust storms. Realism in the former case is tested through the use of observed global air temperatures as a quantitative constraint. Realism in this latter case is defined as generation of spontaneous and inter-annually variable global dust storms in southern spring and summer (and not in northern spring and summer). The twin requirements of continuous haze and distinctly non-continuous dust storm generation places constraints on the model dust injection parameters that would not be in force if either requirement were imposed alone. The solution that arises in the model is that while stress lifting could create either a background haze or global storms, it cannot do both simultaneously with the same injection parameters. Conversely, dust devil injection cannot generate spontaneous and variable storms regardless of the rate coefficient value. As a result, an idea that emerges in this paper, is one of a natural separation between the roles of convective and wind-stress lifting. However, it seems plausible that convective lifting is not important and that two or more different sets of stress-lifting parameter values could be used simultaneously instead. We examine both hypotheses in light of available observations, which appear to favor convective (and specifically dust devil) supply over supply by local dust storms or other wind-stress related lifting.

In this paper, we provide a brief introduction to the observational constraints, and then proceed to describe the Geophysical Fluid Dynamics Laboratory (GFDL) Mars GCM, and the dust lifting schemes specifically added for this study. The model is then used to explore the areas of phase space wherein a realistic cycle of background dust opacity (as gauged by the air temperatures) is obtained. The results of our experiments suggest that a steady (yet slowly, seasonally varying) and widespread source is necessary. This widespread and persistent source can be generated by convective or wind-stress driven sources. We will argue that observational

constraints favor the convective source, in the form of widespread dust devil activity – though this is not conclusive, and further effort needs to be applied to observationally constrain the roles of the potential steady and widespread sources. In the latter part of this paper, we pick a set of dust lifting parameters that provide a "best fit" to the seasonal air temperature cycle, and that also yield inter-annually variable, spontaneous global dust storms in southern spring and summer. The non-dust storm seasonal cycle of this simulation is examined in detail and compared with observations. Finally, we look at the patterns of net dust lifting generated by this model for current orbital parameters. These simulations provide by far the best model estimates of net dust lifting/deposition to date since the model uses a fully interactive dust cycle and this cycle has been strongly constrained by the thermal observations.

**2.2 Observations**

The temperature and dust opacity of the Martian atmosphere has been monitored telescopically and by spacecraft for a substantial portion of the past several decades [Hanel et al., 1972; Martin and Kieffer, 1979; Martin, 1981; 1986; Colburn et al., 1989; Clancy et al., 1990; 1996; 2000; Martin and Zurek, 1993; Martin and Richardson, 1993; Fenton et al., 1997; Smith et al., 2001;2002; Liu et al., 2003; Smith, 2004]. The behavior of the atmosphere can be summarized in terms of the global-mean, mid-level air temperatures derived from the Viking IRTM and synthesized from Mariner 9 and MGS Thermal Emission Spectrometer (TES) data. Mid-level in this context refers to a region between roughly 10km and 40km altitude, with a maximum weighting on values at ~25km. The weighting function is shown in Figure 1 of Wilson and Richardson [2000] and corresponds to the spectral response function of the IRTM

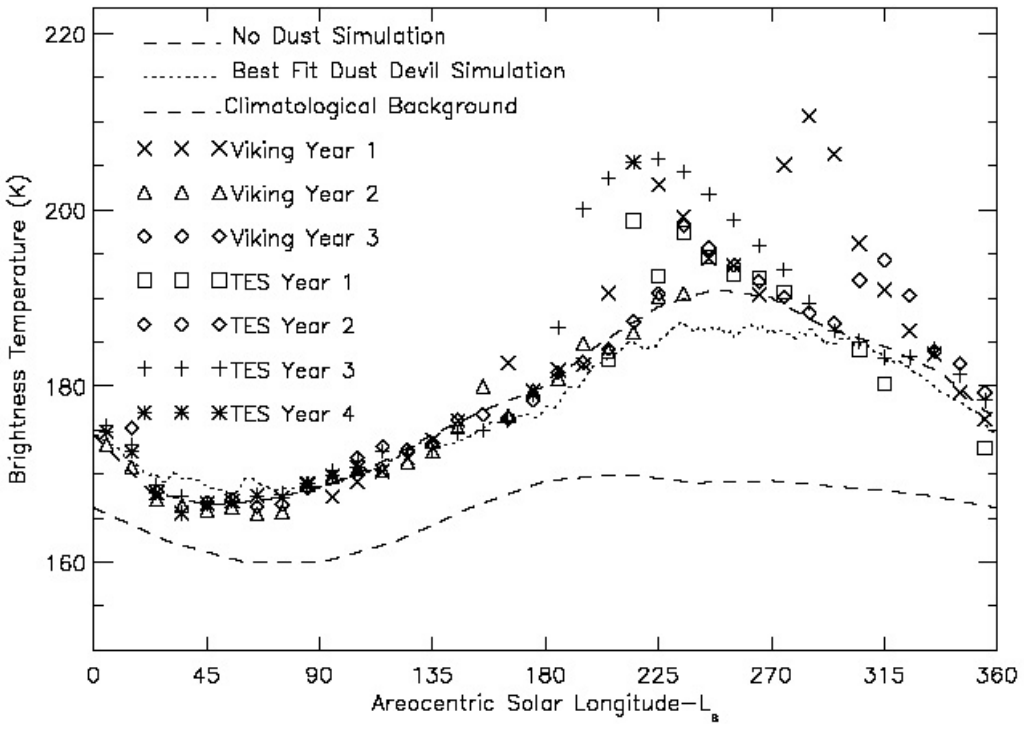


**Fig1:** The seasonal variation of mid-level atmospheric temperatures between 40°S and 40°N derived from spacecraft infrared observations and from selected GCM simulations. The data are taken from the Viking Infrared Thermal Mapper (IRTM) 15-μm channel (corrected, see Wilson and Richardson [2000] and Liu et al. [2003]), and from the Mars Global Surveyor Thermal Emission Spectrometer (TES) spectra after convolution with the IRTM 15-μm channel spectral response function. The corresponding IRTM 15-μm channel weighting function peaks at roughly 25km, with contribution primarily from 10-40km. This weighting function has been applied to the GCM output for optimal comparison with data. A mean seasonal climatology of air temperature (the "background cycle" which excludes large dust storm effects) has been defined via a 'by-eye' fit to the observations. GCM simulations corresponding to the "best fit" dust devil source, and a simulation with no atmospheric dust opacity. The background haze generates about 5-10K of warming compared to a clear atmosphere. Note that the minima near the solstices correspond to the relative deposition of more solar heating pole ward of 40° at these seasons than during the equinoxes.

15-micron channel, which is situated on the vibrational-rotational band of $CO_2$ gas. Brightness temperatures from this channel (or synthesized from other instruments through application of this response function) are often referred to as T15. The T15 data (Figure 1) show a cycle with minimum temperatures in late northern spring, and maximum temperatures during southern spring and summer. The spikes in the data that occur predominantly in southern spring and summer are regional and global dust storms. The combined Mariner 9, Viking, and MGS data record, from which Figure 1 is taken, is more thoroughly described and discussed by Liu et al. [2003]. The repeatability of the cycle throughout northern spring and summer allows a climatological mean temperature cycle to be meaningfully defined. In our case, this

climatology is constructed as a "by-eye" fit to the data: in fact, any number of complex techniques could be used to fit curves to the data, with effectively no impact on the utility and accuracy of the resulting product for our application. This climatology is obviously of much less validity in southern summer - we have chosen to define it as a smooth function, which non-dust storm temperatures in southern summer relax to. This climatology will be used to guide numerical simulations later in this paper. Cross sections of temperature retrieved from TES [Conrath et al., 2000] data provide a more complete constraint on the simulations. The TES data will be used for comparison with the model at particular instants in the seasonal cycle.

Imaging provides a non-quantitative but critical data set for this study. We use these data in the form of condensed summaries [Cantor et al., 2001; Fisher et al., 2002] to constrain the distribution and nature of small-scale dust lifting events.

### 2.3 The Model

The GFDL Mars GCM is a Mars-adapted version of the GFDL SKYHI GCM [Hamilton et al., 1995; Wilson and Hamilton, 1996]. The model has been described in various papers used to study Martian thermal tides [Wilson and Hamilton, 1996; Wilson and Richardson, 2000; Wilson, 2000; Hinson and Wilson, 2004], surface winds [Fenton and Richardson, 2001], the water cycle [Richardson and Wilson, 2002; Richardson et al., 2002], transient waves and cyclones [Hinson and Wilson, 2002; Wilson et al., 2002; Wang et al., 2003], and Martian paleoclimate [Mischna et al., 2003]. Briefly, the model provides a grid point representation of the global atmosphere from the surface to roughly 85km altitude. In this paper, a horizontal grid point spacing of 5° in latitude and 6° longitude is used, with 20 vertical levels of non-uniform thickness. The model includes treatment of: the $CO_2$ cycle, with prognostic seasonal variations in surface pressure and seasonal ice cap extent; the water cycle, with transport of atmospheric water vapor and ice, and exchange with surface water ice deposits; radiative interactions in the visible and thermal infrared with dust and $CO_2$ gas; topography derived from Mars Orbiter Laser Altimeter gridded data; and calculation of surface temperatures using a 12-layer subsurface model and surface energy balance including the effects of measured albedo and thermal inertia.

The model includes transport of dust resulting from advection by the model-resolved winds, horizontal and vertical sub-grid scale diffusion, and size-dependent sedimentation. As mentioned above, the instantaneous dust distribution is used within the model radiation subroutine to determine the solar and thermal infrared heating/cooling due to dust. Two different particle sizes are treated to provide a minimal representation of particle size distribution changes. The radiation scheme treats dust as an absorbers and scatterers in the visible (with a single scattering albedo of 0.92). In the thermal infrared, only absorption and emission are considered (see Wilson and Hamilton [1996], and note that in some versions of the GFDL model, a more detailed radiative scheme has been used [Hinson and Wilson, 2004]). Using fixed dust distributions or finely tuned interactive dust injection, it has proven possible to simultaneously fit air temperatures and observed TES dust opacities.

The new components of the model for this study relate to dust injection. Dust injection in the real Martian atmosphere takes place in association with motions on a variety of scales, running the gamut from synoptic motions to those associated with boundary layer turbulence. Obviously, this full spectrum cannot be explicitly treated in a model with grid spacing of order hundreds of kilometers. We therefore are faced with choices about how we parameterize lifting processes that are not model resolved. Imaging observations suggest that dust lifting is at least sensitive to the "mean wind" (on some scale) and to convective motions. The former is indicated, for example, by dust streaks and the latter by dust devils captured in spacecraft images [*e.g.* Fenton and Richardson, 2001; Cantor et al., 2002]. On this basis, it seems plausible to base lifting around schemes that are related to the strength of the resolved wind (or actually the imparted stress) and the vigor of boundary layer convection. This is not necessarily unique – on the meso- and micro-scales, the "mean wind" can be modified by local topography and surface thermal contrasts such that a number of different stresses are working within a single GCM grid cell. It again seems plausible that these sub-resolved winds would scale with the strength of the grid-resolved mean wind, but it is not necessarily so (profoundly non-linear acceleration processes can be at work in some circumstances [Magalhaes and Young, 1995]). A detailed mesoscale modeling study is necessary to address the importance of micro- and meso-scale influences on "mean wind" dust lifting. In any case, for our initial study of the Martian dust cycle, it would seem to be prudent to devise parameterizations that represent some dependence on mean winds and on convective vigor, while at the same time, keeping the

schemes sufficiently simple that they can readily be comprehended. No doubt more complex and realistic schemes will emerge in the future – their impact in changing the results of this study (or not) will be of great importance for developing an increasingly complete understanding of the Martian dust cycle.

The two schemes used in this paper are inspired by those first implemented in a GCM by Newman et al. [2002ab]. The first relates lifting to the model-resolved wind via relationships worked out in wind tunnel experiments [e.g. Shao, 2001]. The second uses the Renno et al., [1998] thermodynamic theory of dust devils as the basis for predicting convective lifting. The representations of lifting are incomplete in that there is no scale-dependence (no explicit dependence on grid spacing) such that the schemes need to be adjusted for model runs with different resolution. Our experience suggests that the stress scheme requires larger scale-correction than does the convective scheme. In any case, parameterizations in the future should account for resolution variations. More importantly, we have intentionally chosen to take only the functional forms for the lifting schemes from wind tunnel results and from theory: We have chosen to use free parameters to scale the functions as an active part of our experiments. We feel this is an honest reflection of our ignorance of the micro-scale processes involved in dust lifting. Tunable free parameters allow us to side step this ignorance (or rather contain this ignorance within a parameter, whose meaning may be examined at some later time). The connection to reality is provided by well-known constraints: the large-scale atmospheric temperatures and the functional forms of the lifting parameterizations that are based on the observed physics. In the next two subsections, we describe these parameterizations.

### 2.3.1 Convective ("Dust Devil") Parameterization

The parameterization of small-scale convective motions is based on thermodynamic theory of dust devils [Renno et al., 1998]. This choice is rooted in our bias that dust devils are likely the dominant form of convective lifting (not proven and in need of observational testing). However, this choice is actually quite general and reasonable since the functional form relates lifting to the stability of the boundary layer and the vigor of heat transfer between the surface

and the atmosphere: more generally, the scheme links lifting to the strength of convective motions and as such should capture the nature of any convective lifting.

The convective scheme (hereafter generally referred to as the dust devil lifting or DDL scheme) is implemented using a simple fixed function that is based on the thermodynamics of dust devils [Renno et al., 1998]. The Renno et al. [1998] heat engine theory of dust devils relates the dust lifting intensity to the sensible heat input, $F_{heat}$ at the surface and the thermodynamic efficiency, $\eta$, which depends on the depth of the Planetary Boundary Layer (PBL). The lifting rate is then related to the intensity with the application of a multiplicative injection rate constant, $R_{DDL}$. This free parameter allows for potential (and likely) offsets between the lifting of a single dust devil responding to a local heat flux and thermodynamic efficiency, and that of an ensemble of dust devils responding to a range of local environments within a model grid box of roughly 300km width, and with grid-average values of sensible heat flux and thermodynamic efficiency. Since this multiplier is unknown *a priori*, we use it as one of the available tuning parameters in the model, with the seasonal cycle of air temperatures defining the "target" for tuning, as described later in this paper. The dust devil injection function is specifically defined as:

$$F_{DDL} = R_{DDL} \times F_{heat} \times \eta$$

The dust injection rate scheme is implemented in the GCM such that so long as the function is positive at a given grid point, there is some lifting at that grid point. There is no activation threshold defined for DDL. There is no inherent time/space variation or randomness in this

function.

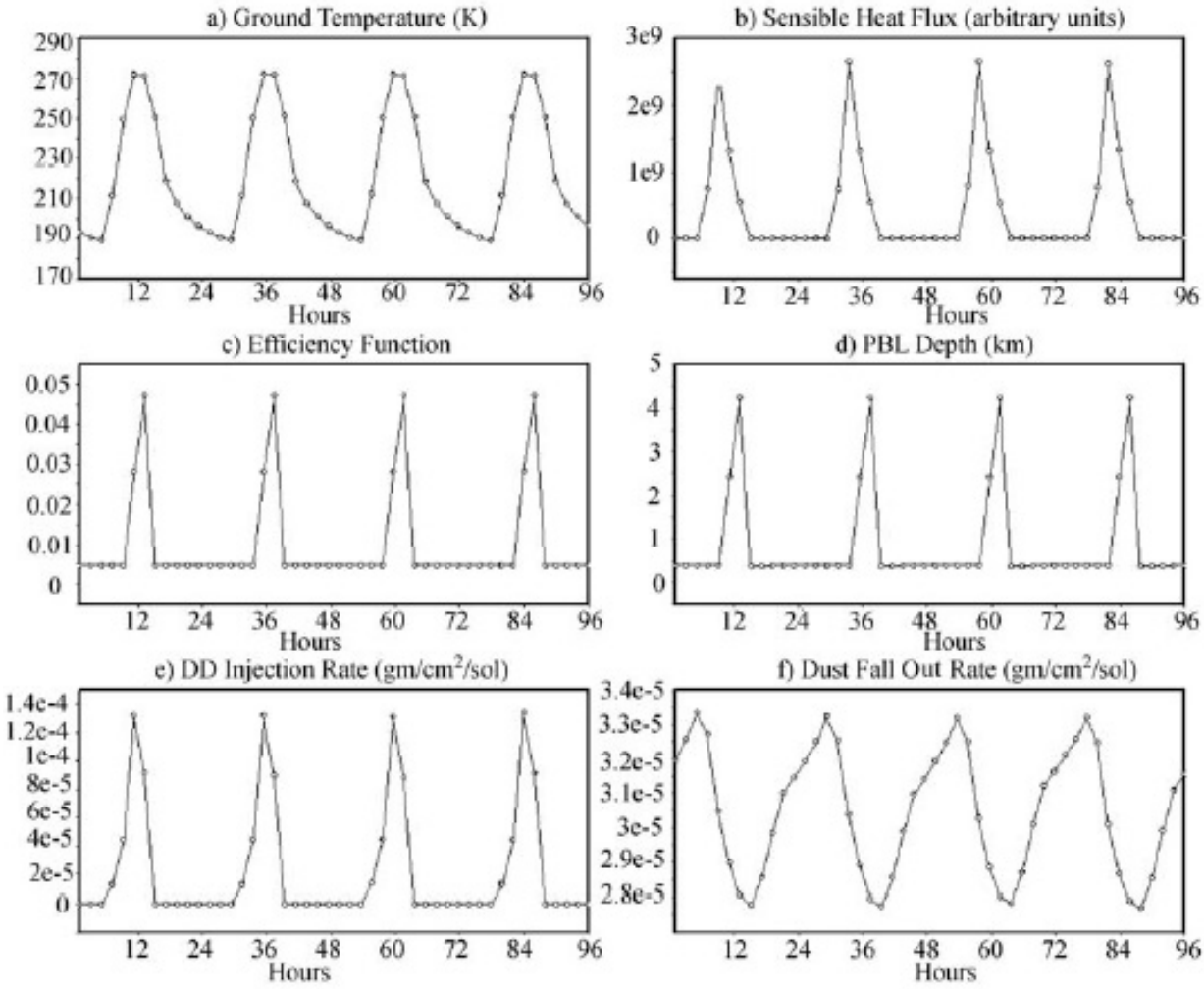


**Fig2:** The relationship between predicted dust devil lifting (DDL) rates and various model variables as a function of local time for a point at 0° longitude and 0° latitude for $L_s$=259°. (a) Solar heating of the surface and subsequent convective motions to shed this heat provides the primary drive for dust devil activity. (b) The sensible heat flux peaks earlier than the ground temperature peak (*i.e.* in the morning). At this time of day there is greatest contrast between the surface and atmospheric temperatures and consequently the strongest convective drive. (c) and (d) The thermodynamic theory of dust devils [Renno et al., 1998] suggests a strong dependence upon an "efficiency function" which is itself dependent upon the depth of the planetary boundary layer (PBL). The PBL depth peaks later than the ground temperature maximum – in the afternoon – as it takes time for the PBL to entrain successively higher portions of the free atmosphere. (e) The resulting dust devil injection is a convolution of the sensible heat flux and to the PBL depth. (f) The net effect of dust devils can only be determined when the dust fall-out rate is also considered. While the fall-out is about an order of magnitude lower, the fall-out never falls below 80% of its maximum value (at this location), providing a very steady sink. The instantaneous spatial pattern, shown in Figure 3, is therefore much smoother than that of injection.

The relationship between the GCM DDL and the model variables upon which it depends are illustrated in Figure 2. These output are taken from a specific grid point in the model at a specific time (latitude, longitude, season), but are representative of the behavior of the DDL scheme generally with that of the surface temperature. The $\eta$ function [Figure. 2c] is related to the ground temperature through the convective boundary layer depth [Figure. 2d], which has a similar shape to the diurnal cycle of surf ace temperature, but offset by a few hours to later local times (since air temperatures lag the surface temperature). The combination of the sensible heat flux and the $\eta$ function result in a shift in peak dust devil activity, and hence dust devil lifting in this parameterization, to the early afternoon. This phase shift is in keeping with (results directly from) the predictions of the thermodynamic theory [Renno et al., 1998]. Clearing of dust from the atmosphere is accomplished in the model by gravitational sedimentation. The settling associated with the particle sizes used in this study have been shown to allow the atmosphere to relax back from prescribed dust storms in a realistic manner (see Wilson and Richardson [1999]).

The spatial relationship between the net dust injection, dust fall-out, and ground temperature (and through intermediary variables) is shown in Figure 3, which presents output from the model at $L_s$=259° (where $L_s$ is the seasonal indicator on Mars, measured in degrees from 0° at northern spring equinox). Aside from dictating the pattern of insolation, the season is not important, and the spatial relationships illustrated here hold generally in the model. Surface temperature very strongly controls instantaneous net dust injection (Figure. 3a), as one would expect and indicated in Figure 2. Ground temperatures and lifting peak near the subsolar latitude and near noon, with the injection delayed slightly with respect to ground temperatures. The spatial pattern of convective PBL height is illustrated in Figure. 3b. This is similar to plots for other Mars GCM's (e.g., Haberle et al., 1993). The PBL parameterization in the GCM does not make an explicit prediction of the PBL height, so this value must be calculated. This is done on each time step and for each grid point by deriving the potential temperature for each layer in each model atmospheric column (i.e., at all levels above each grid point) for the predicted air temperatures prior to convective adjustment. Working upwards from the surface, when a layer is found whose potential temperature exceeds that of the near surface layer, the

pressure of the interface between this higher potential temperature layer and the one below it is recorded as the local PBL top pressure. PBL geometric height is easily recovered by upward hydrostatic integration.

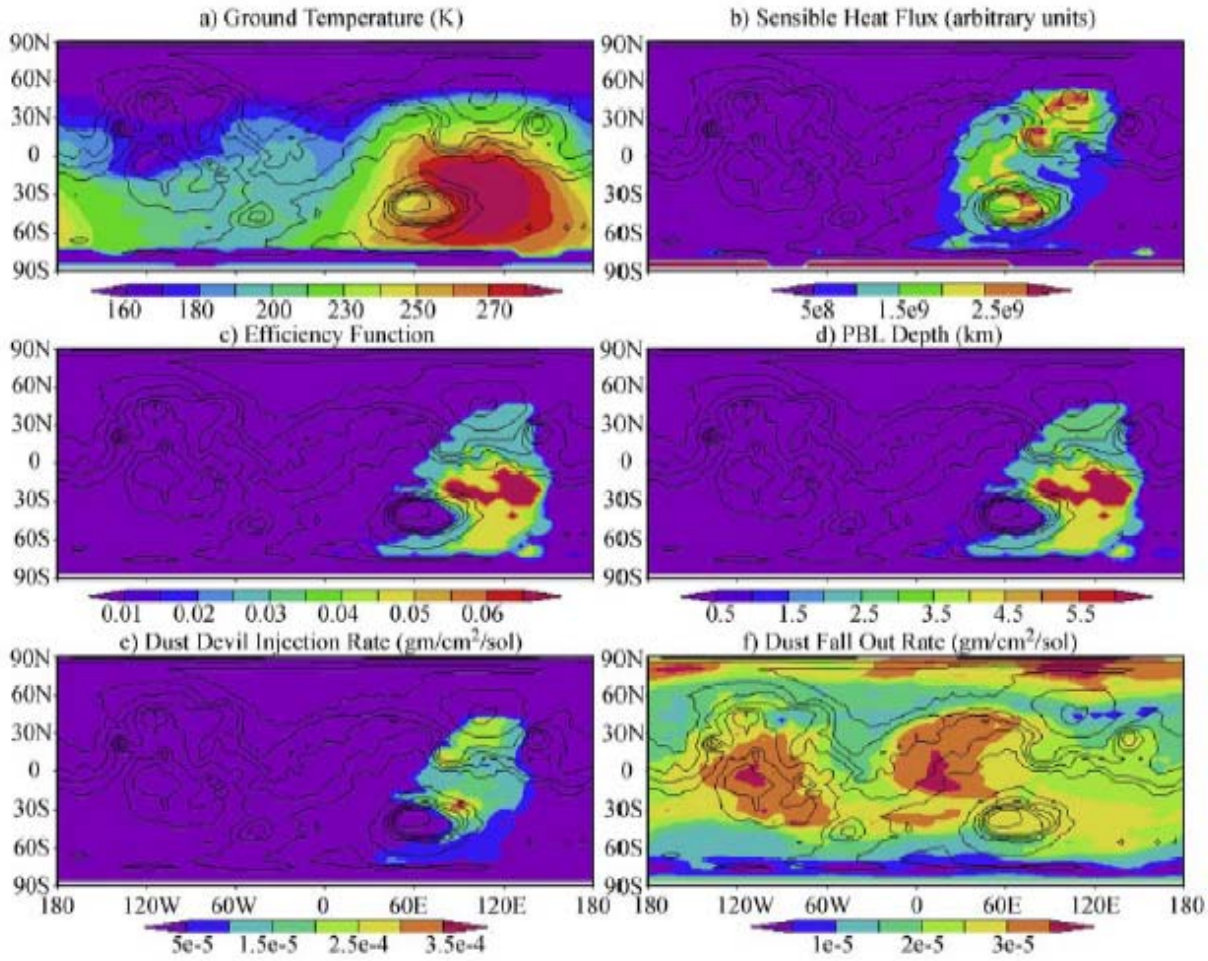


**Figure3:** A single time-step from the sequence shown in Figure 2, but for all locations on the planet, showing the spatial relationships between the variables.

The sensible heat flux (Figure. 3c) and $\eta$ function (Figure. 3d) patterns follow those of the ground temperature and PBL depth, much as would be expected from Figure 1. The deviations from a smooth spatial pattern, with values monotonically falling with increasing latitudinal and longitudinal distance from the subsolar point reflect surface variations in the thermal inertia and albedo of the surface via their influence upon ground temperature. In addition, the sensible heat flux pattern is influenced by the circulation through the surface

wind stress. These functions combine to yield the net DDL, illustrated in Figure. 3e. This figure provides a map of the model-predicted dust devil activity and provides a gauge of the spatial variation in the relative activity (number per unit area, mean size, *etc.*) of dust devils. Figure 3f shows the spatial pattern of dust fall-out. This is a much smoother function, as the fall-out continues whenever dust remains in the atmosphere. In a steady state wherein some dust remains suspended in the atmosphere, the fall-out cannot compete effectively with the rate of dust injection where it is highest. As such, the instantaneous injection function (Figure. 3e) strongly resembles the pattern of net instantaneous injection (injection minus fall-out, Figure. 3a).

### 2.3.2 Stress Lifting Parameterization

Dust lifting owing to the stress applied to the surface by the drag of model-resolved winds, or stress lifting (SL) for short, is implemented in the GCM in addition to DDL. The scheme assumes that a direct relationship can be drawn between the wind stress and dust emission, as has been observed on the Earth [Shao, 2001]. For Mars, this would appear to involve a leap-of-faith, were it not for images of dust plumes and storms apparently resulting from high wind stresses: Wind tunnel experiments under Mars-like conditions of pressure and temperature, suggest that very high (unrealistic) wind stresses, and hence winds would be needed to directly loft the micron and sub-micron sized dust particles found in the Martian atmosphere [Greeley et al., 1992]. Instead, it has become accepted that the wind induces sand-sized particles (~100 micron) into motion, "saltation", which then impact into dust deposits, causing these dust particles to be launched into the atmosphere. The stress threshold required for sand-sized particle motion is lower than that for dust for reasonable estimates of inter-particle cohesion (if there were no electrostatic or other physical cohesion of particles, there would be a continuous easing of the stress threshold for lifting as particle size decreased). As such, while we will talk about the stress threshold for dust injection from this point onwards, what we are really talking about is the threshold for saltation of sand sized particles that then are assumed to inject dust. It should be noted that this conceptual framework requires sand-sized particles (sand or clods of dust) to be present at all locations on the surface, which is of some concern. More generally, the microphysics of dust mobilization is not well understood beyond the general observation from orbit [Briggs et al., 1979; Cantor et al., 2001] and from the ground

[Moore, 1985] that high winds seem to cause dust injection. If this is true, and by analogy with the Earth, it is likely that wind stresses are the important factor. In any case, we use functions for the SL that have a strong dependence of lifting on wind stress, as would be expected from a wide variety of wind related lifting mechanisms, be it via saltation or direct lifting.

The parameterization generally used in this study defines the dust injection flux $F_{SL}$ as follows:

$F_{SL} = R_{SL} X f(U_{drag}); u>u_{thresh};$

$F_{SL}=0; u<u_{thresh}$

where $R_{SL}$ is a multiplicative rate parameter, $\rho$ is the air density, $U_{drag}$ is the frictional velocity, and where $f(U_{drag})$ can be a simple function of the wind velocity, $u$, boundary layer eddy diffusivity, and the threshold wind speed, $u_{thresh}$. SL is threshold dependent–there is lifting only when the wind stress $\tau$ ($\tau=\rho U_{drag}^2$) is greater than $\tau_{SL}$–the threshold wind stress corresponding to $u_{thresh}$. There is no dust lifting when the wind stress is below $\tau_{SL}$. The threshold stress can be taken from wind tunnel experiments (see Greeley et al., 1992). However, due to concerns over the ability of any numerical atmospheric model to accurately predict the absolute values of surface stress, the possibility that wind tunnel experiments miss some important physics (such as electrostatic effects), and the applicability of local thresholds to the average wind over modeled spatial scales of hundreds of kilometers, we believe it more prudent to use the threshold as a free parameter. Thus, the activation threshold wind stress, $\tau_{SL}$, and the multiplicative injection rate factor $R_{SL}$, yield two free parameters associated with our dust SL scheme.

A variety of functional forms for $f(U_{drag})$ have been developed based on wind tunnel experiments and terrestrial field campaigns (*e.g.*, Shao, 2001). Many of these forms show a roughly cubic dependence upon the drag velocity, *i.e.* $f(U_{drag}) \propto U_{drag}^3$. In the majority of the simulations described in this paper and its companion, a form of roughly this kind is employed (Figure 4a).

A more complex form for $f(U_{drag})$ is described in Newman et al. [2002a], which is itself derived from a combination of the formations given by White [1979] and Seguro and Lambert [2000]. In this formulation:

$$f(U_{drag}) = \int_{U_{dragthresh}}^{\infty} V_N \times w(U_{drag}) dU_{drag}$$

$$V_N = 2.61 \frac{\rho}{g} \left(U_{drag}\right)^3 \left(1 - \frac{U_{dragthresh}}{U_{drag}}\right) \left(1 + \frac{U_{dragthresh}}{U_{drag}}\right)^2$$

where $V_N$ is the vertical flux of particles lifted into suspension [White, 1979], $U_{dragthresh}$ is the frictional threshold velocity corresponding to the threshold stress, $\tau_{SL}$, and $w(U_{drag})$ is the Weibull distribution [Seguro and Lambert, 2000].

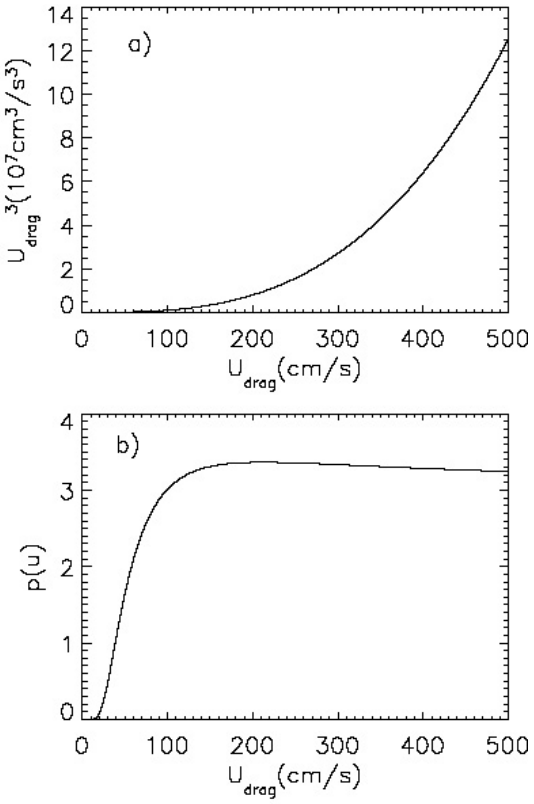


**Figure 4.** (a) The stress-lifting scheme is based on a formulation that relates the dust injection rate to the cube of the frictional velocity ($U_{drag}^3$). This formulation is used, with some variation, in numerous schemes for terrestrial application [Shao, 2001]. (b) In order to capture the statistical effects of gusts, Newman et al. [2002a] used a function, which does not fall to zero at the threshold frictional velocity for lifting (see text for details). However, this functional form yields a very sharp drop in efficiency below the threshold (150 $cms^{-1}$ in this example), which is compounded by the cubic dependence on drag velocity. Above the threshold, the function plateaus and does not modify the lifting rate. Due to the simplicity of a scheme with no lifting below threshold and cubic lifting above, we chose not to employ a "gustiness" parameterization.

The Weibull distribution provides a means of statistically accounting for "gustiness" in the wind by allowing some lifting at wind stresses below the threshold. Use of the Weibull distribution in this way makes $f(U_{drag})$ a continuous function of $U_{drag}$, even though a threshold stress is specified. When this scheme is implemented, $F_{SL}$ is not set to zero when $\tau < \tau_{SL}$, and some lifting occurs for all values of wind, although the amount falls rapidly for stresses below threshold. The Weibull distribution is given by:

$$w(U_{drag}) = (\kappa / c)(U_{drag} / c)^{\kappa-1} exp[-(U_{drag} / c)^{\kappa}],$$

where $c$ is a scale speed (set equal to the drag velocity output every time step) and $\kappa$ is a dimensionless shape parameter (low $\kappa$ values represent high gustiness). Using a value of $\kappa=1$ [Lorentz et al., 1996] we get the following expression for $f(U_{drag})$:

$$f(U_{drag})=k\times\rho\times U_{drag}^{3}\times p(u),$$

where $p(u)=(2u^2+4u+3)/exp(u)$, $u=U_{dragthresh}/U_{drag}$, and $k$ is a constant. This relation provides a function that is zero for Udrag=0, and grows, dominated by the exponential term, to a value at $u=U_{dragthresh}/U_{drag}=1$, at which the function essentially plateaus for $U_{drag}>U_{dragthresh}$ (Figure 4b). The prediction of some lifting for $U_{drag}<U_{dragthesh}$ with this function is an attempt to capture lifting due to gusts at scales not resolved by the model. The value of $\kappa$ chosen determines how sharply lifting declines as the $U_{drag}$ decreases below the threshold.

In either case, for values of wind stress above the threshold, the lifting rate is $\propto U_{drag}^{3}$ and the only difference is the sharpness of the stress threshold cut off for lifting for $U_{drag}<U_{dragthesh}$. Partly because a very much simpler interpretation of the results emerge if the threshold is sharp, partly because it seems useful to employ a physically simple parameterization for a system that is poorly understood, and partly because the observations in hand (*e.g.* Moore, 1985, Zurek et al., 1992) do not appear to readily support the widespread, low rate dust injection that the continuous scheme generates, we chose to use the simple, threshold dependent, $U_{drag}^{3}$ scheme.

A consequence of the threshold dependent scheme is that dust is only lifted where the wind stress exceeds a preset value. Some idea of the fraction of the surface from which dust is being lifted at any moment in the model can be gauged by examining snapshots of the surface wind stress. Figure 5 shows such stress distributions at the central meridian for $L_s=45°$ (mid northern spring) and $L_s=225°$ (mid southern spring). From this Figure, it is easy to appreciate that the choice of stress threshold

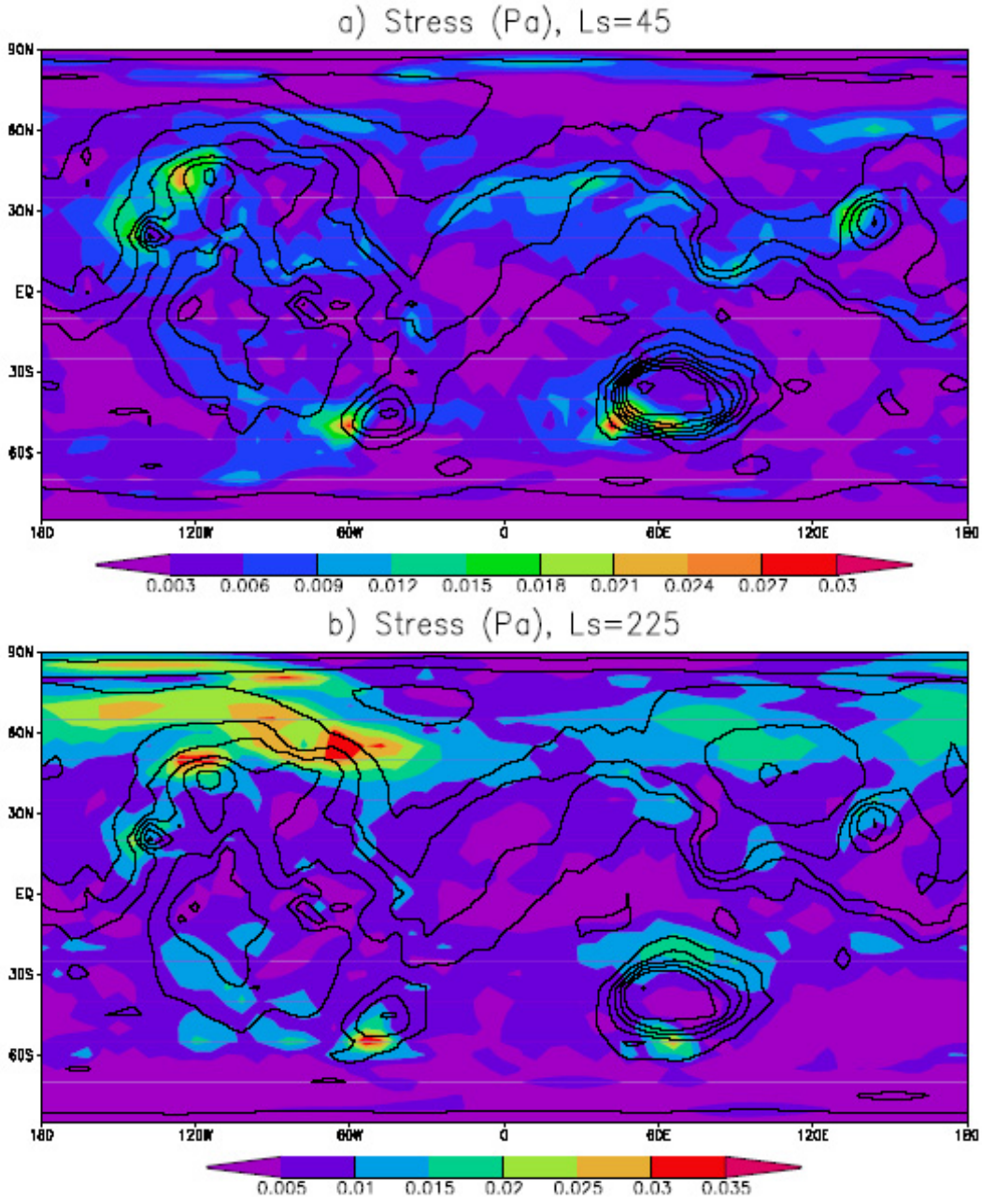


**Figure 5.** Diurnal-mean surface stresses for a) $L_s$=45 and b) $L_s$=225. The topography is contoured in black. The results are for the no-threshold SL case.

effectively is a choice of what fraction of the area of the surface that one wants the model to lift dust from at any given time. Specific regions of the planet tend to be associated with higher stress, such as along the eastern side of the Tharsis plateau, in and around the Hellas basin, along the seasonal ice cap edge, and along the convergence zone of the Hadley

circulation. Lesser dust lifting activity occurs elsewhere in the domain. As the threshold is increased, the locations of dust lifting become increasingly tightly constrained to the major high stress zones.

### 2.4 Fitting the Annual Cycles of Air Temperature and Dust

The combined GCM dust injection parameterization has three free parameters that can be set to unique, globally- and spatially-fixed values for a given simulation. All simulations were run for more than one year to check for variability and to allow assessment of the full annual cycle. The seasonal cycle of globally averaged air temperatures was used as our primary metric for checking the quality of simulations, as it is the thermal state that is most important for determining the dynamic response of the atmosphere. The procedure for evolving the free parameters towards values that yielded a realistic climate simulation involved checking the annual cycle output, assessing whether the simulation was too cool or too warm, and then adjusting the injection to higher or lower values, accordingly. For clarity and in order to develop some intuition about how the two injection schemes influence the climate simulation, we initially examined the convective and wind-stress lifting schemes separately, before proceeding to look at combined injection simulations. For simulations that met the minimum requirement of fitting the global-average temperature trend, the zonal and height variations of temperature were then examined for more detailed insight (Section 5).

In this study, we present both dust injection scheme rate parameters in arbitrary units. The main reason for this is that we have found that a given set of parameter values will not produce the same climate when model resolution is changed. We believe that these parameters would not yield the same climate if used in a different GCM (variations in boundary layer scheme will likely also have a significant impact). As such, we wish to emphasize the importance of the tuning process and approach, rather than the specific values of the rate parameters. In this light, appropriate reproduction of our results (or not) depends upon using our tuning technique, not on using our rate coefficient values. One obvious concern regarding this approach that the reader ought to bear in mind is whether our injection rates yield a characteristic lifetime of dust in the atmosphere that is consistent with observations. We examine the lifetime explicitly at the end of this section, finding lifetimes that are consistent with lifetime observations derived in the decay phases of dust storms.

The climatology of mid-level air temperatures is taken from the multi-year, multi-spacecraft T-15 record compiled by Liu et al. [2003] and introduced in Section 2 and Figure 1. As a curve, the air temperature data provide a very compact and easy-to-digest metric against which to test the model. In all cases, "synthetic" T15 data are generated from the model by application of the IRTM 15- micron channel weighting function to individual pressure-temperature profiles. Such model outputs have been shown by Wilson and Richardson [2000] and Richardson and Wilson [2002].

### 2.4.1 The Dust Devil Source

The dust devil lifting (DDL) parameterization has a single tuning parameter, which is the injection rate coefficient as discussed in Section 3.1. As such, the fitting process is very straightforward. Without any atmospheric dust, the model produces air temperatures that are about 15K cooler than observed (Figure 1). In order to increase these temperatures, dust is needed in the atmosphere to absorb solar radiation. Since the amount of dust injected into the atmosphere is controlled by the rate parameter, it can be adjusted until a good fit is obtained at some point in the year. We place most emphasis on the northern late spring and early summer ($L_s \cong 20°$-$140°$), as this is the period for which the real atmosphere has a high degree of repeatability [Richardson, 1998; Liu et al., 2003], as it is least affected by large dust storms.

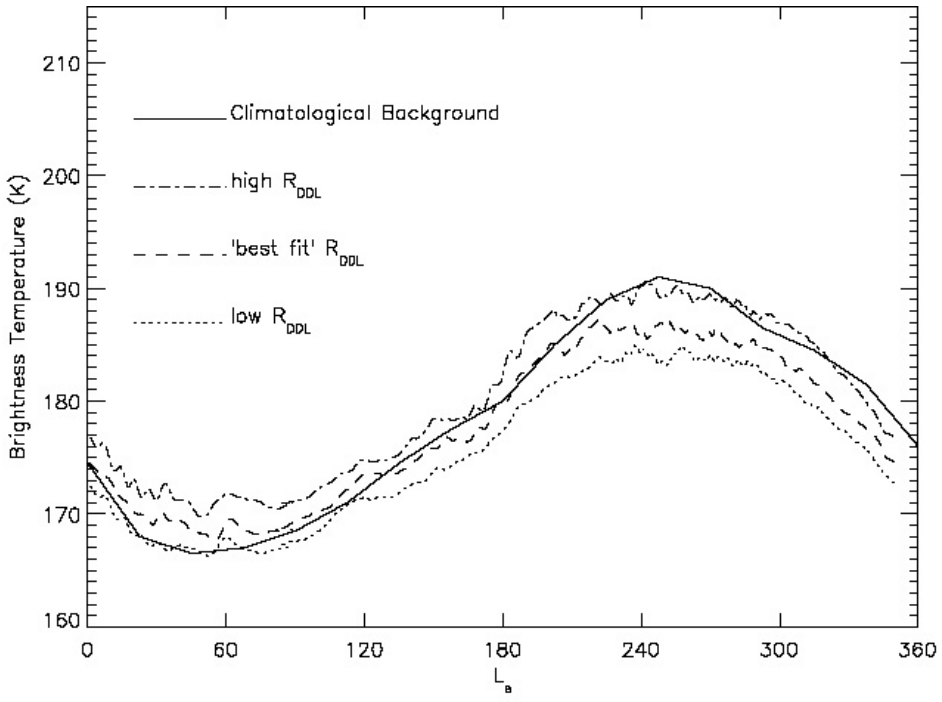


**Figure 6.** Atmospheric temperatures predicted by the model and observed. Model results are shown for different values of the dust devil lifting scheme rate parameter, $R_{DDL}$. The climatological background (Figure 1) is plotted for reference. A very good fit to the air temperature curve through northern spring and early northern summer is obtained with relatively low rates. Somewhat increased values are needed to fit the late northern summer temperatures – though the observed temperatures in this seasonal range may be influenced by increasing dust storm activity. In southern spring and summer the determination of the "background" climatology is extremely difficult, and there is likely always some influence of dust storms.

Figure 6 shows several curves corresponding to different dust injection rate parameters ($R_{DDL}$) in Section 3.1. In each case, the shape is similar, with the main difference being translation of the curve to higher (lower) temperatures with increased (decreased) injection rate. As there is no physical basis for allowing the injection value to change with location or season, we use a single value of $R_{DDL}$ at all grid points and at all times in any given simulation. Each simulation is begun from an initially spun-up state, with the simulation being run for sufficient time that there is no sensitivity to dynamical initial conditions. The pressure cycle is tuned by modifying the total amount of available $CO_2$, which partitions itself between seasonal ice and atmospheric gas. As a result of starting from a steady-state condition, startup transients for each simulation set are minimized. The simulations are allowed to come to steady state by running the model

for one year before analysis of any given simulation (the simulations were found to come into steady-state in less than 100 days). Note that the particular thermal state of the restart file does not influence the final climate simulation, as has been gauged by running the model with a fixed set of injection parameters from "restart" files with different initial states.

Since the DDL scheme has no time-varying parameters, we have no control over the "shape" of the modeled annual air temperature cycle (by "shape" we mean the curve in the air temperature data as a function of season). The shape is therefore an intrinsic character of the DDL scheme and its response to forcing. It has been shown before that very simple schemes designed to mimic convective processes (using a very a simple function of surface-atmosphere temperature contrast) can produce a seasonal cycle shape that is in relatively good agreement with observations [Richardson and Wilson, 2002]. The details of the shape are interesting and somewhat more complicated than they may superficially appear. However, their discussion is deferred to a later paper focusing on detailed interpretation of the observed seasonal cycle on Mars. Suffice it to say that ability to fit the shape is not a controllable factor and, in consequence, the fact that the DDL scheme can fit the curve reasonably well [Figure 6], is an important piece of evidence suggesting that either DDL itself or the pattern of forcing driving it are of fundamental importance in generating the annual cycle of air temperatures via the dust loading. In contrast, constant opacity simulations yield quite different curves, with dual temperature maxima in southern spring and summer. It should be noted that no matter how high the $R_{DDL}$ parameter was set, variable global dust storms could not be generated (we take the firm view that a simulation with inter-annually repeatable high dust loading in both summers is not generating global dust storms, but instead is simply generating a climate with unrealistically high background dustiness). Further, as the $R_{DDL}$ value was increased above the "realistic" range shown in Figure 6, the shape of the northern summer temperature trend worsened progressively.

As shown in Figure 6, it is possible to find values of $R_{DDL}$ that provide a good fit to the climatology curve to the level of precision of the climatology (the dust devil fits do show a slight deviation in shape in northern spring, where they can be up to 3-5K too warm). The particular $R_{DDL}$ value that gives the fit (in fact there is a range of values within which it is difficult to pick due to uncertainty in the data and noise in a given year's simulation) is

provided in the figure caption (but see the note at the beginning of Section 2.4 for our advice on use of this value).

### 2.4.2 The Model-Resolved Wind Stress Source

It is possible that dust lifted by winds associated with mesoscale and synoptic scale systems (>10 km), rather than microscale convective systems (<10km) provide the continual dust injection that supplies the background haze. An analysis of dust devil streaks in Hellas has recently been used to argue that dust devils indeed cannot supply this haze, and that injection by larger systems is necessary [Balme et al., 2003] – however, a study of dust devils at the Mars Pathfinder site suggest just the opposite [Ferri et al., 2003]. These analyses are discussed further in Section 2.6. In any case, clear motivation exists to see whether wind stress lifting alone can maintain the background dust haze – and if it can do so within the constraints of dust lifting observations from imagers, and while simultaneously generating dust storms. Unlike the DDL experiments, the stress lifting (SL) experiments require investigation of two parameters: the rate and threshold parameters. As such, our procedure has been to find the set of combined rate and threshold parameters that yield a reasonable seasonal temperature trend.

Figure 7 shows results from 15 different GCM multi-annual simulations exploring combinations of stress threshold and rate parameters. The results show that there exist combinations of the two parameters that yield seasonal temperature curves that fit the observed climatology as well as the best-fit DDL case. For each stress threshold, the trend with increasing injection rate is simply to translate the seasonal curve to high temperature values, just as was found for the DDL-only scheme. The quality of the shape fit for the SL-only scheme is found to be best for the no-threshold case,

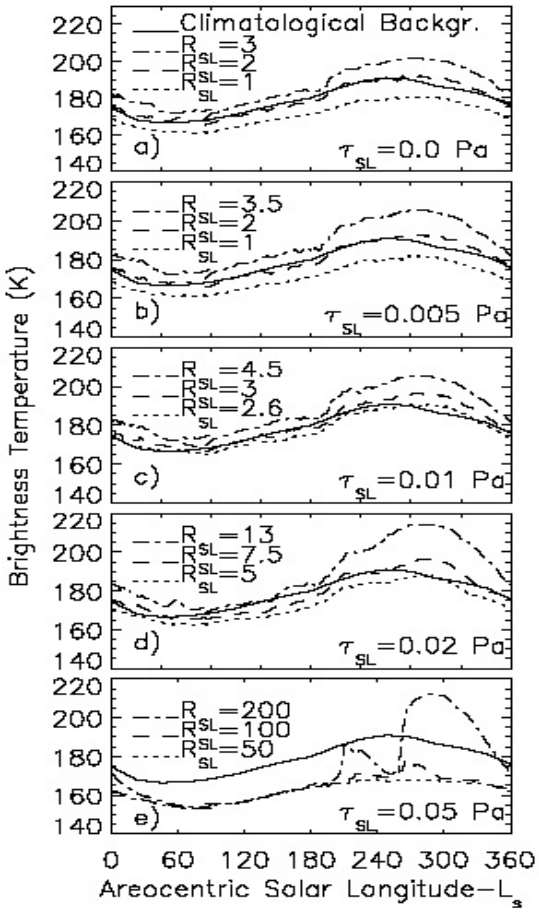


**Figure 7.** The seasonal cycles of simulated air temperatures compared to the climatology for various values of stress threshold and injection rate parameter. The threshold is shown in the lower right of each panel ($\tau$=0, 0.005, 0.01, 0.02, and 0.05 Pa for panels a-e). The rates in each case but e) bound the observed temperatures. The best fit to the northern late spring and early summer temperatures is provided by the no-threshold case, with the fit worsening as the threshold increases. The injection rate values can meaningfully be compared between figures (*i.e.* the highest injection rate multiplier shown in d) is thirteen times greater than that of the lowest rate multiplier in a)). For panel e), the threshold is sufficiently high that essentially no lifting occurs in northern spring and summer, despite the use of injection rate two orders of magnitude higher than in panels a-c). Note instead that panel e) exhibits air temperature spikes associated with dust storms in southern spring and summer, which are not produced in the other cases.

worsening very slightly with increasing threshold up to a value of roughly 0.02 Pa (for our model). By the time a threshold of 0.05 Pa is reached, no amount of dust injection will allow the model to fit the observations. In this case, the threshold is too high for the surface winds to activate dust lifting. The temperature curves for the periods between $L_s$=60° and $L_s$=180° for this threshold correspond to that of a completely dust free atmosphere.

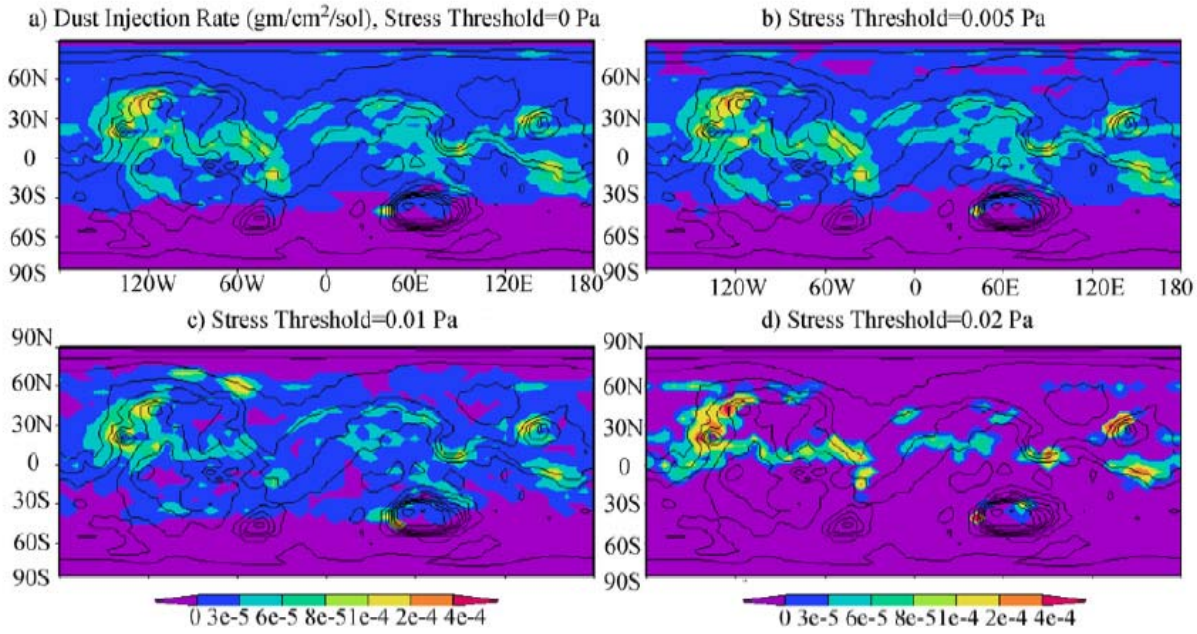


**Figure 8.** The spatial distribution of dust lifting predicted by the model for a single two-sol period, at northern summer solstice, for the middle injection rate cases shown in Figure 7a-d. Very widespread dust injection is required by the model – this pattern compares reasonably well with that for convective lifting. Relatively steady and widespread predicted lifting provides the opportunity to test the importance of wind stress lifting. The local dust storm catalog developed by Cantor et al. [2001] shows local storm activity to be much too concentrated and limited to too few occurrences to fulfill the role required by the model.

The effect of increasing the threshold is to decrease the fraction of the planet's surface area that can participate in dust injection. Inhomogeneity of topography, other surface properties, and the large-scale circulation generate spatial variations in the maximum obtained stresses – as the stress threshold is increased, this threshold exceeds the maximum obtained values for certain regions, and they are no longer active dust sources. This trend can be seen in Figure 8, which provides a snapshot of dust injection (not net injection) for the best-fit curve for each of the thresholds shown in Figure 7. While the spatial pattern of peak lifting remains constant (for all but the 0.05 Pa threshold case), the area contributing dust decreases monotonically. This trend of less of the surface contributing to dust injection as stress threshold increases (and hence greater sensitivity to small variations in stress behavior at these few locations) is an important part of the mechanism of inter-annual dust storm variability to be discussed in chapter 3.

Figure 7e also provides support to the idea that global storms cannot be responsible for the maintenance of the background dust on Mars. The highest dust injection rate simulation in this set generated a significant dust storm in the early southern summer, which exhibited dust, and temperature decay rates that are consistent with observations of the decay of the 1971 and 1977b storms. However, by $L_s$=60° in the following year, temperatures had returned to the "clear atmosphere" level, consistent with the other simulations for this threshold. To the extent that the model provides a good simulation of the Martian atmosphere, it confirms the idea that the Martian atmosphere does not have system "memory" that extends over more than half of the annual cycle.

### 2.4.3 Summary of Dust Source Results

One important question regarding the DDL and SL simulations described above centers on the injection parameters yielding realistic injection rates. Realistic in this case means that the mass of dust moved between the surface and atmosphere is consistent with the mass of dust suspended in the atmosphere. It also involves issues of control – if the amount of dust cycling daily between the surface and atmosphere is vastly greater than the mass in the atmosphere, it suggests a less direct control of atmospheric opacity by the injection scheme than by the boundary layer mixing scheme, for example. Our use of arbitrary injection coefficients makes determining this realism difficult without further discussion. In this light, Figure 9 shows the trend in global-mean dust injection and global mean dust fall-out for the best fit DDL-only, SL-only, and combined DDL and SL "best fit" simulation (for years with and without a global dust storm). These figures show the phase delay between injection and fall-out, and particularly for the dust storm case (Figure 9c), the smoothing of the storm fall-out signal compared to the sharp injection signal. More importantly, combined with knowledge of the annual-mean atmospheric dust mass, the annual mean injection can be used to derive the atmospheric lifetime of dust. Using an annual injection rate of $2.35\times10^{-5}$gcm$^{-2}$sol$^{-1}$ and an atmospheric dust mass of $2.9\times10^{-4}$gcm$^{-2}$ (both from the DDL simulation), we obtain a lifetime of roughly 12 sols for an average dust grain. Other simulations yield lifetimes in the low tens of sols (10-30 sols). These mean lifetimes are consistent with injection-control of the dust abundance and with the injection rates being realistic in comparison with fall-out rates

determined following large dust storms – our rate parameter values are not masking dramatically unrealistic injection rates.

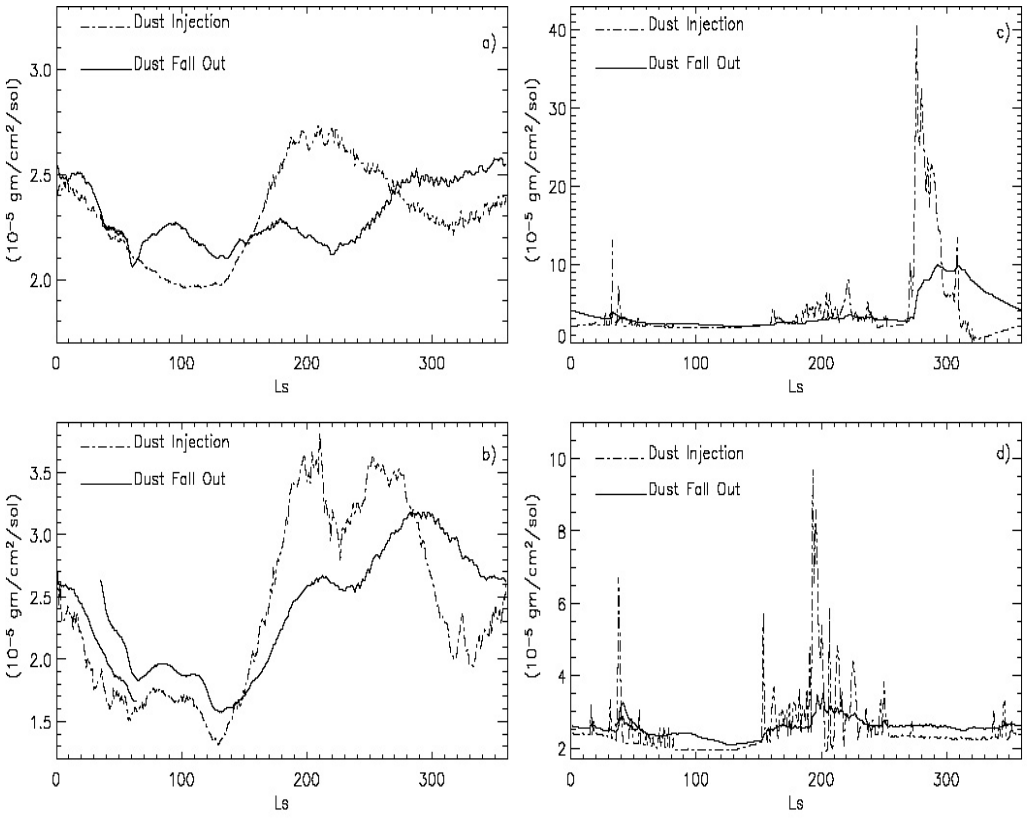


**Figure 9.** The globally averaged rates of injection and settling of dust indicate an atmospheric exponential lifetime for dust of a few tens of days. The seasonal trends in dust injection and settling show perturbations in settling lagging perturbations in injection. The cases shown are a) convective lifting only, b) no-threshold stress lifting only, and years from the combined "best fit" simulations for years c) with and d) without a global dust storm. For the dust storm it is interesting to note the smoothing of the settling pulse relative to the injection pulse, and the abnormal suppression of dust injection in the wake of the global storm. During this storm decay period, the high dust opacities cause the model surface-atmosphere temperature contrasts to become much smaller than usual, producing a strong negative feedback on dust lifting. The phase lag is of course due to the fact that settling is proportional to dust loading and so the source must have time to build a dust loading before settling can build up. The smoothing represents the different influences on injection time scales (dynamical mixing) and settling (gravitational sedimentation).

Comparison of Figure 9c and 9d, showing annual cycles from the same simulation, but for years with and without a global dust storm, shows an interesting feedback on DDL lifting. In the wake of the global storm (at $L_s$=270° in Figure 9c), the injection rates fall to the lowest level observed at any time during the simulation. Comparing the values at $L_s$=325° in the two years, following the storm the injection is about $5\times10^{-6}$ gcm$^{-2}$sol$^{-1}$, compared to the non-dust storm year value of about $2.25\times10^{-5}$ gcm$^{-2}$sol$^{-1}$. In this case, the greater stability of the

atmosphere (and smaller daytime surface-atmosphere temperature contrasts) corresponding to higher atmospheric temperatures induced by dust heating, yields a significant reduction in convective activity and DDL injection. Examples of this kind of negative feedback on the DDL scheme were also pointed out in Newman et al. [2002a]. Feedbacks within the atmosphere associated with global dust storms are discussed in B04.

The low-threshold SL simulations yield good fits to the seasonal cycle of atmospheric temperatures. However, a given set of SL parameters cannot simultaneously yield both a good cycle of background temperatures and spontaneous and variable global dust storms (discussion of which is provided in B04). This suggests either that SL is not responsible for maintenance of the background haze or that the real system corresponds to multiple SL values being used simultaneously. For example, if injection were to be the sum of an SL scheme with low threshold and low rate, and another with high threshold and high rate, it is possible to yield a simulation with a good seasonal fit and with spontaneous and variable global dust storms. How reasonable is this? One can imagine that within the area of a given GCM grid-box, substantial variability exists such that certain sub-portions of the domain can easily be prompted to inject dust, whilst others require much higher wind stresses to trigger – much as is the case on scales resolved by the model. However, the injection rates employed when these two stress thresholds are exceeded are vastly different (orders of magnitude differences are needed to simultaneously yield the right climatology and dust storms). It is far less clear how physically defensible these differences are (though one possibility is downslope wind storm acceleration on the lee of unresolved topography [Magalhaes and Young, 1995]).

The spatial pattern of no-threshold SL lifting is similar to that of DDL during northern spring and early summer (see Section 2.5.2 and figure therein). This similarity in spatial pattern likely explains the similarity in the ability of these two schemes to fit the background haze cycle. The dominant control of this pattern for DDL is clearly associated with the spatial variation of thermal convective vigor, as discussed in Section 2.3.1. That the no-threshold case SL and DDL produce a very similar spatial pattern suggests that a major control on the injection, via the imparted wind stress, is through the variation of the drag parameter associated with variations in the vigor of convective activity during the day. This similarity doesn't argue for

one injection process over the other, but suggests instead that the controlling physical processes might not be as distinct in the two schemes as one might expect at first glance.

Discrimination between DDL and SL roles in the maintenance of background haze most likely can be made on the basis of observations. The DDL scheme predicts widespread and on-going dust devil activity, and particular seasonal variation of injection. Images of Mars from orbit and from landers show abundant dust devil activity in the form of dust devils and dust devil tracks across the planet [Metzger et al., 1999; Malin and Edgett, 2001; Cantor et al., 2002; Fisher et al., 2002; Balme et al., 2003; Ferri et al., 2003]. As shown at the end of Section 2.5.2, the model predictions of dust injection during northern summer agrees remarkably well with the estimates of dust devil lifting from Imager for Mars Pathfinder data analysis [Ferri et al., 2003].

The model also predicts that if low- or no-threshold SL controls the background haze, widespread and continuously on-going non-dust devil lifting should be active. Figure 8 shows low-threshold injection averaged over 2 sols, requiring dust lifting within each grid-box over a very large fraction of the planet's surface. However, in the exhaustive survey of local dust storms described by Cantor et al. [2001], for the period near $L_s$=110°, on any given day, only two or three storms with areas over $10^3$ km$^2$ were counted over the entire planet. This is a vastly smaller area of dust lifting than that predicted by the no-threshold SL case, and more in keeping with the very much higher threshold SL cases required for generating large storms. Systems smaller than about 100 km$^2$ cannot be observed in the MOC daily global map images, but are very rarely even seen in the MOC narrow angle images (at 1-10 m resolution), which would seem to be inconsistent with the widespread, regular lifting predicted by the no-threshold SL simulation (the low resolution of the daily global map images also precludes the use of this data to capture the total number of dust devils occurring on a given day below the spacecraft track).

Other types of dust lifting, apart from dust devils and local storms are possible. Dust streaks are evident on the surface associated with craters and other forms of sharp topography [Thomas et al., 1981; 1984], and the high stresses in the lee of these objects might be important (obviously it is only dark, erosional wind streaks that are of interest as potential sources of dust). One factor arguing against the role of lee stresses is frequency of activity: fitting of wind

directions to observed streaks suggest that they form rapidly by eroding non-equilibrium dust deposits (such as those deposited following a large dust storm) at specific times of day when the stresses are highest [Fenton and Richardson, 2001; Thomas et al., 2003]. However, lifting can only be sustained until these very limited areas are depleted (yielding the dark streak). We are therefore dubious of the role of such lifting, but this is a bias that requires a focused study before conclusions can be drawn. Finally, it is possible that some microscale lifting process is at work that is below the resolution of orbiting cameras, but is also never seen in lander images. To determine if such "stealth" lifting is ongoing to the degree required by the SL scheme, it may be necessary to measure the net vertical flux of dust on future landers.

In summary, the observed lack of dust motion at the Viking Lander sites except during extreme wind events [Moore, 1985], and the only observation of dust lifting at the Pathfinder site being associated with dust devils [Metzger et al., 1999], also argue that non-convective lifting of dust is rare at most locations on Mars. Local dust storms are insufficiently active, based on comparison with the Cantor et al. [2001] catalog. Given the abundant evidence for dust devils across the surface, and the lack of observations of an adequate non-dust devil lifting mechanism, it seems that the dust devil lifting mechanism is the most plausible. This interpretation is further supported by the ease with which the annual cycle can be fit with a combination of DDL and high-threshold SL, but that a combination of high and low SL is needed if DDL does not dominate the haze maintenance, and that these two SL modes require orders-of-magnitude different injection rate parameters. Plausibility would currently seem to us to strongly support a dominant role for dust devils in the maintenance of the background haze. However, further observational study is needed before this opinion can be established as a fact.

### 2.5 Characteristics of the "Best Fit" Model Annual Cycle

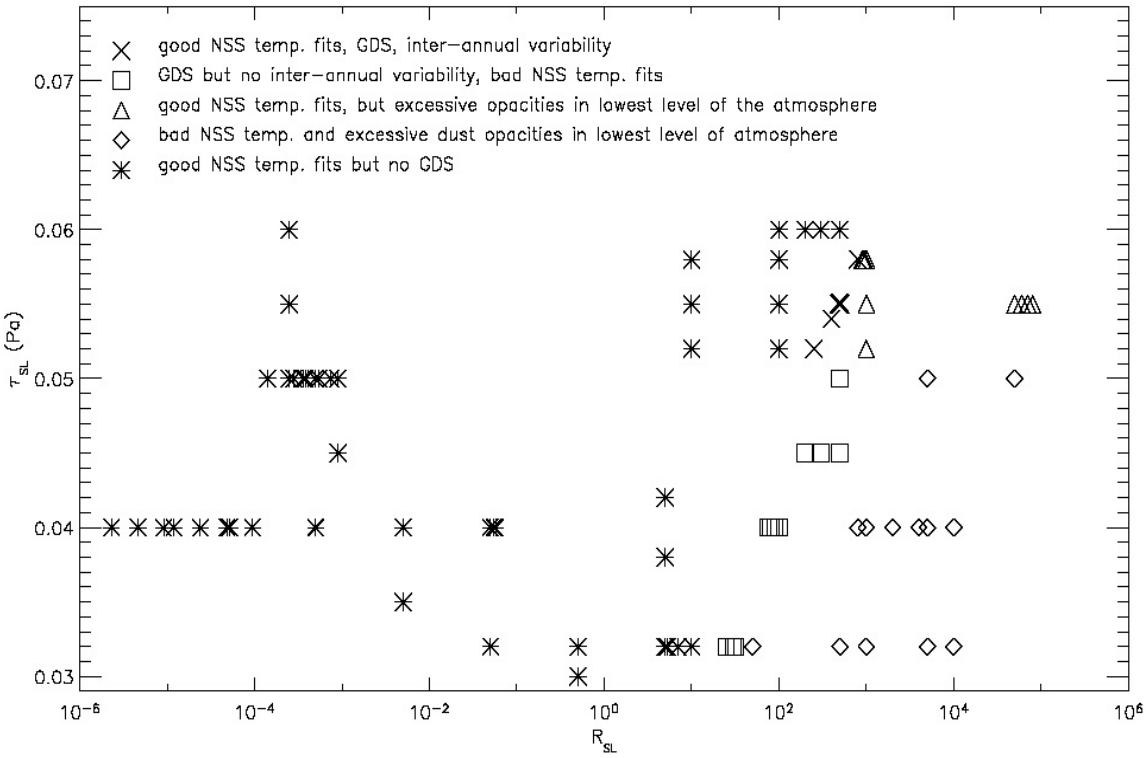


**Figure 10.** A summary of the wind-stress scheme phase space examined for various dust storm behavior. In all cases, the best-fit DDL injection parameters were used, and only a single set of wind stress parameters were used in a given simulation. In a specific area of phase space (indicated), spontaneous and variable global dust storms were simulated in southern summer, emerging from and returning to realistic non-dust storm states in northern spring and summer. Significantly, these simulations exhibited years with and without global storms within the same multi-annual simulation. This figure and the study are discussed in greater detail in B04.

Examination of the model seasonal cycles described in Section 2.4 and associated arguments can lead to a paradigm for a "best fit" model climate in which DDL lifting provides control of the seasonal haze cycle and SL control of dust storms. In this way, a "best fit" annual cycle simulation can be found by varying the $R_{DDL}$ until the background seasonal air temperature cycle is fit (with emphasis on northern spring and summer), and then varying the $R_{SL}$ and $\tau_{SL}$ values until variable dust storms are generated in southern spring and summer. A very large amount of phase space was examined, as shown in Figure 10. This Figure summarizes the dust storm simulations (all using the same DDL parameters), categorizing them on the basis of whether they yielded realistic non-dust storm climates and the nature of the dust storm activity generated. An area of phase space was found in which spontaneous and inter- (and intra-) annually variable global dust storms were produced in southern spring and summer, and which would relax back to a realistic thermal state after these events. Output from such a "best fit"

case is described in this section. The dust storms generated by this simulation are described in some detail in B04.

### 2.5.1 Meridional and Vertical Distribution of Air Temperature

For a year without a major dust storm, Figure 11 shows the comparison of the seasonal cycle of meridional mid-level air temperatures with observations (IRTM T15 values synthesized from the TES data [Liu et al., 2003). This comparison indicates that not only have "global mean" temperatures been fit, which was the tuning metric, but also the meridional gradients. In particular, the double peak of air temperatures in both mid-latitudes, and local minimum in the tropics during summer is an indication of the Hadley circulation. The TES data are an average of day and night spectra from the mapping orbit. In order to provide best comparison, the GCM has been sampled at 2pm and 2am local times to mimic the MGS mapping orbit. Specifically, the observation-by-observation sampling of the model mimics that of the TES sampling of the atmosphere at the same latitudes, longitudes, local times, and seasonal dates (obviously, some interpolation of model output is involved as the GCM generates output for a simple cylindrical grid at 5° by 6° grid-spacing, and with an output interval of 2 Martian hours). As such, there are no biases due to the small changes in local time of the MGS orbit, due to gores in the TES latitudinal coverage, or due to asymmetry in the number of dayside versus night-side observations.

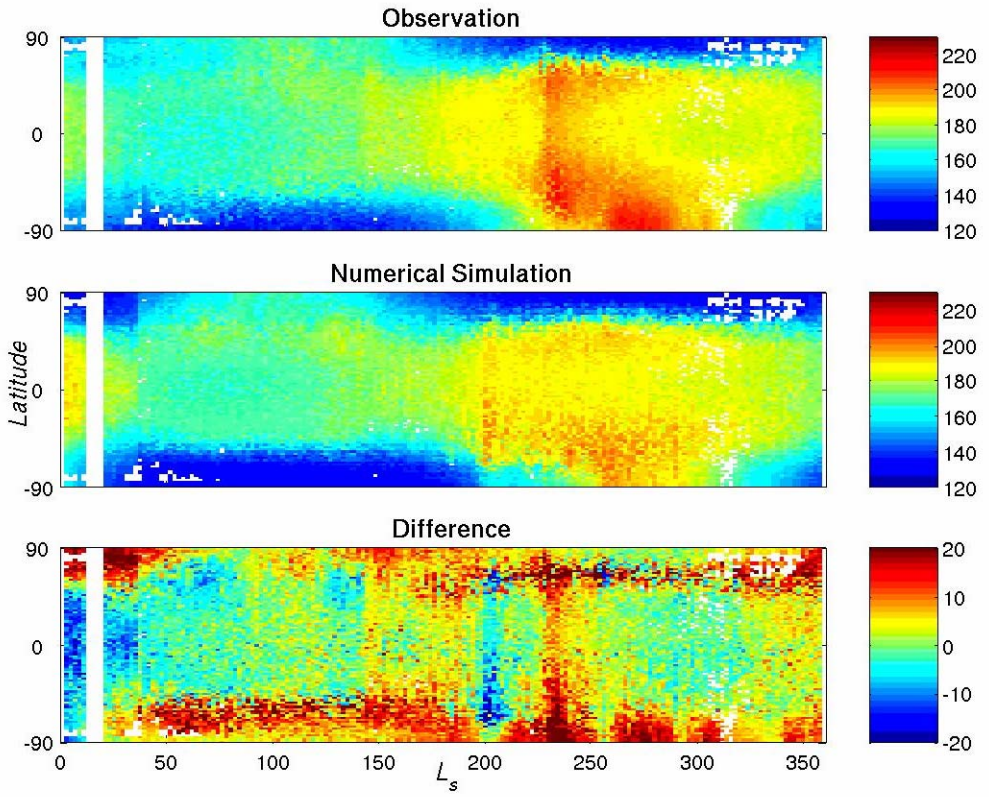


**Figure 11**. A comparison of zonal-mean115μm channel temperatures derived from the MGS TES spectra and from the GCM. The GCM output was sampled using the TES observational pattern to maximize comparability. A full annual cycle is shown for each, along with the difference between the model and data. The results are for a non-global dust storm year (the first MGS mapping year from northern summer and rolling around into the second) and from the "best-fit" GCM simulation.

The difference between the GCM output and the TES observations (Figure 11c) suggest that the model captures mid-level air temperatures well throughout most of the year. In the tropics and mid-latitudes, the individual bin differences are within ±5K, with no discernable spatial pattern, and averaging to much less than 1K. Major exceptions to this consistency in the tropics and mid-latitudes occur at roughly $L_s$=200° and $L_s$=235° when, first the GCM develops a small regional storm not present in the TES first mapping year observations, and then the real atmosphere develops a planet encircling dust storm (while not global, this storm was the largest event of 1999, and began in a most interesting manner, see Wang et al. [2003]), which is not present in the GCM simulation. In very late southern summer, the GCM cools somewhat faster than that of the real atmosphere, ending the year roughly 5K cooler. This is

not a consistent, multi-annual offset, however. At the beginning of the model year shown, the dust and hence air temperature decay is somewhat slower than the MGS second mapping year data shown. As a result, the simulation is as much as 10K warmer than the observations for the first 30°-40° of $L_s$ of the year. These discrepancies occur during the periods of the year known to be more variable from the observations [Liu et al., 2003]. During the majority of northern spring and summer, the air temperatures are very close, and again within the spread of observed year-to-year variability (which during this season, is mostly due to "weather" and instrument noise).

The Polar Regions show more of a discrepancy than the tropics and mid-latitudes. In southern spring and summer, this is mainly due to the action of the 1999 planet-encircling storm and a regional southern polar storm. Real atmospheric temperatures are warmer than the model in the high southern latitudes where there is higher dust opacity and solar dust heating, and in the high northern latitudes, in a band near 60°N. This corresponds to stronger Hadley cell downwelling, and a consequent poleward movement (contraction) of the polar vortex wall. Temperatures over the northern winter pole (>70°N) are well simulated. In southern autumn and winter, the GCM predicts southern polar temperatures that are too cold by between 5-15K (with the larger discrepancy at the vortex wall – at the latitude of maximum temperature gradient). It would seem that the GCM somewhat over predicts the isolation of the southern polar vortex in southern winter. Over the pole (>85°S), the error is less than 5K. The GCM also substantially under-predicts (15-20K) air temperatures in the decaying northern polar vortex in late northern winter and early northern spring. Again, the GCM seems to be somewhat over predicting vortex isolation (under-predicting meridional heat fluxes). After $L_s$=50°, the fit becomes very good all the way to the northern pole. Thus, with the exception of the winter polar vortices, the GCM is able to fit the latitudinal distribution of mid-level air temperatures to better than 5 K. This fit includes a good prediction of the seasonally varying polar vortex walls, and the locations of downwelling in the solsticial Hadley circulations (illustrated by the double maxima in the latitudinal temperature gradient in both northern and southern summer, see Wilson and Richardson [2000]). The winter polar area arises due to under-prediction of meridional heat transport across the vortex, due to error in prediction of cap-edge dust storms and/or other atmospheric eddies.

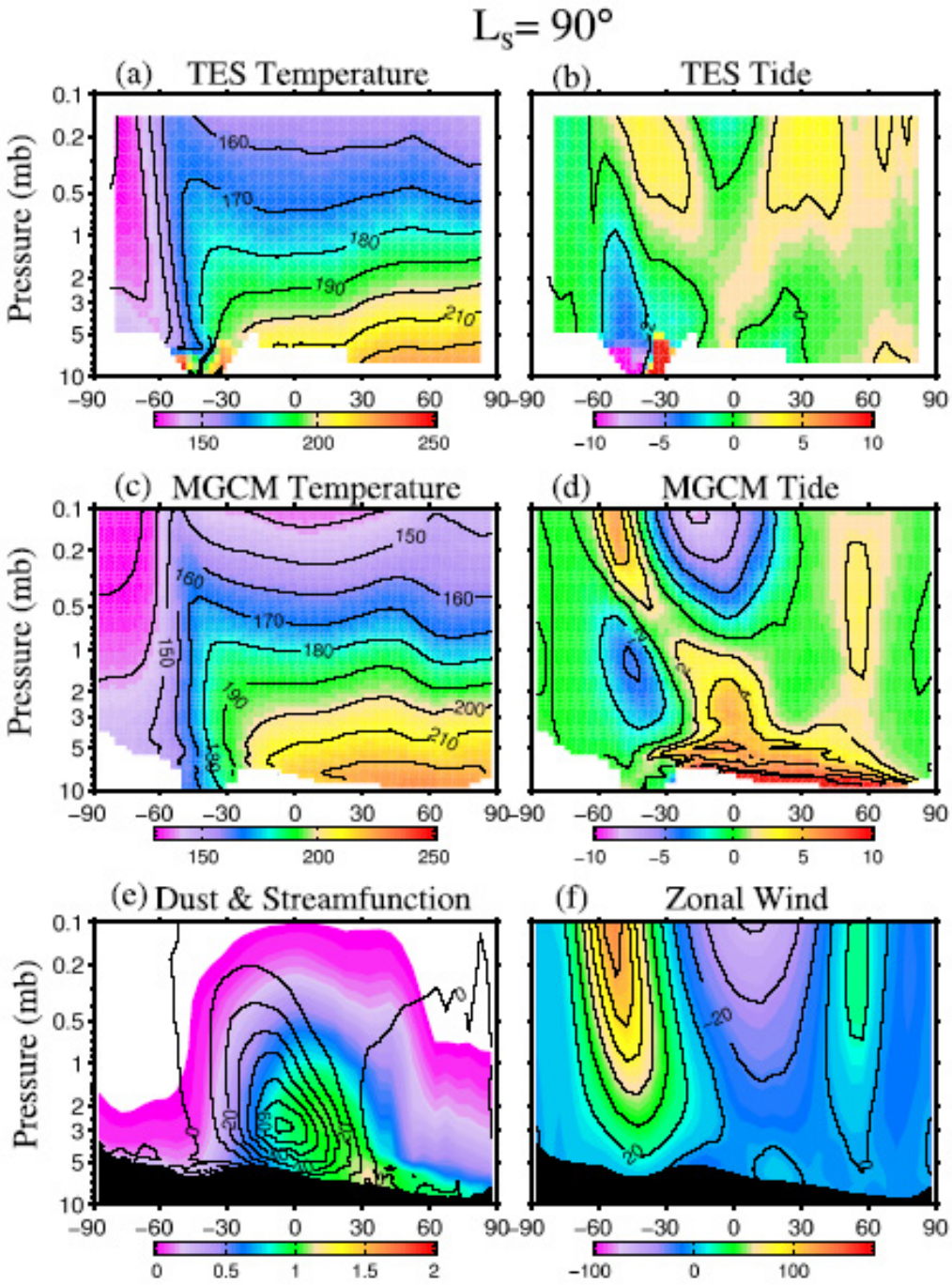


**Figure 12**. Cross-sections of zonally-averaged thermal structure for Ls= 90º. a) Observed TES diurnal-average temperature structure. The diurnal average is defined as 0.5×(T2pm+T2am). The contour interval is 10 K. b) The corresponding diurnal difference field (T2pm-T2am). The contour interval is 2 K. c) Temperature structure simulated by the GCM. d) The simulated diurnal difference field. Simulated fields have been interpolated to a common pressure grid prior to zonal averaging. e) The simulated dust distribution (color shading) and mass transport stream function (contours). The aerosol opacity is scaled to show the contribution to column integrated total opacity as if the local contribution were representative of the total column (*i.e.* the local mass mixing ratio value has been used to calculate the total column opacity, were the total column to be uniformly that mass mixing ratio). Stream

function contours are in intervals of 10 by$10^8$ $kgs^{-1}$. Positive (negative) contours are associated with a counterclockwise (clockwise) circulation. f) Simulated zonal mean zonal velocity. The contour interval is 10 $ms^{-1}$.

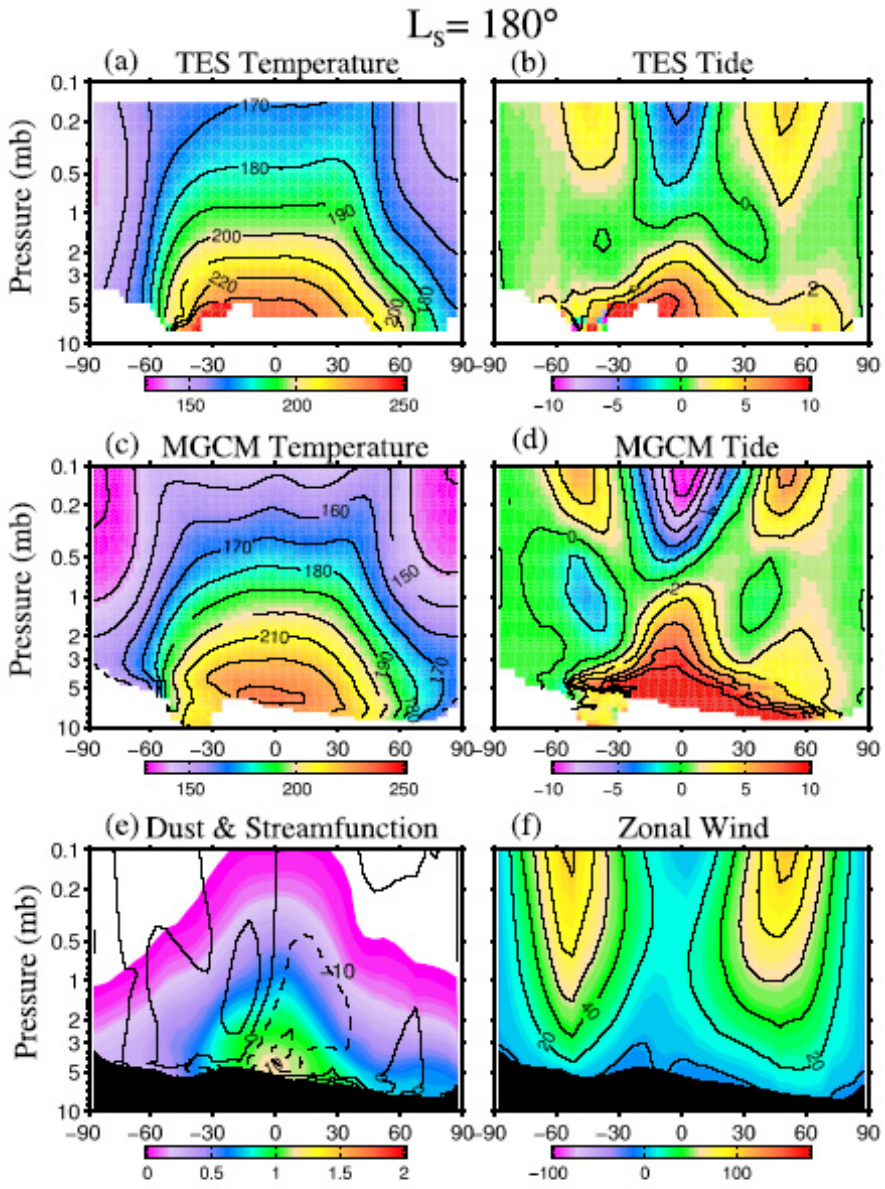


**Figure 13**. Same as Figure 12 but for $L_s$=180º.

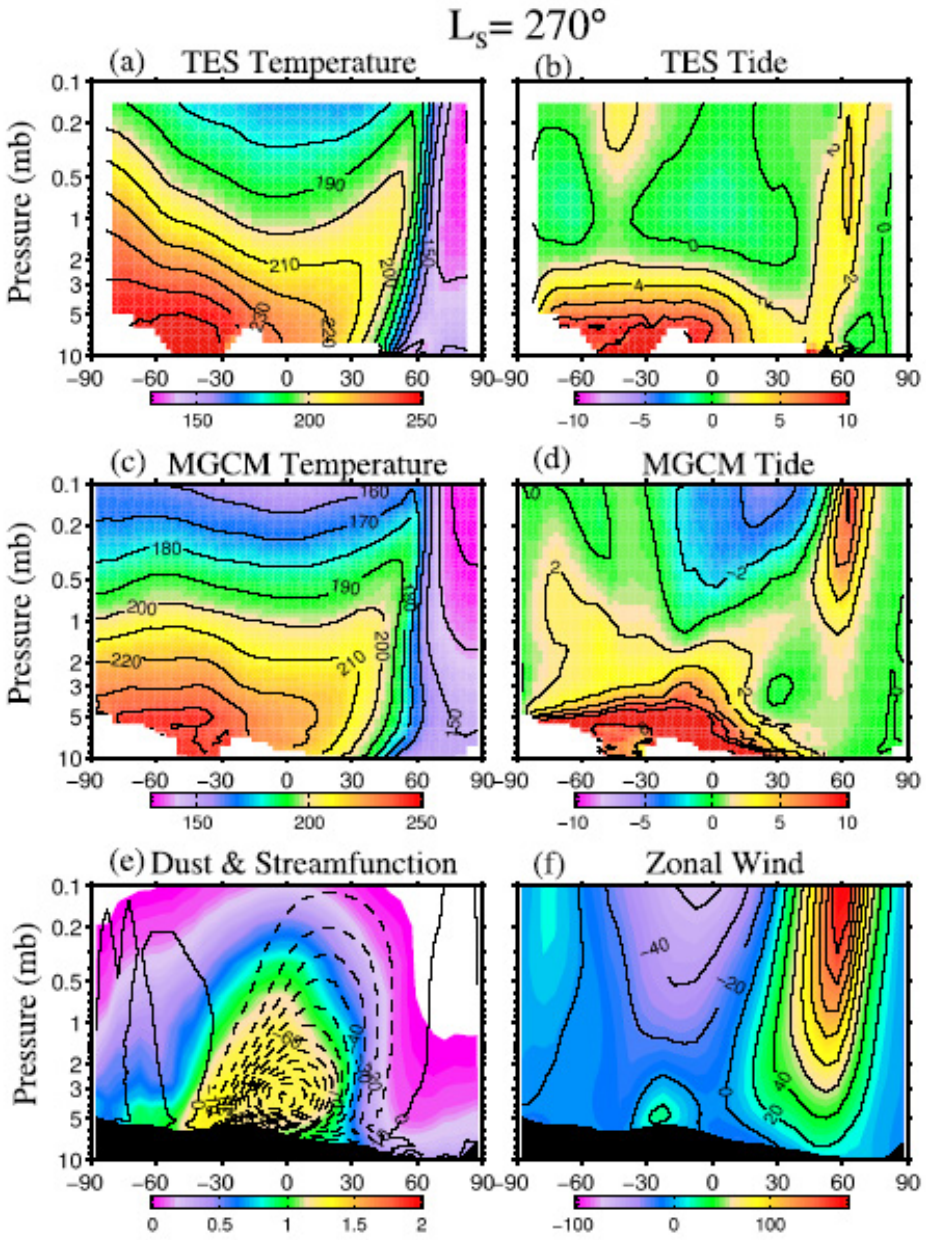


**Figure 14.** Same as Figure 12 but for $L_s$=270º.

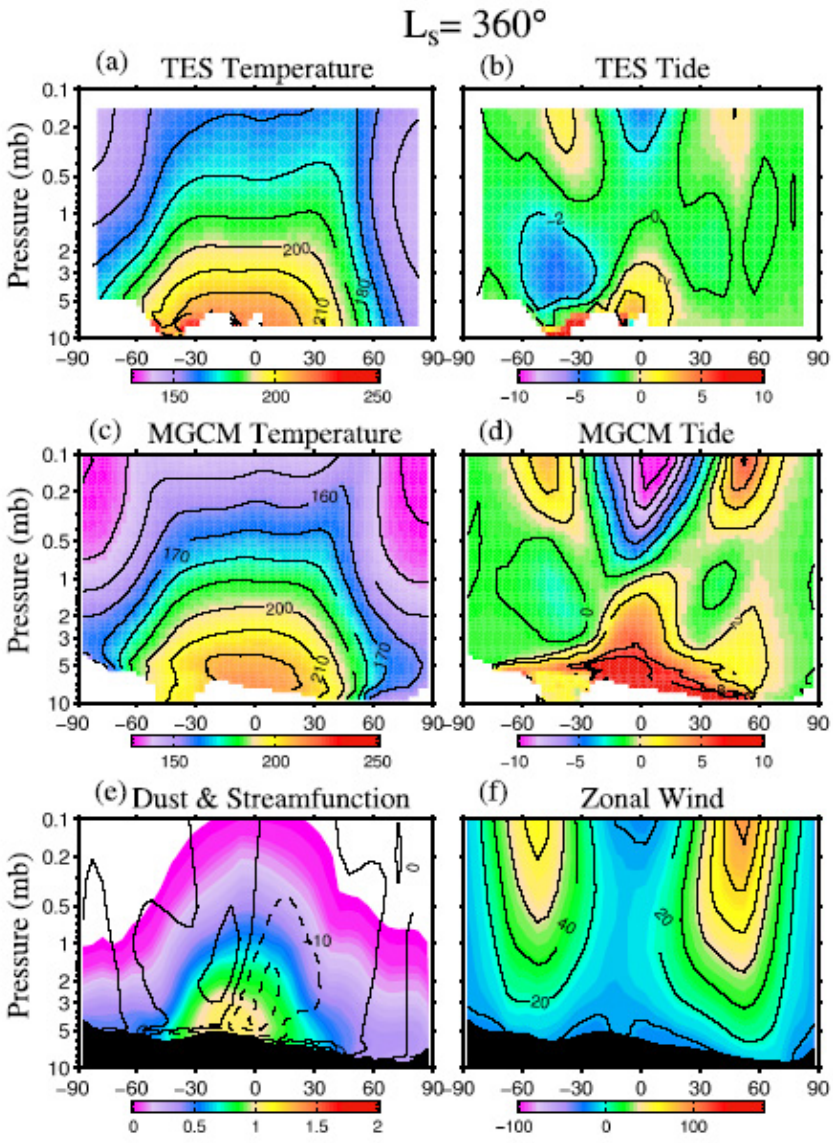


**Figure 15.** Same as Figure 12 but for $L_s$=360º.

Zonal-mean temperatures are compared with TES observations for both solstices and equinoxes in Figures 12-15. In addition, the model dust distribution, stream function, and zonal wind distributions are shown. For northern summer solstice (Figure 12), there is generally good agreement between the observed and simulated diurnal average temperature fields. The most notable differences are in the tropical lapse rate and the meridional temperature gradient at high latitudes in the summer hemisphere. Below roughly the 1 mb, the highest observed temperatures are in the summer pole region where insolation is greatest at

this time of year. By contrast, the simulated temperatures are more meridionally symmetric, with maximum temperatures (on a given pressure surface) at mid-latitudes. The temperature differences most likely stem from the lack of dust at high latitudes in the summer hemisphere. The simulations fail to reproduce the observed dust storm activity along the margin of the retreating $CO_2$ ice cap with the observed vigor (though some cap edge storms are generated – see Section 3.5.3). There is a tropical temperature bias such that the simulated low level temperatures are slightly too warm while above 0.5 mb the simulated temperature profile becomes increasingly cold. This bias may reflect deficiencies in the simulated dust distribution, deficiencies in the temperature retrieval, or the absence of additional radiative agents, such as water ice clouds. The simulation includes dust presenting 0.6 and 2.5 micron particles. It is possible that a different size distribution would lead to a deeper distribution of dust, and possibly greater radiative forcing at higher altitudes. More detailed simulations to be described in a future paper suggest that water ice clouds can contribute sufficient radiative heating to yield a more isothermal temperature profile consistent with TES observations. There is general agreement between the modeled and observed pattern of the thermal tide fields; here defined as (T2pm-T2am). This field is strongly aliased by the limited diurnal monitoring by TES (twice daily), as described by Wilson [2000] and Banfield et al. [2003]. The limited vertical resolution of the TES nadir observations does contribute to a damping of the observed tide signature [Banfield et al., 2003]. This is particularly likely in the tropics where the vertically propagating tide has a vertical wavelength that is readily smeared out by the TES retrieval. Figure 12e shows that the simulated dust distribution is strongly influenced the Hadley circulation, which is indicated by the mass transport streamfunction. The simulated vertically integrated column opacity is ~0.8 in the tropics, which is high relative to observations. The column opacity is particularly weak at midlatitudes in the winter hemisphere.

For $L_s$=180° (Figure 13), there is again broad agreement in the diurnal-average temperature fields. In this case, the most notable difference is the tropical lapse rate. The diurnal tide fields are quite similar, with the observed field having about half the strength of the simulation. There is a cold temperature bias at both poles in the simulation at levels above ~1 mb. The temperature field appears to suggest that the dust forcing is somewhat weak, as the simulated temperature distribution lacks the flat meridional distribution in the tropics that is evident in the observations. The mass transport stream function is quite weak relative to the solstitial case

and the simulated dust field is somewhat shallower. The optical column is similar in depth to that in the summer solstice simulation (Figure 12e). The opposite equinox ($L_s$=360°, shown in Figure 15) is quite similar.

For northern winter solstice (Figure 14), there is good qualitative agreement between the modeled and observed the temperature fields, but the simulated temperatures have a cold bias in the summer (southern) hemisphere that is most likely attributed to insufficient dust raising at the polar cap edge and in the southern polar latitudes generally (*i.e.* a similar deficiency in the vigor of small-scale dust storm lifting mentioned for northern summer). The meridional temperature gradient in the observed field is much stronger than that for the NH summer solstice season. The differences in the tide field is also consistent with greater dust heating at high southern latitudes in the observations than in the simulation. The total column opacity is greatest in this simulation, with a tropical maximum of ~1.2. The stream function is roughly double that in the summer solstice season. The dust distribution is deeper as well. The zonal wind field shows a subtropical jet in the southern hemisphere.

### 2.5.2 Spatial Pattern of Dust Devil Lifting and Dust Devil Occurrence Predictions

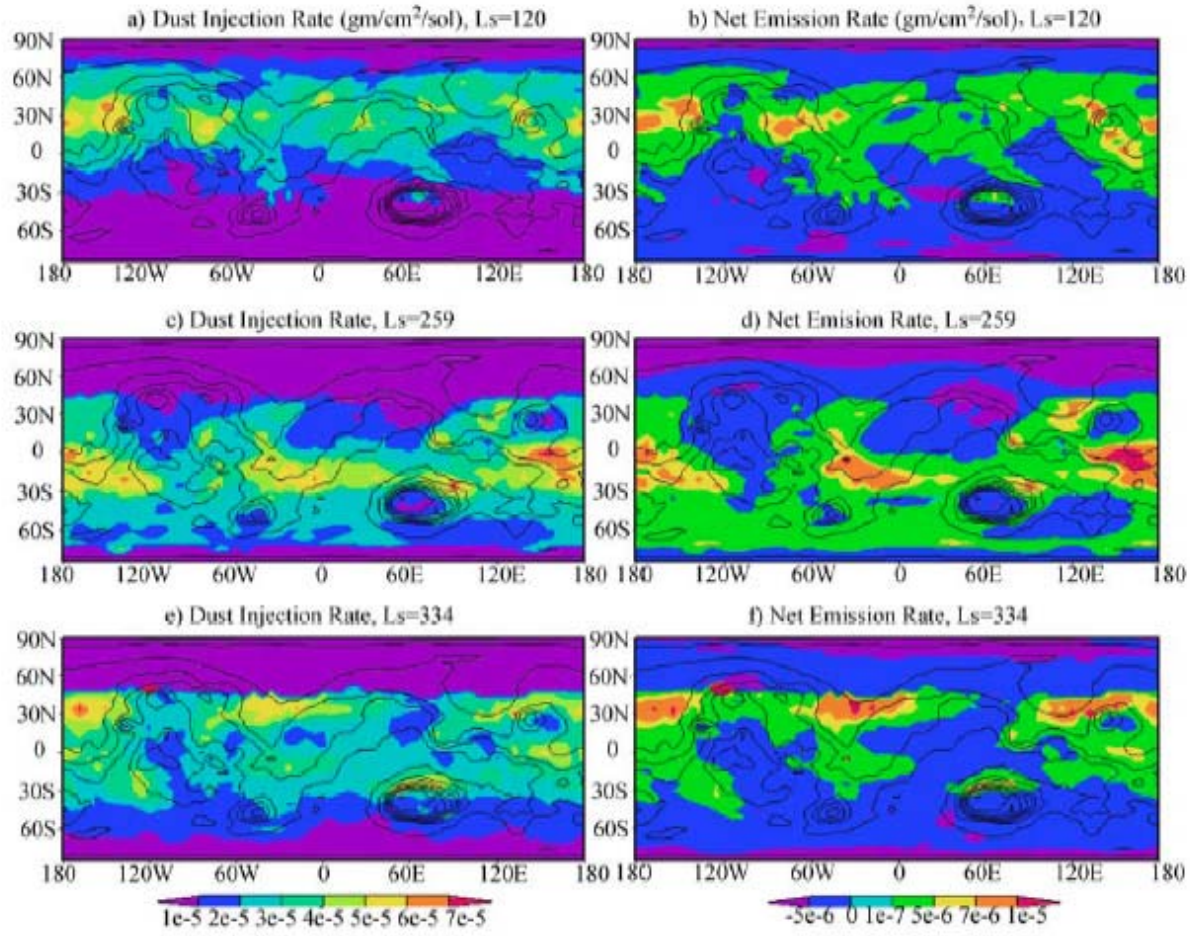


**Figure 16.** The relationship between (a,c,e) diurnal mean injection of dust by dust devils and (b,d,f) the net emission of dust from the surface (the residual between lifting and fall-out). Maps are shown for $L_s$=120°, 259°, and 334°. The net emission values are about a factor of three lower than the dust devil injection. The spatial patterns are quite similar. Note the peak in dust devil activity over Amazonis in northern summer, which is consistent with a high abundance of Mars Orbiter Camera images of dust devils in this region.

To the extent that the model produces a good annual cycle, and does so with a dust injection scheme that is based on the thermodynamics of dust devils, the injection provides a prediction of the spatial distribution of dust devil activity. In Figures 16a, 16c, and 16e, we show diurnal-average maps of DDL dust injection at three different seasonal dates for the best-fit scheme. A major trend in the position of predicted dust devil activity is due to the changing sub-solar latitude with season. Figures 16a and 16c are close to northern and southern solstice,

respectively, and show bands of dust devil activity that are biased in northward and southward directions, respectively. Figure 16e shows a map for $L_s$=334°, which is significantly closer to equinox, and corresponds to more latitudinally uniform lifting. This broad-brush dependence on the sub-solar latitude is entirely consistent with the assumed functional dependence of dust devil activity on peak solar heating (Figure 3).

There is a great deal of spatial structure in the map for each season, beyond that simply due to latitude. The near-equinox pattern shown in Figure 16e is most directly interpretable. The sharp cut-off in lifting activity north of about 50°N is due to the presence of the seasonal $CO_2$ ice cap. The lifting scheme is designed not to lift dust when ice is present on the surface, and in any case, the drive for such lifting in the very strongly statically stable environment above the seasonal cap is negligible. At $L_s$=334°, the sub-solar latitude is still in the southern hemisphere, however, the peaks in dust devil activity are located in the north. These peaks all correspond to lower elevations where the pressure is higher and greater amounts of dust can be lifted. A secondary maximum of dust lifting occurs in a broken band just south of the equator–this corresponds to the sub-solar latitude.

The $L_s$=120° output (Figure 16a) shows several peaks in dust devil lifting in the northern hemisphere. The largest of these peaks covers the Amazonis region (15°N-45°N, 170°E-140°W). This is encouraging as this is the most vigorous region of dust devil activity observed on Mars [Cantor and Edgett, 2002; Fisher et al., 2002]. Other peaks exist close to Elysium and on Lunae Planum and Acidalia. Dust devil lifting is a function of PBL top height and the sensible heat flux from the surface. Examination of the these components within the Amazonis peak (at 180°W) and at other longitudes with lower dust devil activity but similar surface pressure (90°E and 45°W) shows that the Amazonis peak is due to elevated sensible heat fluxes. While the peak PBL top height is roughly the same at all three locations (~4.5km at this season), the sensible heat flux within Amazonis is nearly double that at the other two locations. This is directly ascribable to lower thermal inertia and 5-10K higher daytime temperatures within Amazonis at this season than at the other two longitudes.

Near southern solstice, the band of peak dust devil activity is biased to the southern hemisphere (Figure 16c). Significant localized peaks of dust devil activity are predicted in the

southern tropics between 60°W and 60°E, and between 130°E and 120°W. Examination of the dust devil lifting function components suggest that neither the PBL height nor the surface temperatures are especially unusual within these regions, as compared to the gaps in dust devils activity in this belt, or compared to the regions just north and just south of the belts. Indeed, one interesting aspect of the $L_s$=259° activity is that it maximizes in such a sharply confined zonal belt. This region coincides with the convergence zone of the Hadley circulation, and it is found that the critical factor in the elevated lifting is the enhanced sensible heat flux. This enhanced heat flux is directly ascribable to the high winds within this latitudinal band. Unlike the Amazonis dust devil activity, which peaked just in the afternoon along with surface temperatures, the southern tropical activity peaks in the late morning when winds are highest and the PBL is not yet full developed. The "dust devil" function in this case is capturing the effects of strong convective mixing of heat, but with strong mean winds, it is not clear whether this mixing would manifest itself as dust devils. Conventional wisdom suggests that dust devils may not be a preferred form of convection under conditions of high winds, while Large Eddy Simulation experiments suggest that dust devil formation may be insensitive to the strength of the background wind [Toigo et al., 2003]. The $L_s$=259° output may also be compared with the "season 10" output ($L_s$=270°-300°) shown by Newman et al. [2002a]. The band of dust devil activity found here is similar to that found by Newman et al. [2002a], save for the fact that the band in this study is wider in latitude and less longitudinally uniform.

Figure 16 also includes panels that show the net lifting (over a diurnal cycle) of dust for the same seasons as the dust devil injection output (Figures 16b, d, f). "Net" in this case refers to the resultant effects of injection and gravitational settling of dust (there is no mean wind stress lifting in this simulation). Thus, if dust is injected during the day, but falls out at the same location at night, there is no net injection. The net injection can also be negative for regions that are net dust sinks for the seasonal dates shown. The net injection is compared with the dust devil injection to assess the degree to which patterns of dust fall-out, and the ability of the atmosphere to export dust from different regions, causes differences in the spatial patterns of "gross" and "net" dust supply of dust.

The near equinox case (Figure 16f, $L_s$=334°) shows the largest areas of sign change between convective and net injection. Large regions of Tharsis, Arabia, and Sabaea show positive

convective injections (predicted dust devil activity), yet they exhibit net accumulation of dust. These large areas provide a good example of the need to use predictions of the dust devil injection component, rather than the net injection, to predict dust devil activity from the model.

The two more nearly solstitial simulations (Figures 16b and 16d, $L_s$=120° and 259°) show net deposition of dust on the seasonal $CO_2$ ice deposits, while all three frames show net deposition of dust in the majority of Hellas. This strong and nearly continuous deposition of material may be an important link in the cycle of large-scale dust storm activity, as discussed in B04. The southern solstitial simulation provides an example of the differing efficiency of dust injection at different locations. In the southern high latitudes (<60°S), a very high percentage (30-100%, depending on exact location) of the dust injected during the brief period of daytime dust devil action is lost from the surface. This suggests very efficient removal by atmospheric transport from these locations. Conversely, in the lower northern mid-latitudes, similar rates of dust devil activity correspond to net deposition of dust. Figure 16c and output for times a little later in southern spring and summer suggest that dust devil activity would have been observed even at the high latitude of the Mars Polar Lander (75°S), and as indicated in MOC imagery.

The GCM results suggest that dust devils should occur at some point in the day, and at some locations within the area defined by each GCM grid-box, for essentially all non-ice covered locations on the planet. The average northern summer dust injection required by the model is about $2\times10^{-5}$ $gcm^{-2}sol^{-1}$ (Figure 9). This can be compared with the lifting capacity of a typical dust devil derived from Mars Pathfinder observations by Ferri et al. [2003] of $7\times10^{-5}$ $kgm^{-2}s^{-1}$ or 0.62 $gcm^{-2}sol^{-1}$. Assuming dust devils are active for only a quarter of the day, the fractional area of dust devil activity required by the model is roughly $1.3\times10^{-4}$, which is very close to the $2\times10^{-4}$ estimated by Ferri et al. [2003], again on the basis of the Imager for Mars Pathfinder observations. As such, the model predicted dust devil activity area and required dust devils per unit area are consistent with observations.

### 2.5.3 Prediction of Local and Regional Dust Storm Activity

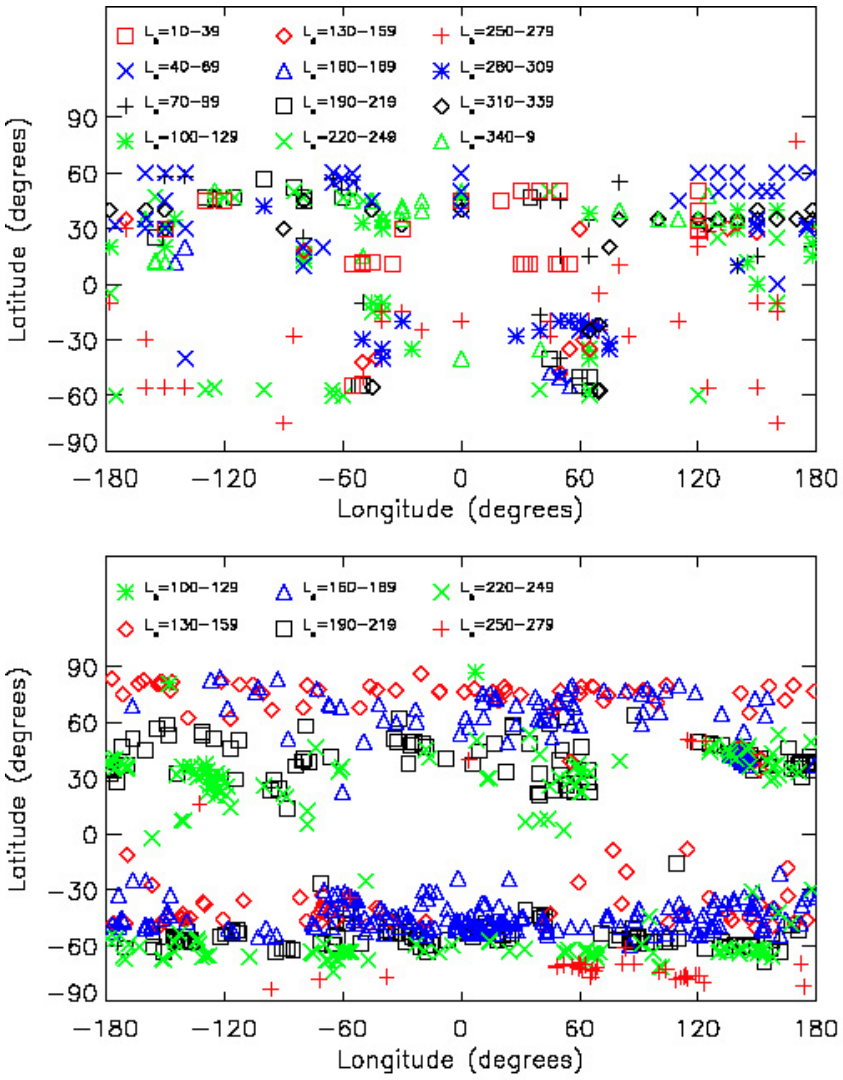


**Figure 17.** The spatial distribution of the origin locations of local and regional dust storms a) as predicted by the "best fit" GCM simulation, and b) as observed in MOC WA images [Cantor et al., 2001]. Note that while the minimum dust storm size detectable by MOC in this survey was about 60 $km^2$, the GCM grid box size is 108,000 $km^2$.

The presence of an interactive dust-lifting scheme allows the model to generate predictions of the number and spatial distribution of local and regional dust storm events (scales greater than $10^5$ km). This model prediction allows the Cantor et al. [2001] dust storm catalog to be directly used to constrain a GCM simulation. Previous studies have used model-predicted stress patterns to compare with the observed storm occurrence [Haberle et al., 2003; Newman et al., 2004]. Figure 17a shows a map of the origin locations of local and regional dust storms in the

"best-fit" simulation. The model output is available for all times of year, while the published catalog covers the period from $L_s$=109°-274°, but otherwise Figure 17a and the Cantor et al. [2001] Plate 1 can be directly compared (the data from Cantor et al. [2001] have been plotted as Figure 17b, for easier comparison with the model output). Major, "broad-brush" agreement between the model and data include the general paucity of storms over the regions centered on Terra Meridiani (0°N, 0°W), Tharsis (0°N, 120°W), and Hesperia (0°N, 120°E), and the elevated dust storm activity in the mid-to-high latitudes of both hemispheres (>40°N, <40°S). The GCM appears to under-predict cap-edge dust storm activity, especially at the very high latitudes. However, investigation of the dust opacity and surface wind stress output suggest that very high latitude (>60°) localized high wind stress events do occur, but that the polar Fourier filter prevents the development of sharp, localized dust opacity maxima, which was the basis of the dust storm identification method used to construct Figure 17. (Fourier filtering is needed in grid-point GCMs to prevent computational instability as the longitudinal grid points converge towards the pole–all current, published Mars GCMs are grid-point models, except for the Oxford Mars GCM [Read et al., 1997; Newman et al., 2002ab].)

The model appears to somewhat over-predict dust storm activity in Hellas and Argyre, although this is more likely a reflection of under-prediction of events at other latitudes in the southern mid-latitudes. This can be verified by comparing the number of events in Hellas within a given seasonal bin (say $L_s$=190°-219°), during which the model predicts 5 events in and around Hellas, while Cantor et al. [2001] count over 20. The model predicts a peak in local events in (and to the north of) Hellas during $L_s$=280°-309°, after the end of the Cantor et al. [2001] study period. Some of the offset in storm numbers is likely due to the smallest resolvable dust storm size in the GCM ($1.08\times10^5$ km$^2$) being larger than a good fraction of the Cantor et al. [2001] storms. The effect of resolution, especially in critical regions such as the high latitude seasonal cap edge zones, needs to be studied further in the future.

Noticeable increases in storm activity can be seen in the northern mid-latitudes in the seasonal bins near the equinoxes. A distinct spatial pattern to the distribution of these storms can be seen, with three "fingers" of activity dipping to lower latitudes near 50°W, 80°E, and 160°E. These are locations where baroclinic storm activity peaks [Hollingsworth et al., 1996], and also correspond to the "flushing channels" where these storms can become entrained in the

tropical circulation, transporting dust to lower latitudes, as discussed by Wang et al. [2003]. The predicted peaks in activity correspond reasonably well with the observations [Cantor et al., 2002]. Additional mid-northern latitude storm activity is predicted over eastern Amazonis (150°W), in correspondence with observations. This lifting is apparently associated with the sharp topographic gradient as the Amazonis lowlands rapidly grade into the flank of Olympus Mons and the Tharsis plateau.

### 2.6. Spatial Distribution of Net Dust Lifting and Deposition

Prognostic simulation of the full annual atmosphere dust cycle allows us to examine the fluxes of significance for the Martian surface dust deposits in a manner that has not been possible to date. Large areas of thick dust mantling have been identified mapped using thermal and visible remote sensing [Christensen, 1986]. Ultimately, these "dust continents" must result from an imbalance of dust erosion and deposition on a timescale that depends strongly on the deposition/erosion rates. Since the prediction of net deposition/erosion rates requires prediction of dust lifting by wind stress and by convective dust devils, dust transport by the model winds, and the patterns of dust fall-out, prior predictions of deposition/erosion rates have been incomplete [e.g., Haberle et al., 2003].

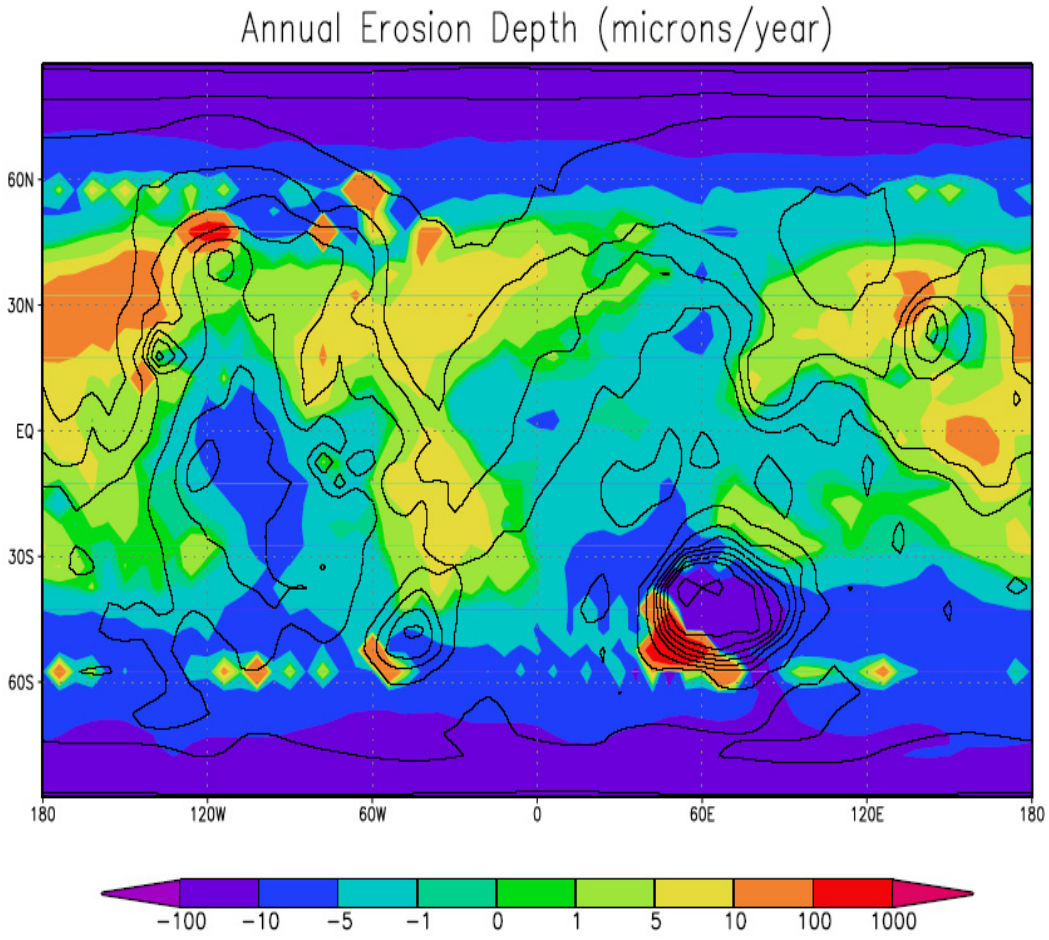


**Figure 18.** The GCM-predicted, annually integrated net dust erosion depth (micron) for the "best-fit" case. The topography is contoured in black for context.

Figure 18 shows the annually integrated, net dust erosion depth for the "best case" simulation described in the previous section. This simulation includes dust devil and wind stress lifting, and comes from a simulation that generates variable global dust storms. The year shown does not include a global dust storm. Similar output for a year with a global dust storm is described by Basu et al. [2004]. The Figure shows that across the tropics and mid-latitudes there is a near balance of lifting and deposition: regions of similar areas exhibit similar magnitudes of lifting, but with opposite signs, suggesting patterns of net regional dust transport. For example strong winds in the Chryse region (30°-60°W), which are generated by concentration of the Hadley cell return flow generate strong net lifting. Net deposition occurs on the high Tharsis Plateau (80°-120°W, 30°S-10°N). In general, the annual amounts of dust deposition/erosion are smaller than about 10 micron, and the average over the tropics and mid-latitudes is over an

order of magnitude smaller than this. The maximum settling rates in the tropics and mid-latitudes are at the lower end of the Pollack et al. [1979] and the Landis and Jenkins [2000] estimates of mean fall-out, and somewhat higher than estimated by Cantor et al. [2001]. A large fraction of the planet that experiences deposition does so at rates about an order of magnitude smaller than this (~1-5 micron/Martian year). This rate is nearer to, but still about an order of magnitude higher than settling rate estimates from the fading of slope streaks (~0.3micron/Martian year) [Aharonson et al., 2003] (while the spatial mean value of about 0.3micron/year is very close to this estimate, the GCM predicts significant net dust erosion in the region of Amazonis where the longest baseline of observations for this deposition estimate were available). The Landis and Jenkins [2000] observations are not for a full year–when we examine fall-out for the Mars Pathfinder operational period relevant to that study ($L_s$=142°-160°), we find an equivalent annual rate of about 10micron/year versus the Landis and Jenkins [2000] measurement of 6micron/year. Finally, the Pollack et al. [1979] and the Cantor et al. [2001] estimates were based on consideration of dust fall-out following the 1977 dust storms and fall-out from observed regional storms only. The applicability to fallout of dust generated by all sources is questionable. The GCM peak net injection rates (~10 micron/Martian year) are about three orders of magnitude smaller than the "erosion potential" estimates calculated by Haberle et al. [2003], but similar to values obtained by Newman et al. [2004]. About an order of magnitudes-worth of this discrepancy is ascribable to the difference between instantaneous dust injection and instantaneous dust injection minus dust fall-out. Most of the remainder is due to the fact that as the seasons change, the regions of instantaneous dust injection change. As a result, areas of strong net lifting at, say $L_s$=120°, become regions of deposition at other seasons. The "erosion potential" takes into account neither of these factors of deposition, and thus if interpreted as the net dust injection or erosion rate (which Haberle et al. [2003] warn against doing), it is grossly in error.

Averaged between 75°S and 75°N, the net annual effect for current orbital parameters is one of erosion–a very small amount of dust is removed each year, corresponding to much less than 1 micron (~0.3 micron to be exact, but an estimate of 0.1-1micron probably better captures uncertainties). Net loss over most of the planet is required by net deposition at both poles, as discussed by Pollock et al. [1979]. The net deposition at the poles proceeds in the simulation at roughly 20micon/Martian year. This rate approaches the dust-settling rate estimated by

Pollack et al. [1979] of 10-40micron. This deposition rate is uniform (to the factor of a few level) over the seasonal and residual caps, so a dust deposition rate onto the residual caps of roughly this rate (10-20 microns/year) is our best estimate for consideration, say, of dust incorporation for models of layered deposit formation.

The pattern and rates of dust deposition/erosion shown in Figure 16 are problematic for the development and maintenance of the low-latitude "dust continents". The model predicts a distinct pattern of net erosion and net deposition at a sufficient rate that deposits of dust over 100m thick could be formed. This is likely much thicker than many of the actual deposits, which have been observed to undergo geographical redistribution on timescales of a few Martian years. Further, the spatial pattern of predicted dust deposition/erosion does not correlate perfectly with the observed distribution of dust deposits. Christensen [1986] discussed the possibility of redistribution of the surface dust deposits over time as the circulation changed with changing spin/orbital properties (obliquity, eccentricity, and argument of perihelion). Such changes require deposition/erosion rates of ~10micron/year, which are not far from the higher values found over a good fraction (maybe a quarter) of the planet between 50°S and 50°N.

**2.7 Summary and Conclusions**

This paper presents results from GCM simulations of an interactive dust cycle on Mars. The version of the GFDL Mars GCM used in this study differs from that described by Fenton and Richardson [2001], Richardson and Wilson [2002ab] and Mischna et al. [2003]. Instead of a dust injection scheme based only on the surface-air temperature contrast, the present model includes detailed, physically based parameterizations of dust lifting, similar to the approach of Newman et al. [2002a]. These schemes represent the injection of dust by convective motions, using thermodynamic theory of dust devils [Renno et al., 1998; 2000], applied on the coarse resolution of the GCM grid, and by large-scale wind stresses, using a functional dependence on the frictional velocity [Shao, 2001]. As before, the model treats dust as a transportable trace species, the dust distribution being affected by the model-resolved winds, sub-grid scale diffusion, and particle-mass-dependent sedimentation. The dust is radiatively active in the GCM, influencing thermal infrared and visible radiative heating of the atmosphere.

The convective and resolved-wind dust injection schemes introduce three free parameters. A given simulation, extending for multiple Martian years, uses spatially and temporally fixed values for each of these free parameters. These parameters are the rate constants applied to the two injection schemes (simple multipliers) and the threshold lifting stress for the resolved-wind lifting scheme. Convective lifting is prescribed without a threshold. We chose to use the seasonal cycle of globally averaged air temperatures as our primary quantitative means of assessing the quality of the GCM simulations. The first question we address with the model is whether the injection schemes can generate a dust cycle in agreement with observations, and what combination(s) of parameters allow the best fit. We find that the shape of the seasonal air temperature curve in northern spring and summer, when air temperatures are observed to be highly repeatable [Liu et al., 2003], can be fit either by the convective lifting scheme or by the stress-lifting scheme with low values of stress-threshold and lifting rate. The northern spring and summer temperatures cannot be fit if the dust opacity only results from the fall-out of dust from a global storm in the previous southern summer. Both the convective and low-threshold stress-lifting schemes require steady and widespread dust lifting throughout northern spring and summer. Widespread convective (dust devil) lifting seems consistent with the widespread observation of dust devils and dust devil tracks, and indeed the model predicts injection rates that are in good agreement with analysis of Imager for Mars Pathfinder data [Ferri et al., 2003]. Widespread wind stress lifting seems much less consistent with the relatively few and sporadic local dust storms observed in northern summer [Cantor et al., 2001]. Specifically, cap edge storms, other local dust storms, and lifting associated with dust streak formation appear insufficiently frequent. Further work is needed to provide quantitative support for these qualitative arguments. However, on the basis of the model results and inferences from observations, we propose that dust devils are the primary dynamical system providing the dust injection necessary to sustain the background haze on Mars.

Regardless of the convective scheme rate parameter, dust storms cannot be generated in the model. From this we suggest that dust devils are not the precursors of dust storms, in agreement with imaging observations. It is also not possible to generate dust storms with the stress-lifting scheme set with parameter values necessary to sustain the background dust haze. Conversely, with stress values and injection rates high enough to initiate storm activity, lifting does not occur throughout much of northern spring and summer. Simulation of the dust cycle

involving storms and the background haze requires two schemes: a combination of high rate, high threshold lifting, and either convective lifting or low threshold, low rate stress lifting. Justification for the use of two different sets of injection parameters in two parallel stress-lifting schemes is possible, but seems a more complex and observationally less-well supported solution than the convective plus high threshold injection scheme option. When run with a combination of convective and high threshold dust injection schemes, the model is able to generate both a realistic background dust cycle, and for the first time, spontaneous and inter-(and intra-) annually variable global dust storms. These storms are discussed in greater detail in B04.

Varying injection parameters, a multiyear "best fit" simulation can be produced with optimal air temperature and dust storm emulation. This simulation uses convective and high threshold stress lifting. The model develops a range of local and regional storms, the variety and distribution of which compares reasonably well with observations [Cantor et al., 2001]. Specifically, seasonal ice-cap edge dust storms are simulated, as are storms associated with various topographic features. Comparison with air temperature cross-section data suggests that cap edge lifting is somewhat under-predicted. Several small dust storms are generated in the northern early autumn and later winter, associated with low-pressure frontal storms, as described by Wang et al. [2003] and also generated in the Oxford Mars GCM [Newman et al., 2002b]. One such storm develops into a large regional event, resembling the 1999 storm and the dust storm that preceded the Mars Exploration Rover landings [B04]. The model also predicts the distribution and seasonal variation of dust devil activity (if the convective lifting is ascribed to dust devils). A distinct peak in activity is found in the model in Amazonis, a region of observed enhanced dust devil activity.

The rates of dust injection and the net removal/deposition of dust on the surface are predictions of the model. It has not been possible to predict annually integrated net dust deposition/erosion rates until this point as it requires a validated dust cycle that includes interactive lifting, transport, and deposition of dust. Previous estimates of dust erosion have had to rely on "lifting potential" derived from the model wind stresses to predict lifting and have ignored the other side of the cycle: deposition [Haberle et al., 2003]. Our results suggest that net; annually integrated erosion/deposition rates are roughly one to two-orders of

magnitude lower when the full dust cycle is taken into account. Thus extreme caution must be taken when interpreting the previously generated "lifting potential" erosion values. Net annual erosion/deposition rates compare well with estimates from the Mars Pathfinder solar panel experiment [Landis and Jenkins, 2000] and from analysis of the darkening of slope streaks [Aharonson et al., 2003]. Between 75°S and 75°N, the net annual erosion rate is 0.3micron/Martian year (0.1-1 micron/Martian year, conservatively), which is balanced by net polar deposition at roughly 20micron/Martian year, consistent with estimates from Pollack et al. [1979]. Although these values are the best possible GCM estimate at this time, the model still neglects processes of potential importance, including dust-ice interactions. These must be assessed in future models.

# Chapter3

# Simulation of Spontaneous and Variable Global Dust Storms with the GFDL Mars GCM

**Abstract**

We report on the successful simulation of global dust storms in a general circulation model. The simulated storms develop spontaneously in multiyear simulations, and exhibit significant inter-annual variability. The simulated storms produce dramatic increases in atmospheric dustiness, global-mean air temperatures, and atmospheric circulation intensity, in accord with observations. As with observed global storms, spontaneous initiation of storms in the model occurs in southern spring and summer, and there is significant inter-annual variability in storm development: years with no storms are interspersed with years with storms of various size and specific seasonal date of initiation. Our results support the idea that variable and spontaneous global dust storm behavior can emerge from a periodically forced system (the only forcing being the diurnal and seasonal cycles) when the dust injection mechanism involves an activation threshold. The role of finite surface dust reservoirs is not examined here. In our simulations, surface wind stresses associated with resolved, large-scale (>300 km) wind systems initiate the storms. These winds are generally associated with the seasonally migrating $CO_2$ cap boundary and sloping topography of the Hellas basin. A very limited number of large storms begin with lifting along the frontal zones associated with traveling waves in the northern hemisphere. Explosive growth to global scales results from the intensification of the Hadley circulation and the activation of secondary dust lifting centers.

## 3.1. Introduction

Global dust storms (GDS) are major atmospheric events observed to rage for months in the Martian atmosphere. At their peak, these storms are so extensive that they were observed through terrestrial telescopes decades before they were documented in detail from orbiting spacecraft [Leovy et al., 1972; Briggs et al., 1979; Kahn et al., 1992; Martin and Zurek, 1993; Martin and Richardson, 1993; Fenton et al., 1997; Smith et al., 2002; Liu et al., 2003]. During a GDS, the atmospheric haze becomes sufficiently thick that surface features become almost completely obscured, as was the case for weeks after the arrival of the Mariner 9 spacecraft at Mars in 1971, and most recently during the 2001 GDS. The presence of large amounts of dust in the atmosphere during a GDS modifies atmospheric temperatures and the global circulation. The dust is a mineral aerosol [Kahn et al., 1992] that interacts with visible and infrared radiation, modifying atmospheric heating rates. By influencing heating rates, and hence atmospheric temperatures and circulation, GDSs can modify the cycles of water and $CO_2$ on Mars. Observations during the course of the past century or so suggest that GDSs occur only during southern spring and summer. Global-mean air temperatures show highly repeatable behavior in northern spring and summer, with the clear indication of GDS activity in southern spring and summer [*Liu* et al., 2003]. This timing is consistent with greater forcing of the Martian atmosphere during the period around perihelion (at $L_s$=251, where $L_s$ is the seasonal indicator, measured in degrees from $L_s$=0 at northern spring equinox). The observations also show that global storms do not occur every Martian year. Based on spacecraft and telescopic observations, *Martin and Zurek* [1993] estimated that a GDS occurs once every two-to-three Martian year. Even in years with global events, the size and exact season of their occurrence vary significantly: The 2001 storm began at southern spring equinox ($L_s$=180), while the 1977b storm began just after southern summer solstice. Understanding of the Martian climate requires an understanding of the dynamics of these variable phenomena.

Triggering is the key puzzle behind GDSs: What makes a tiny fraction of the many small dust storms that occur each year grow into global-scale events, why do they only occur in some years, and why are the sizes and timing of occurrence different from year-to-year? Hypotheses for triggering rely on radiative-dynamical feedback in which the lifted dust plays a key role. They include explosive growth of low-pressure hurricane-like systems [*Gierasch and Goody*, 1973], transitions in the extent of the Hadley circulation [*Schneider*, 1983], and interactions

between different atmospheric wave and circulation modes [Leovy et al., 1973; Zurek and Leovy, 1981; Tillman, 1988]. Gierasch and Goody [1973] proposed that GDS begin with a weak vortex in the presence of relatively light surface winds. As air converges to form a dusty core, it is heated up and rises, pulling in more air at lower levels. While a true hurricane, involving strong rotational motion, or a rotational convective vortex as a precursor to global storms is ruled out by imaging observations of the early phases of the 1977 and 2001 global storms [Briggs et al., 1979, Strausberg et al., 2005], circulation induced by the presence of dust in the atmosphere is still likely an important part of storm growth. The second theory, proposed by Schneider [1983], invokes a transitional extension of the southern summer Hadley cell across the equator and into the northern hemisphere. While substantial expansion of the Hadley circulation is required to explain observations of winter polar warming during global dust storms [Wilson, 1997], air temperature measurements suggest that the Hadley circulation is fully cross equatorial prior to GDS development in many GDS years (except in the 1977a storm). However this is not true for the 2001 dust storm. The third hypothesis is focused on explaining transient high surface winds. Leovy et al*.,* [1973] proposed that the superposition of the Hadley cell circulation, the planetary scale topographic winds, and the thermal tide would produce wind speeds high enough to raise dust from the surface. Zurek [1976] suggested that the onset of a GDS may require a combination of efficient, near resonance response and amplified thermo-tidal forcing. Thus this third hypothesis allows a range of possible storm triggering mechanisms that need to be specified and examined in detail.

The variability of GDS triggering can be viewed in two ways. The mechanisms delineated above likely would not repeat perfectly each year, due to a variety of circumstances, depending on the dynamics of the particular system in question. This bias is borne of our experience of weather: only in special circumstances is weather highly predictable. This internal variability in the Martian atmosphere is only significant for GDS development if the threshold for run-away storm growth falls somewhere in the range of naturally-occurring variability: presumably at an extreme. In this case, rare internal perturbations (such as a strong coherence of dynamical systems, as suggested by Leovy et al. [1973] and most recently for a smaller storm by *Wang et al.* [2003]) could push the atmospheric system into a state that generates a GDS. Pankine and

Ingersoll [2002] illustrated this idea with a low-order numerical model forced with prescribed noise. However, it is possible that GDS variability is not limited solely or at all by low-probability weather events. Availability of dust on the surface may be a key factor, or it may be that spatial redistribution of dust on the surface (or ice in the seasonal polar caps) modifies the forcing of the circulation in such a way as to allow GDS's in some configurations, but not others. In both cases, these changes in the surface are sensitive to the action or inaction of global storms in previous years [Haberle, 1986]. Here, the surface retains a "memory" of previous atmospheric states that provides the key to whether a GDS occurs in a given year or not. Obviously, a major question we wish to address here is whether internal variability in a full General Circulation Model (GCM) can generate "weather noise" of the right character to allow the first means of variability to operate, and whether a surface memory site is required for inter-annual and intra-seasonal variability of global storms.

Work on the numerical modeling of global storms began with investigations of the degree to which dust can influence the Martian circulation. Two- and three-dimensional modeling showed that the atmosphere responds quite dramatically and there exists ample opportunity for non-linear feedback in the system once dust is injected [Haberle et al., 1982; Murphy et al., 1993; 1995; Wilson, 1997]. Some of these modeling efforts also showed that once a significant amount of dust is injected into the atmosphere, global-mean air temperatures and the signatures of the thermal tide in pressure and temperature observations could be explained reasonably well throughout the storm decay phase [Murphy et al., 1993; 1995; Wilson and Hamilton, 1996; Wilson, 1997; Wilson and Richardson, 2000]. Results of experiments with interactive dust lifting, where dust injection is controlled by model-resolved winds and near surface static stability were first published by Newman et al*.,* [2002ab]. The Newman *et al.* [2002ab] work demonstrated that a range of variable dust-related phenomena (dust storms on various scales) could emerge from the natural, steady forcing of a GCM by diurnal and seasonal cycles. It also defined the two-process dust injection formalism that we use in this work, with dust injected by sub-grid scale convective processes and resolved-wind stresses. However, the questions outlined above remain open following the Newman et al., [2002ab] work–their model was not able to obtain global dust storms in any realistic way (while "global" dust events were simulated, they corresponded to wholly unrealistic dust injection scenarios),

and the year-to-year variability in dust activity was very muted compared with observations. Simulating the emergence of GDS's from a realistic background state is very important for correctly representing the Martian dust cycle. Newman et al., [2002ab] simulations do have limitations. In particular, their parameterizations lead to simulated storms in the northern spring and summer season while such activity has never been observed. The NSS dust activity has been observed to be quite dormant. All the big dust storms have been observed to occur only in the south summer season. Thus there seems to be something fundamentally wrong in their representation or tuning of the actual phenomena responsible for dust lifting on Mars. Their model also is not very stable with respect to large opacities.

Newman et al. [2002ab] for the first time showed results from a radiatively active model where there was feedback between the circulation, the dust lifted and the heating rates. Also this was the first time that anyone simulated spontaneous storms without prescribed or artificial lifting on Mars. The lifting schemes though simplistic were able to capture the two basic forms of lifting i.e. lifting due to dust devils and lifting due to near surface wind stress. These schemes will be discussed below.

The stress lifting schemes individually produced dust lifting that was reasonable keeping in mind that none of them could successfully simulate the Martian dust cycle realistically with the background haze, regional storms, global storms and inter-annual variability of these storms.

1) **GST (Gustiness) scheme**-When Newman et al., [2002] employed the GST scheme, which is the stress lifting with gustiness parameterization, they got similar looking storms every year with no inter-annual variability. This is expected as the GST scheme gives smooth lifting and there is no dramatic increase in the dust loading of the atmosphere and the radiative dynamical feedback doesn't work as effectively in the explosive growth of the storm as observed in the Viking storms or 2001 GDS. Therefore GST alone cannot simulate the Martian dust cycle accurately. Inter-annual variability occurs when the atmospheric sensitivity is increased and this cannot be achieved with smooth, predictable lifting

2) **DAC (Dust Devil Activity) lifting only**- They employed the DAC lifting only, in their simulations which is the Dust Devil lifting with no threshold. This gives lower opacities as

expected due to the negative feedback of the dust devil lifting scheme- i.e. as more dust is lifted the boundary layer becomes stable and the temperature contrast between the top of the boundary layer and the surface also reduces, this prevents further rising of dust which is dependent on the depth of the planetary boundary layer and this temperature contrast. But this kind of lifting gives high dust opacities in the northern hemisphere, which is not observed anywhere. These results suggest that dust devils cannot be involved in dust storm evolution and development a) because of the negative feedback b) because of the high northern summer opacities they produce.

3) **Combined GST+DAC lifting**- this also produced storms similar to the GST only case since 80% of the lifting was due to GST and there was no inter-annual variability.

4) **Simulations with NOG (No Gustiness) +DAC lifting**- threshold sensitive stress lifting+ no-threshold dust devil lifting. When they employed this scheme, they observed sharp lifting ~Ls=190, from the Hellas region and these are some attributes that have been observed in 2001 global dust storm. They also got a second storm ~Ls=270 (which is what we also observe in the preliminary calculations with our upgraded advection scheme). Even by using different inter-particle cohesion parameters, they were not able to get inter-annual variability and besides the optical depths were low for categorizing these as global storms. The optical depths were much lower than the GST only parameterization and also lower than the DAC only lifting scheme. The simulations they show were at the upper level of their stability limits. High dust loading started a radiative dynamical feedback with this scheme that gave high temperatures and their model crashed. This might be an inherent problem with their model. Thus they were not able to test the effects of increased lifting with this scheme. To make the atmosphere sensitive, there has to be high explosive dust loading according to the threshold dependent stress-lifting scheme. We use a similar scheme with no threshold dust devil lifting and threshold dependent stress lifting and get temporal and spatial inter-annual variability with a better annual dust cycle and realistic Northern Spring and Summer (NSS) temperatures. Inter-annual variability (in our simulations) occurred only when the source term was higher than a certain amount, the aspect that Newman et al. were unable to explore with their current model. Also the Chryse storms simulated by Newman et al. using this scheme were very rare

events, once in 10 years. However it has been observed that Chryse storms are very common phenomena that typically occur several times every year [Wang et al., 2005] and have a periodicity of 2-3 days. The time of occurrence of the simulated Chryse storms was also different from what has been observed [Wang et al 2005]. These storms have been observed in the pre-solstice (Ls=210-235) and post-solstice (Ls=310-350) seasons. However Newman et al. simulate these storms close to Ls~255 which is quite late in the season.

5) **DTH (Dust devil threshold) + NOG scheme**- they use the threshold dependent dust devil lifting and the threshold dependent stress lifting in their final simulations where they get some inter-annual variability. These simulations that they suggest might be able to best reproduce all the aspects of the observed Martian cycle are however quite unrealistic.

In their parameterization, the DTH scheme is the main cause of the large global storms. But the same DTH scheme produces unrealistically high opacities in the northern spring and summer that has never been observed. To get the background haze that one observes on Mars, it is therefore necessary to shut off the DTH mechanism in the northern summer. There is no physically plausible explanation for why the strength of the DTH lifting would vary according to different seasons especially since the dust devils are observed to be quite widespread all over the planet, at all times of the year. Also the DTH negative feedback reduces NOG lifting. There is again no physical basis for this kind of shut off mechanism. All the DTH scheme does is to suppress high opacities that are produced by NOG only (that made their model crash in the NOG+DAC scheme). So the DTH+NOG scheme is more successful in coping with model inadequacies with high opacities than trying to capture the physics of lifting on Mars. Thus even though there is some amount of inter-annual variability in the storms, the unrealistically high northern spring and summer temperatures and opacities renders these simulated cycles quite unrealistic.

The conclusion of this review is that the importance of the background cycle has been underestimated by Newman et al. [2002a]. Simulating the NSS (northern spring and summer) temperatures accurately itself would have eliminated certain kinds of lifting like DTH or DAC as being responsible for global storms on Mars. This would have narrowed the choice down to

NOG or GST. Since GST lifting is smooth and does not increase atmospheric sensitivity that much it is less likely to produce inter-annual variability than NOG, which injects huge amounts of dust in a short period of time, that enables explosive growth of the dust storm as observed. This also gives a lot of inter-annual variability in the Martian dust cycles as the stress patterns change from year to year.

Hence we employ a DAC like parameterization for background lifting in our scheme. This maintains the background haze on Mars. The NOG like scheme is added on top of this scheme and it plays an important role in the development of the global dust storms and their inter-annual variability.

Even though the exact conditions for initiation of GDSs are not clear at this time, it is reasonable to argue that the dust activity in each season might leave some kind of a memory that influences the dust activity in the following seasons or years. Hence for any realistic simulations of the Martian dust cycle it is important that the basic constraints in terms of temperatures and opacities are satisfied to first order for each season. In our study we find it is relatively easy to independently simulate the correct weather conditions (in agreement with observations) for a particular season or location. What is difficult is a good global representation of the Martian dust cycle, which can be achieved only when all the interactions between various lifting schemes, the boundary layer phenomena and the radiative dynamical feedback is formulated accurately.

In this paper, we describe the simulation of global dust storms with the GFDL Mars GCM. The model uses dust injection parameterizations described below, and in more detail by Basu *et al.* [2004]. Our parameterization is relatively simply described with 2 adjustable tuning parameters. We initially provide a sweep of dust injection parameters to map out the range of model behavior. We then proceed to examine some of the decadal simulations that generate spontaneous and variable global storms. The triggering and growth mechanisms are examined in some detail: global storms are primarily found to initiate in the southern mid-latitudes near the Hellas basin in southern spring. A very limited number of large storms are found to initiate in the northern high latitudes in association with frontal cyclones, via the mechanism

proposed by *Wang et al.* [2003]. In all cases, growth to global scales is found to require the "spin-up" of the Hadley circulation and activation of secondary dust lifting centers.

## 3.2. Model Description

The simulations discussed in this paper are undertaken with the GFDL Mars GCM, using the model in the form described by *Basu et al.* [2004]. Briefly, the model is a Mars-adapted version of the GFDL SKYHI GCM [Hamilton et al., 1995; Wilson and Hamilton, 1996]. For these simulations, grid-point spacing is 5° in latitude by 6° in longitude, with 20 vertical levels between the surface and ~85 km. Radiative heating by dust and $CO_2$ in the visible and thermal infrared is treated. The surface and boundary layers are treated with a Monin-Obukhov (MO) surface drag scheme coupled to a diffusive boundary layer with a Richardson number dependent diffusion coefficient. Dust is advected by large-scale winds, by sub-grid diffusion, and by dust sedimentation. Currently employ two dust particle sizes- 0.625μm and 2.5μm to represent dust particle distribution. For simplicity, we assume that each particle size is characterized by the same optical properties. We can adjust the relative contributions to total opacity. This is effectively equivalent to specifying different injection rates. The sedimentation rates of these two are proportional to their sizes (radii), hence the bigger particles settle faster and the smaller particles have a greater residence time in the atmosphere. Since the water-ice clouds are generally insignificant during the dust storm season [Smith et al. 2002], we are not representing the possible scavenging and radiative impact of water ice clouds.

Dust is injected into the atmosphere using two schemes. The first represents small-scale, convective lifting, which observations suggest is primarily in the form of dust devil activity. This scheme relates the injection rate to the sensible heat flux and boundary layer depth (following Renno et al. [1998; 2000] and Newman et al. [2002a]), using a multiplicative, tunable injection rate parameter [Basu et al., 2004]. This rate parameter is labeled as $R_{DDL}$. The second scheme relates dust injection to the surface stress generated by model-resolved winds. The functional form sets the injection equal to the cube of the drag velocity scaled by a multiplicative, tunable rate parameter (labeled $R_{SL}$). There is no wind-stress injection when the stress is below a threshold value. We regard this threshold value as a free parameter ($\tau_{SL}$). As

such, there are three free parameters which provide the range of available exploration space: $R_{DDL}$, $R_{SL}$, and $\tau_{SL}$. The dust injection schemes, their behavior, and the ability of the GCM to simulate the observed annual cycle of midlevel air temperatures and dust column opacity are described in much greater depth by Basu et al. [2004]. Finally, dust is assumed infinitely available at the surface.

### 3.3. Exploration of Model Behavior as Wind Stress Lifting Parameters Vary

The philosophy of this study has been laid out in some detail in the companion paper [Basu et al., 2004]. In that paper, we describe the generation of a seasonal cycle of dust and air temperatures that are quite close to those observed. An important result from that paper, of relevance to this study, is the finding that convective processes must provide the majority of the dust injection to supply the seasonal dust cycle. For wind stress lifting to play a major role, the stress threshold has to be lowered to a point wherein local and regional storms are essentially continuously on going over a large fraction of the planetary surface. This is inconsistent with observations [Briggs et al., 1979; Cantor et al., 2001]. As the parameters are changed to generate fewer and bigger dust storms, more in keeping with the observations, the model produces an air temperature cycle that is increasingly discordant with observations [Basu et al., 2004]. This is a useful result for our purposes as it allows us to separate convective and wind stress lifting. The convective lifting can be tuned to fit the air temperature cycle (by choosing a spatially and temporally fixed value of $R_{DDL}$ for use in all of our subsequent simulations), leaving only a range of values for $R_{SL}$ and $\tau_{SL}$ to be explored for dust storm behavior. In support of this separability, we find that if we allow stress lifting to generate the background dust, and ignore the over-generation of local and regional storm activity, we find that in simulations extending over more than a decade (10 Mars years) there is no development of global storms and essentially no inter-annual variability within the simulation.

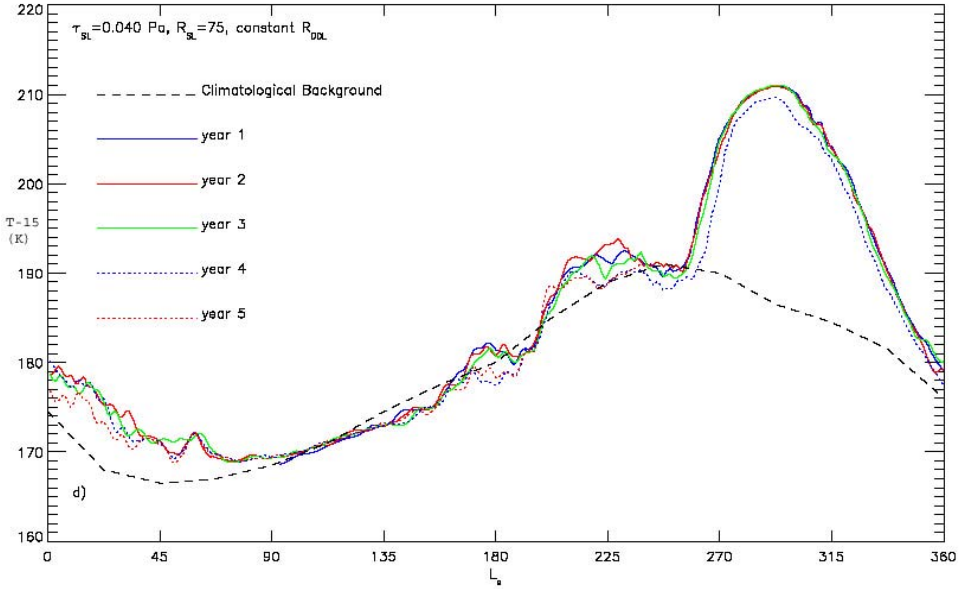


**Figure 1a:** Multiyear globally averaged T-15 temperatures as a function of areocentric solar longitude for a low threshold case of 0.04 Pa. Every year the global storms behave the same way; have the same intensity and same time of initiation. There is no inter-annual variability at these low thresholds.

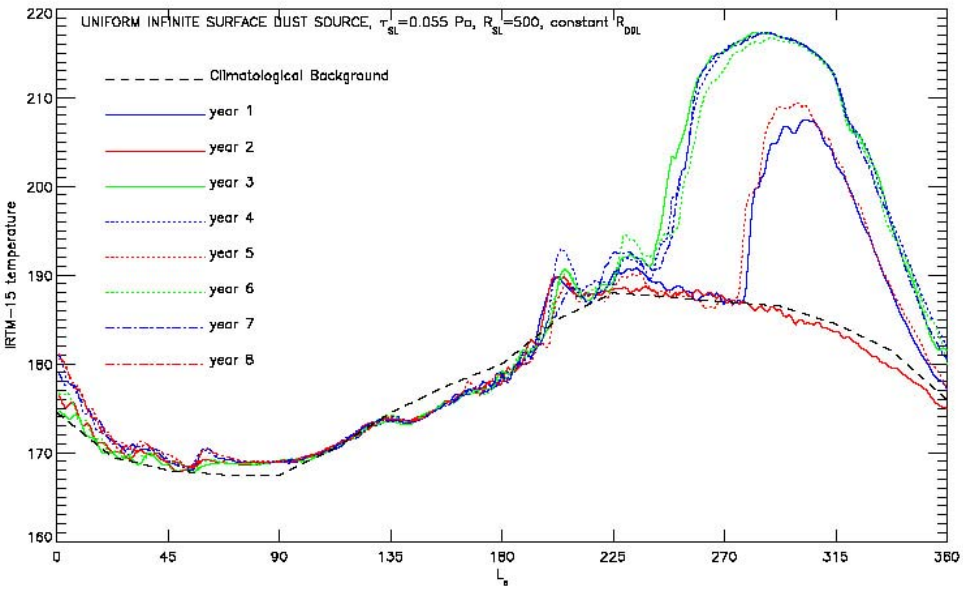

**Figure 1b:** Multiyear globally averaged T-15 temperatures as a function of areocentric solar longitude for a simulation that is in the critical threshold range i.e. there is inter-annual variability from year to year. The stress threshold in this case is 0.055 Pa.

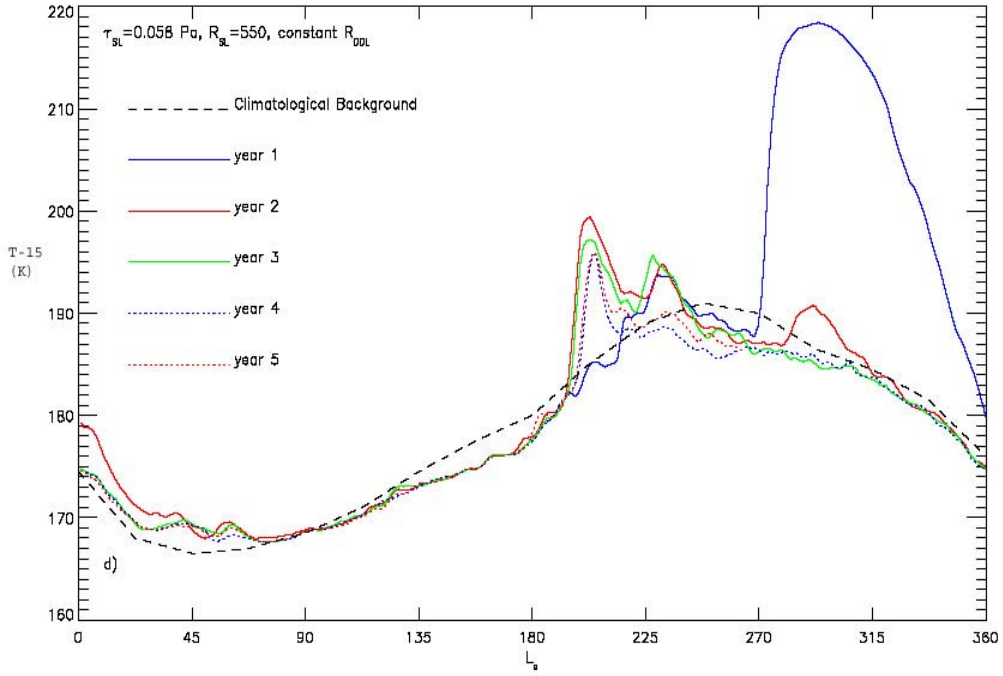


**Figure 1c:** Multiyear simulations showing the globally averaged T-15 temperatures as a function of the areocentric solar longitude for a stress threshold of 0.058 Pa. This gives multiple storms in a year- an early Hellas storm and a late Hellas storm combined with Chryse storms in pre and post solstice seasons.

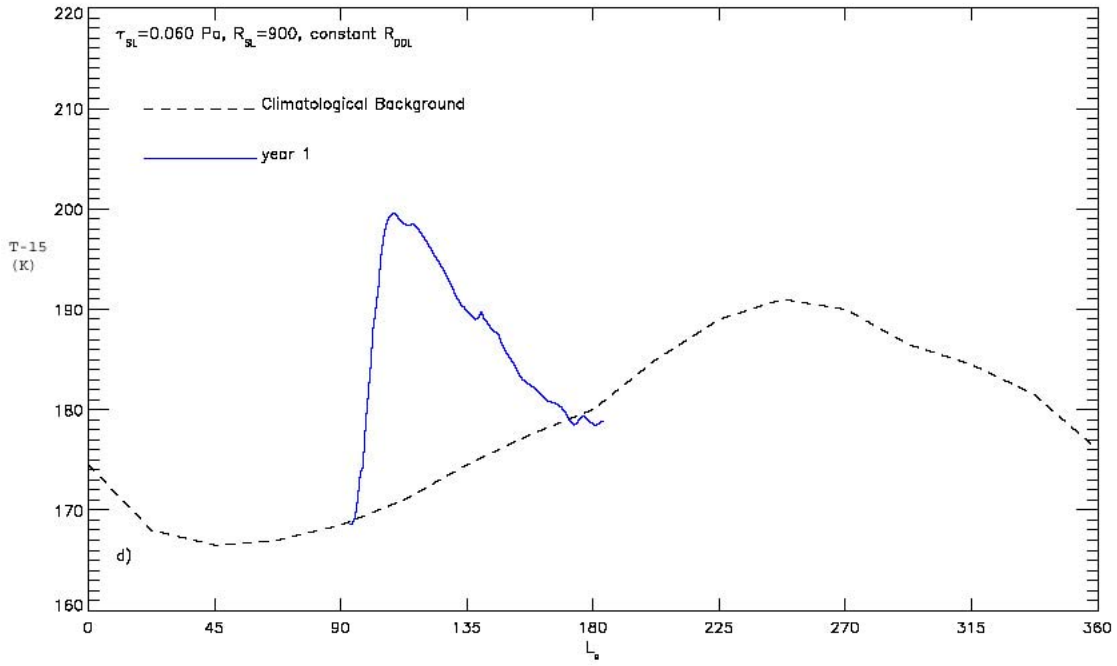


**Figure 1d**: Global average T15 temperatures for a simulation with a high stress threshold of 0.060 Pa. This gives unrealistic storm activity in the northern summer season and hence is outside the critical threshold range.

A very large number of multiyear simulations (~100) have been undertaken to search the $R_{SL}$-$\tau_{SL}$ parameter space for variable global dust storm behavior. The minimum run length of any of these simulations was two Martian years, with most extending for considerably longer. The dust cycle and dust storm behavior in each of these simulations has been assessed by examination of the integrated, mid-level (~25km) air temperature cycle, and the evolving behavior of the spatial variation of dust (undertaken be examining "movies" of dust distribution maps). Example air temperature cycles are shown in Figure 1a-d. The comparison climatology is derived from seven Martian years of spacecraft thermal infrared data [Liu et al., 2003; Basu et al., 2004]. Figure 1a shows output from a simulation with a relatively low value of the threshold stress for lifting ($\tau_{SL}$). In this particular case, the injection rate parameter is set high enough that global dust storms are generated in the model. However, the simulated storms are found to repeat almost exactly in each year. It should also be noted that elevated seasonal cap edge dust storm activity in northern spring cause the shape of the

simulated air temperature cycle to deviate from observations, with a shift of the temperature minimum to near $L_s$=90, while the observed minimum is nearer $L_s$=45. Very high values of stress threshold and low values of injection rate leads to essentially no stress lifting, no dust storms, and essentially no inter-annual variability. Figure 1b shows an example of variable global dust storm generation in the model. In this case, the stress threshold and injection rate parameter are set such that realistic local and seasonal dust storms develop [Basu et al., 2004], but that in addition, global dust storms with peak temperatures close to those observed can develop in southern spring and summer. Critically, unlike the case in Figure 1a, the global dust storms do not repeat every year, are not the same size nor begin at exactly the same seasonal date each year, and only develop during southern spring and summer. As the storms decay, air temperatures relax back to a realistic state, and the following year may or may not have a global storm. The details of these storms are discussed in the next section.

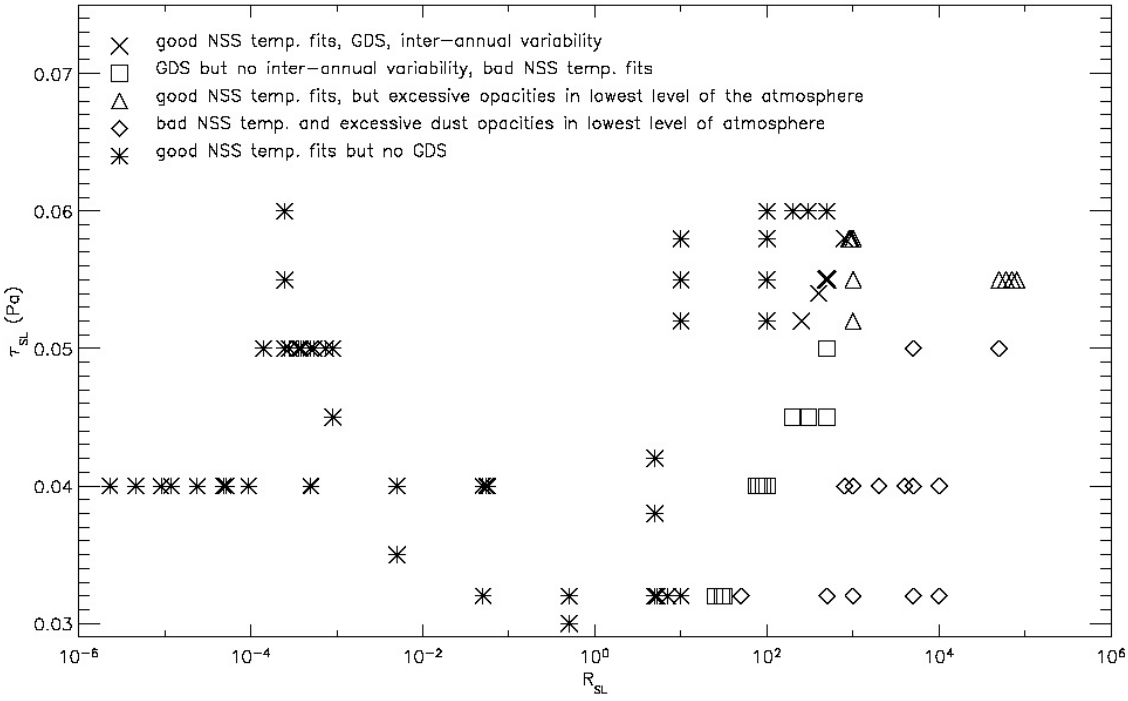

**Figure2.** Parameter space searched for the realistic inter-annually variable dust storms. Different shapes are used to represent different model behaviors. For low injection rates (RSL), no global dust storms are generated. For very high injection rates the air temperatures are abnormally high. For reasonable values of lifting rates, low stress thresholds ($\tau_{SL}$) give repeatable storms every year, high stress thresholds give no global dust storms at all and medium values of stress thresholds give inter-annually variable realistic storms. As can be seen from the plot, fine-tuning of these parameters is required to get the realistic variable global dust storms.

Using criteria laid out in the previous paragraph, the archive of simulations was examined to search for the development of global dust storms, variability of these storms, and the quality of air temperature predictions for northern spring and summer. Only $R_{SL}$ and $\tau_{SL}$ were varied between simulations, and all parameters were held constant during each individual simulation. The results are summarized in Figure 2. Different colored shapes are used to represent different model behaviors. This figure shows several distinct and coherent domains of behavior. For low injection rate ($R_{SL}$), the stress lifting does not significantly impact the simulations: no global storms are generated, and insufficient dust is lifted to cause the modeled dust and air temperature cycle to deviate from that generated by the convective lifting scheme. This domain of no global dust storm behavior eventually terminates as the injection rate is increased to a high enough value. This "termination" injection rate has higher values for higher threshold stresses. This makes sense: when a smaller fraction of modeled winds can loft dust, the model requires higher lifting rates for a given stress value to loft the same mass of dust. At the other extreme in the phase-space, if the injection rate is set too high, the atmosphere is incapable of moving this dust out of the lowest atmospheric level (~200-300m thick). While these simulations can still be carried forward, and a subset generate northern summer air temperatures that are not too unrealistic, the lowest-level opacities become unrealistically high. In some of these simulations "global dust storms" can be generated, but not within a global and annual context that is in any sense realistic.

A thin wedge of domain space, constrained mainly by the lifting rate parameter, separates under- and over-prediction of wind stress dust lifting. This area of domain space is where global dust storms occur within the context of a somewhat realistic model state. This domain can itself be further subdivided. For values of threshold stress that are too low, global dust storms develop, but without inter-annual variability. In many of these cases, as shown in

Figure 1a, the northern spring air temperatures are not well simulated (these simulations are distinct from those mentioned above with excessive lifting rates in that these simulations do not generate events like global dust storms in northern summer, which are totally at odds with observations). Only in a limited area of the $R_{SL}$-$\tau_{SL}$ parameter-space do spontaneous and variable global dust storms develop. For $R_{SL}$ and $\tau_{SL}$ values that are neither too large nor too small, the model is able to generate simulations resembling that shown in Figure 1b. Within this area, variations in the parameters, especially the stress threshold, cause variations in the nature of the simulated global storms. Figure 1c shows an example for a threshold of $\tau_{SL}$ =0.058Pa, verses $\tau_{SL}$=0.055Pa for the simulation shown in Figure 1b. In the Figure 1c case, some variability in the evolution of the storms can be seen, including some evidence for multiple, global storms in a single year. The stress threshold can only be raised so far: at some point it exceeds the maximum value of stress generated in the model and no lifting can occur. If the lifting rate $R_{SL}$ is increased beyond a certain value (dependent on $\tau_{SL}$), unrealistic storms start developing in northern summer from the Acidalia-Chryse region if the lifting rate is set too high Figure 1d, contrary to observations.

It should be noted, as discussed in Basu et al. [2004], that the specific values of $R_{SL}$ and $\tau_{SL}$ corresponding to a particular dust cycle behavior are specific to the current formulation of the MGCM. The values do show sensitivity to the model horizontal and vertical resolution and also the boundary layer mixing scheme. As the model resolution is increased, the stresses at the lifting centers become higher, hence higher stress thresholds and higher rates of DDL and SL are required for getting the 'best fit' simulation When the Monin Obukhov (MO) physics is switched on, global IRTM temperatures are higher than the simulation in which the MO physics is switched off. This is an evidence for sensitivity to the boundary layer mixing scheme, hence the model parameters have to be tuned accordingly with the incorporation of the MO scheme. While dust storms occur in the model for a range of $\tau_{SL}$ that is consistent with laboratory estimated thresholds [Greeley et al., 1992; 2003], it is likely that the values of $\tau_{SL}$ and $R_{SL}$ used in our study compensate for a range of model imprecision. As such, we believe that if our exact parameterizations were placed in a different GCM, different values of the parameters would be needed to regenerate our results. Put another way, while we have great confidence in

the behaviors exhibited by the model and the qualitative accuracy of the parameter space results shown in Figure 2, we have much less confidence in the specific parameters because of known problems with the exact prediction of surface stress values between different numerical models. This likelihood is one of the main reasons to use tunable parameters with atmospheric observations as our guide, rather than using laboratory derived relationships for threshold and injection rate.

### 3.4. Simulated Global Dust Storms

Several tens of global dust storms have been generated by the GCM for climate states that simultaneously provide a good simulation of the non-dust storm atmosphere and strong variability of GDS activity. The simulated global storms can be broadly divided into two categories.

**Storms initiated in the Hellas basin**

The first kind of storms originates from the Hellas basin. These storms can be further divided into two categories: early Hellas storms and late Hellas storms. The stress thresholds for such storms lie in the range 0.05-0.058 Pa.

The early Hellas storm that starts ~Ls=195, is propagated eastwards by westerlies much like the 2001 global dust storm described by Smith et al. [2002] and Strausberg et al. [2005]. This starts from the southwestern rim of the Hellas basin. There is no westward propagation as the easterlies are not strong enough in this season. The storm decays as the westerlies get weaker with approaching summer solstice. The storm spreads to most of the southern hemisphere but does not spread effectively in the northern hemisphere. These kinds of storms are more regional than global and are weaker in intensity than the late Hellas storms that are truly global in nature. Together with the Chryse storm in the northern hemisphere, the early Hellas storm is capable of raising the globally averaged temperatures to ~ 200K (Figure 1c). The active lifting centers in the northern hemisphere are Alba Patera, Amazonis, Olympus Mons, Arcadia, Acidalia/Chryse, Syrtis Major, Isidus and Elysium Mons. Most lifting centers in the northern hemisphere are activated by the Chryse storm and are independent of the storm

originating from the Hellas region. It is possible that the Chryse storms intensify the early Hellas storms or vice versa.

The second kind of Hellas storm that starts around Ls= 270 or a little earlier in some cases (figure 1b) is much bigger than the early Hellas storms as the intensified Hadley cell circulation in the southern season helps propagate this storm. These storms originate mostly from the northeastern rim of the Hellas basin. The global dust storm season in the model extends from Ls=230-285, while smaller storms occur throughout the year [Basu et al., 2004]. In some years there are two storms, in some years there is only one big storm and these are interspersed by no storm years (Figure 1c).

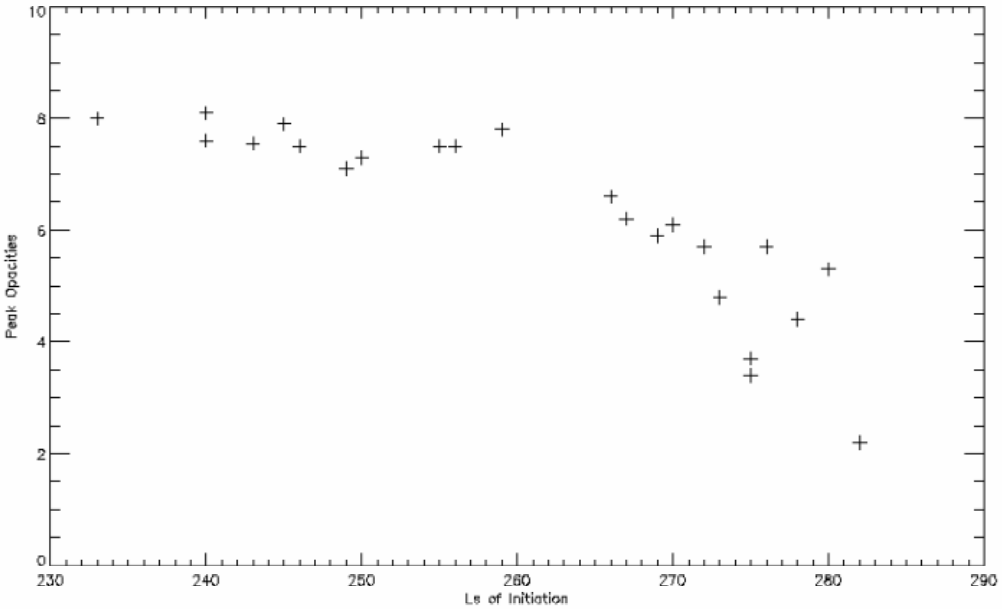


**Figure 3.** Plot of initiation time (Ls) vs peak opacity for the "best fit" variable global dust storms. Storms that originate earlier in the season, reach higher peak opacities than the ones that originate later

Figure 3 provides a summary of the initiation season vs. peak opacity for these storms. The earlier the storm is initiated, the greater is its intensity and it reaches higher peak opacities. This is illustrative of the fact that once the storm starts, the radiative dynamical feedback kicks in and with higher opacities, the temperatures rise and this results in stronger stresses that lift even more dust than before. Figure 1b shows the temperature cycles for our best fit, "variable

GDS" inter-annual simulation. This model readily generates a range of GDS sizes and initiation dates within the "dust storm season", and yields peak air temperatures, which are quite close to those observed. The individual storms within this simulation can be examined more closely and compared with spatially resolved data. This storm spreads along the zonal collar in the beginning and then spreads out in all directions. The subtropical jet helps in putting a lot of dust in the circulation, this in turn strengthens the Hadley cell circulation further. When the Hadley cell circulation becomes strong enough, it activates a secondary lifting center along the zonal collar near Argyre. This secondary lifting center helps in making the storm truly global. The years that the secondary lifting center is not activated, the storm is contained as a local Hellas storm and does not become a global storm. The storm decays as the Hadley cell circulation becomes less intense towards the end of southern summer. The trend in peak opacity results from the fact that the modeled GDS's do not "switch-off" properly. This issue is discussed further in Section 3.6. The spread of GDS initiation date compares well with the historical record [Martin and Zurek, 1993]. GDS events are limited to southern spring and summer, with a bias towards mid-to-late southern spring. This bias can also be seen in Figure 1b, where the predicted global-mean, mid-level air temperatures are compared with observations of Martian storms.

The GDS of 2001 administers a healthy dose of humility, however. That storm began almost at equinox ($L_s$=185°), an very early date of initiation which the GCM has not generated. Indeed, the date is so early that the southern spring and summer Hadley circulation is only just established and is very weak. (Viking 1977a storm at $L_s$ = 204°; another early dust storm suggested in surface pressure data in 1982) Simulating the 2001 GDS will be a challenge. In any case, the GCM-predicted window for GCM development overlaps substantially with, but is somewhat smaller than that observed. We have encouraging results from the high resolution simulations. These simulations will be discussed in detail in forthcoming papers.

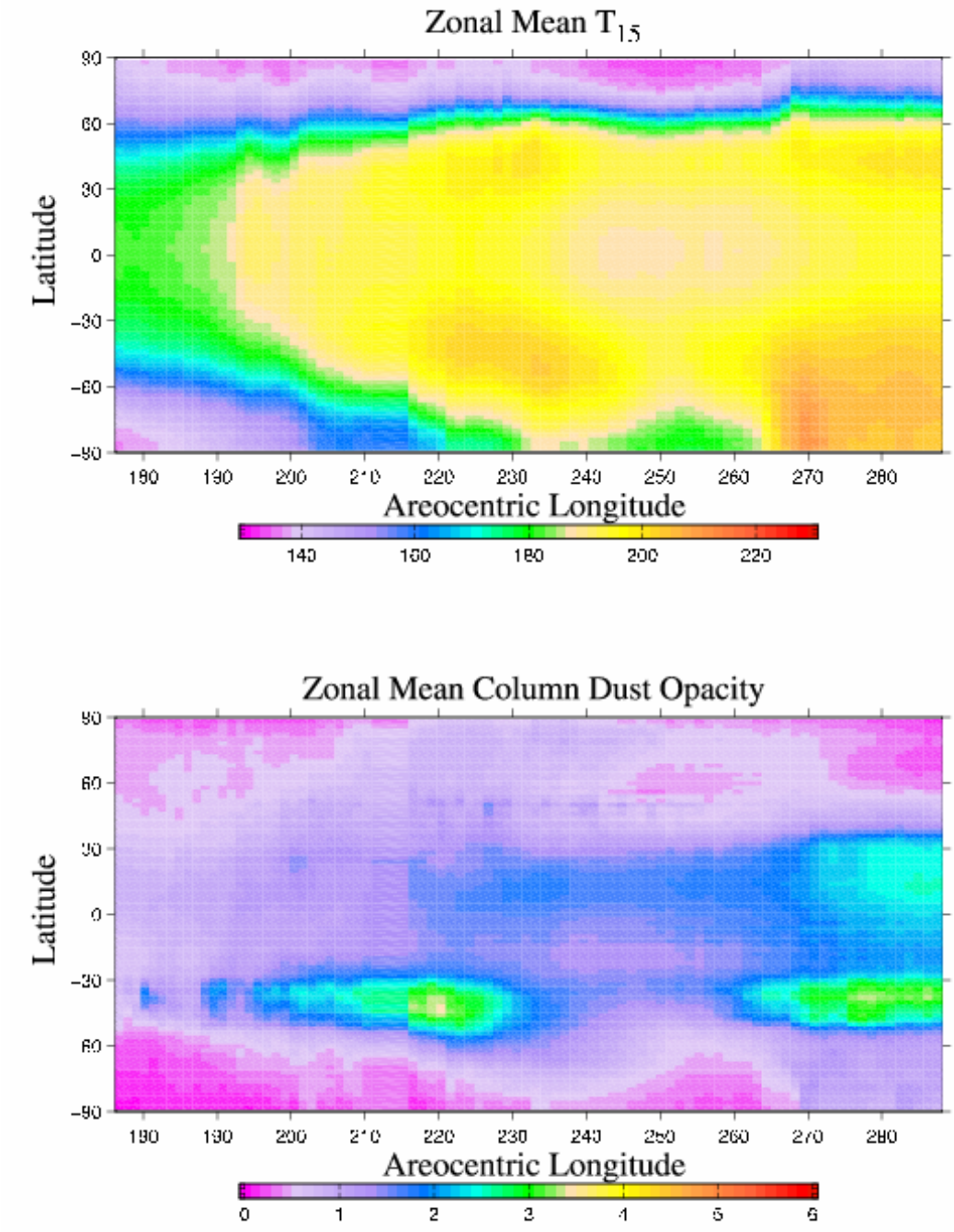


**Figure 4:** Zonal mean $T_{15}$ temperature (top) and zonal mean column dust opacity (bottom) as a function of latitude and areaocentric longitude. These results were obtained from a high-resolution simulation. Two storms are evident. The first storm starts as early as Ls=185° in the Hellas basin and is followed by a second storm that starts decaying by Ls=300°, much earlier than those observed in the low resolution runs

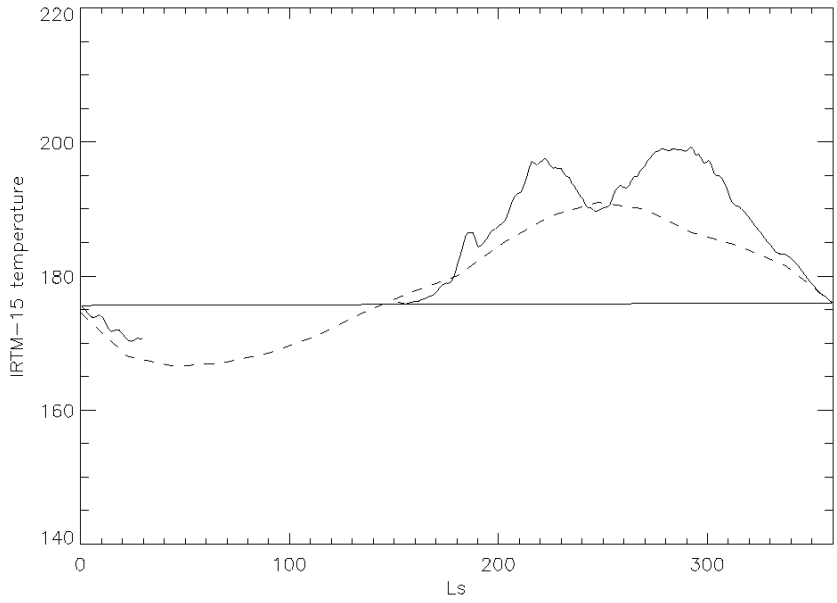


**Figure5-** Globally avearged T15 temperatures as a function of areocentric solar longitude for a high resolution simulation shown in Figure 4.

Some of our preliminary high resolution runs are promising. These have storms that start as early as Ls=180° (Figure 5) from the Hellas basin followed by a second storm after the first one decays. The simulated t15 temperatures for one of these storms [Figure4] however are lower than observed. Detailed runs with adjusted rates of lifting will be carried on in the future.

### 3.4.1.1 **Evolution**

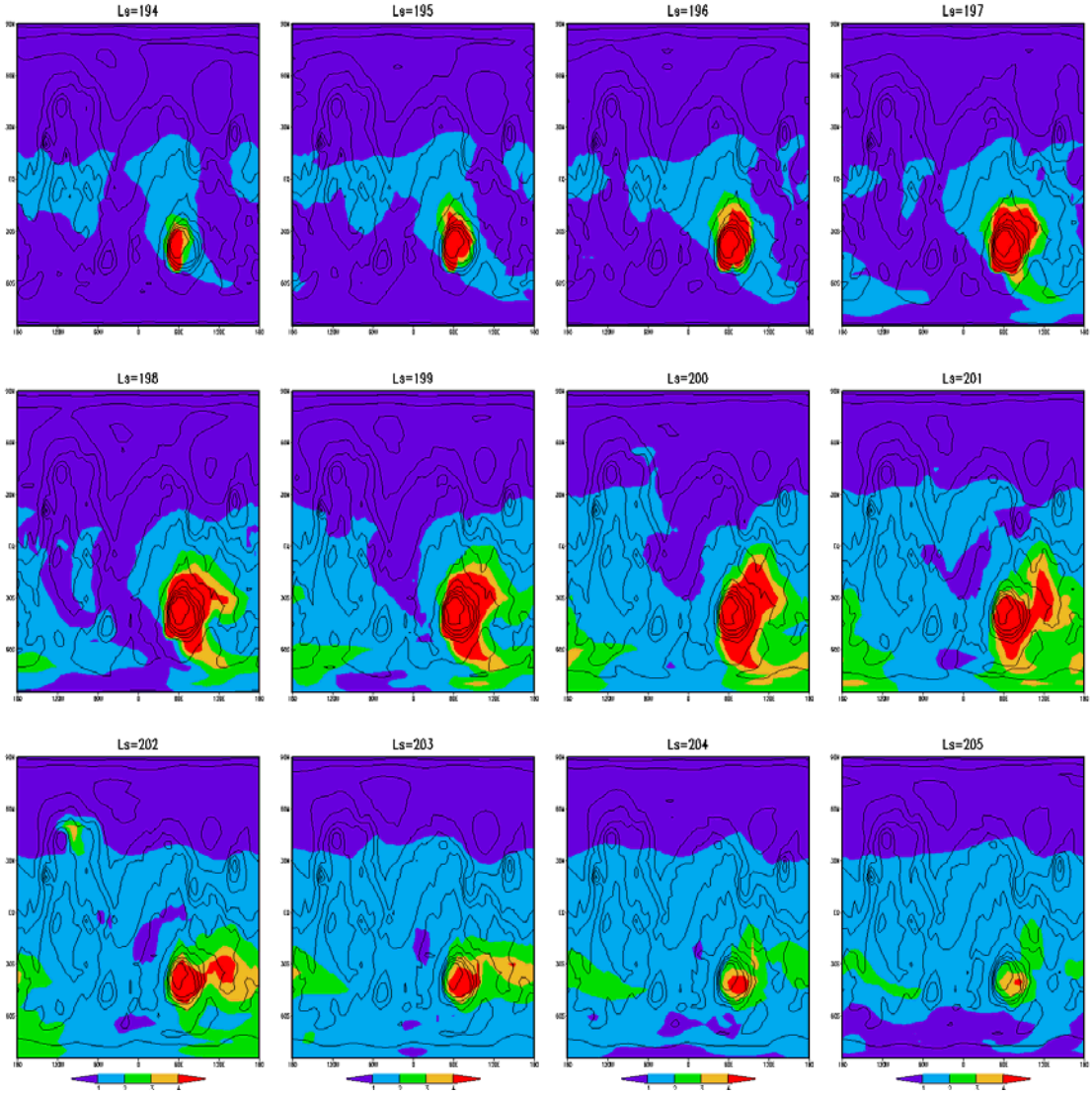


**Figure 6: Geographic distribution (latitude vs. longitude) of normalized opacity (to 6mbar) at six time intervals covering the storm evolution. Normalization serves to remove the effects of topography. The storm starts ~Ls=195°. This is similar to the 2001 dust storm on Mars in some ways. Strong westerlies prevail at this time. Dust continues to be lifted in the vicinity of the Hellas basin and is advected eastward. An independent storm in the Chryse basin can also be been at Ls=203°.**

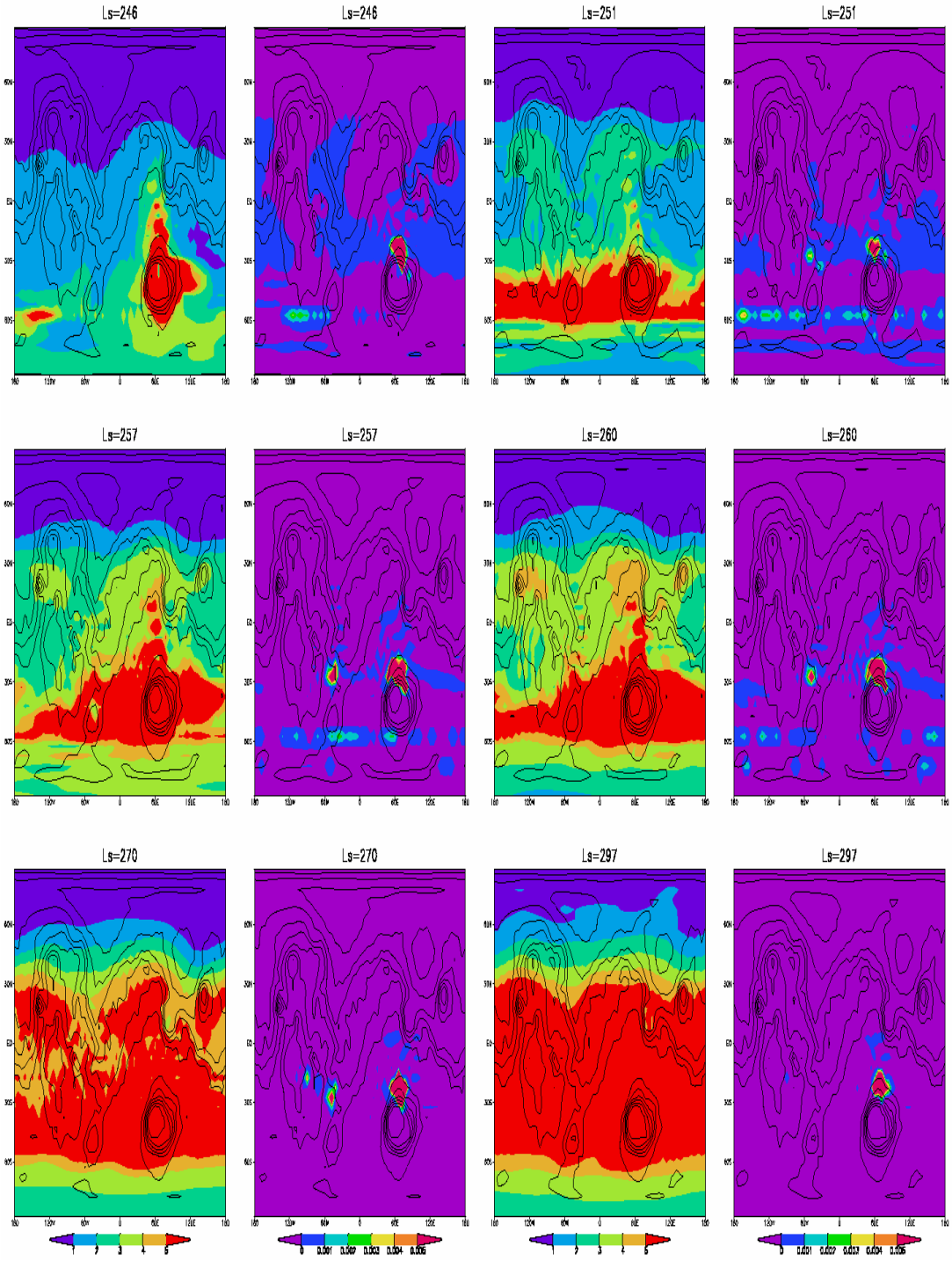
Ls=246
Ls=246
Ls=251
Ls=251
Ls=257
Ls=257
Ls=260
Ls=260
Ls=270
Ls=270
Ls=297
Ls=297

**Figure 7. Geographic distribution (latitude vs. longitude) of normalized opacity (to 6mbar) at six time intervals covering the storm evolution. Normalization is done to remove the effects of topography. The net lifting of dust per day for the six time intervals is also shown. The storm begins from the northwestern rim of the Hellas basin. It spreads into Syrtis Major in the north and towards Hesperia in the east. The secondary dust-lifting center can be seen along the southern cap edge south of Tharsis. The topography is contoured in black.**

We get some small local dust storms in the Hellas region in northern spring and summer. These storms may well be supressed somewhat by the effects of water ice cloud formation on dust nuclei. Currently we don't have any water physics switched on for our simulations but in the future we will test out these hypotheses. We are not representing the possible scavenging and radiative impact of water ice clouds. Water ice clouds are generally insignificant during the dust storm season [Smith et al 2001. Figure 6 shows the general evolution of one the early Hellas storms as described in section 3.4. The dust opacity has been normalised to remove the influence of topography. The storm starts from the southwestern rim of Hellas ~Ls=193°. It fills the whole basin and starts spreading eastwards from the southeastern rim of Hellas into Eridania and Sirenum. This is similar to the 2001 GDS which began even earlier ~Ls=185°. A storm event in the Alba Patera region can be see in the northern hemisphere at Ls=202°. This is most likely an independent event in the northern hemsiphere. In some instances such events in Alba Patera and the Chryse region give rise to cross equatorial storms that together with the Hellas storm fill most of the planet and raise the global average temperatures to ~200K. The storm decays ~Ls=205° when the westerlies become weaker.

The general evolution of one of the global dust storms beginning at roughly $L_s$=240° can be seen in Figure 7. This figure shows the geograhpic distribution of column opacity at six time intervals covering the storm evolution. The dust opacity has been normalized to remove the influence of topography. The net lifting/deposition of dust per day for each of the six time steps is also shown. The storm begins on the northwestern rim of the Hellas basin. By the first time-step, dust is beginning to "probe" to the north and to the east of Hellas. We use the word "probe" to convey dust transport which is not smooth, advective transport, but instead reflects the pulsating transport associated with the strong modulation of the winds by the

diurnal thermal tide, and dissipation of dust pockets advected from Hellas and cut-off by the tidal reversal of the winds. The northward transport moves dust into Syrtis Major, while the eastward transport moves dust into Hesperia. In Figure 7a and 7b, one can also make out a secondary dust lifting center along the seasonal cap edge to the south and west of Tharsis. The early evolution of the storm, including initiation in Hellas, transport to the north and east within distinct fingers, and the activation of lifting along the southern cap edge south of Tharsis all provide strong echos of the actual development of the 2001 GDS. We must be careful, as that storm began much earlier than our $L_s$=240° event, and the subsequent evolution of the modelled storm and the 2001 Mars GDS differ. However, the similarities provide some confidence in the fidelity of the model.

By the next frame ($L_s$=251°, Figure 7c), the dust has encircled the planet at high southern latitudes. The northern latitudes also experience increased opacities, but not to the same degree: the dust distribution is strongly biased to the south. The majority of the dust lifting remains concentrated on the northern rim of Hellas (Figure 7d). Additional lifting occurs along the southern seasonal $CO_2$ ice cap edge. A local peak in lifting can be seen to the south and east of Tharsis. Comparing Figures 7d and 7b, it can been seen that net lifting outside of these major lifting regions is diminishing and turning into net deposition in many areas. This represents some reduction in dust lifting by dust devils, but also a significant increase in dust fall-out associated with the higher atmospheric dust opacity.

The following ten degrees of $L_s$ (from $L_s$=250°-260°, Figures 7e-7h) see the model exporting much more dust to the northern hemisphere, with opacities exceeding 2 everywhere south of roughly 40°N by $L_s$=260°. In fact, while there is substantial change in the storm between Figures 7a, 7c, and 7e, there is much more muted change between 7e and 7g. Figure 7g corresponds to $L_s$=260°, or roughly 20° of $L_s$ after storm initiation. This is roughly the interval after which the 2001 GDS began to decay. However, the simulated storm does not decay (see Section 3.6), as dust lifting continues with gusto. Figures 7f and 7h show that the lifting on the northern rim of Hellas and southeast of Tharsis has increased relative to the state in Figure 7d. Only a very small fraction of the planet exhibits net injection of dust by this point, being overwhelmed by dust sedimention, as mentioned above. Observations of the

2001 global storm suggest that the lifting center on the northern rim of Hellas switched off after the secondary lifting center southeast of Tharsis initiated [Strausberg et al., 2005]. This is not simulated, and both centers remain active until roughly $L_s$=260°-270°. Indeed, even at $L_s$=297°, the Hellas northern rim lifting center remains very active (Figure 7l). This steady injection of dust allows the model to produce a very smooth distribution of opacity (ie a relatively uniformly mixed aerosol distribution) in the final two timesteps of Figure, corresponding to $L_s$=270° and 297°. As can be seen in Figure 1b, the storm decays only after roughly $L_s$=300°.

### 3.4.1.2 Dust and Air Temperature Distributions

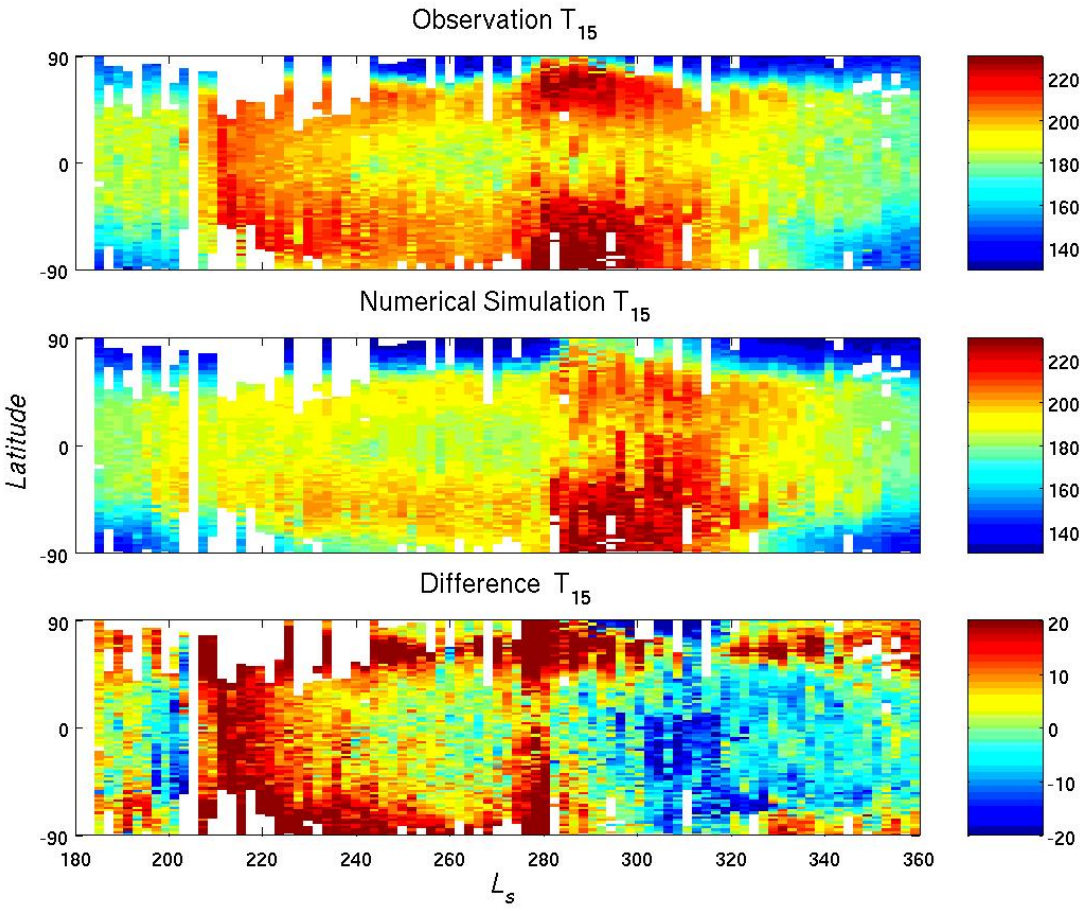


**Figure8:** Synthetic IRTM data alongside data derived from a GCM simulation that has a late storm ~Ls=280 alongside data from the 1977 dust storm season. The GCM output was sampled using the Viking observation pattern to maximise comparability. The southern

spring and summer season is shown for each, along with difference between the model and data.

The latitudinal distribution of mid-level air temperature provides additional information on the dynamical response of the atmosphere during a GDS that is not captured in the global-mean temperature plots. In Figure 8, we present synthetic IRTM T15 data [Wilson and Richardson, 2000; Liu et al., 2003] derived from the GCM simulation shown in Figure 1b alongside data from the 1977 dust storm season. The T15 values are synthesized from the model through application of the IRTM 15- micron channel weighting function [Wilson and Richardson, 2000]. As the IRTM data contains non-random changes in observation local time, associated with drift in the orbits of the Viking Orbiters, we have sampled the GCM using the same latitude, longitude, local time, and seasonal pattern of the IRTM observations. As such, local time offsets between the observations and data are eliminated.

As the storm decays, the data and the observations are characterized by a strong, double-peaked latitudinal distribution of temperature. The peaks are in the mid-latitudes of both hemispheres. The southern peak corresponds to direct heating, while the northern peak is a result of adiabatic warming associated with the descending branch of the Hadley cell. Both the model and the observations show a trend of poleward motion of the temperature peaks during this period.

The 1977b GDS began at roughly $L_s$=275, while the model GDS begins after $L_s$=280. As a result, there is a short period of very large temperature differences at most latitudes between these dates. After $L_s$=280, the differences at most latitudes fall to less than 5K. The exception is the region north of about 45N, where the model is cooler between 45N and 80N and warmer right over the pole. Since this temperature peak is associated with the down-welling branch of the Hadley cell, it suggests that the model meridional circulation is somewhat weaker than that of the observations. Despite this difference in strength, the model again emulates the data well in the formation of a strong double peak in the meridional temperature gradient, in the maximization of temperatures over the southern pole, and in the development of a strong northern polar warming. The mechanism of this polar warming, once a major mystery of Martian atmospheric dynamics, is described by Wilson [1997] and Forget et al. [1999]. In fact,

at very high northern latitudes, the model predicts higher temperatures than observed during 1977b. This may be due to poor resolution of the very compressed northern polar vortex within a region of the model strongly smoothed by the polar Fourier filter (this is a required component of a grid-point GCM, needed to deal with the convergence of grid points at the pole and the desire to retain numerical stability with reasonable model time steps [e.g., James, 1994]). This warm bias of the pole dissipates with the spin-down of the Hadley cell by roughly $L_s$=320 - thereafter the model generates an over cool polar vortex. Interestingly, the decay of the model storm in terms of rate and trend in latitudinal distribution agree rather well with observations of the 1977b storm. The southward drift of peak northern hemisphere temperatures between $L_s$=285 and 320 is particularly well caught. After $L_s$=320, the modeled and observed air temperatures again agree to within ~5K everywhere, except in the high polar latitudes. In short, while there are some significant differences, the model does extremely well at emulating the observed seasonal variation of meridionally resolved, mid-level air temperatures before, after, and during a major dust storm. This is particularly gratifying, as we put no particular effort into emulating the 1977b storm when this simulation was run (indeed, it can be seen from Figure 1b that one gets from the model only what the model "wishes" to generate).

Figure 9 shows the diurnal variation of observed and simulated T15 temperatures from Wilson and Richardson [2002]. There is a strong diurnal tide signature, particularly at the mid-latitudes while the semi-diurnal tide is particularly strong in the tropics. The present storm temperatures are rather similar to those for the 1977b global dust storm. The south polar temperatures are somewhat weaker; consequently, the Northern Hemisphere vortex temperatures are weaker as well. The simulation does show a rather substantial stationary wave, which may bias the comparison with observations. There certainly was wave activity in the Northern Hemisphere vortex in the 1977b storm, but its behavior defied classification. It is probably not very meaningful to try a strict comparison since nothing is known about the phasing of these waves. The semi-diurnal temperature variation appears to be in reasonable agreement with the Viking observation, suggesting that we roughly have the right amount of globally integrated dust heating in the simulation. Figure 10 shows the simulated diurnal (red) and semi-diurnal (blue) tide components or the migrating tides. The semi-diurnal tide is an excellent measure of

global heating. Its amplitudes at 22N and 48N are in very good agreement with those observed at the Viking Lander 1 and Viking Lander 2 sites at the peak of the 1977b global dust storm.

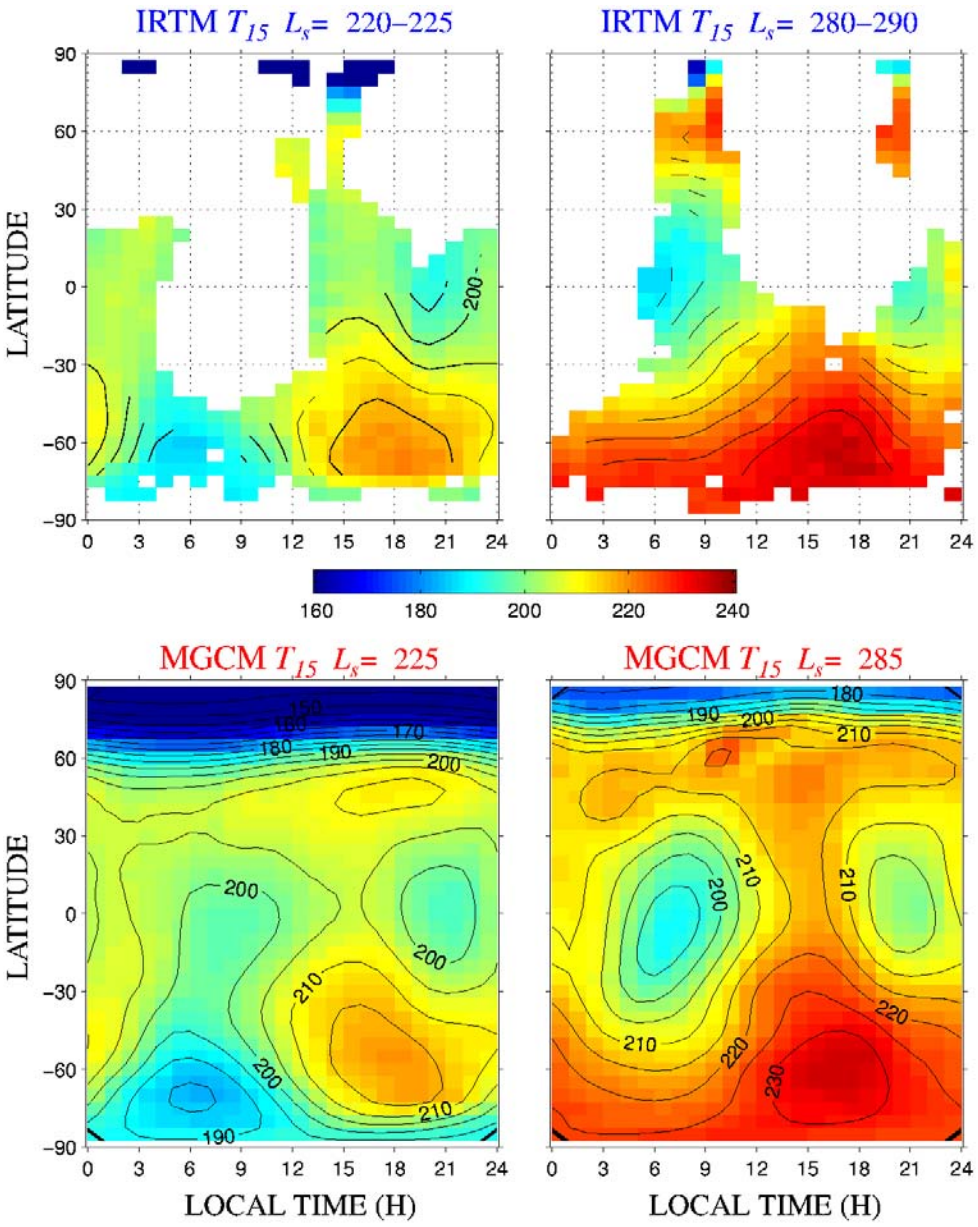


**Figure 9:** Comparison of the diurnal variation of T15 temperatures between the Viking storms and the MGCM simulations. There is a strong diurnal tide signature. The present storm temperatures are rather similar to the 1977b global dust storm.

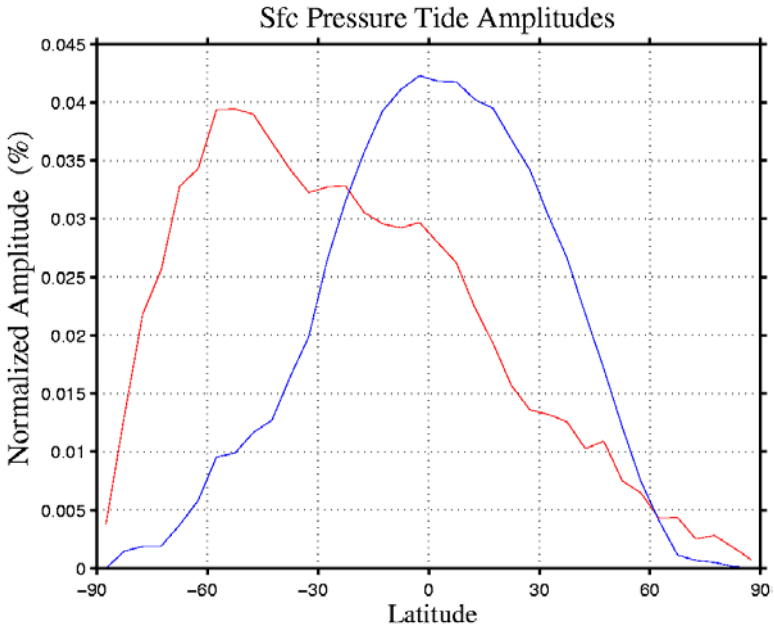


**Figure10:** Simulated diurnal (red) and semidiurnal (blue) tide components (the migrating tides) at Ls=280 for a year that has a global dust storm. The semidiurnal tide is an excellent measure of global heating. Its amplitudes at 22N and 48N are in good agreement with those observed at VL1 and VL2 at the peak of the 1977b global dust storm

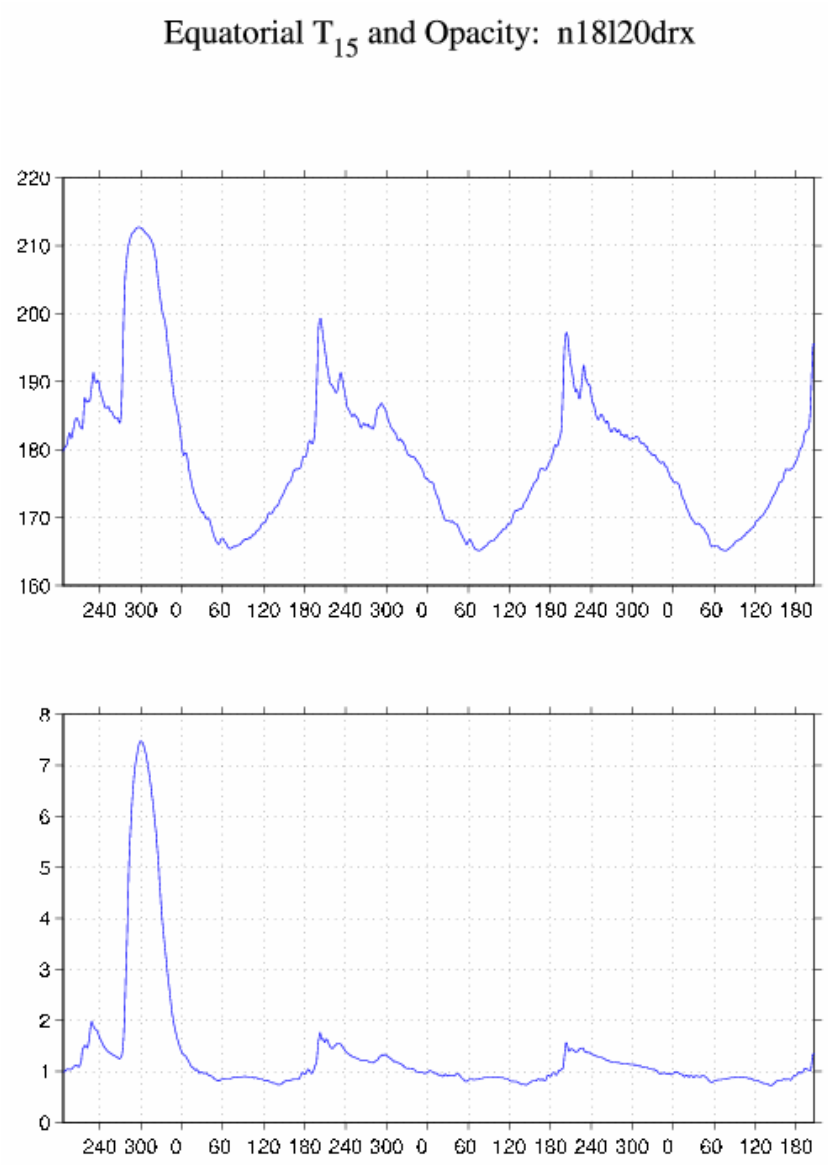


**Figure 11:** Evolution of the equatorial T-15 and dust opacity for a particular simulation that yield early season Hellas storms that go global in some years. The character of the temperature 'peaks' at Ls=240 is different in the 2nd and the 3rd years as well. The first year shows significant dust lifting in the northern hemisphere, which is largely absent in the 2nd and the 3rd years.

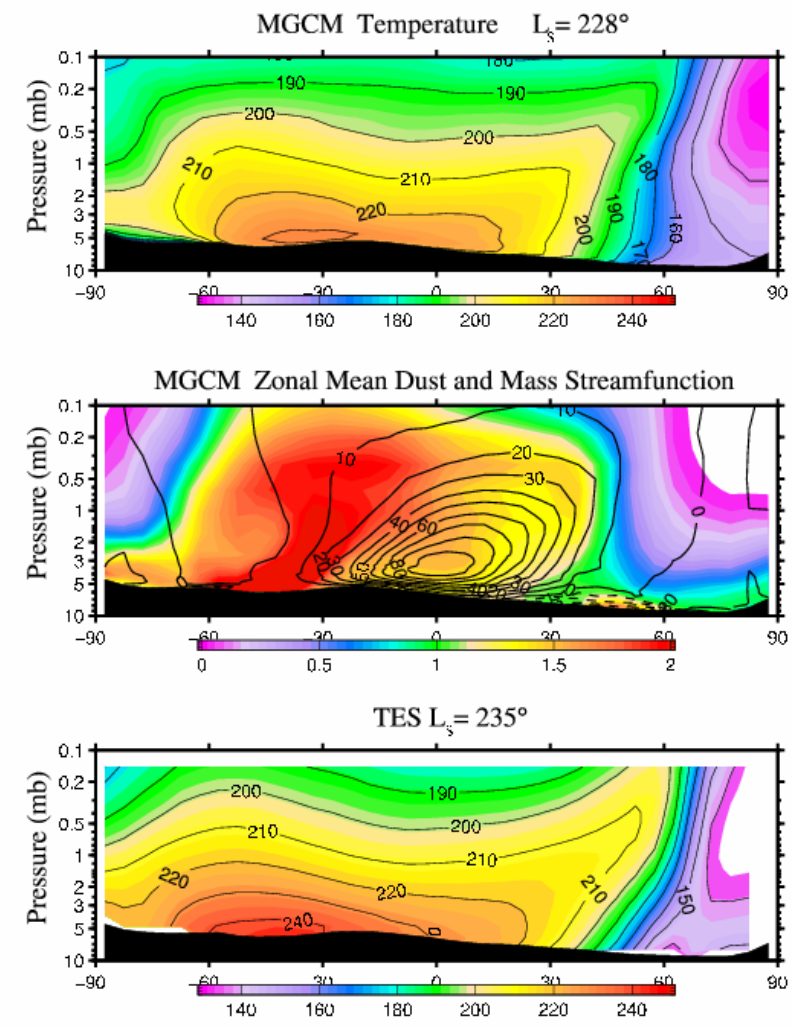


**Figure 12:** Comparison of TES and MGCM diurnally averaged temperatures at Ls=235 in first mapping year. The dustiness and temperatures maximized at this time following the Chryse dust activity. TES temperatures are warmer than the simulation. Note that TES is 0.5*(T2am+T2pm) compared to MGCM which is true zonal and diurnal average. The MGCM storm peaks at Ls=228 where as the observed storm peaks at Ls=235. The storms in both cases start in the Hellas region and spread eastwards. The TES Hellas storm was preceded by a series of flushing events out of the Chryse basin.

The latitudinal cross sections of temperature and dust in the simulations compared to data give us additional means of investigating the similarities and differences between the model and the actual atmosphere. In figure 12 we compare the temperature profiles as a function of height and latitude for our simulations and TES observations from the first mapping year. These are compared for ~Ls=230 when both reach peak temperatures during a Hellas storm. This is the

early Hellas storm in the simulation that we discussed in section 3.4.1. It shows up as a sharp peak in the second year of the simulation shown in Figure 11. The northern hemisphere warming is stronger in TES data indicative of a stronger Hadley Cell circulation. The MGCM is too warm at 50-60N near the surface. This might be due to insufficient dust at these latitudes in the simulation due to lack of traveling wave lifting. The MGCM southern polar temperatures at Ls=228 are colder especially in the higher levels of the atmosphere than the TES temperatures at Ls=235, when atmospheric temperatures and thermal tides maximize. Of course, high latitude temperatures in the southern hemisphere will increase with the evolving season.

The temperature and dust cross-sections of the late Hellas storm that starts ~Ls=270 are shown in Figure13. This storm appears in the first year in Figure11. It peaks around Ls=295. There is major northern hemisphere polar warming in this simulation. The distribution of dust, with advection over the South Pole at high altitude is similar to that shown in Wilson, 1997 for the 1977b storm observed by Viking. The temperatures here are warmer than in the 1977b storm. There are no storms observed by the Mars Global Surveyor to properly compare against. The 2001 storm occurred much earlier in the season and so, is qualitatively different.

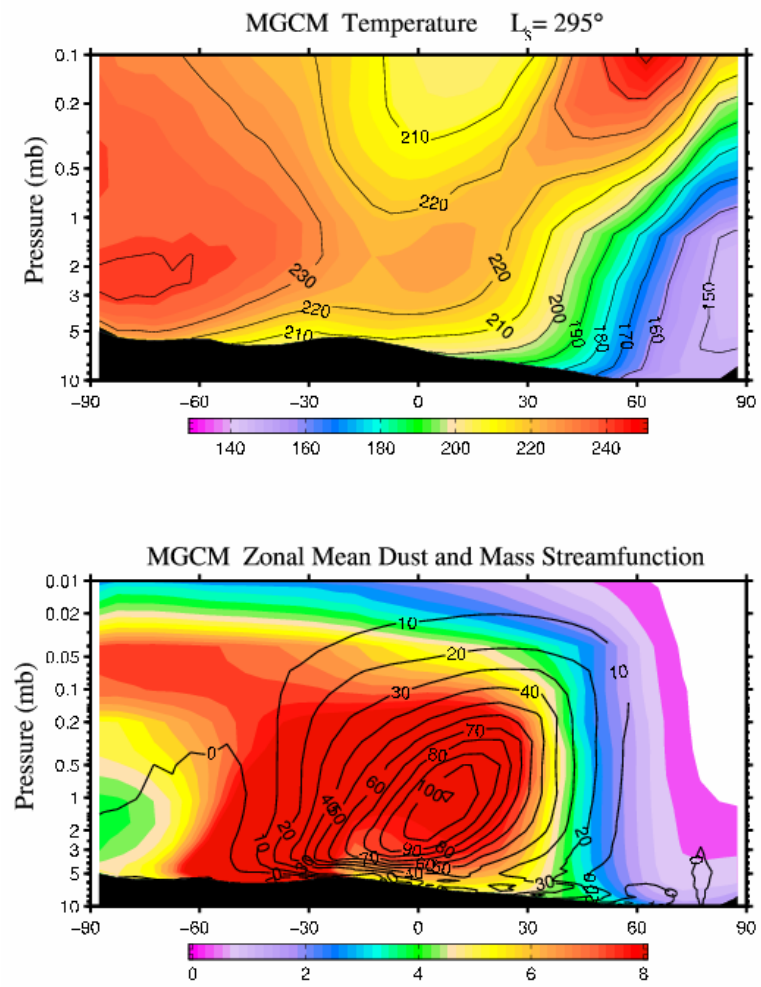


**Figure 13**: Temperature and dust cross-section of the Ls=270 storm at its peak around Ls=295. There is a major Northern Hemisphere polar warming in this simulation.

Figure 14, 15 and 16 show two consecutive years from a simulation that has early Hellas storms in both years. The first year the storm starts ~Ls=199 [Figure 14]. This gets entrained into the Hadley cell circulation ~Ls=203 and subsequently settles out ~Ls=219. The Hadley cell is not very strong at this time hence the storm is not very strong either. Note that the Hadley cell circulation intensifying rapidly as the season evolves away from equinox towards summer solstice. This plays a more important role than dust, for this storm. The figure also shows the mass transport - in this season is much more tropically confined than in the solstice seasons [Haberle et al., 1993; Wilson, 1997; Forget et al., 1999; Wilson et al., 2004], with the

strong upward branch centered near the sub- solar latitude, just south of the equator. The maximum stream-function value (~50x$10^8$ kg/s) is significantly weaker than seen in simulations of the SH summer solstice case, where values range from 100-150X $10^8$ kg/s. The simulated dust distribution in Figure 14 is clearly influenced by the axi-symmetric circulation, with maximum vertical extent in the rising branch of the Hadley circulation. The intense downward branch of the Hadley circulation significantly limits the pole-ward extent of dust in the northern hemisphere. This adiabatic descent accounts for the relatively warm temperatures in the NH. The model does indicate leakage of dust into higher northern latitudes at low levels, which is attributable to stationary and traveling waves, as this behavior is not seen in axi-symmetric model calculations. Similarly, dust is confined to relatively low altitudes in the SH polar region. The pattern of the dust distribution and atmospheric circulation is quite robust, and is not dependent on the details of the source specification or dust lifting rates.

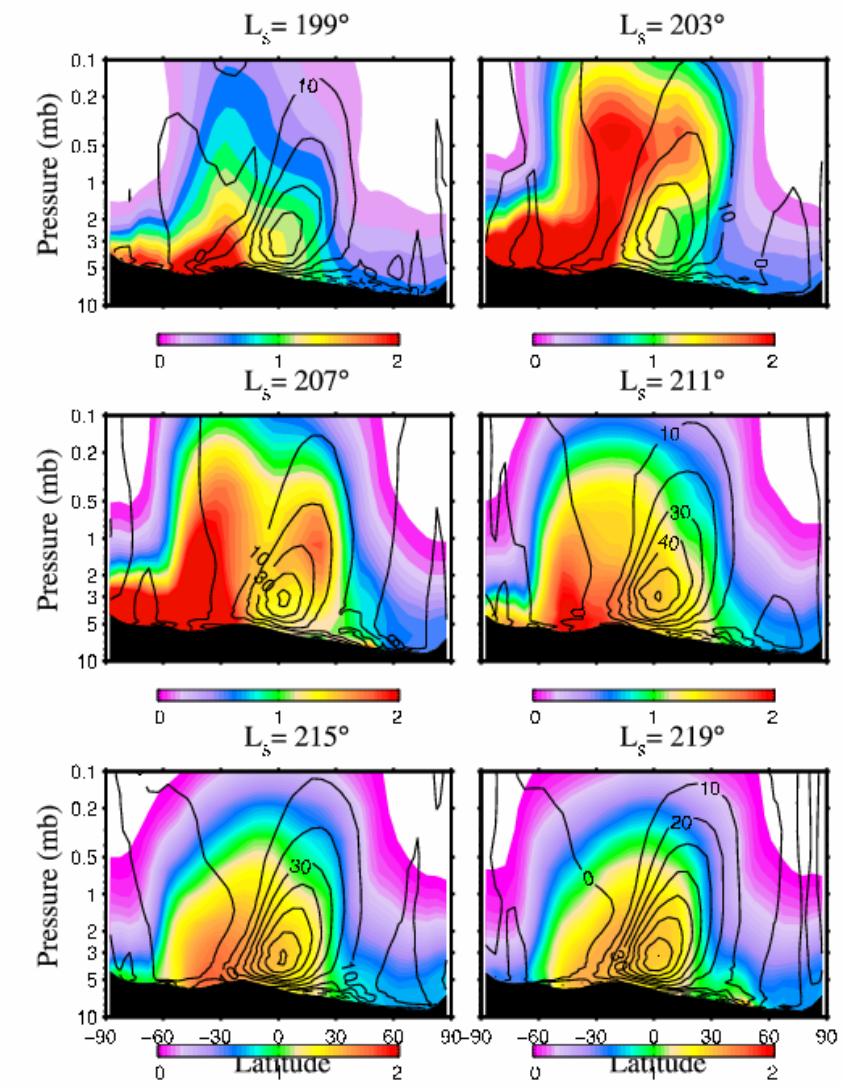


**Figure 14:** The evolution of zonally averaged dust (shaded) and stream-function (contoured) for the first major dust event in the first year of a simulation. The units are in local opacity, allowing the reader to vertically integrate by eye to obtain the column opacity. Obviously the strong source in the Hellas region makes the distribution less than uniformly mixed. The convention for the contour lines is clockwise signifies positive stream-functions.

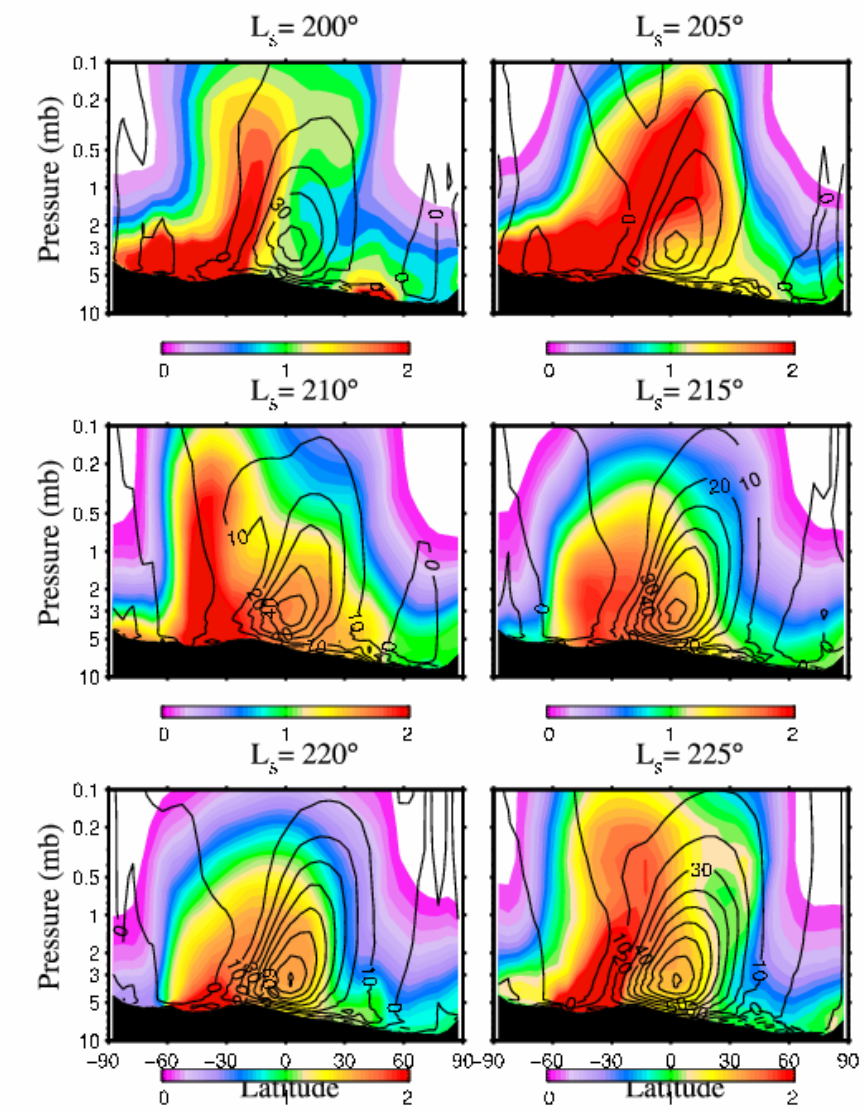


**Figure 15**: As for figure 14 but for the following year. In this year there were two temperature peaks: one at Ls=205 and one at Ls=228. Note that at Ls=200 there is Chryse storm activity in the northern hemisphere, which is much weaker than the Hellas storm.

The second year from the same simulation is shown in Figure 15. In this year there are two temperature peaks: one at Ls=205 [Figure15] and one at Ls=228 [Figure 16]. There is Chryse storm activity in the northern hemisphere ~Ls=200. There are other such storms at Ls=219,

222 and 228 [Figure16]. These storms are much weaker than the Hellas storm. There is insufficient lifting in the Northern hemisphere compared to observed storms. The baroclinically raised dust events do not intensify sufficiently as they travel southwards. Comparing the two years it can be seen that there is inter-annual variability in terms of the intensity and timing of the early Hellas storms. There is some variability in the Chryse storms as well.

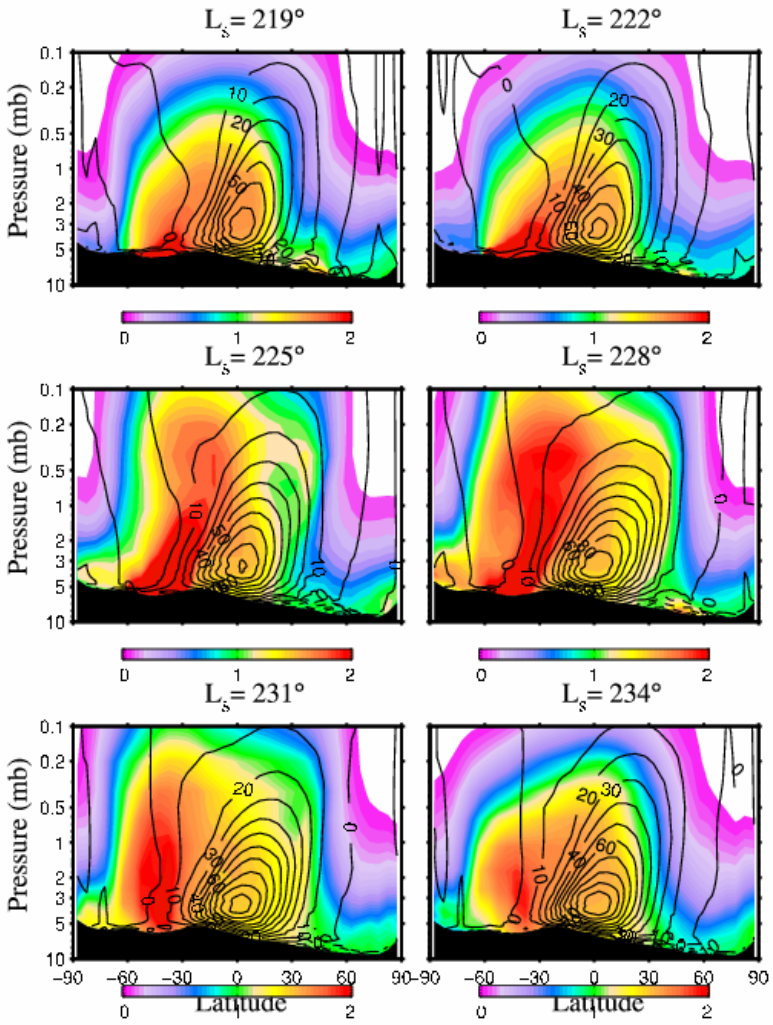


**Figure 16:** Second dust event in the same year as the previous simulation [Figure 15]. This is intended to mimic a 'Chryse' storm event although there is insufficient lifting in northern hemisphere to convincingly make this identification. The baroclinically raised dust events do not intensify sufficiently as they travel southwards.

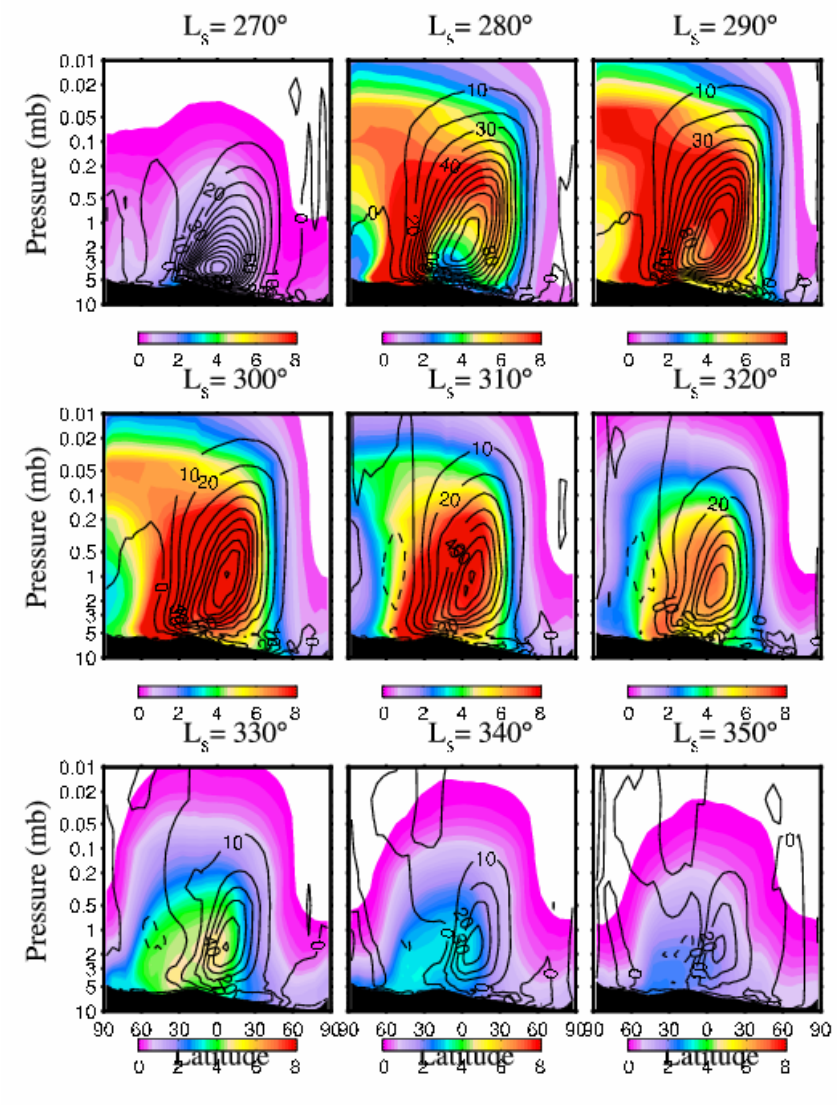


**Figure 17:** Dust Evolution for the Ls=270 storm. Note the intrusion of clear air in the low shallow, lower branch of the Hadley circulation.

The dust cross-sections for the late Hellas storm that starts ~Ls=270 is shown in Figure 17. It can be seen that the Hadley cell circulation is quite intense between Ls=270-300 after which it weakens and so does the dust storm. The maximum stream-function value (~100x$10^8$ kg/s) is significantly stronger than seen in simulations of the pre-solstice storms [Figure14], where values range from 40-50 x $10^8$ kg/s. The signature of a strong source of dust from the Hellas

region is present until Ls=320, when the dust distribution tends towards being well mixed. The lack of a more rapid storm shutdown is an unrealistic element in this simulated storm. In observed storms (e.g. 1977b) the storm starts decaying as soon as it reaches the peak opacities. In our storms however it can be seen even though the peak opacities are reached ~Ls=295, the source does not shut down till Ls=320 when the Hadley cell circulation also decays. The temperature and dust cross-sections for another late Hellas storm from a different simulation with a slightly lower threshold are shown in Figure 18 and Figure 19.

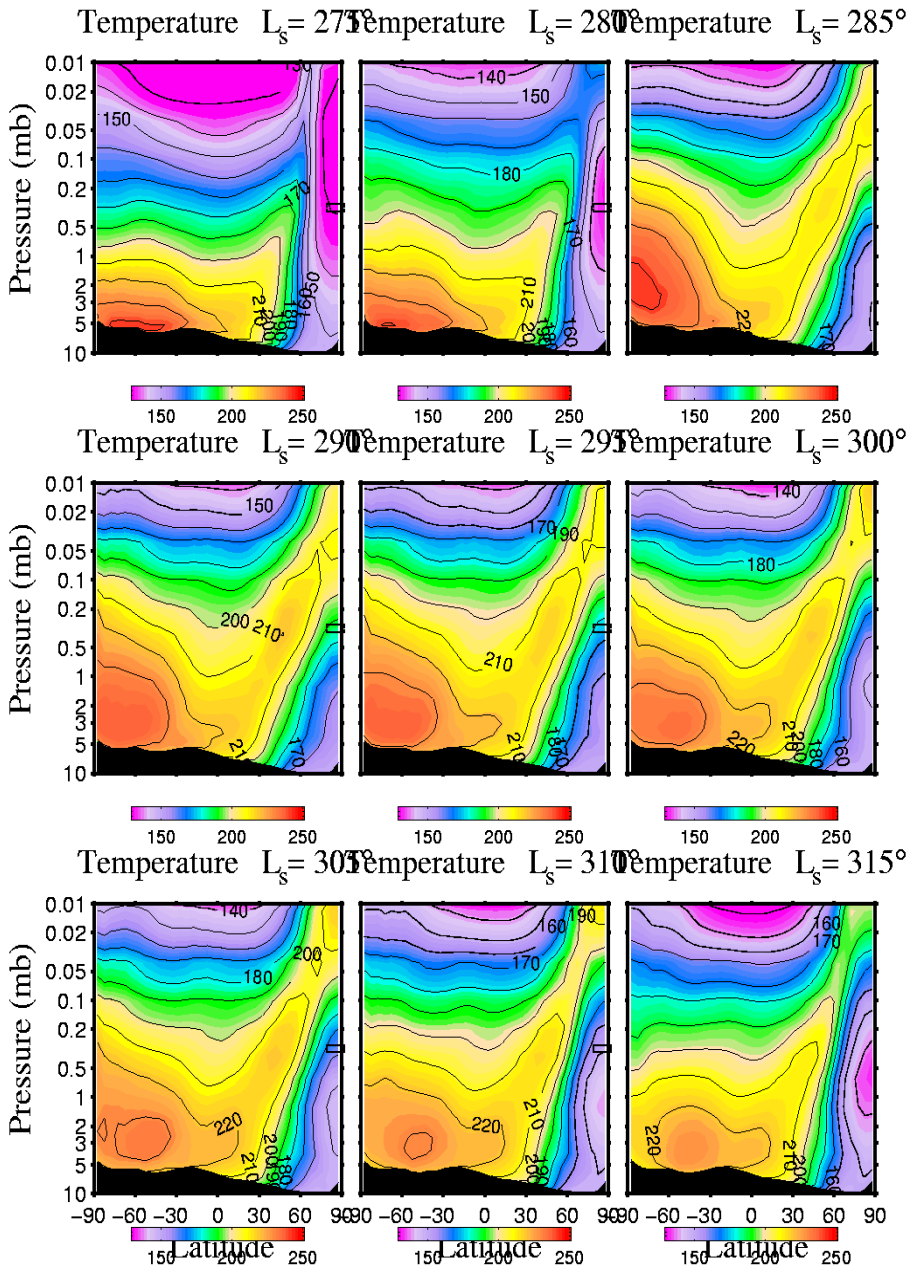


**Figure 18.** Vertical profile of zonally averaged temperatures as a function of latitude for dust storm evolution. The dust storm starts out in Hellas basin where the dust is lifted into lower levels of the atmosphere. It spreads into the northern hemisphere predominantly through higher levels in the atmosphere ~ 25 km. The explosive development of the global dust storm occurs when dust lifting in Hellas is sufficient to intensify the Hadley Cell Circulation and wind stresses in a portion of the southern tropical convergence zone exceed $\tau_{SL.}$ This activates the secondary lifting centers and the dust storm becomes global.

.

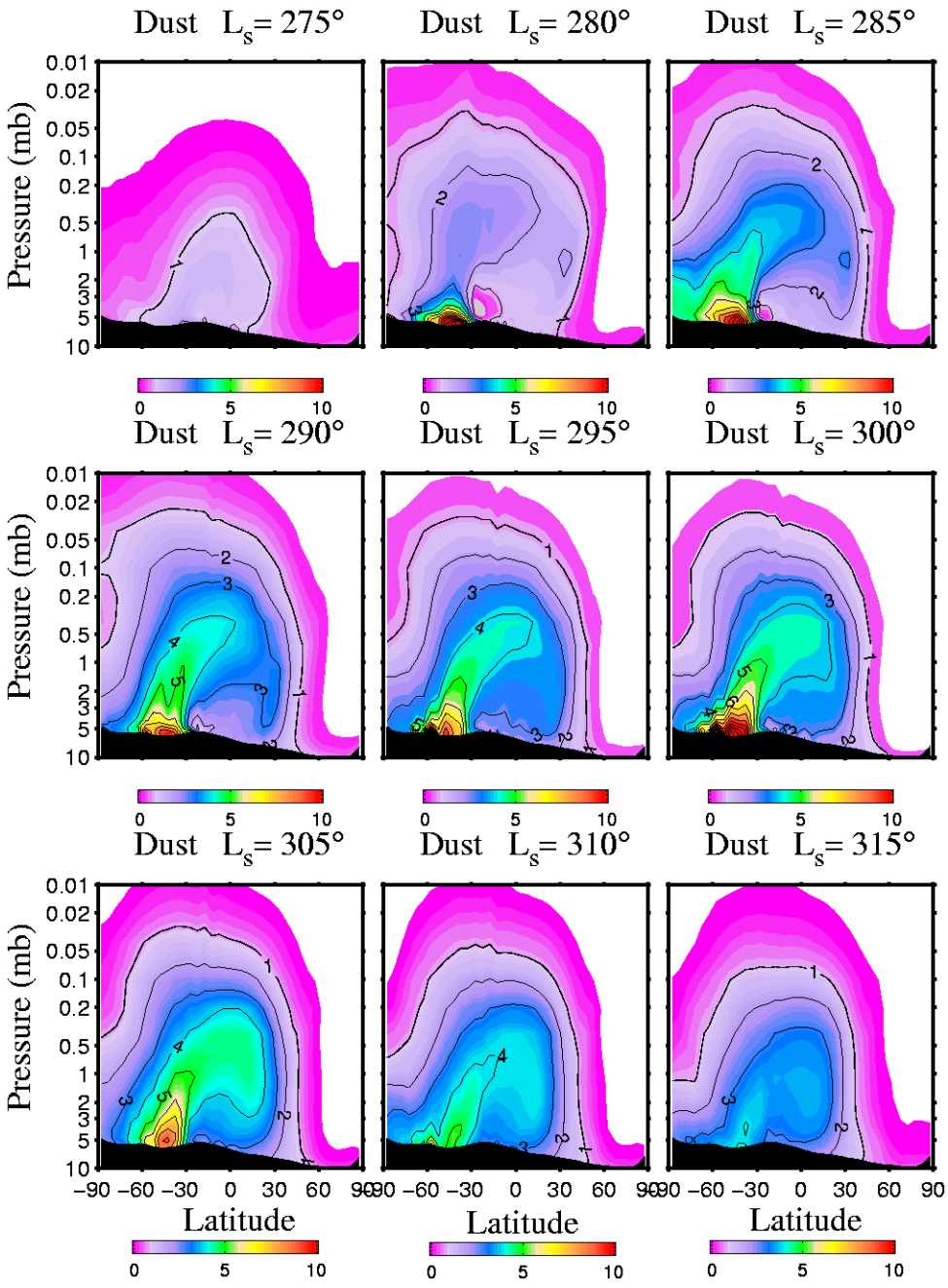


**Figure 19:** Corresponding zonal mean dust (from Figure 18). The units are in local opacity, allowing the reader to vertically integrate by eye to obtain the column opacity. Obviously the strong source in the Hellas region makes the distribution less than uniformly mixed. Roughly the dust column gets up to around 5 in some average sense.

### 3.4.2.1 A regional Dust Storm initiated by a Northern Hemisphere Baroclinic Storm

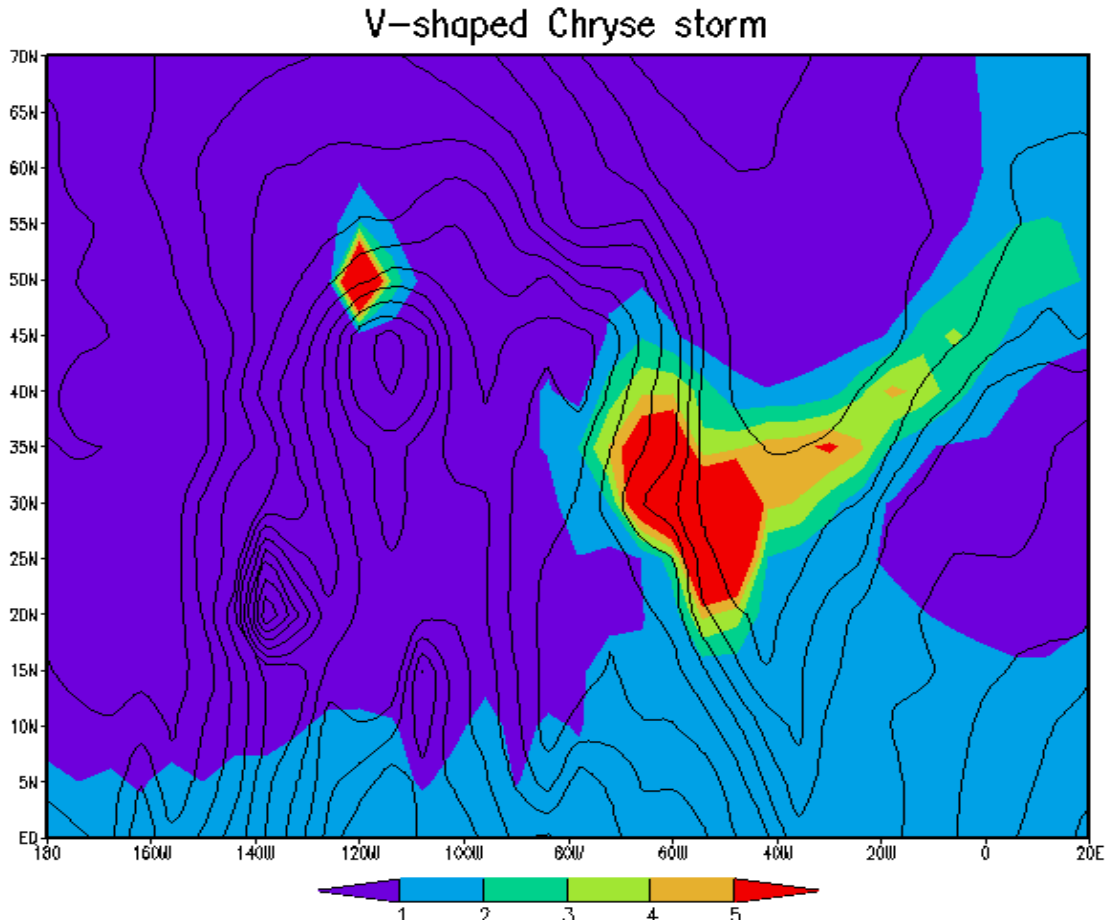


**Figure 20:** Spatial plot of normalized dust opacity showing the development of a V-shaped Chryse storm as observed (Wang et al 2003, 2005). The white contours show the topography. The geographic region shown here is the Acidalia Chryse region.

While most global storms generated by the model initiate in or near the Hellas basin, rare events trigger in and evolve in different ways. Figure 20 shows the output from a simulation in which dust-lifting initiates in the northern (autumnal) hemisphere is shown in Figure 20. The evolution of dust opacity for one such storm is seen in this figure. The V-shape that the storm assumes has also been observed by TES (Wang et al. 2003). This particular storm starts ~Ls=220 and becomes a cross equatorial flushing storm eventually. The intensity and spatial extent of the Chryse storms is possibly affected by the latitudinal extent of the seasonal ice caps in the northern hemisphere. Experiments that were run with lower obliquities produced

much bigger Chryse storms that went global in some cases. The extent of the seasonal ice caps in the northern hemisphere is less than a higher obliquity case and this is likely to affect the intensity of the traveling waves and hence the intensity of the Chryse storms.

The evolution of dust opacity and dust lifting centers from such an intensified storm is illustrated in Figure 21, paralleling the presentation for a Hellas dust storm in Figure 7. The storm begins in mid-northern autumn (somewhat before $L_s$=220, Figure 21a), at the northeastern edge of Tharsis. Within this region, Mars Orbiter Camera images show the development of frontal dust bands associated with low-pressure frontal storms (cyclones) [Cantor *et al.*, 2001, 2002; Wang *et al.*, 2003]. In the first frame of Figure 21, dust is lifted to the north of Alba Patera. The dust from this source is spread to the east in a band that extends into Acidalia. By the next time step [Figure 21c], the region of very high opacity extends along the eastern side of Tharsis, along the channel of observed frontal storm flushing in 1999 and 2003. This channel is associated with the concentration and enhancement of the Hadley cell southward return flow along the flank of Tharsis – the western boundary current of the Acidalia-Chryse lowlands [Joshi et al., 1995; Wang et al., 2003]. By this stage, over 15° of Ls after initiation, dust has spread to fill most of the northern hemisphere with opacities near 2. Dust lifting has extended along the edge of the Tharsis plateau from northwest of Alba Patera, along to the east and then to the south, and into Chryse. In later frames, the region of very high opacity is seen to extend across the equator and into the southern hemisphere [Figure 21c, 21e, 21g]. Thereafter, the dust spreads to the east, and to the north of Hellas, in the strong westerlies of the Hadley convergence zone. Throughout the storm, dust lifting remains concentrated in the northern mid-latitudes to the north of Tharsis. Dust lifting does not develop in secondary centers in the southern hemisphere. However independent storms in the Hellas region in a couple of simulations rage at the same as the Chryse storm, both acting as primary lifting centers in their respective

hemispheres.

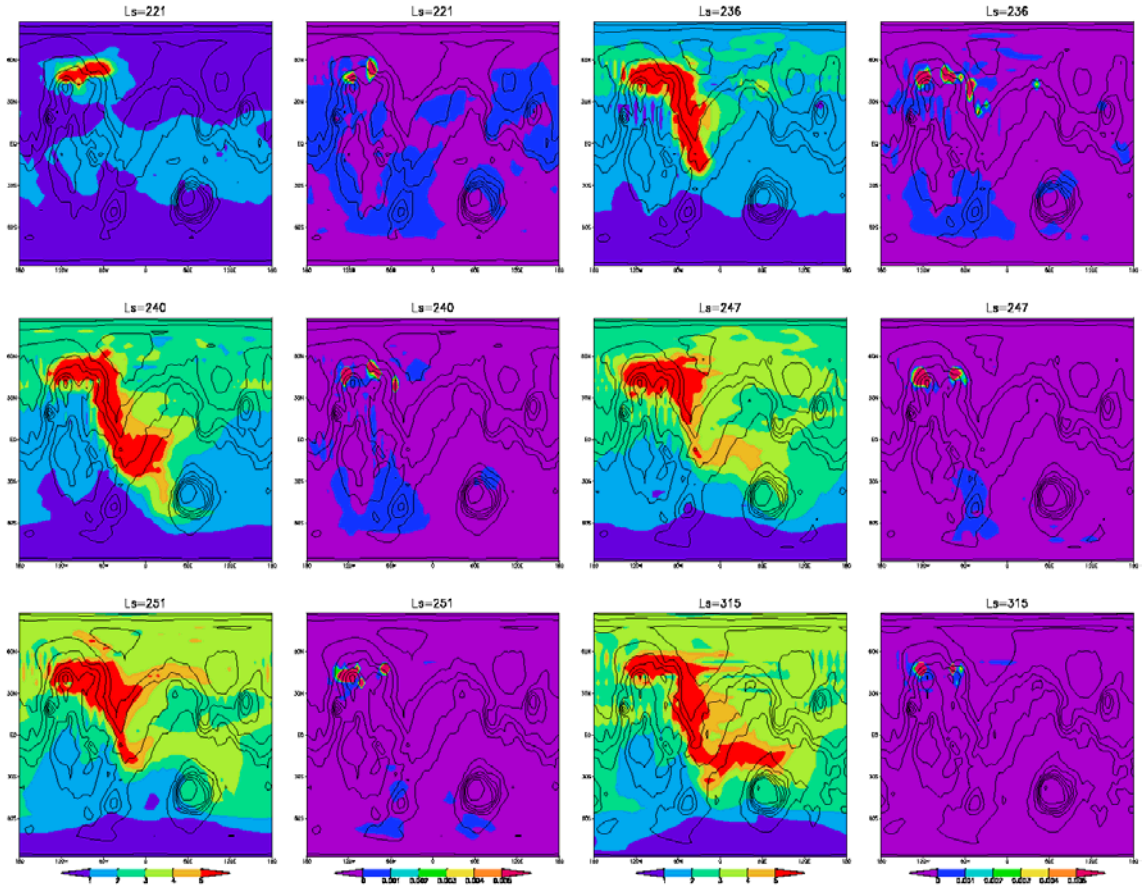


**Figure 21.** Geographic distribution (latitude vs. longitude) of normalized opacity (to 6mbar) at six time intervals covering the evolution of a cross equatorial flushing storm. The storm begins ~Ls=220 at the northeastern edge of Tharsis. In the first frame dust is lifted to the north of Alba Patera and then it spreads to the east in a band that extends into Acidalia. The concentration and enhancement of the Hadley cell southward return flow spreads the dust to the eastern side of Tharsis. The storm extends into Chryse and across the equator. It then spreads to the east and north of Hellas. The dust lifting sites are concentrated in the northern mid-latitudes to the north of Tharsis. The topography is contoured in black.

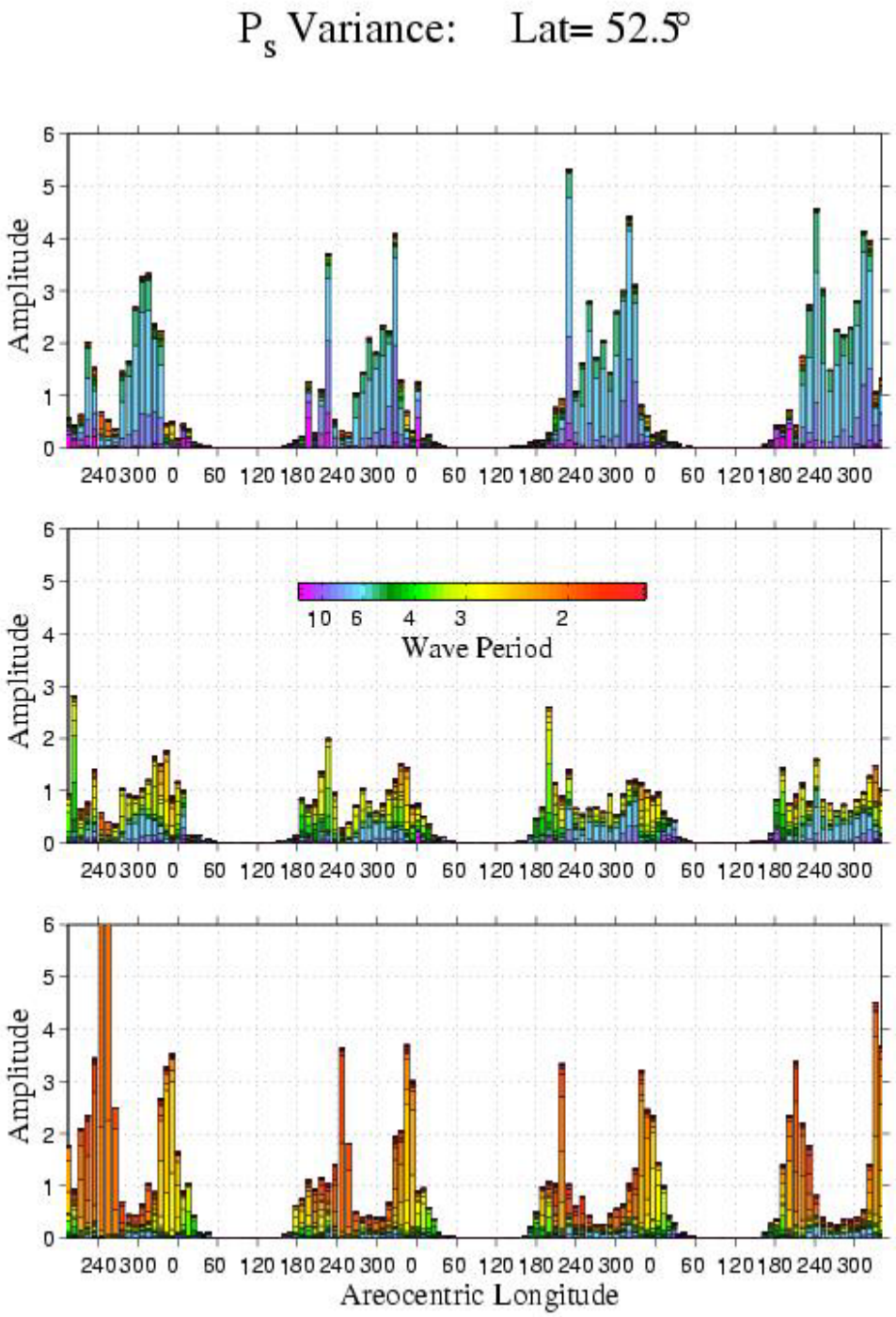


**Figure 22:** The seasonal variation of eastward propagating zonal waves 1, 2 and 3 (top, middle, and bottom) derived from simulated surface pressure. At each Ls, the contributions to the total variance are represented in color. For example, periods around 6 sols dominate the zonal wave 1,variance (cyan), while wave 3 is dominated by periods of ~2 sols (red) as has been observed. Wave 3 is particularly active in the first year of the simulation. There is a clear pattern of pre- and post-solstice activity and compares well with the observations.

The seasonal variation of the eastward propagating zonal waves 1,2 and 3 (top, middle and bottom) for the current obliquity case can be seen in Figure 22. The variable in this case is the surface pressure. At each Ls, the contributions to the total variance are represented in color. Periods around 6 sols dominate the zonal wave 1 variance (cyan), while zonal wave 3 variance is dominated by periods of ~ 2 sols (red). A clear pattern of pre and post solstice activity is obvious for all the 3 zonal waves. Wave 3 is particularly active in the first year of the simulation. The peak period of wave activity is at Ls=190-240 and Ls=310-350. There is very little activity at solstice. Flushing storms are most closely associated with zonal wave 3 since they have comparable seasonal variability. This has also been observed to be true by the analysis of MOC imagery and TES temperature retrievals [Wang et al 2003]. It has also been observed that the zonal wave 3 is associated with a period of ~ 2 sols- a result that we obtain in our simulations as well. The TES temperatures indicate that the temperature variance is strongest near the surface—i.e. these traveling waves are shallow, consistent with GCM simulations.

Even though the post-solstice wave activity in the simulations is not particularly weaker than the pre-solstice waves, yet the flushing storms are much less frequent than observed storms in the post-solstice period.

The flushing storm events in the MOC imagery analysis are active in all 3 channels: Acidalia (into Chryse); Arcadia and Utopia [Wang et al 2003]. Acidalia is most active. In the simulations, Acidalia is active but the other two channels in Arcadia and Utopia are not active. Figure 23, 24 and 25 show the spatial maps of the eddy fields for temperature (at 2km), surface pressure and velocity (at 2km) at different times in the southern spring and summer season. The pre-and post-solstice activity is clear from these figures.

On the basis of eddy V winds only [Figure 25], one can see that that storm initiation (and southward propagation) should be favored in all 3 lowland channels (Acidalia, Arcadia and Utopia). The Acidalia/Chryse channel does seem to be the region of most of the flushing storms in our simulations. In the model, the dust lifting is influenced by both tides and traveling waves. For these cross equatorial storms, greater dependence on frontal lifting than

tides would give greater inter-annual variability as this would capture the transient wave variations. Since the low-resolution model lacks the ability to simulate smaller-scale circulations associated with topography, this effect can be achieved artificially by removing the influence of the Alba Patera that strengthens the tidal waves in the region. Minimizing the influence of tides in the Alba Patera region- the volcano NE of Olympus Mons at latitude~40N, would minimize the strong diurnal variations in winds that trigger much of the Northern hemisphere storm activity overwhelming the effect of traveling waves. By removing the Alba Patera region and smoothing out the Martian topography in this region, the localized tidal circulation was weakened and the traveling waves assumed a more prominent role in the dust lifting events and this triggered cross equatorial storms in channels other than Chryse e.g. Arcadia [Figure 26]. The modifications in the topography required adjustments in the stress threshold. The lack of storms in all the three lowland channels can also be attributed to the fact that local circulation components like topographical waves etc. are not simulated accurately due to uniform stress threshold conditions and a relatively low resolution. Thus the interaction of the traveling waves and tides with the other components of the circulation is not captured accurately. The high-resolution simulations that we plan to run in the future will deal with these issues.

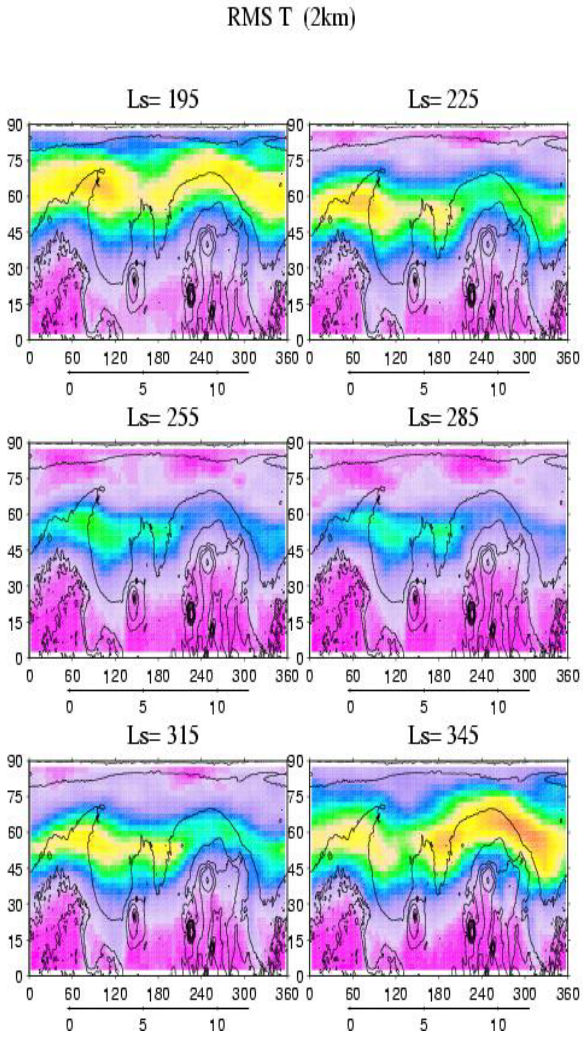


**Figure 23**: Spatial map of the rms temperature at 2 km for different times of the year. The pre- and post solstice activity is clear from the plots. This is comparable to what has been observed. This can be compared to Wang et al. [2005] and Banfield et al. (2004; Figure. 20)

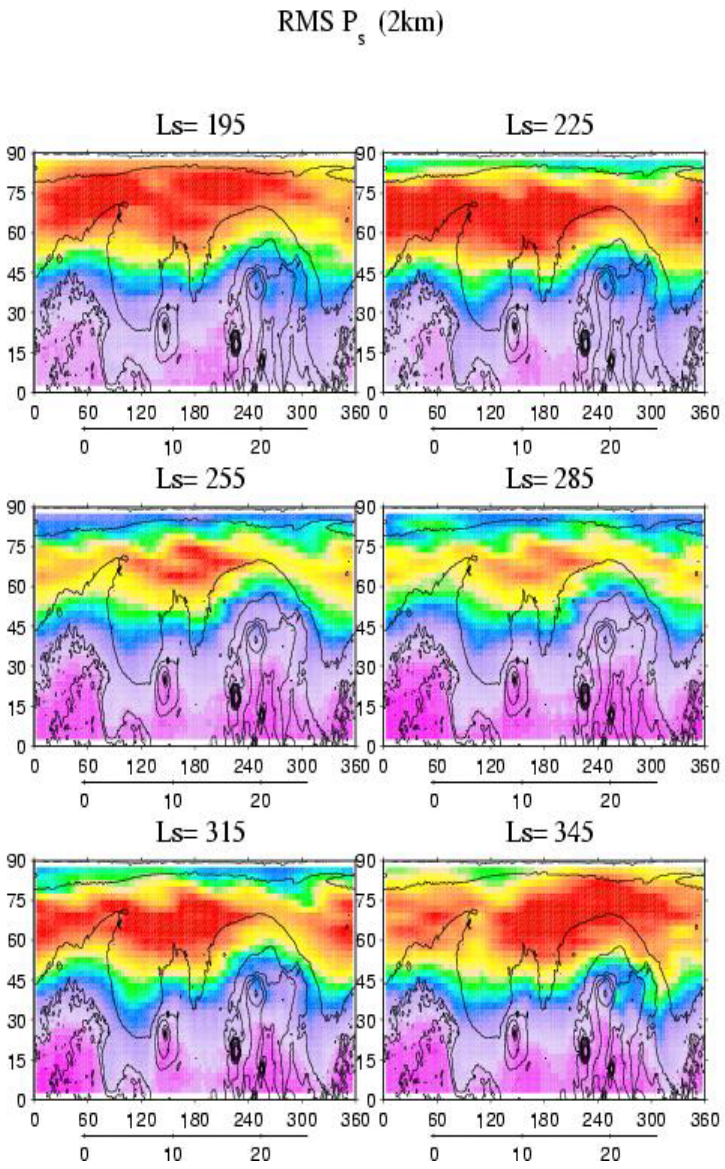


**Figure 24:** Spatial map of the rms surface pressure anomaly at different times of the year. It has been normalized by the diurnal average surface pressure. The pre and post solstice activity is clear from the plots. There is not a great deal of modulation in the eddy pressure plots as compared to V or the temperature field.

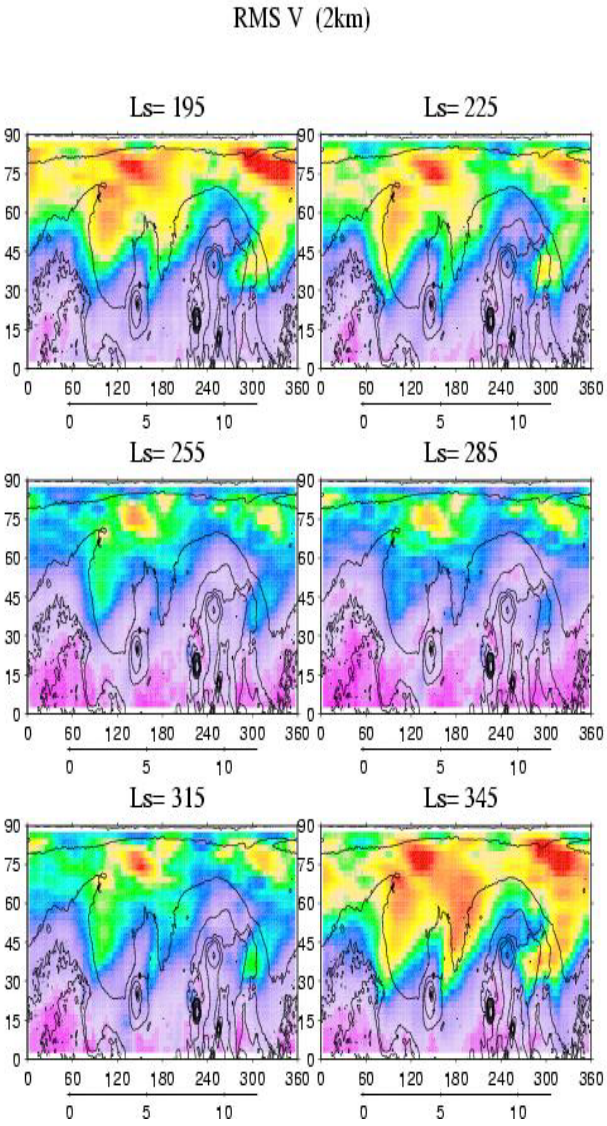


**Figure 25:** As in Fig. 23 but for eddy V winds at 2 km above ground. On the basis of eddy V winds only, one can see that that storm initiation (and southward propagation) should be favored in all 3 lowland channels. The Acidalia/Chryse channel does seem to be the region of most of the flushing storms in our simulations. The model dust lifting is influenced by both tides and traveling waves. It would be worthwhile to minimize the influence of tides in the Alba Patera region---- the volcano NE of Olympus Mons at about 40 N. This produces very strong diurnal variations in winds and triggers much of the NH storm activity overwhelming the effect of traveling waves. Smoothing the topography out in this region weaken the localized tidal circulation and give the traveling waves a more prominent role in dust lifting events. This removing Alba Patera from the topography triggers other channels- Arcadia especially for the cross-equatorial storms.

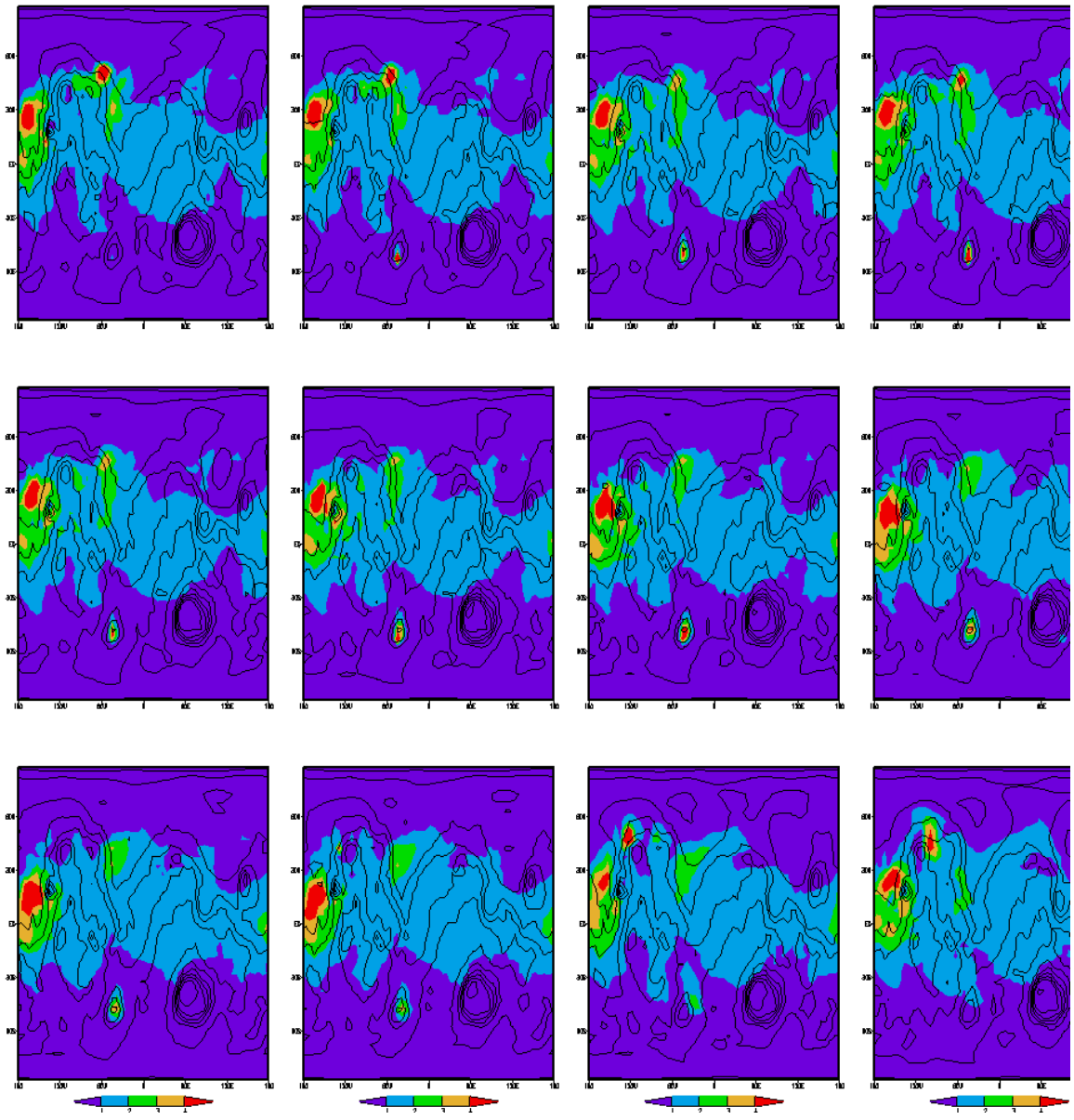

**Figure 26:** Spatial maps of normalized dust opacities during a cross equatorial storms in both the Arcadia and the Chryse channels. Alba Patera has been removed from the topography in this case. These storms become global and the simulation crashes eventually due to bad temperatures

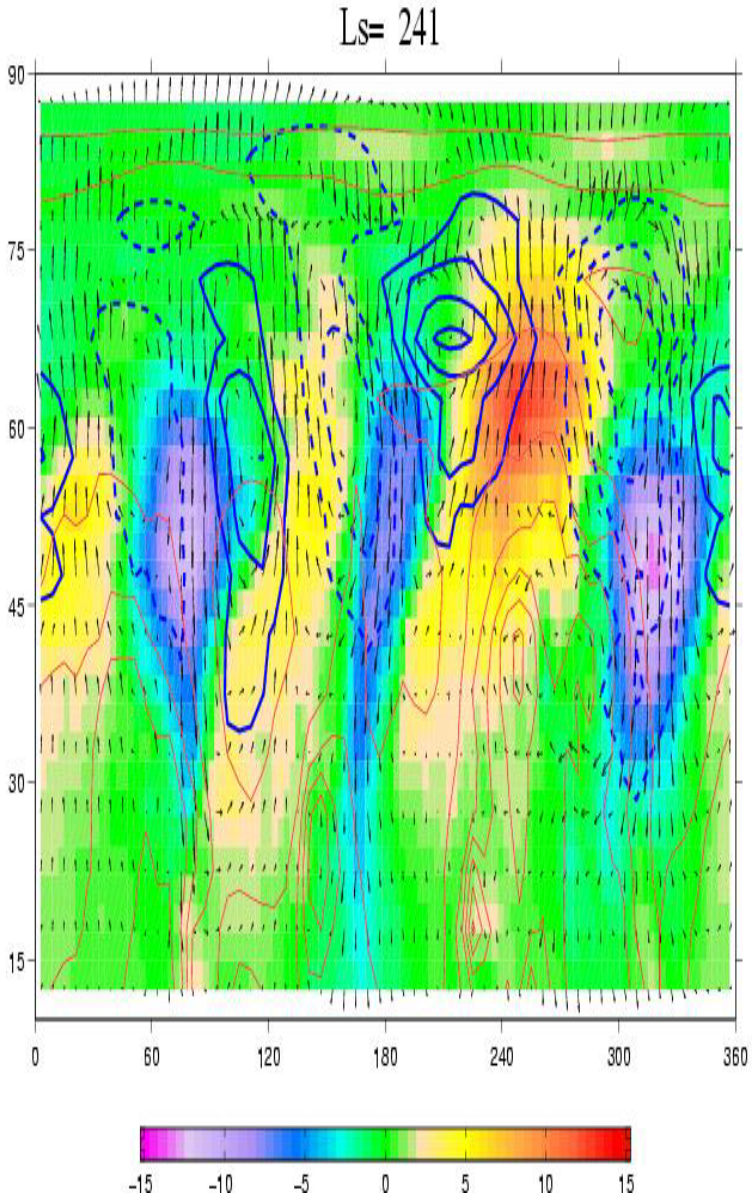


**Figure 27**: Spatial variation of eddy fields are plotted. The quasi-stationary and tidal waves have been filtered. The shaded field is the eddy temperature field. The eddy pressure fields are plotted in dotted (high) and solid(low) contours. The eddy velocity field is shown by the arrows. The velocity fronts can also be seen. At this time, there is a dominant wave 3, 2-sol period traveling wave. There is strong southward motion in the cold regions and northward motion in the warm sectors The CO2 ice cap has an influence so that the negative temperature anomalies are clamped around 60N latitude because the minimum temperatures cannot fall below the condensation temperature. Greater dependence in frontal lifting rather than tidal lifting also gives greater inter-annual variability.

The eddy fields at Ls=241 for Mars are shown in Figure 27. The zonal wave 3 is clearly visible in the eddy temperature, pressure and velocity fields. The fronts are formed at the intersection of the northward and southward traveling eddies. These kinds of figures can be readily compared with the TES data and highlight the storm tracks.

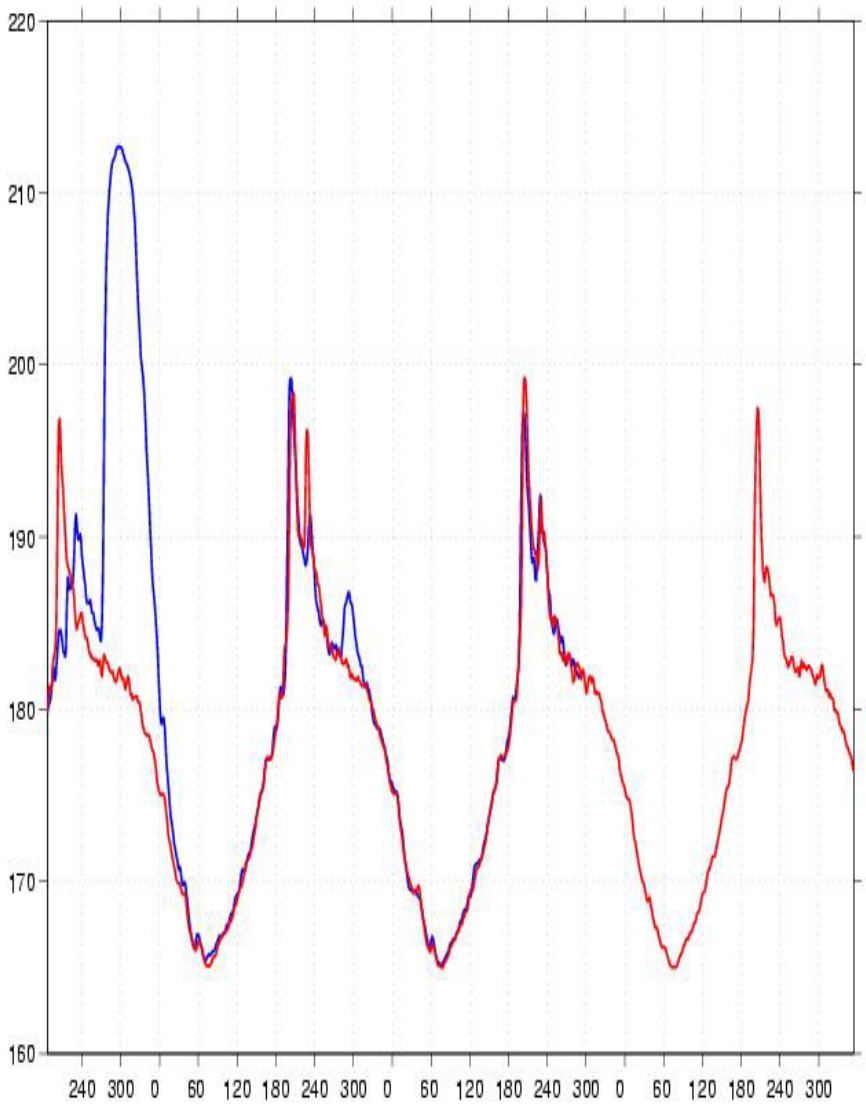


**Figure 28:** Transient wave activity in Northern hemisphere (blue) and southern hemisphere (red). As can be seen from the figure the transient waves are weaker in the southern hemisphere and these might be instrumental (along with diurnal tides) in triggering the early storms in the Hellas basin. In the northern hemisphere, the first year shows strong traveling wave activity and it can be seen in the

second year, there is a second peak ~Ls=310- 330 as has been observed. The transient waves in the NH peak around 65 degrees latitude.

The transient waves are stronger in the northern hemisphere compared to the southern hemisphere. They tend to peak around latitude=65 N. Figure 28 shows the seasonal and latitudinal variation of surface pressure RMS amplitude. The traveling wave activity in the southern hemisphere has a local maximum at Ls=180. It is likely that these waves combined with the diurnal tide trigger the dust activity in the Hellas basin. The interactions of the retreating CO2 frost cap with the circulation in the Hellas basin possibly introduces some transience that results in occasional storms in the Hellas in the early southern spring season.

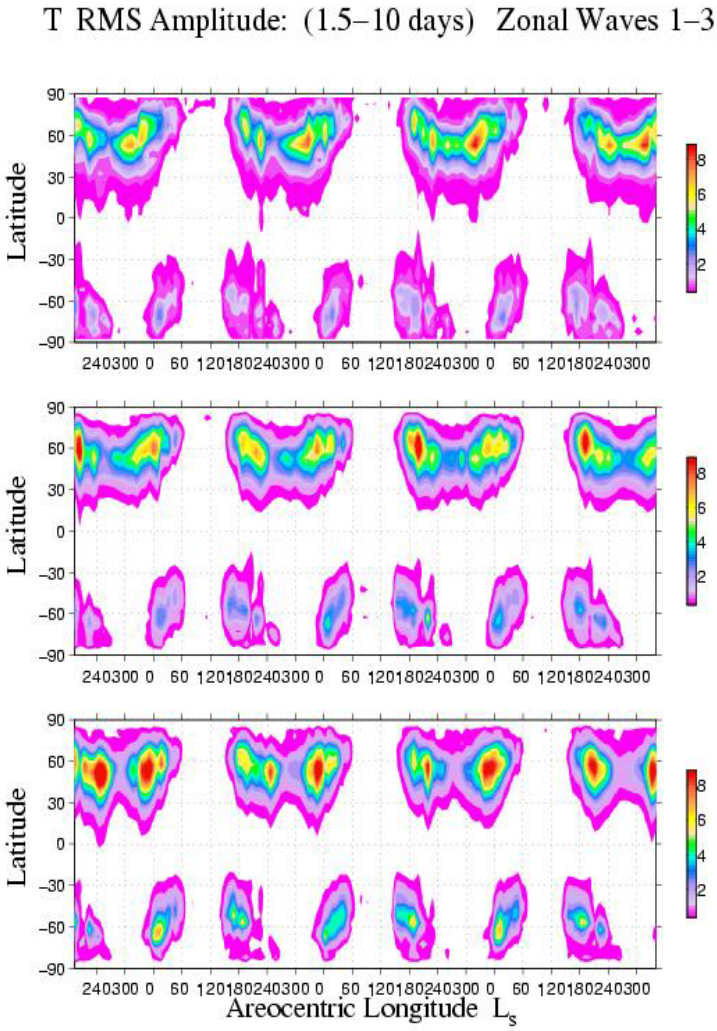


**Figure 29:** Traveling waves from zonal wave 1 to zonal wave 3, their periods respectively ranging from 1.5 days to 10 days. The low-level temperature anomalies have been plotted in this case and a rough variation in latitude can be seen that correlates with the advance and the retreat of the polar caps.

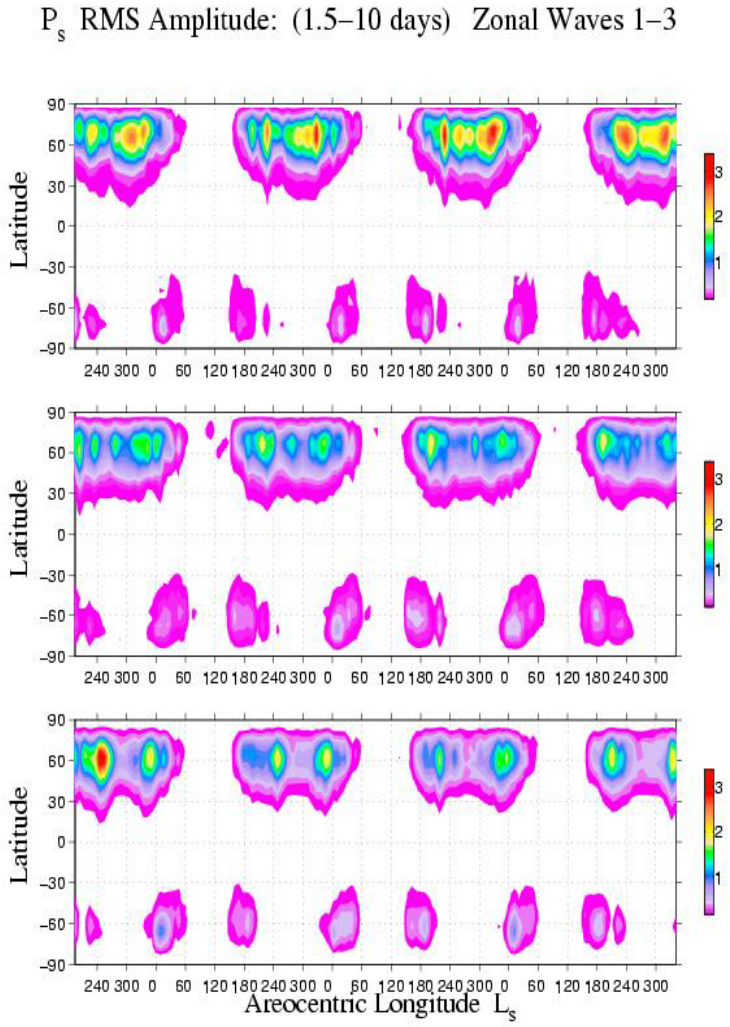


**Figure 30:** Traveling waves from zonal wave 1 to zonal wave 3, their periods respectively ranging from 1.5 days to 10 days. The surface pressure anomalies have been plotted in this case.

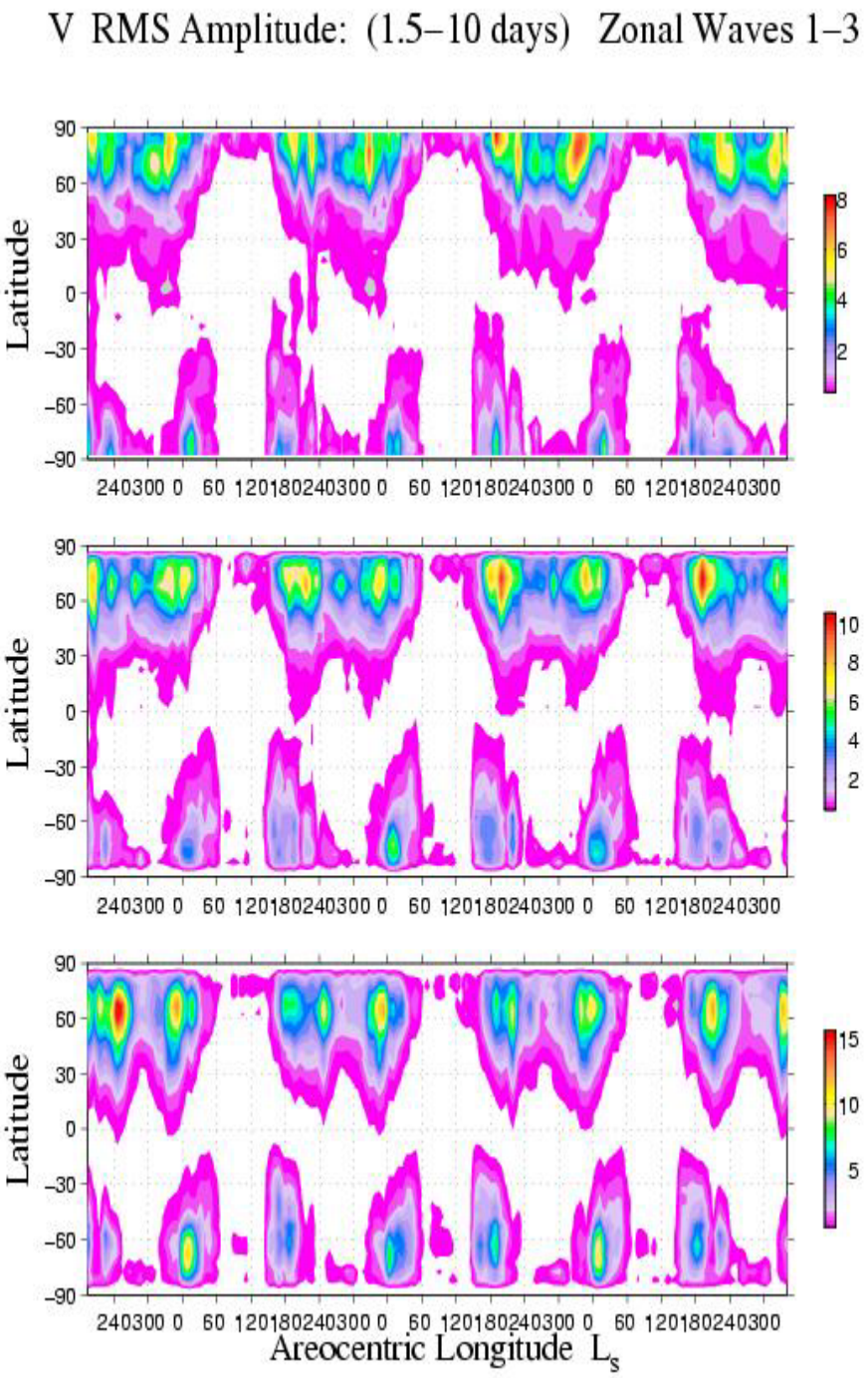


**Figure 31:** Traveling waves from zonal wave 1 to zonal wave 3. Their periods respectively range from 1.5 days to 10 days. Same as the previous plot- in this case the velocity amplitude has been plotted. The amplitude of wave 3 is dominant particularly at latitude 50N.

### 3.4.2.2 Dust and air temperature distribution for Chryse type storms

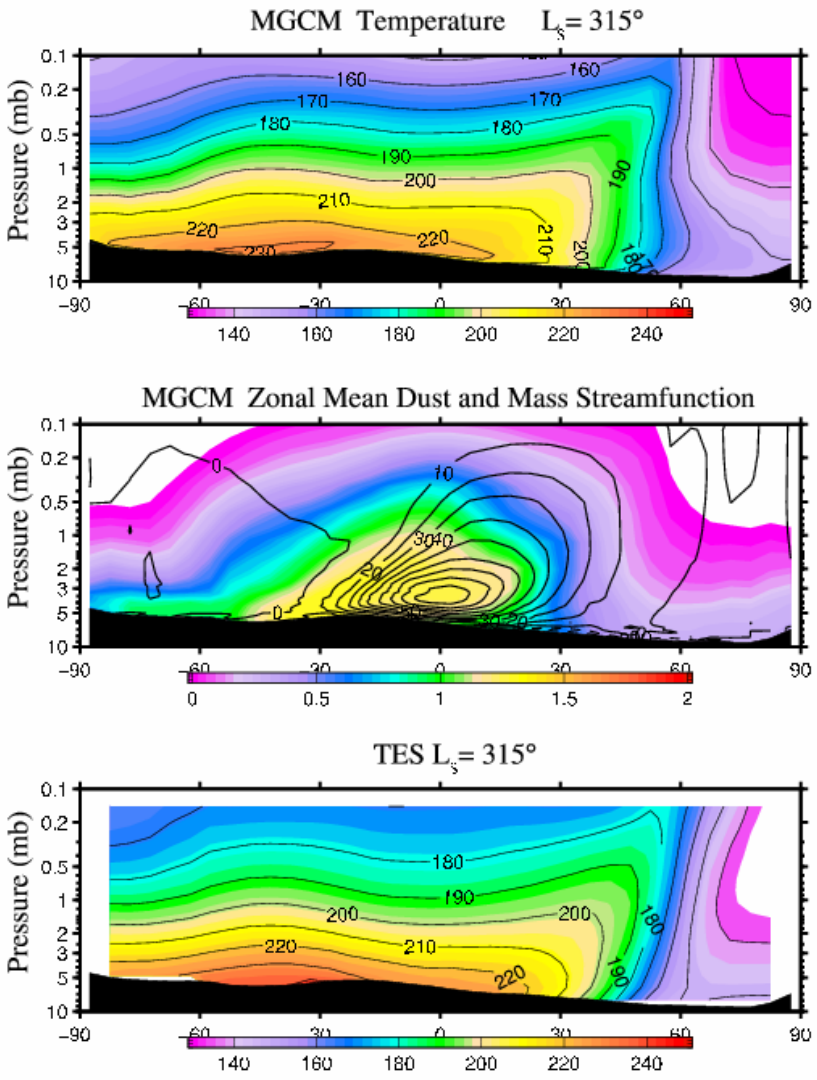


**Figure 32:** Simulated dust distribution and T15 temperatures as a function of latitude and height compared against the MGS TES data for Ls=315. This is the period when the post-solstice Chryse type storms are most active.

The pre-solstice temperature cross-section comparisons with TES data for a typical storm year with a Chryse storm and an early Hellas storm have been shown in Figure 32. Pre-solstice Chryse storms are much more frequent than post-solstice ones. On real Mars these storms are quite frequent even in post-solstice season. Figure 32 compares post-solstice storm activity for

the MGCM simulation and TES data. The temperatures are in good agreement. The southern polar temperatures are colder in the simulation. Figure 33 and Figure 34 show two consecutive storm years. In these years, an early Hellas storm was missing and hence the Chryse storm can be seen clearly in the cross section figures.

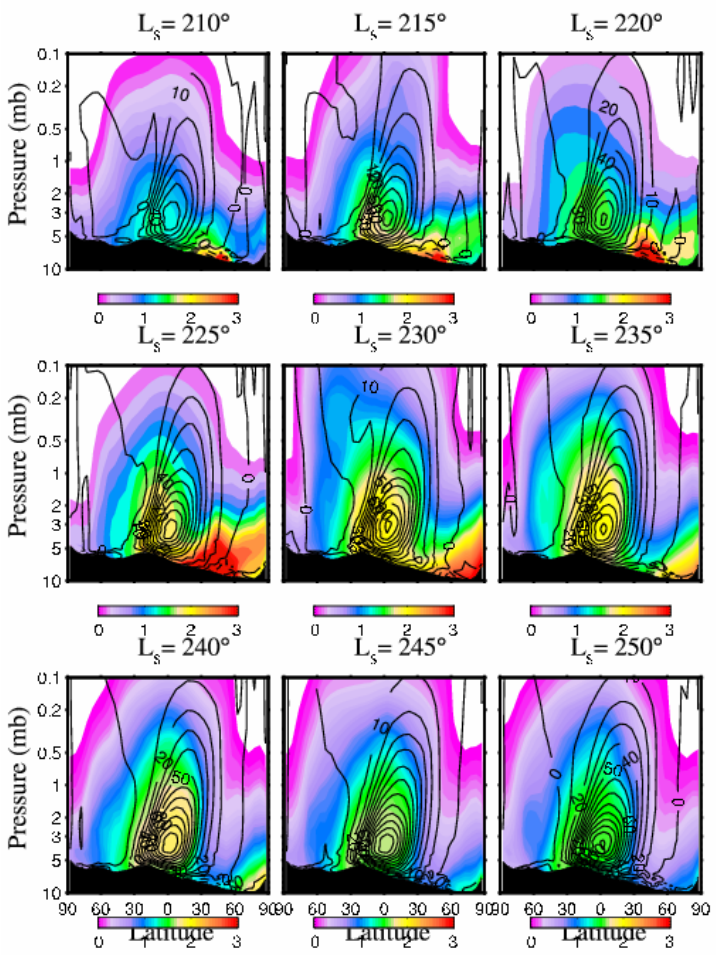


**Figure 33**: Dust distribution resulting from a Northern Hemisphere dust-lifting event, largely in the Chryse region. The zonal mean tropical temperature at Ls=240 is comparable to the temperatures in this season in subsequent years though the time evolution is different. A critical difference appears to be the lack of an early season (Ls=205) storm event in Hellas that we see in some of our other simulations.

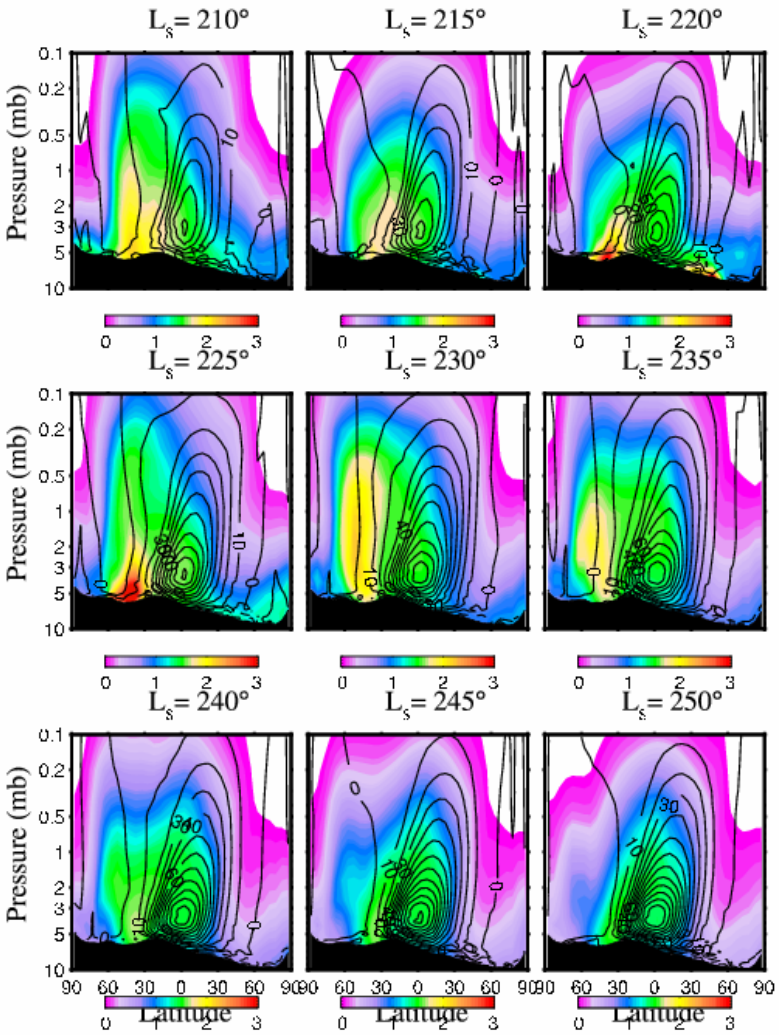


**Figure 34:** Dust distribution from the following of same simulation as in Figure (33). This is qualitatively different from the 1st year when northern hemisphere dust was more significant. There is some dust lifting at Ls=220, perhaps this remotely triggers a response in the southern hemisphere which appears to be strongest by Ls=225-230.

### 3.5. Global Dust Storm Initiation

The initiation of the type of storm shown in Figure 20, has been described by Wang et al. [2003]. The initial event which begins the first major dust lifting is associated with a

particularly strong baroclinic storm. This initiates dust lifting, which becomes entrained in the Hadley circulation. Wang et al. [2003] demonstrate that favorable baroclinic storm for dust lifting occur in two seasonal "windows" centered upon and separated by the northern winter solstice. A variety of factors influence the strength of these storms and their ability to transport dust from the northern to southern hemispheres, including initial storm center latitude, strength of the high-pressure center behind the low, and most importantly, the timing of storm center propagation through Acidalia [Wang et al., 2003,2005] with respect to the diurnal tide.

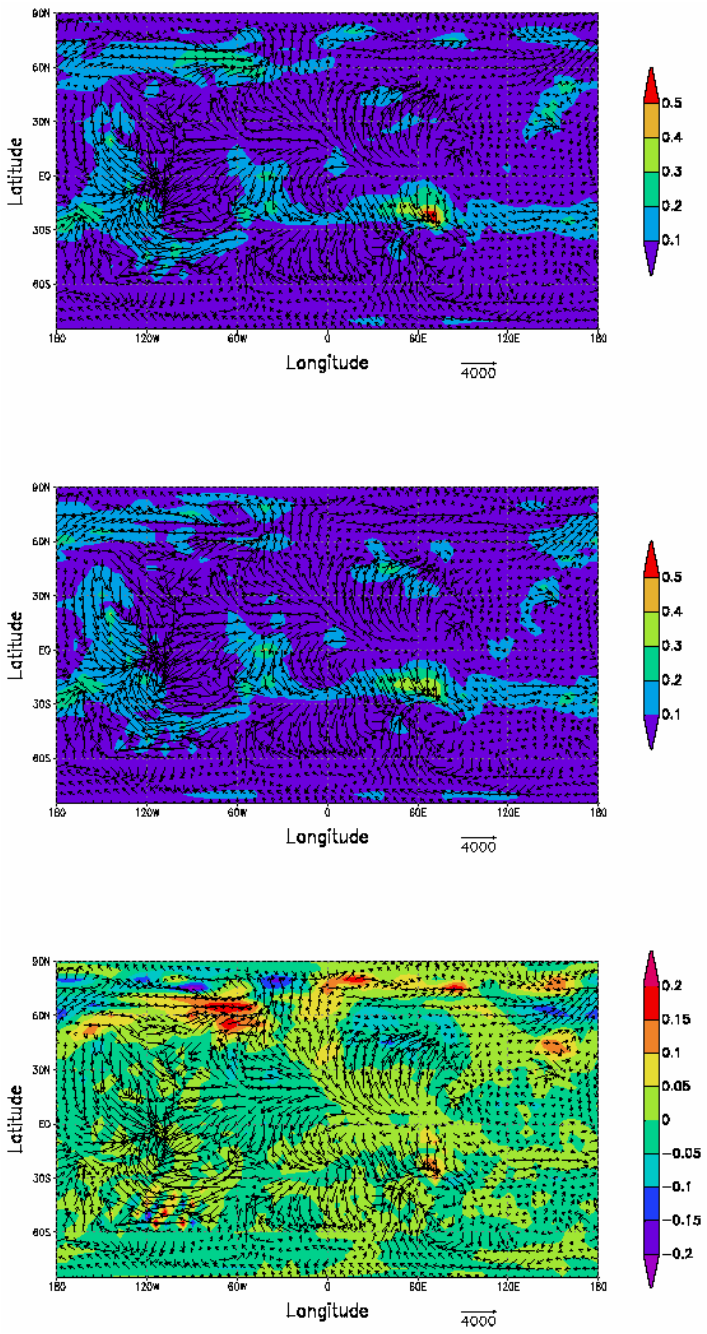


**Figure 35:** a) Spatial map of stresses (0.1 Pa) and wind just before the beginning of a global storm. b) Similar map for a no storm year, same time of the year. c) Difference plot of the two above

The variation of intensity of these baroclinic storms provides the "random seed" from which global storms of this type can form.

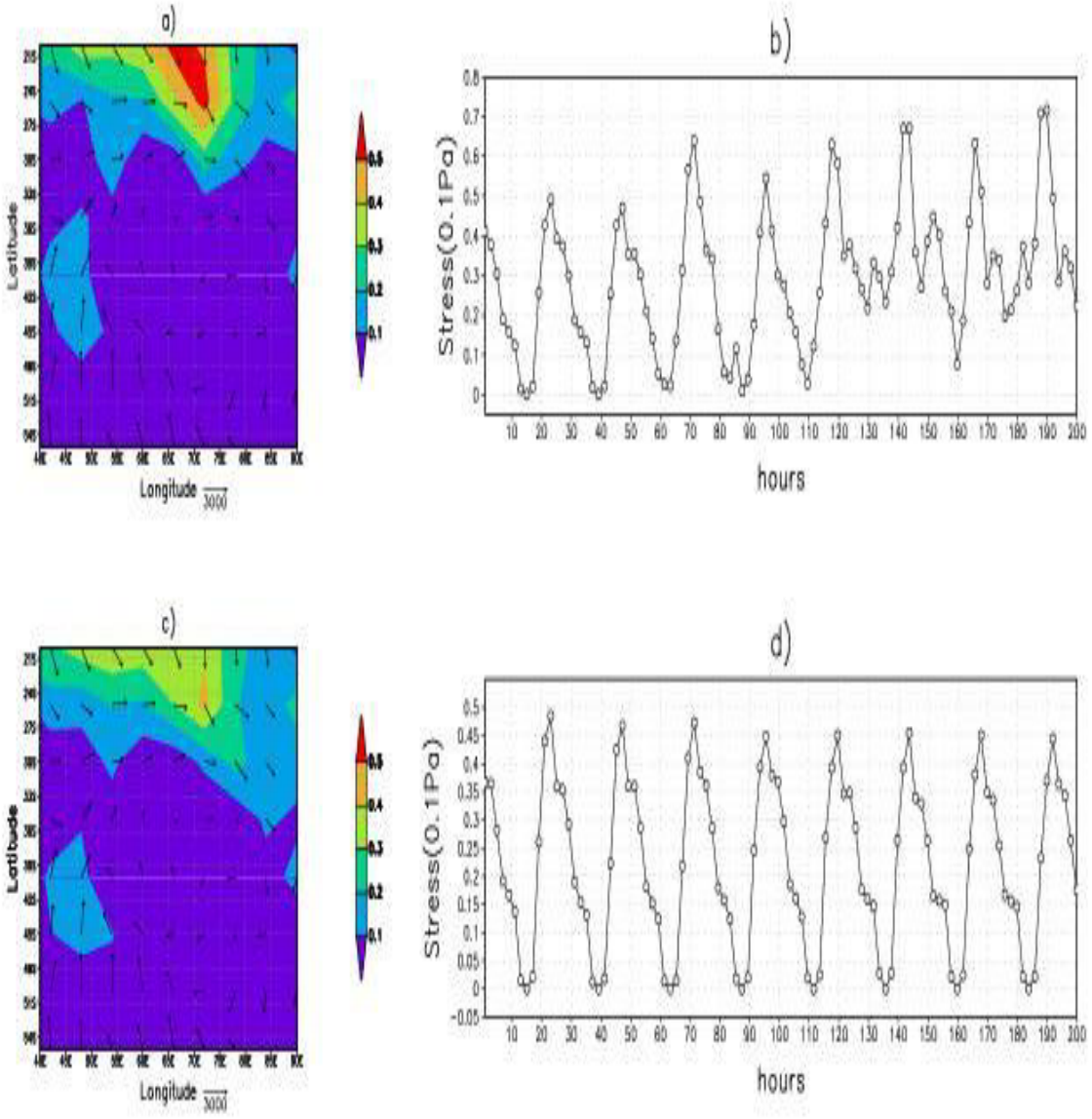


**Figure 36:** a) The first plot shows the stresses in the Hellas basin (25-50S, 40-80E) just before the global dust storm begins. b) Shows the variation of stresses on an hourly basis in the Hellas region- it can be seen that when the storm begins the diurnal pattern slowly begins to be lost. c) Shows the stresses in the Hellas same time of the year in a no dust storm year d) Shows the time variation of stresses- it can be seen that the diurnal pattern is maintained.

The big regional storms that develop from the Hellas basin early in the storm season are possibly triggered by the transient wave activity arising from the interaction of the retreating polar caps with the Hellas basin circulation [Figure 28].

The global storms that develop from the Hellas basin do not occur regularly, and it is important to understand what is different in the model in years with and without global storms. The pattern and magnitude of the maximum surface wind stresses just before the initiation of the storm shown in Figure 7, is shown in Figure 35a, and for the same seasonal date in the same simulation for a year without a global storm is shown in Figure 35b. Comparison of the two panels [Figure 35c] shows that just before the initiation of the global storm, the surface winds stresses were roughly 50% higher on the northern rim of Hellas in the year with the storm. It is at this location that the first major dust lifting in the simulated storm begins.

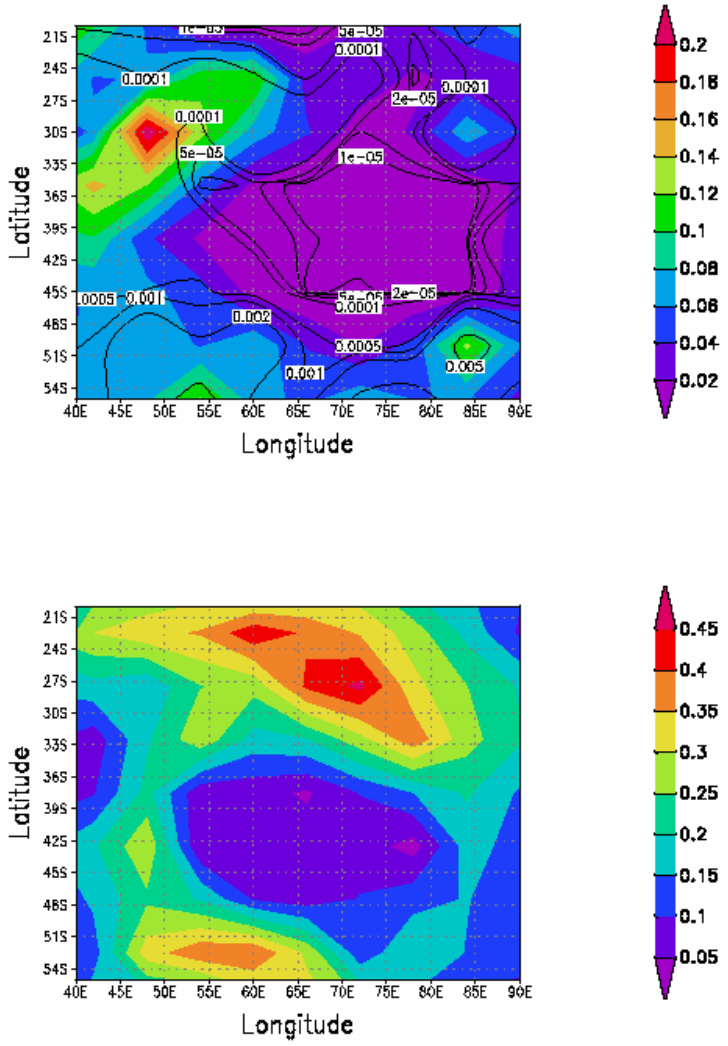


**Figure 37:** The mean and variance of stress evaluated over 10 years in the period between $L_s$=230° and 240° is shown in Figure 37a, with the maximum wind stresses at each point in the periods sampled shown in Figure 37b

The behavior of wind stresses around the Hellas basin in late southern spring is shown in Figure 37. The mean and variance of stress evaluated over 10 years in the period between $L_s$=230° and 240° is shown in Figure 37a, with the maximum wind stresses at each point in the periods sampled shown in Figure 37b. The basin itself is associated with low stresses and weak variability. The high stresses are associated with flows up and down the rim of the basin. The peak mean stresses are found on the northwestern rim of the basin, with the maximum variance extending from the west and south, along the western and northern rim. The

maximum variance is found to the south west of the basin. These patterns of maximum variance in the stress are consistent with the locations of dust lifting prior to the development of the 2001 dust storm. The maximum wind stresses also echo this pattern, with peak values on the highlands just north of the basin, to the south and west of the basin, and along the western rim. Peak pre-storm stresses exceed 0.045Pa. As the circulation within and near the Hellas basin is driven largely by the diurnal variation of heating and associated slope flow into and out of the basin, the day-to-day variance is associated with slight differences in the strength of these diurnal flows. The precise dynamical origin of these differences is less obvious than for the variability of stress in Acidalia, and further study is deferred to a later paper. What is clear, however, is that "weather noise" associated with the Hellas basin flow allows stresses in rare occasions to exceed the threshold for dust lifting and to such a degree that a global dust storm is sparked.

We ran some experiments with changed opacity weighting to see if the lighter particles, that have longer residence times in the atmosphere, could start an earlier storm. The results did show an earlier storm but and not as early as Ls=185 like it did for the 2001 global dust storm. On increasing the heating rates by decreasing the single scattering albedo of the dust particles (from 0.92 to 0.86) the overall temperatures were higher by 5K and the global dust storm started a little earlier than the default case but again, no storms as early as Ls=185 were simulated.

**Comparisons of Model Simulations with observed dust storm activity on Mars**

Dust storms on Mars have been observed telescopically and with spacecrafts. However the exact location of the dust storms is not always as accurate especially when the storm is in its initial stages. Sometimes the observations have low resolution or they are no frequent enough. Here we try to broadly correlate the observed and the simulated dust storms on Mars.

**The 1956 global dust storm** started around Ls=249 from the western Hellas region and decayed ~ Ls=304 [Martin and Zurek, 1993]. The active lifting centers were in Argyre, Hellas, Noachis, Ausonia, southern Thaumasia and some parts of Chryse. The area of activity was predominantly in a zonal collar from latitude 30-50S. This storm is quite similar to some of our

simulated storms. The sub tropical jet in the zonal collar becomes the strongest near perihelion, a period of maximum solar insolation.

In our simulations once the storm starts going, it makes the circulation even stronger, both the diurnal tides and the Hadley cell circulation. When the Hadley Cell becomes strong enough it activates other lifting centers near Argyre that put more dust in the atmosphere and make the storm global. However our storm decay is not as early as Ls=304. The decay is purely seasonal and as the Hadley cell becomes weaker the wind stresses become weaker and the lifting stops from the active lifting centers. All the dust in the atmosphere falls out and the storm decays by Ls=360. Since we employ single wind stress thresholds for the entire planet the lifting centers are limited in our simulations and they occur from the high stress regions mostly. Hellas is the region that has the highest stresses in the southern summer and spring seasons.

**Regional dust storms as the 1971 regional dust storm** have also been simulated. These start in the Ls=210-221 time period as observed. The initial lifting center is the Hellas region and the dust cloud remains over Hellas for most of the time. In some cases secondary cores also formed over Argyre as observed in the 1971 storm. Isolated local Hellas events are also simulated in the northern spring and summer seasons but in these cases the secondary lifting center is not activated over Argyre as the subtropical jet does not help in this season.

**1971 global dust storm. (Ls~260-329) [Martin 1974]**

This global storm is also similar to the storms simulated by our model. The storm starts in the Hellas region and starts around perihelion. The subtropical jet is instrumental in making the local Hellas storm a global dust storm event at this time. Dust spreads out eastwards, westwards and southwards out of Hellas. The secondary core forms over Argyre and then the storm starts spreading towards the northern hemisphere. The observed storm decayed entirely by Ls~340. But the dust from the simulated storms lingers around for a longer time, as the lifting centers don't shut off immediately after the episodic growth of dust from the Hellas region.

**1973 global dust storm:**

This one started later in the season at Ls~300 and decayed soon after. Initial dust clouds were observed in the Claritas region with brightening over northern Hellas as well. We also get late global storms in our simulations. These start around Ls~290 and are much smaller than the storms that start earlier. This is because at this time in the season the solar insolation to the planet is decreasing and hence there is less scope for the storm growth.

Most of our storms start in the Hellas region as it has the highest stresses. Since we have a uniform stress threshold for the entire planet, the dust lifting at other regions is overwhelmed by Hellas, which plays a major role in initiating and maintaining the global dust storms. When the region is shut off, and a lower stress threshold is set, the global storms start off from other lifting centers some of which are in northern hemisphere like Tharsis and Chryse. On real Mars the wind stress-lifting threshold is of course variable. It depends on the surface roughness, the ease of lifting of the particles due to inter-particle cohesion etc. Thus a single threshold does not capture the widespread lifting effectively.

The surface roughness can be varied with thermal inertia arguing that the thermal inertia tells us about the rock properties and surface roughness depends on rock properties. There are no good observations based on which the stress threshold might be varied to capture the surface roughness etc.

**The Viking Missions (1976-1982):**

The 1977a storm started at Ls~204 in the Thaumasia region. This storm decayed completely by Ls~278. This is also when the second global storm, the 1977b storm started probably from the Argyre region. It expanded mostly in the western and the northern directions. The storm decayed completely by Ls~330. In our simulations we also get an earlier storm that starts at Ls~190-205 and decays completely by Ls=240. The Hadley cell is not strong enough at this season so the storm decay is quick. Our simulated second global storm that starts at Ls~270, the same time as 1977b however is a bigger storm. Some of these storms start from the Hellas region and some start from the Argyre region. They spread in all the directions. These two regions are the major dust lifting centers in our simulations. Dust is picked by the sub-tropical jet and the major dust lifting centers are along a zonal band at latitude=30S. The decay of this

storm is purely seasonal unlike the 1977b, which has the decay rates the same as dust fall out rates. There was no dust lifting or negligible dust lifting once the peak dust opacities were reached. This tells us that the active dust lifting centers were shut off either due to the expiration of dust or due to some kind of negative feedback that ensued once the peak opacities were reached preventing further lifting. This is not the case with our storm that starts later in the season. Our simulated storm is bigger, with a less sharp peak, indicating that lifting was going on even after the peak opacities were reached. The negative feedback can be incorporated by the dust devil lifting scheme as was shown Newman et al. 2002. But such schemes give very high opacities in the northern hemisphere spring and summer, which is not realistic.

**MGS TES observations:** Observations from **MY 23** show that there was a regional storm in the southern mid-latitudes at Ls~190. There was lifting at the polar ice cap edge. At Ls~225, a large regional storm began at Ls~225. This started in the Noachis region. The storm did not spread to the northern hemisphere but expanded eastwards and westwards.

In our simulations we also observe storms at the polar cap edge boundary. The storms that start later in southern summer season also spread both eastwards and westwards and then northwards unlike the earlier Hellas storms that start at Ls~190. These spread only eastwards as the westerlies are strong during this season.

Most of our storms start from the Hellas basin or Argyre. No storms have been seen to start from the Noachis region. This is again due to the fact that the two basins- Hellas and Argyre are overactive and they are the major dust lifting centers that fire off before any other location. Also since we have a single threshold for the entire planet and infinite supply of dust everywhere, the lifting centers are limited to a few regions only.

**MY 24:** Regional storms were observed in Amazonis, Olympus Mons and Alba Patera region. Dust loading started at Ls~170 in the southern midlatitudes. This storm started from Hellas, Argyre and the polar cap edge. This storm died by Ls~245. At this time two regional storms started in the northern hemisphere and traveled southwards. At Ls~260, more dust activity was observed at the southern polar cap edge, Olympus Mons and Alba Patera. In our

simulated storms we also get similar regional storm behavior. The active lifting centers in the northern hemisphere are Alba Patera and Olympus Mons. We also observe the cross equatorial storms that start in the Chryse region and travel southwards.

**2001Gobal dust storm**- This storm began in the Hellas region at Ls~177. Local storms on the northwestern rim of Hellas, probably triggered by the slope winds and cap edge contrasts apparently helped start this global storm. Dust activity extended northwards and eastwards. At Ls~185 the storm began to rapidly spread eastwards. There was no propagation to the west. As the dust storm extended into the northern hemisphere, secondary lifting centers were activated in Daedalia and Solis region. The storm was global by Ls~195. Once the storm was full blown, Hellas seemed to be less important than Solis as an active lifting center.

By Ls~212 the storm started to decay and the lifting centers became inactive. In our simulations, we also get a similar storm that starts early in the southern spring season at Ls~190. This storm also originates from the western Hellas rim and propagates only eastwards. There is no westward propagation since the easterlies are not strong at this season. The storm propagates to the northern hemisphere and the active lifting centers in the northern hemisphere are Alba Patera, Amazonia, Olympus Mons, Arcadia, Acidalia/Chryse, Syrtis Major, Isidus and Elysium Mons. Most lifting centers in the northern hemisphere are activated by the Chryse storm and are independent of the storm originating from the Hellas region. However the dust raised from the Hellas storm and the Chryse storm together raise the zonally averaged temperatures quite a bit reaching 200K.

**The Chryse storms**: The largest dust storm in MGS mapping year 1 is associated with southward moving dust fronts that start from the Acidalia-Chryse region. The observations suggest that these are responsible for the big storms in this region. These storms have been regularly observed on Mars in southern spring and summer season and a few storms also occurring in the early northern spring season. These have a periodicity of 2-3 days. We also get very similar storms in our simulations. These are possibly caused by the constructive interference between the tidal waves and the traveling waves. The periodicity of these storms is also 2-3 days. They originate in the Acidalia-Chryse region, spread eastwards and southwards

forming the famous 'V' shape in some cases. These storms spread southwards crossing the equator and spread close to Argyre in some cases. Some of the weaker pulses dissipate eastwards and do not travel across the equator. These storms associated with the traveling waves have been seen to be somewhat symmetric about solstice. But in our simulations, we find that these Chryse storms are much more frequent in the early southern spring season (before solstice) than after solstice. This is due to weaker traveling waves later in the season. Some of these storms have also been observed to occur at Ls~10-20, but we rarely get these storms in this season. The traveling waves in the southern hemisphere are weaker than in the northern hemisphere. They are responsible for occasional Hellas storms in the Northern spring/summer season but do not cause any dramatic storms as the ones originating from the Chryse basin in the northern hemisphere.

**Summary of the storms:** Regional storms have been observed in the Hellas region, Argyre, Noachis, Chryse, Amazonis, Hellespontus, Syrtis, Thaumasia and Chryse regions. These big storms start in the southern hemisphere spring/summer season. Our simulations also capture most of these storms except for the ones from Thaumasia and Noachis region. The simplistic uniform stress threshold condition does not capture the local circulation and threshold conditions at these places and hence these are not active lifting centers in our simulations.

The global dust storms have been seen to start from Hellespontus, Argyre, Solis, Claritas, Meridiani and the Hellas region. We are not able to simulate the storms from the Solis, Meridiani and the Hellespontus regions. Again the reason for this is that Hellas has the highest stresses. Most global storms start either from the Hellas region or Argyre and these overwhelm dust lifting from any other lifting centers.

A truly realistic Martian dust cycle would capture the various dust lifting centers, have inter-annual variability in these storms in terms of the intensity of the storm, beginning season and the place of initiation and have a realistic background temperature cycle matching the observations.

Our simulations have been able to capture most of these aspects of the Martian dust cycle. However since we have a single uniform threshold and infinite uniform dust on the surface,

we are not able to capture many of the storms and lifting centers that are observed by the spacecraft data. There isn't enough data available to implement a variable wind stress threshold map for Mars. But looking at the observations it is almost certain that stress threshold varies from one region to another depending on the ease of dust lifting from the surface which in turn depends on surface roughness, local circulations, inter-particle cohesion and other such factors.

### 3.6. The Dust Storm "Switch-Off" Problem

The comparison between observed and simulated global dust storms shows one substantial discrepancy. While the simulated storms initiate at a reasonable range of seasonal dates and develop peak air temperatures consistent with the observations, the storms do not terminate as observed. The Hellas storms early in the season [Figure 1c], are much smaller and are propagated in the southern hemisphere by the westerlies. As the westerlies weaken with approaching summer solstice season, these storms decay. However, the storms that initiate around southern summer solstice in the simulation shown in Figure 1b provide a good example. The growth rate and peak temperatures of the storms are consistent with observed behavior. However, albeit limited observations would suggest that after about $L_s$=260, when the storms have reached their initial peak, decay ought to set in. This prejudice is based on the fact that both the 1977b and 2001 storms began to decay about 20-30 of $L_s$ after initiation [Martin and Richardson, 1993; Smith et al., 2002] and that there was no "rounding off" of storm activity at a sustained peak–explosive growth was immediately followed by rapid decay. In contrast, the simulated $L_s$=230 storm remains active and in a fully developed state from before $L_s$=260 until just before $L_s$=315. Only after $L_s$=315 does the storm decay. Once it does start to decay, however, it does so at a rate that is similar to that of observed storms. Thus, after the termination of dust lifting in the storm, the model emulates the observations well, which is consistent with previous storm-decay experiments with GCMs [*e.g.* Murphy et al., 1995, Wilson and Richardson, 1999]. The problem, then, is not the decay process itself, but "triggering" of the decay phase. The dust source does not shut down quickly in our simulations.

The feedback between increased atmospheric dust opacity, increased circulation vigor, and increased dust lifting is an essential part of explosive GDS development, and is well captured by the GCM. However, it has always been apparent that at some point either this feedback must become inactive, or the dust in the source region must deplete. In these simulations we have assumed an infinite supply of dust and hence the dust is never depleted from the lifting centers. It has variously been speculated that the development of strong static stability in the boundary layer associated with high opacity causes a reduction in wind stresses and a cessation of dust lifting. Although the GCM does develop an increasingly stable boundary layer at storm peak, it does not reduce stresses dramatically and does not cut off dust lifting. However, in our preliminary high-resolution simulations ($2^o$x$2.4^o$ resolution) we find that we get a realistic switch off of the storms. The storm peaks are sharp and the decay of the storm starts much sooner than in the low-resolution case. In one simulated year, we even get two big storms in the same year [Figure5]. These results suggest that the interactions between the various phenomena can be accurately captured only if the wind stresses and other fields like temperature, opacity etc. are resolved properly. If the small signatures of critical processes are lost in the coarseness of the grid then we might not be able to accurately simulate all aspects of the GDS.

The GCM storms do eventually decay, and to see how this happens, it is useful to take a different view of storm life cycles. The development of a GDS in the GCM actually corresponds to a transition between two stable climate states (two model steady-state climatic solutions). The years without a GDS demonstrate that the "low-dust" state is a perfectly acceptable steady-state climate solution, which is not particularly surprising. This state is explored further in Basu et al. [2004]. The sustained GDS state shown in Figure 1b corresponds to a "high dust" state, where opacities are maintained at a high value. However, this climate is also in steady state, with injection and deposition of dust globally balanced after the storm peak is attained after $L_s$=260. This state is steady because as the elevated dust injection causes the amount of dust in the atmosphere to increase, the deposition rate increases. After the visible dust opacity exceeds 2 or so, further increases in opacity increase dust fall-out more aggressively than they do the circulation and lifting. Thus the global dust opacity increases until the fall-out balances injection. The problem of dust storm initiation was

one of forcing the transition from the "low" to "high" dust state, and the solution is the radiative-dynamic dust lifting feedback, triggered by an initial perturbation. GDS decay is the problem of a forced "high" to "low" dust state transition.

The GCM GDS decay, or the state transition, is triggered by the spin-down of the Hadley circulation in late southern summer. As the Hadley circulation naturally slows as the sub solar point moves equator ward, stresses in the Hadley cell convergence zone (which predominates GDS dust lifting) decrease to a point where lifting stops. There is a feedback here. As the Hadley cell weakens due to changes in solar forcing, the amount of dust lifting and hence opacities are reduced. This causes a further slowing of the Hadley circulation. Eventually, active stress lifting terminates and the GCM drifts back to the "low" dust state. The results of the low-order model of *Pankine and Ingersoll* [2002] can also be interpreted in this manner. In that case, the model was limited in the range of possible behavior. However, the generation of similar behavior in a full circulation model suggests that storm switch-off may be a significant challenge if internal feedbacks are of dominant importance. Higher resolution simulation of the boundary layer or improved treatment radiative heating may be necessary, but there is no obvious *a priori* guarantee that such improvement will yield qualitatively different behavior than that currently expressed by the model.

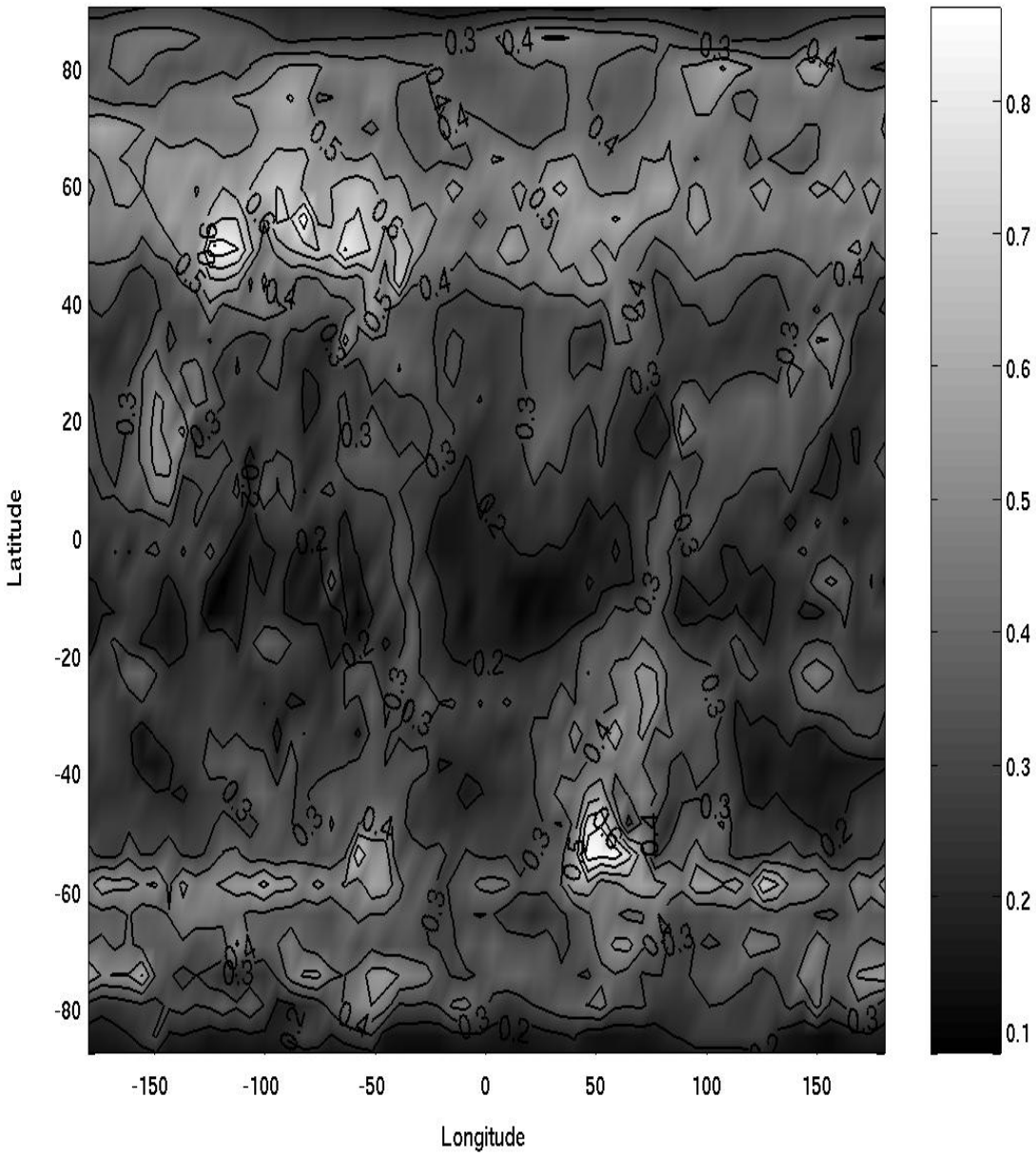
Latitude
80
60
40
20
0
-20
-40
-60
-80
-150
-100
-50
0
50
100
150
Longitude
0.8
0.7
0.6
0.5
0.4
0.3
0.2
0.1

**Figure 38:** Geographic distribution of maximum stresses encountered at each grid point in a given annual cycle. The high wind stresses are not uniformly distributed but are concentrated in specific regions, largely due to topography and the position of the wintertime baroclinic storm tracks. These are active dust lifting regions.

The other option for storm switch-off is source region depletion. Figure 38 shows the maximum wind stress experienced at any point on the planet in a ten year run without wind-stress lifting. This experiment yields a very good simulation of the non-dust storm Martian climate [Basu et al., 2004]. It is clear from Figure 38 that high wind stress is not uniformly distributed, but concentrated in specific regions, largely due to topography and the position of the wintertime baroclinic storm tracks. These high stress regions are the dominant source regions for storms, and thus there is a tendency for dust to be exported from these locations (see Section 3.7). Observationally, these high stress regions are anti-correlated with the bright, low thermal inertia dust deposits [*Ruff and Christensen*, 2002]. As such, there is reason to expect that the dust deposits in the source regions are not uniformly more than a few millimeters to a few centimeters deep (otherwise they would appear as "dust" in visible and thermal infrared retrievals, which has a low thermal inertia signal). During a large, sustained dust storm, the GCM predicts dust removal in source regions of about this thickness, while the predicted fall-out would take over 10 years to re-supply this much dust. Exhaustion of dust source regions during a dust storm would thus seem plausible.

Some initial simulations have been undertaken with the GCM using exhaustible surface dust deposits. As might be expected, the storms develop sharp temperature and dust opacity maxima as the primary source region depletes. The trend of air temperature in these simulations mimics that of the real atmosphere much better than that of the "inifinite dust source" model, shown in Figure 1. These simulations provide a much richer variety of behavior as the surface distribution of dust becomes an additional source of internal model variability. Discussion of simulations with exhaustable surface dust deposits is defered to a later paper.

We also ran some experiments with changing the dust particle size distribution opacity weightings, i.e replacing the 2 bin dust particle distribution entirely with the larger particle.

Since larger particles have higher sedimentation rates, the storm shut-off was much more realistic than the default case. The storm peak was sharper and the Northern spring temperatures were much more accurate than the default simulations with the mix of two particle sizes.

### 3.7. Net Dust Transport by Global Dust Storms

The net annual dust deposition/erosion predicted by the GCM for non-dust storm years has been shown and discussed by Basu et al. [2004]. For completeness, and in order to illustrate the residual signature of a GDS in the annual surface dust deposits, the annually-integrated dust deposition/erosion for years without and with a GDS are shown in Figure 39. The non-dust storm year shows dust erosion on the southwestern rim of Hellas, in Acidalia/Chryse (45N-45S, 30-60W), in Amazonis, and on the northern plains to the west and south of Elyssium. High deposition rates occur at both poles, on Tharsis, and in the Hellas basin. This simulation is discussed in more detail by Basu *et al.* [2004].

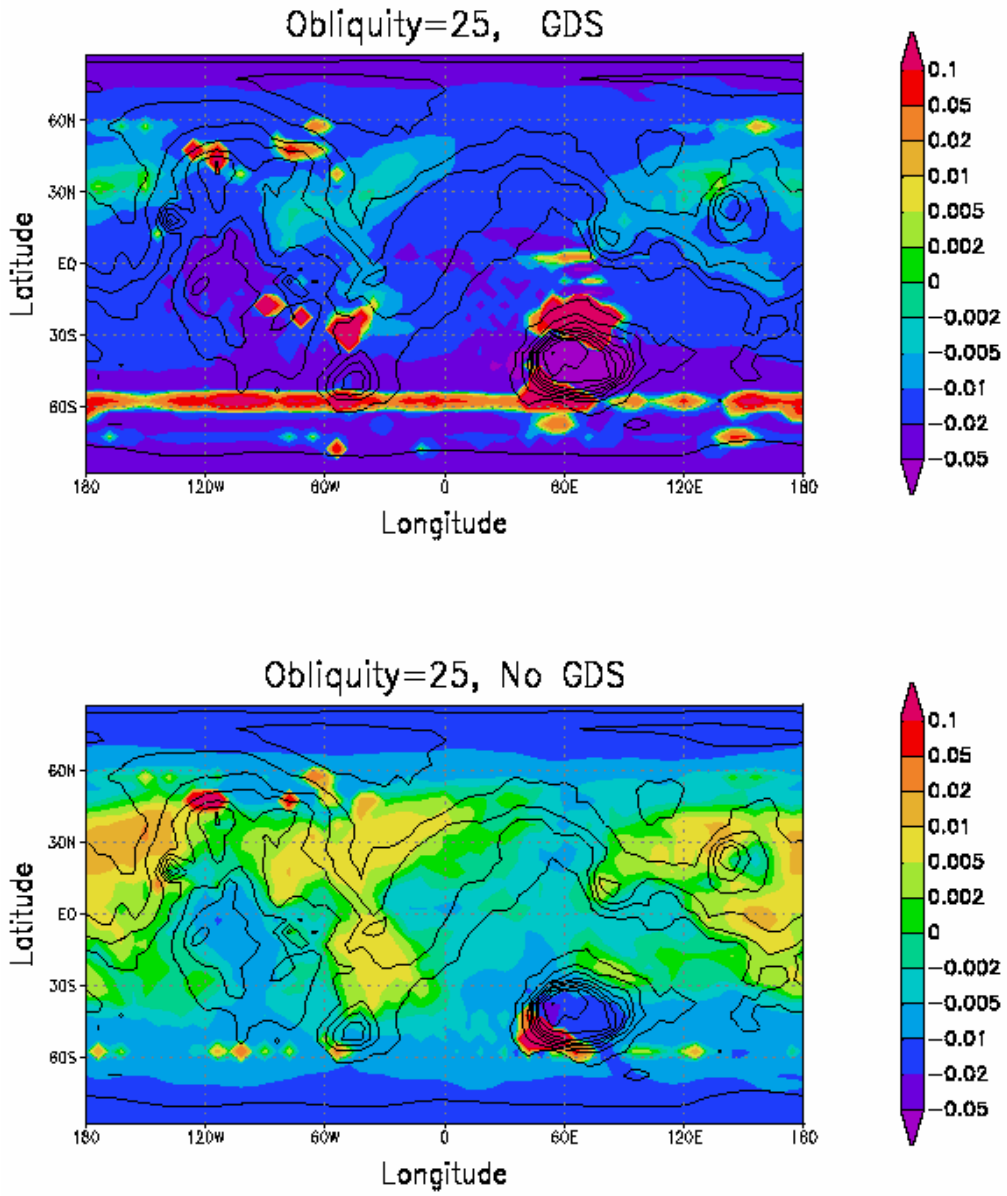


**Figure 39** The net annual deposition/erosion predicted by the GCM for years with and without a global dust storm. The effect of the GDS is to generate large erosional signals in the storm source regions-northern and southwestern rims of Hellas and points within Syria and Solis and north of Argyre. The non-dust storm year shows erosion on the southwestern rim of Hellas, in Acidalia/Chryse, Amazonis and northern plains to the west and south of Elysium. High deposition rats occur at both poles, on Tharsis, and in the Hellas basin. Increased deposition from dust fall out in the GDS case results in broad areas of net sinks that were net sources in the no GDS case.

The effect of the GDS is to generate large erosional signals in the storm source regions. In this case, those regions are the northern and southwestern rims of Hellas and points within

Syria and Solis, and to the north of Argyre. These regions were observed to be active during the 2001 GDS [Strausberg et al., 2004]. The GDS has a major effect on the surface deposits at most other locations. Increased deposition resulting from dust fall-out in the wake of the GDS results in broad areas that were net dust sources becoming net sinks. In fact, the majority of the tropics and lower mid-latitudes are predicted to be net annual sinks during a year with a GDS, as might be expected.

### 3.8. Inter-annual Variability of Global Dust Storms at this and Other Climatic States

Mars currently exhibits inter-annual variability of GDS development. Based on the results shown in Figure 2, there is a very limited range of injection scheme parameters that allow variable GDS development in the GCM. In particular, the stress-lifting threshold must be within a range only 10-20% wide. The fact that Martian dust storms are variable immediately suggests that initiation is a "threshold" problem: one gets a storm when a certain threshold is exceeded, and the system is close to that threshold. Realization that surface wind speeds and stress likely change dramatically with orbital parameters [Fenton and Richardson, 2001; Haberle et al., 2003] presents an obvious question: are we observing Mars at a special time in its history – a time when GDS events are variable? At higher obliquity do GDSs occur regularly, while at low obliquity they never occur? Or does the system adjust so as to keep GDSs variable? The extremely low probability of observing Mars during a "special time" makes the former possibility unpalatable.

Maintenance of inter-annual variability requires a negative feedback mechanism which returns the system to a state of variable GDS development–it must get harder to generate a GDS as more GDS's develop, and easier as fewer develop. Ultimately, this mechanism must involve the surface dust deposits themselves and the ease with which the atmosphere can lift dust from them. It is possible to speculate about the nature of such mechanisms. *Pankine and Ingersoll* [2002, 2004] suggested that the local distribution of dust on the scale of rocks and individual "roughness elements" might be important. One can imagine a situation, such that when winds increase in strength during periods of higher obliquity, dust is only trapped on the surface in deposits that are shadowed from the wind (in rock crevices or trenches). Higher

stresses would then be needed to generate a given dust storm event. Conversely, as surface winds decrease, the dust could be removed from shadowed regions by dust devil or other convective processes until the dust is located in sufficiently exposed locations that the wind stresses can again lift it. In this situation, a lack of GDS activity allows dust devil action to dominate, and spread the dust uniformly, while the development of excessive GDS activity would tend to "hide" the dust.

On the other hand, the feedback mechanism may have nothing to do with the local scale dust distributions. Instead, the regional scale distribution of dust may be critical. Figure 38 shows the highest wind stresses experienced on the planet in a given annual cycle for a year without a GDS. There is strong spatial heterogeneity apparent in the map, and while the details of this distribution may change somewhat as obliquity changes (though not much [Fenton and Richardson, 2001; Basu et al., 2004]), strong heterogeneity is always present. A feedback mechanism involving the geographical distribution of dust then comes to mind. As drive for GDS activity becomes stronger as obliquity increases, dust is removed from the most easily eroded locations (such as the southwestern and northern rims of Hellas, Syria/Solis, and the northern storm tracks). As the prime sites are eroded, GDSs can only develop if stresses become sufficient to activate lifting in regions where storms could not previously initiate. As the winds and stresses increase with obliquity, the dust would "roll back" (be cleaned out) progressively from the most easily eroded regions and would remain only in the geographical locations that exhibit lower wind stresses. This process would continue until a steady state is reached with variable GDS activity. The steady state is maintained when a balance is struck, for a given region, between the multi-annual-average export of dust by GDSs and import due to fall-out of dust lofted by dust devils elsewhere on the planet. In this way, GDS activity would be maintained in an inter-annually variable mode until the planet were uniformly covered by dust at the low-obliquity extreme or dust was entirely removed from the exposed surface and locked up in ice sheets (in the tropics! [Mischna et al., 2003]) at the high-obliquity extreme. In fact, the low-obliquity extreme may be limited by the deflation of the atmosphere after the formation of permanent $CO_2$ ice caps [e.g. Kieffer and Zent, 1992].

The tendency for a climate model to lock itself into a variable GDS regime when a negative feedback system is imposed has been illustrated in a low-order model [*Pankine and Ingersoll*, 2004]. Indeed, once one decides to put such a feedback system into such a model, the outcome is unavoidable. Experiments with a GCM with active and exhaustible dust deposits are required to further explore the likelihood that Mars is driven to find such a steady-state. The GCM will have the freedom to internally generate a spatial dust source feedback system (*i.e.* as an emergent behavior not externally imposed on the model) and as such, the model possesses the potential to surprise. If the feedback involves the micro-scale distribution of dust, however, parameterized mechanisms may still need to be imposed. In either case, the distastefulness of the idea that we are viewing Mars at a special time in its history, combined with the ability to construct simple, intuitive mechanisms that would lock Mars into a variable GDS state, drive us to suggest that the general components of the Martian dust cycle we observed today, including variable global storms, have operated in an essentially unchanged manner throughout Martian geologic history.

### 3.9. Summary

This paper reports on the successful generation of global dust storms within a GCM that simultaneously provides a good simulation of the non-dust storm climate [Basu et al., 2004]. The dust storms develop spontaneously within the GCM, without *ad hoc* forcing, during southern spring and summer, consistent with observations. Simulated global storms are seeded by spontaneously generated local events, and grow by a radiative-dynamical feedback involving increased radiative heating associated with the lofted dust, increased Hadley cell vigor, and increased wind stresses and dust lifting. Growth from regional to global scales involves the activation of secondary lifting centers. During the simulated global storms, dust is lifting from a relatively small number of sites where wind stresses are maximized. Common areas are the rim of the Hellas basin, the southern seasonal cap edge, Syria/Solis, and Acidalia.

Model-resolved wind stresses are responsible for the generation of simulated storms. Only when the threshold stress for lifting is set low enough, and the injection rate parameter (linking the stress function to the injection rate) is set high enough, do global storms develop. In a

limited area of this phase-space, the GCM develops inter-annually-variable global storms. Within a given, continuous simulation, the model will generate years without any major storm activity, interspersed with years with global storms of various size and specific timing of initiation. This variability is internal to the atmosphere and the $CO_2$ cycle, as the surface dust deposits do not deplete, and the surface albedo and thermal inertia are not modified by the presence of dust. It is possible that additional richness in the complexity of the dust cycle will emerge in a model with an interactive surface dust distribution, but this work suggests that such interplay with a surface memory site is not required for inter-annually-variable storms. Instead, they are an emergent property of the smoothly and periodically (annually and seasonally) forced system.

The simulated storms remain unrealistic in a number of ways. The most important way, being the inability of the storms to shut down in the observed manner. For example, the 2001 global storm began its decay phase around $L_s$=214 [Smith et al., 2002], about 35 of $L_s$ after initiation. However, the simulated storms do not spin-down until the Hadley cell begins to spin-down in mid-southern summer. Storm switch-off must result from either an internal feedback mechanism that kicks in once opacities reach a specific level, or from depletion of the active surface dust source (supply). The physical processes that would have to be involved in the former are inherently included in the model, but do not generate such a feedback. While it is possible that the fidelity of their representation needs to be improved, the model shows no tendency towards spin-down at high opacity, but the reverse. The latter mechanism is not included in the standard model, initial work with exhaustible sources suggest (not surprisingly) that realistic storm evolution, including switch-off can be simulated. More work is clearly warranted on storm spin-down. While the inability of the model to generate two storms in a given year (such as the 1977a and 1977b events) might seem like a distinct, additional model problem, it is actually a trivial consequence of the spin-down problem. In order for there to be two global storms in a year, the first must happen in early-to-mid southern spring. Given that the model is quite capable of generating early- and late-season storms, it seems likely that once the spin-down or switch-off problem is solved, dual storm years will emerge. Finally, the range of locations on the surface at which storms initiate and at which secondary dust lifting centers are generated is in pleasing agreement with observations (the western and northern rim of

Hellas, the Syria/Solis in the southern part of Tharsis, and in the northern mid-latitudes in the Acidalia/Chryse "flushing storms" channel [Wang et al., 2003]), the range of behavior seems a little stilted compared to observations. After a while, one recognizes similar types of storms being generated, albeit in a continuously randomized sequence.

Additional variability mat require interaction with depletable surface dust deposits and one in which the surface albedo and thermal properties depend on the amount of dust present. Such feedback with the surface may also be necessary to explain the occurrence of variable global storms, despite the fact that a very limited area of model domain space permits these kinds of storms. We speculate, as do Pankine and Ingersoll [2004], that a negative feedback system may pull the Martian climate towards a state with variable storms.

# Chapter 4

## Simulating Dust Activity on Mars with an Evolving Surface Dust Distribution

**Abstract**

A general circulation model is used to evaluate changes to the circulation and dust transport in the Martian atmosphere for simulations with a finite supply of dust on the surface. The focus is on changes to atmospheric temperatures and dust-related surface features, as these may potentially be verified by observations. Raised dust, which affects atmospheric heating rates, has a large impact on the circulation. This impact can be highly nonlinear due to several radiative-dynamical feedbacks, and allows for a certain amount of inter-annual variability (Basu et al. 2005). In previous work (Basu et al. 2004, 2005) an infinite supply of dust was assumed on the surface, hence lifting never ceased simply because a source region had been depleted. In this work, the use of a finite surface dust supply increases the amount of inter-annual variability the system can produce. This is due to a new set of initial conditions, in the form of available surface dust, being present at the beginning of each storm season. The simulations predict peak net removal of surface dust within western boundary currents and southern mid-latitude bands, and net transport from the southern to the northern hemisphere with net deposition in the Tharsis, Arabia and Elysium regions.

The wind stress threshold for dust lifting may depend, to some extent, on the surface dust abundance, as this affects airflow within the near-surface boundary layer in a hard-to-predict manner. To investigate this at first order, simulations were performed in which the threshold was either 1) increased or 2) decreased slightly when the surface dust abundance fell below a critical value. These runs resulted in new dominant lifting centers as the original primary centers were depleted, for case (1) because lifting became easier in regions with more surface

dust present, and for case (2) because the primary centers were depleted more rapidly, leading them to become completely dust-free, hence removing them as source regions.

Finally, a finite dust source simulation was initialized (in terms of surface dust) using albedo maps from shortly before the 2001 dust storm season. The simulation produced a global dust storm that resembled the 2001 storm in many ways. The simulated dust distribution following the storm compares relatively well to the post-2001 albedo maps. The main areas of disagreement were the rims of Hellas and Argyre basins which are the major source regions in the simulations but on Mars itself turned out to be sinks of dust as they were re-supplied with dust from secondary source regions as Solis Planum, Daedalia Planum, Isidis and Sinai. These were probably largely due to the low model resolution used, as this does not allow smaller scale circulations to be represented properly (e.g. those associated with finer topographic variations). This means that, for example, many secondary lifting centers, which can play a major role in replenishing the primary lifting regions, may not be activated. This will be investigated with high resolution models in future work.

**4.1 Introduction:**

Global dust storms on Mars are catastrophic events that have considerable inter-annual variability from year to year [Liu et al, Cantor et al. Smith et al.]. The Martian surface-atmosphere system is strongly related to the seasonal variation of incoming solar radiation, which repeats from year to year, and at least the upper soil layer, which is dry and dusty, has short thermal time constants and in this sense is not a system which responds on much longer timescales and may cause such variability (such as the Earth's oceans).

In Basu et al. (2004) we included a dust transport scheme, including parameterizations of two dust lifting mechanisms, into a Mars general circulation model (GCM). The parameterizations, described in more detail in section 4.2.1, consisted of lifting by near-surface wind stress (which was assumed to activate above some threshold stress value) and by dust devils (or convective vortices, though conceptually this is applicable to other convective motions as well). We obtained significant inter-annual variability from the nonlinear response of our lifting parameterizations to the small innate variability of the atmospheric circulation. This may be an

example of a stochastic resonance, a phenomenon in which a nonlinear system is subjected to a periodic modulated signal that is so weak as to be normally undetectable, but which becomes detectable due to resonance between the weak deterministic signal and stochastic noise in the system.

We did not however explore the possibility of inter-annual variability due to finite dust sources on the surface, which may be exhausted if lifting exceeds deposition for some period of time, thus preventing any further lifting until they are replenished to some degree. This is expected to increase inter-annual variability, as it allows for a different initial condition (in terms of availability of surface dust) to exist at the same season in different years. Changes in the surface dust distribution as a result of dust storms have been observed from orbit [Christensen, 1988, Smith et al 2004] and has been suggested as an important part of inter-annual variability of global dust storms on Mars [Haberle, 1986]. The observations of air and surface temperatures following the 2001 global dust storm provide the first direct evidence for climatic coupling between the changes in surface dust and the atmosphere [Smith et al. 2004].

In this paper we limit the available surface dust in our simulations to study the effect on the types of large storms and the amount of inter-annual variability produced. Our goals, explained in more detail in the four subsections below, are to 1) examine the impact of globally uniform finite dust sources on the seasonal cycle of background dust, then 2) to examine the impact on the evolution of dust storms and the inter-annual variability produced. We 3) consider the impact on storm type and inter-annual variability of using an initial finite surface dust distribution which, being related to Mars's surface albedo, is more like that on Mars than any uniform case. We also look at the effect of surface dust on global dust storm evolution. We set up a 'realistic' initial surface dust distribution using observed albedos prior to a large global dust storm, and then a) compare the ensuing storm simulation with both the observed storm and a control experiment, and b) compare the final change in surface dust in the model with that observed. We then conclude 4) by examining (to first order only) the effects on allowing the stress threshold to vary, as it may do on Mars itself, with surface dust abundance.

### 4.1.1 The impact of finite dust sources on the seasonal cycle of background dust

The experiments with radiatively active dust lifting and transport described in Basu et al. 2004 assumed dust was available for lifting at all locations on the planet, and suggested strongly that dust devil (by which we mean 'convective') lifting produces the background dust cycle on Mars. We calibrated a single rate lifting parameter for dust devil lifting by requiring that simulated temperatures, sampled as if observed by the 15μm band of the Viking spacecraft IRTM (Infrared Thermal Mapper) instrument, matched those obtained by the instrument itself (Richardson and Wilson 1998). These are referred to as T-15 temperatures for the remainder of the paper. Dust devil lifting is more widespread (less confined to certain source regions) than wind stress lifting, and varies over the year as the sub-solar point moves in latitude. Hence it was possible that the effect of a limited dust supply would be either negligible or be an overall lowering of T-15 temperatures at each point during the year. Either result would still support the earlier conclusion that dust devil lifting produces the background dust cycle, though the latter result would require an increase in the lifting rate parameter. If, on the other hand, it is no longer possible to reproduce the observed background T-15 temperature cycle, even by varying the rate parameter, this might suggest for example that Mars has more surface dust available than we have specified, or that wind stress lifting is also important to the background dustiness.

### 4.1.2 The impact of finite dust sources on the evolution of dust storms and the amount of inter-annual variability

The infinite surface dust supply simulations shown in Basu et al. 2005, with a combined wind stress and dust devil lifting scheme, showed significant inter-annual variability, yet some features of storm development and decay did not match observations. Mars Global Surveyor Thermal Emission Spectrometer (MGS TES) observations [e.g. Basu et al 2004] produced decay rates for the observed global dust storms that are similar to calculated dust fallout rates [Basu et al 2004]. This suggests that on Mars itself all dust-lifting stops (leaving only fallout to dictate further changes in atmospheric abundance) once the peak opacities are reached. In our

simulations with an infinite supply of dust, however, dust lifting continued even after the peak opacity was reached, with the modeled decrease in lifting being strongly related to the seasonal decline of the Hadley circulation (and associated surface winds). Opacities thus remained high long into southern autumn, and in particular were unrealistically high in the Hellas basin (the primary source region) throughout this period.

One possibility is that dust devil lifting is more important in producing the observed global dust storms on Mars than we have allowed for. Newman et al. 2002 found that by increasing the relative amount of dust devil (over wind stress) lifting, and by using a more threshold-sensitive formulation for this mechanism (which basically enables dust devil lifting to produce steeper, more storm-like opacity increases), they could reproduce the observed rapid decay of global dust storms, even in the middle of the storm season when the Hadley cell is strongest. This is because there is a negative feedback effect: the dust lifted into the atmosphere by convective motions stabilizes the boundary layer and decreases the surface-atmosphere temperature difference, both of which tend to prevent further dust lifting. However this lifting formulation also produced large amounts of dust devil lifting in the northern spring and summer season, which is unrealistic as discussed in Basu et al. (2004). It is possible that some of this dust would be removed via scavenging by ice particles, but this hypothesis is yet to be investigated.

Another possibility, which we explore here, is the exhaustion of dust at the active lifting centers during the storm. It is clearly impossible for regions to have a literally infinite surface dust supply. Potentially some regions have so much dust, and/or are so continually replenished, that the source is effectively infinite, but others may have a thin veneer of dust only a few particles thick [Szwast et al 2005]. If an infinite dust supply is assumed, some areas will contribute more dust than they would in fact contain, thus skewing results towards inaccurately high opacities in these areas and overall.

It has been noted (e.g Mc Kim 1996) that some storms in the same year originate in the same general region, and it is hard to see how the source dust could be replenished, in the short time between the two storms, if the first decayed due to the depletion of source dust. The

explanation to this can be found in our previous paper on inter-annual variability (Basu et al 2005). The early Hellas storms that we generate at Ls~190° decay on their own, not due to expiration of dust from active lifting centers but due to weakening of westerly winds as southern summer solstice approaches. Thus it would be wrong to generalize that all storms decay due to expiration of dust from active lifting centers, though it could be the sole mechanism of storm decay for some of the storms observed. Newman et al 2002 also discussed the effect of imposing a finite dust source. They found a drop in the peak storm season opacity as a result of dust exhaustion from source regions, and found that it was necessary to increase the lifting rate parameters to compensate for the loss of lifting regions until equilibrium was reached after several years. At this point the dominant source regions were those which could be replenished within a few years, and were not necessarily those that dominated for an infinite surface dust supply. They also found an increase in inter-annual variability, partly due to a resetting of the initial surface dust supply prior to each storm season, but in fact mostly due to the new dominant source regions having a greater sensitivity (in terms of dust lifting) to slight variations of the atmospheric circulation.

In this work we begin by rerunning some of our most realistic simulations from previous work (Basu et al. 2004, 2005) but now using globally uniform, finite surface dust deposits, in order to observe the impact of dust exhaustion on the evolution and decay of the global dust storms. Our primary concern is whether source exhaustion is important/ necessary in producing the observed decay of global dust storms prior to the end of the storm season. Also of key importance is to examine whether it is possible for our extended simulations to come into equilibrium with exhaustible dust. Preferred areas for dust lifting are exhausted at some point, and it is an interesting question as to whether the model can re-supply these regions (through fall out of background dust), and if so, on what time scale. For this reason these simulations typically last at least ten Mars years. Our overall goal is to investigate how exhaustible dust affects the ability of the model to generate multi-annual simulations with 'realistic' global dust storms and the observed amount of inter-annual variability.

### 4.1.3 The impact of using non-uniform initial finite dust distributions based on observed albedo pattern

Getting the finite dust effect right requires that the spatial variation of the initial surface dust distribution be as realistic as possible. Otherwise we will be almost certain to miss some aspects of the dust cycle. For example, if we use an initial uniform dust cover that is far lower than actually exists in some net source regions, they may become inactive far more easily than they should. Conversely, if we use a higher value, it may be far higher than actually exists for some other lifting regions, and prevent the depletion (and possible re-supply) here which might be vital to produce realistic inter-annual variability and storm decay.

We therefore begin here by setting up an initial finite dust distribution based on albedo, as described in section 4.2.2, and look at how this effects the overall dust cycle and storms produced. The model itself will rearrange the surface dust distribution year by year, and because the model is not a perfect representation of Mars it will thus gradually shift away from the initial distribution, but we can still gain some idea of the potential impact by looking at how the first few years differ from previous runs.

We also investigate the impact on the dust storms produced – and test the model's ability to reproduce the true rearrangement of surface dust deposits on Mars, mentioned above – by looking at a specific test case over a restricted time period for which we have good observational data. We choose a simulation of a global dust storm (from one of our finite dust experiments), which is very similar to the 2001 global dust storm that occurred while MGS TES was in orbit. We keep this simulation as our control experiment, and then restart it from a point well before storm onset but with the surface dust distribution adjusted using observed pre-storm albedo maps [Szwast et al. 2005]. We then look for any improvement in the match to observations of the second simulated storm over the first (in terms of atmospheric temperature maps, duration, decay time etc.), and also look at whether the change in surface dust cover due to the storm is more consistent with observations in the second case.

### 4.1.4 The impact of finite dust sources when the stress threshold is varied with the amount of dust available on the surface

In Basu et al. 2005 we showed that inter-annual variability in our modeled dust storms only occurs for a narrow band of threshold wind stresses. This suggests that, if the model is a reasonable representation of actual Mars, the threshold value of wind stress for dust lifting on Mars is also within this narrow band. Pankine and Ingersoll [2002] noted similar behavior in a simple low-order model of Martian dust storms, finding the desired inter-annual variability when the lifting threshold was finely tuned. They later [Pankine and Ingersoll 2004] suggested there is a negative feedback mechanism that causes the threshold wind stress for dust lifting to fall within this 'critical range' required to produce inter-annual variability in dust storm activity. They suggested that when there is a global storm, increased atmosphere activity and stronger winds expose non-erodible particles in source regions. This leads to an increase in the threshold wind stress due to aerodynamic sheltering of the erodible particles. When the threshold is high there are no global storms and the rearrangement of dust by smaller-scale processes such as dust devils enables dust to accumulate once again, thus again lowering the threshold wind stress required here. Hence the conditions again become conducive for a global dust storm to occur.

In reality, when aerodynamic sheltering occurs, we are not so much changing the threshold stress required for lifting dust particles, as changing the surface roughness, and thereby changing how the wind stress at the location of these particles relates to the wind stress at some hypothetical surface with roughness = $z_0$. It is this wind stress (which increases with wind magnitude and $z_0$), which we actually calculate in the GCM. We could therefore have parameterized the amount of aerodynamic sheltering by modeling it as an effective decrease in

$z_0$ (and hence wind stress), but have chosen instead to use a constant value of $z_0$ and increase the threshold stress, as we are already familiar with the model's response to varying this parameter.

We have also chosen to begin by varying the wind stress threshold as a step function (i.e., change it by a set amount when the dust abundance falls below some level), rather than in a smooth way. This produces a sharper, clearer response than would probably occur in reality, but thus enables a simpler analysis of the model's behavior, and is a reasonable simplification to make when exploring this hypothesis at the first order level. Future work will involve extending the idea to smooth variations in wind stress threshold or wind stress itself. At this point we will also use a more complex parameterization of threshold wind stress, such as the wind tunnel derived semi-empirical equations given in White et al. 1979, Lorenz et al 1996 and Newman et al 2002, which allow the threshold to vary with time and location, particle diameter and inter-particle cohesion, even before surface dust cover effects are considered.

In our simulations here we increase the threshold stress by 5% when the dust falls below a certain level. This effectively means that there are now two 'cut-off' points possible due to the use of an exhaustible surface dust supply: one when the dust drops below the level at which the threshold is raised (which prevents further lifting if the local wind stress no longer exceeds the higher threshold), and the other when dust is completely exhausted. We are interested in two things: firstly, whether we do see regions shifting from one threshold value to another (or whether they become 'trapped' at a single value), and secondly, what is the effect of including this behavior on the types of storms which occur and the dust cycle's inter-annual variability.

We also run simulations where we decrease the stress threshold by 5-10% once dust falls below a certain level. It might be possible that due to changes in microclimate the dust at lower depths might be loosely packed and easier to lift. We are interested in changes in the storm behavior with the inclusion of such a parameterization.

## 4.2: Description of Method

### 4.2.1 The Model:

As in our previous work [Basu et al. 2004, 2005] we are using the Geophysical Fluid Dynamics Laboratory general circulation model. The model integrates primitive equations on a discretized grid and includes a significant number of Mars-specific parameterizations. These include a $CO_2$ cycle with prognostic variations in surface pressure and seasonal ice caps [Mischna et al. 2003]; a water cycle, which includes atmospheric transport, simple cloud microphysics, and water ice seasonal caps [Richardson and Wilson, 2002; Richardson et al., 2003]; and radiative heating due to solar and thermal infra-red interactions with dust and $CO_2$ gas [Wilson and Hamilton, 1996].

Dust is transported in the atmosphere by the model-resolved winds and sub-grid scale diffusion, falls under the influence of gravity, and is injected by representing the effect of both dust devils (plus other convective motions) and near-surface wind stress [Basu et al 2004, 2005].

The dust devil lifting parameterization uses the modeled sensible heat flux and convective boundary layer (CBL) depth to predict dust devil activity, and then generates lifting rates by multiplying this value by a rate parameter $R_{DDL}$ (lifting rate=$R_{DDL}$ x sensible heat flux x a function of CBL depth). This formulation comes from a thermodynamic theory of dust devils [Renno et al. 1998] and was used by Newman et al. [2002a,b]. The implementation is described in detail in our previous paper [Basu et al 2004], as is the method of comparing with smoothed T-15 temperatures by which the single parameter $R_{DDL}$ (assumed to be spatially and temporally constant) can be tuned to produce a realistic background dust cycle.

The wind stress lifting parameterization (described in detail in Basu et al. 2004, 2005) uses the surface wind stresses $\tau$ predicted by the model's boundary layer scheme to generate vertical dust fluxes. Monin-Obukhov theory is first used to find surface wind stresses based on the near-surface winds and stabilities. The dust flux is then set equal to a lifting rate parameter $R_{SL} \times \tau^{3/2}$ when $\tau$ exceeds a stress threshold $\tau^t$, and is zero when $\tau$ is below this value [Shao et al 2001], hence this scheme has two tunable parameters, $R_{SL}$ and $\tau^t$.

The surface dust deposits are introduced into the model as two-dimensional surface budgets (one for each particle size used). We currently carry two particle sizes of radii 0.625 and 2.5 microns. The two surface budgets are tracked in a manner analogous to the way the GCM currently tracks the surface budgets of water and $CO_2$ ice in the seasonal caps (i.e. we update at every time step a value of surface dust in $g/cm^2$ for every grid point). Dust is added to the surface in response to fluxes from the lowest atmospheric level predicted by the sedimentation scheme. Dust is removed from the surface so as to provide the injection amounts predicted by lifting schemes. If a surface element is exhausted, dust is not injected into the atmosphere, regardless of the injection rates required by the lifting schemes.

### 4.2.2 Initializing the Finite surface dust distribution

#### 4.2.2.1 Uniform surface dust

The main problem here involves deciding how much dust should be assumed initially at each surface point. Estimates of the actual dust cover on Mars may be made using several approaches. One method is to estimate the amount of dust present in the atmosphere during a planet-wide global dust storm [Newman et al 2002]. This provides a lower limit on the amount of dust present on the surface, but gives no indication of its distribution. Another method uses thermal inertia maps to infer particle size and abundance [Newman et al 2002], but it is necessary to make a correction for the variation of atmospheric properties with elevation [Bridges (1994)]. Bridges found, for example, that height-corrected particle sizes in the Tharsis region were as much as two orders of magnitude larger than the uncorrected values, and were generally particles larger than dust, in contrast to previous interpretations of a thick dust cover

[e.g. Christensen (1986)]. Such work has not been carried out for the entire Martian surface, however. Thus, we chose to start with an initial uniform surface dust cover in the range of 0-6 gm/cm$^2$ which are the two limits for no dust and infinite dust cover on the surface [Richardson and Wilson, 1998].

#### 4.2.2.2 Non-uniform surface dust based on albedo

In section 4.3.3 we initialize the surface dust cover to be spatially variable based on observed albedo patterns. We use albedo maps obtained using Mars Global Surveyor data (Szwast et al. 2005) to decide where (and by how much) to adjust the dust amounts up or down. The method is relatively simple where the higher albedo regions are assigned with higher dust amounts and vice versa. The relative dust amounts are chosen based on the uniform finite dust run results so that we can see the effects of depleting dust sources on relatively short timescales ~ 5-10 years. As a result of this process, the amount of dust varies from 0.1gm/cm$^2$ for low albedos (below 0.11), to 3gm/cm$^2$ for high albedos (above 0.29) for these experiments.

## 4.3: The Experiments

### 4.3.1 The impact of finite dust sources on the seasonal cycle of background dustiness (dust devil lifting only)

We performed a series of experiments, each initialized with globally uniform surface dust, but with a different amount in each case (e.g. 0.0001, 0.001, 6 gm/cm$^2$). For an initial surface dust amount > 0.1gm/cm$^2$ we found no difference between these results and those using an infinite dust supply, because no areas ran out of dust (even during the peak lifting periods) for the duration of these simulations (see the red line in Figure. 1). Using lower initial surface dust amounts we found that the total dust injected fell from year to year, as shown by the drop in brightness temperatures for the blue and green lines in Figure. 1.

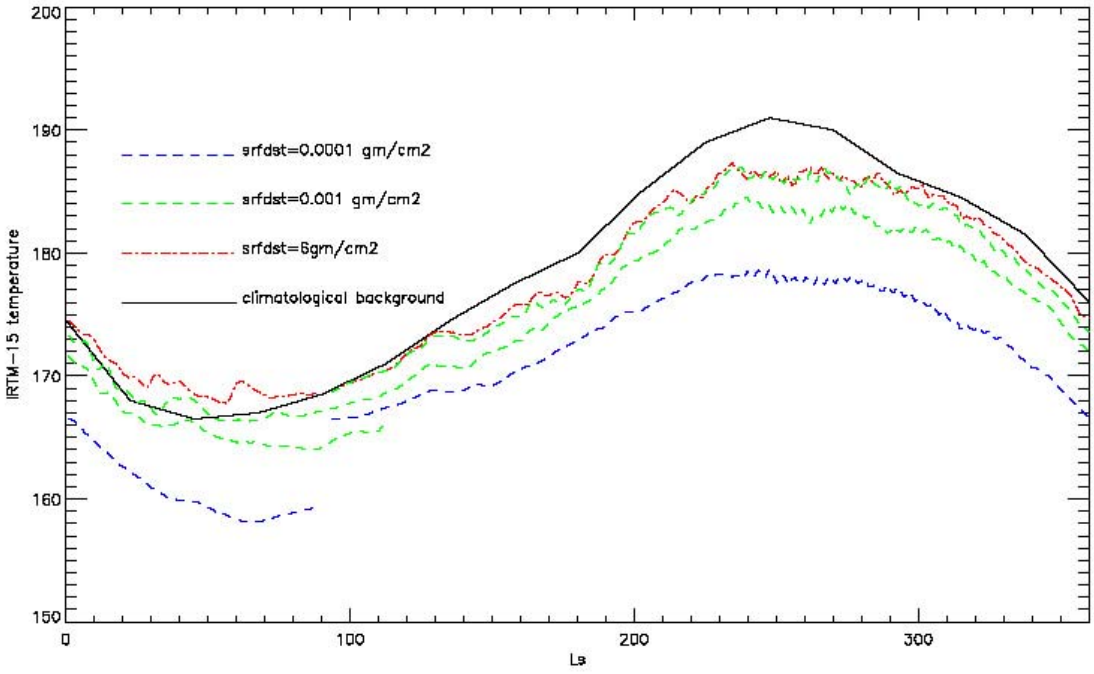


**Figure1.** This plot shows the globally averaged T-15 temperatures for dust devil lifting only. As the dust amount on the surface is reduced it can be seen that the temperature curves converge towards maintaining the same shape. For a specific case with initial surface dust = 0.001 gm/cm$^2$ (green curve), it can be seen that the temperature curves shift lower each year (the blue curve, initialized with an even lower initial dust cover, appears to show the same type of behavior).

The smoothness of the green and blue curves in Figure. 1 is expected due to the widespread, smoothly varying pattern of dust devil lifting. If a lifting process doesn't vary much spatially, we would expect the dust distribution in the atmosphere (and transport between regions) to also be relatively uniform. Thus when finite dust effects are included we would expect there to be a gradual loss from several regions (with no huge impact when each eventually drops out), resulting in a smooth decline in dust opacity. If, however, lifting is confined to a few grid points (with much of the dust transported away to regions with no lifting at any time of year), as is more applicable to wind stress lifting, we would expect a far greater impact due to dust expiring from certain areas (particularly as there are also strong positive feedbacks on dust lifting, which can be very sensitive to details of the atmospheric dust distribution).

To understand why a critical value of surface dust appears necessary, suppose we consider one region and treat it initially as if it were decoupled from all other regions – that is to say, the balance between dust in the atmosphere and on the surface is not affected by transport into or from other regions. We can begin an experiment with zero atmospheric dust – all dust is on the surface – then lift it (allowing vertical transport and diffusion) according to predicted lifting rates using the same rate parameter as in a 'control' run, and let it sediment out using calculated fallout rates. We can imagine a control experiment with infinite surface dust cover, which is identical except for being unaffected by the possibility of the dust supply expiring. At the time of year when the control atmosphere is dustiest, the amount of dust present tells us the maximum amount of dust we would find in the finite dust experiment's atmosphere at the same time of year, provided that dust never runs out completely at the surface. We are considering only two reservoirs, atmosphere and surface, so, in the finite dust run, dust in the atmosphere is dust missing from the surface. Hence we can see that there must be at least this much dust on the surface initially, in order to never see the effects of the dust cover being finite.

If we then include transport between different regions, we have a more complex situation, but the same ideas can be applied. If we again think about finite and infinite (control) dust experiments, and now consider the region which would run out of sufficient surface dust first in the finite dust run, then everything up to this point (including transport into or from neighboring regions) should be identical between the two experiments. (We'll assume that in the absence of transport all regions would have enough dust.) To not see finite dust effects during the first year, we require that the peak dust in this column (at the dustiest time of year) in the control region is exceeded by: the initial surface dust cover, x, minus the net amount of dust transported out of the region up to this point, y. Assuming years are more or less repeatable in terms of lifting and transport, to not see effects during the second year, the peak amount must be exceeded by: initial, x – net out to this time in first year, y – net out in intervening year, z. For the third year, by: x-y-2z. And so on, until eventually the 'y+iz' losses accumulate (we say that the region will be affected at some point, which is equivalent to saying we know transport produces net losses rather than gains here overall) and we fall below the minimum, at which point finite dust effects are seen. Depending on the sizes of x, y and z, this

point may occur during year one or potentially much later, e.g. not for hundreds of years. If the latter case, we would be reaching timescales over which dust production becomes a relevant factor. y and z are determined by the predicted lifting rates and the system itself, so it is only x which we can increase to delay the effect by this amount of time. Hence again there is a critical value of x for each net erosion region, although this time one that varies from region to region. And if x is lower than this but still fairly large, we would not expect to see any effect during the relatively short (<10 years) simulations shown here.

The simple model (ignoring transport) can explain the results for very low initial dust cover – some regions can't produce peak values in year 1, and each year (depending on fallout rates) happens earlier hence overall T curves don't even get as high as previous year, and continuous downward. By considering transport effects, we can also show a slow drop-off in dustiness (hence T-15 temperatures) could be produced in later years even if we start with higher initial dust cover. We might thus expect to see a gradual decline in opacities and temperatures after several tens (or hundreds) of years, as a small then larger number of regions are cleared of dust. In our longest simulation, lasting 30 years, however, we see no evidence of any source regions becoming fully depleted.

### 4.3.2 The effect of finite dust sources on the inter-annual variability and dust storms produced in full simulations (including both lifting mechanisms)

In section 4.3.1 we discussed finite dust effects on dust devil lifting and the background dust opacity and T-15 cycle. The simple models proposed to explain the observed behavior assumed that lifting and transport would vary very little from year to year if surface dust cover effects were ignored, and the smooth decline in dust abundance through each year (for initial dust < critical value) resulted from the smooth variation of dust devil lifting in space and time. Here we look at the effect of including wind stress lifting, which (due to non-linear feedbacks) can vary hugely from year to year, and which tends to be far more concentrated to specific regions.

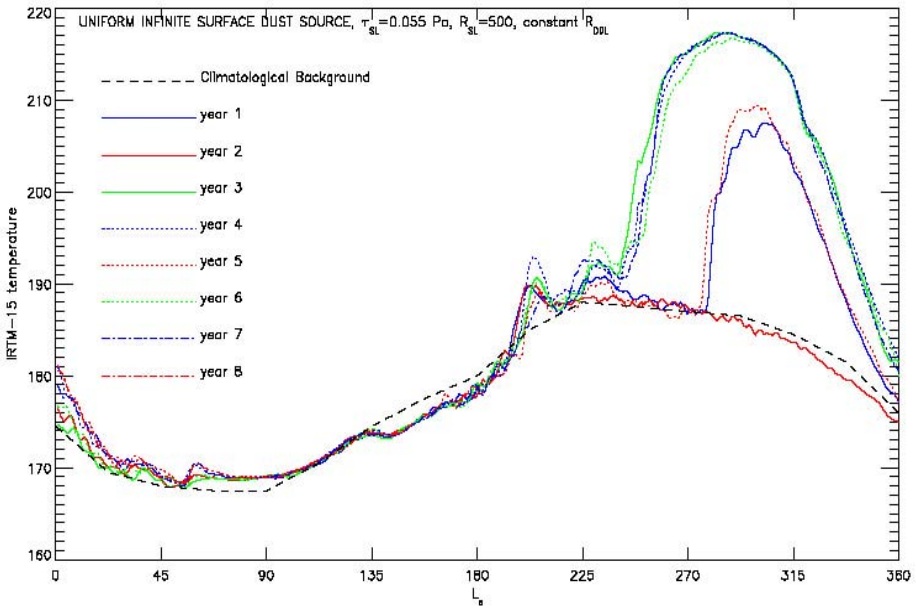


**Figure 1a-** Shows the globally averaged T-15 temperatures for a simulation with infinite, uniform dust supply. This is a good example of the innate variability in the dust-lifting scheme with inter-annual variability in the dust storms and a repeatable temperature cycle in NSS.

These simulations were begun with negligible atmospheric dust and used the lifting parameters $R_{SL}$=500, $\tau_{SL}$= 0.055 Pa and $R_{DDL}$=4.2e-7. As shown in Figure1a (Included here for ease of comparison) a simulation using these parameters and assuming infinite surface dust amounts produces a good match to background temperatures and substantial inter-annual variability, though as discussed earlier all the dust storms produced continue until the end of the storm season, regardless of their start time, in disagreement with observations.

The simple model described in section 4.3.1 can still be applied when wind stress lifting is included. We again expect there to be some minimum surface dust amount required to enable the peak opacities observed, although because wind stress lifting is more spatially variable it is even more important to consider a distribution (i.e. varying with region) of minimum surface

dust amounts, rather than a single value, if trying to do this properly. Varying initial surface dust amounts are considered in section 4.3.3, but in the experiments described here we use a globally uniform value. Again, the minimum values needed are modified when we consider the effects of transport, which are of vastly increased importance now that lifting is far from spatially uniform. However, because transport effects are now capable of rearranging large dust quantities in sub-yearly timescales (particularly during and after large dust storms), there is the potential for the distribution of surface dust in a particular year to be unable to supply enough dust for one sort of storm season (say one with a global storm) yet able to do so two or three years later provided the main source regions can be re-supplied. Given that the exhaustion (and possible re-supply) of regions may be vital to produce the observed storm types and inter-annual variability seen on Mars, there may also be a distribution of maximum surface dust amounts required. Again, this is not fully addressed here, as we are using a single value, but it is considered in section 4.3.3.

#### 4.3.2.1 The effect of initializing with insufficient surface dust [for a simulation of a given duration]

Figure. 2a shows T-15 temperatures for a long simulation for which the initial surface dust cover of 0.1gm/cm$^2$ (distributed uniformly over the entire surface) appears insufficient to enable recovery to occur. The redistribution of dust that takes place during (and following) the global storm in the first year is such as to prevent any further large storms occurring in subsequent years. Clearly the initial amount in those primary wind stress lifting regions which are net sources of dust was only just sufficient to produce a global storm in year 1, and were probably already dropping earlier in the storm season than would have happened for a infinite dust run, explaining the more rapid decay rates than shown in Basu et al. 2004. Figure 2b shows the change in dust cover after the first year (gm/cm$^2$/yr), with yellow and red indicating regions with net deposition and blue and purple indicating net erosion. The areas of strong erosion in the southern hemisphere correspond to the most active lifting locations on the slopes of the Argyre and Hellas impact basins, and in the northern hemisphere to lifting on the eastern slopes of Tharsis (at the northernmost position of the strong western boundary current flow). Regions where net erosion values are shown as solid purple actually exceed the lowest

contour level shown by more than 20 times, which for an initial cover of 0.1gm/cm$^2$ has completely stripped them of dust.

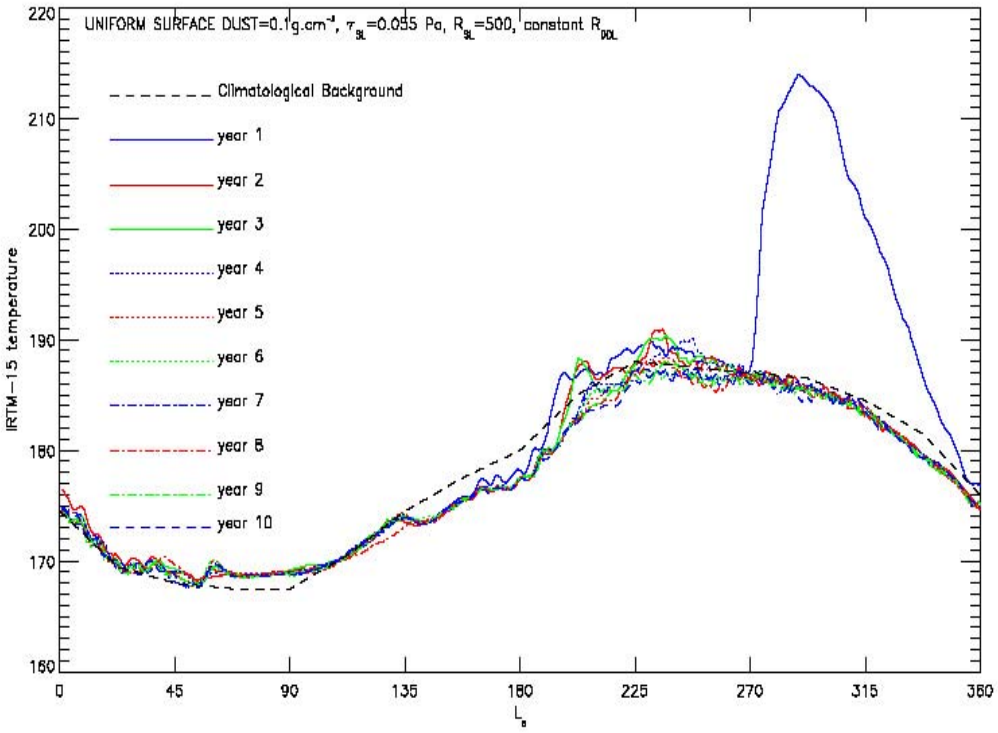


**Figure 2a-** Shows the multiyear simulations from a run that had a finite uniform supply of dust=0.1 gm/cm$^2$ initially. It can be seen that the first year there is a sharp storm and there are no storms in the subsequent years as the lifting centers remain exhausted or not replenished enough for a global storm. Presumably they're being refilled at some rate but it is not enough to start a dust storm in subsequent years.]

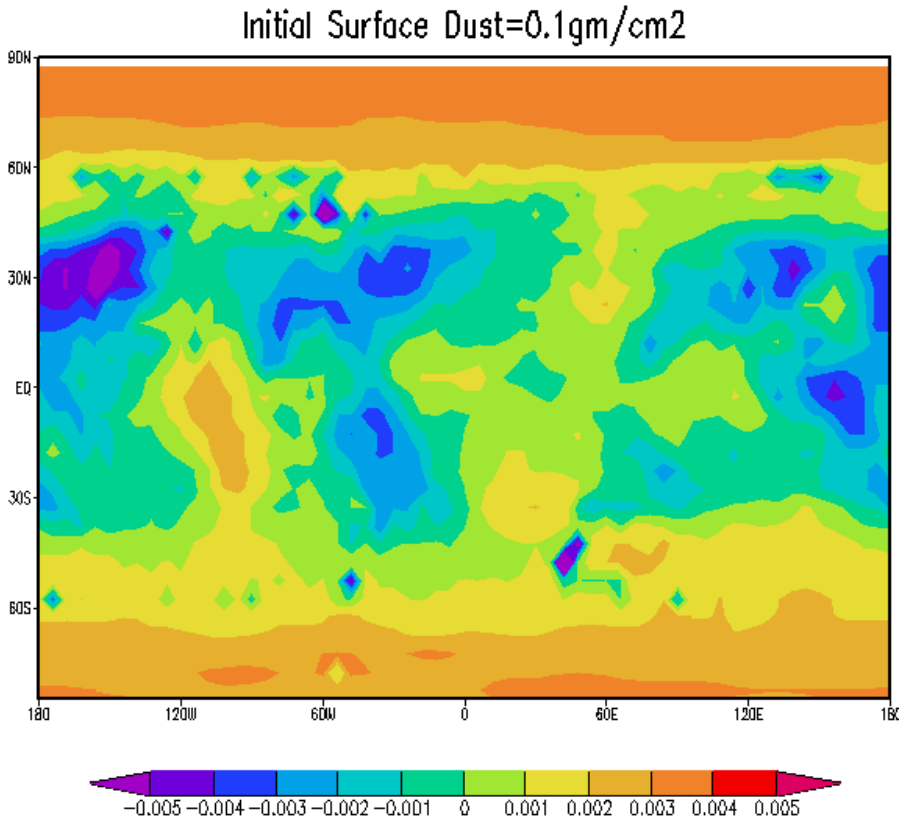


**Figure 2b-** shows the erosion potential (gm/cm$^2$/yr) after the first year of the storm. The violet and blue regions are the lifting centers or sources of dust for the simulation from Figure 2 and the yellow and red regions are net deposition regions. It can be seen that maximum deposition is taking place at the North Pole. The active lifting centers are rims of Hellas and Argyre and the Alba Patera regions. Here negative values signify dust erosion and positive values signify dust deposition.

An intermediate case is shown in Figure. 3, for an initial dust cover of 0.8gm/cm$^2$. Here the source regions for global storms are not completely depleted within the first storm season, and global storms continue for several years (note also the different shape of the T-15 curves early in the storm season, and the difference in peak values reached, suggesting that in the 0.1gm/cm$^2$ simulation the effects of some regions becoming inactive due to lack of dust are felt relatively early on). The plot shows regions of net erosion and accumulation by the end of

year 1. The erosional peaks are lower. Hence lifting continues from these regions for further years.

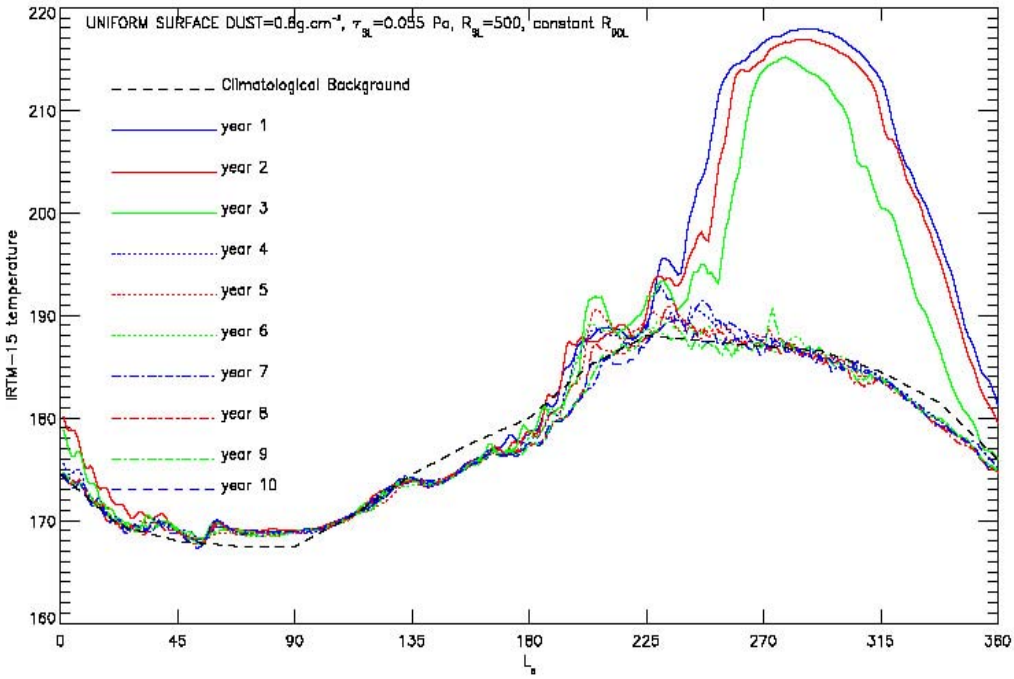


**Figure 3a** shows multiyear plots of globally averaged T-15 temperatures from a simulation that began with an initial surface dust supply of 0.8 gm/cm$^2$ everywhere. The storms rage for the first 3 years after which dust expires at the active lifting centers and there are no storms in the subsequent 6-7 years as the dust devils and dust fall out are not effective in maintaining a replenishing rate that is higher than the erosion rate.

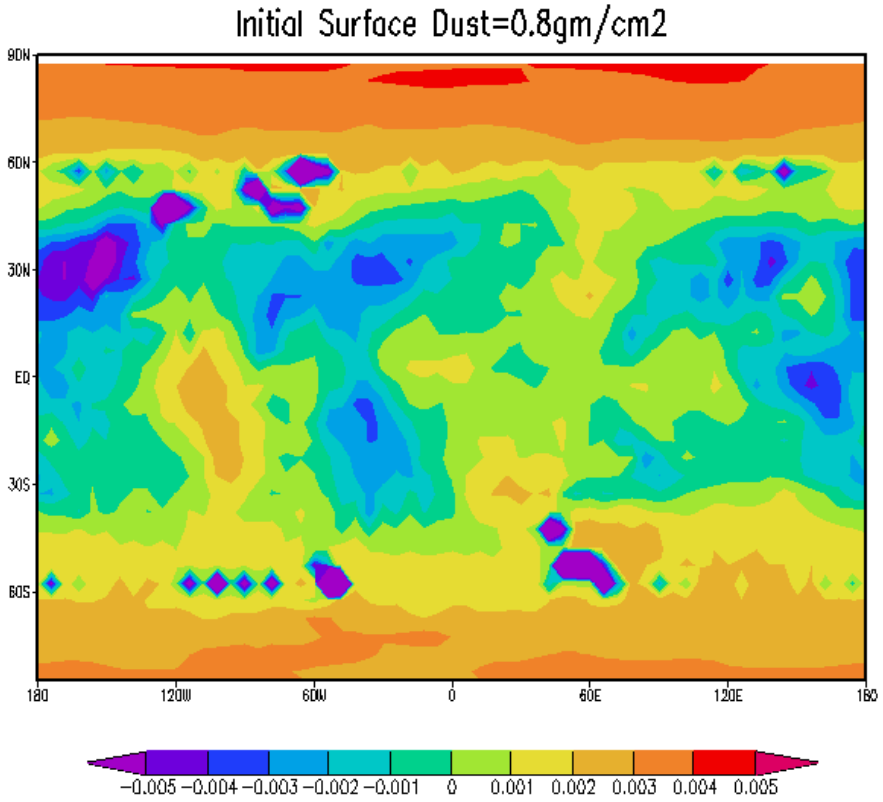


**Figure 3b** shows the erosion potential (gm/cm$^2$/yr) for the simulation in Figure3a. It can be seen that lifting centers around the Hellas region are bigger in size than in Figure 2. This simulation ran out further for 10 years but produced no global dust storms.

#### 4.3.2.2 The effect of initializing with sufficient surface dust [for a simulation of a given duration]

Figure 4 shows results from a simulation with 2.0gm/cm$^2$ of initial dust cover. The left panel T-15 temperatures for a simulation having global storms in years 1-3, no storm in year 5, then a smaller (though still planet-encircling) storm in year 5. The remaining two years have no storms. This amount of variability is comparable to that found by using the same dust lifting parameters but an infinite surface dust supply, hence suggests that we are now initializing with sufficient surface dust cover in the net source regions to prevent dust running out when it is needed. The strong erosion from a band at 60 degrees south latitude was not produced in the

earlier simulations and is due to strong cap edge storms that occur in this case. The previous global storms with insufficient dust supply had been produced despite certain key source regions becoming depleted during the earlier storm seasons, whereas these global storms have lifting from these regions too (e.g. part of Hellas southern slope) producing maximum dust injection and peak circulations, stripping northern slopes of Hellas and around south polar cap edge as well.

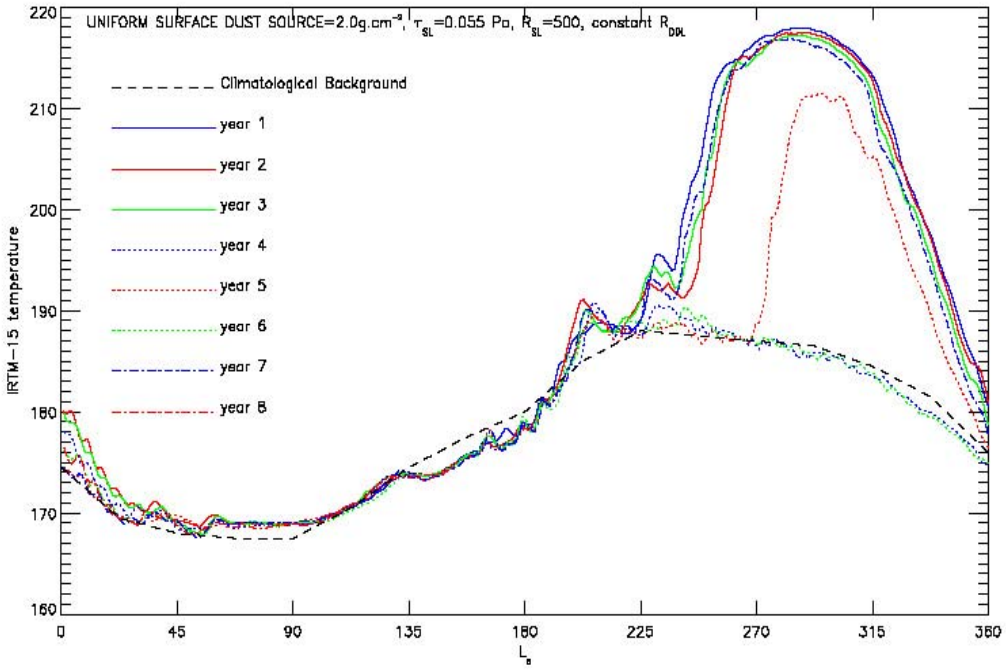


**Figure 4a** shows the multiyear runs for an initial uniform surface dust of 2.0 gm/cm$^2$. It can be seen here that the dust expires and the storms stop after the third year but the active lifting centers are replenished and the storms start back up in the 5$^{th}$ year with a no storm year in between. Show a time series showing that the dust on the surface is gradually getting lower.

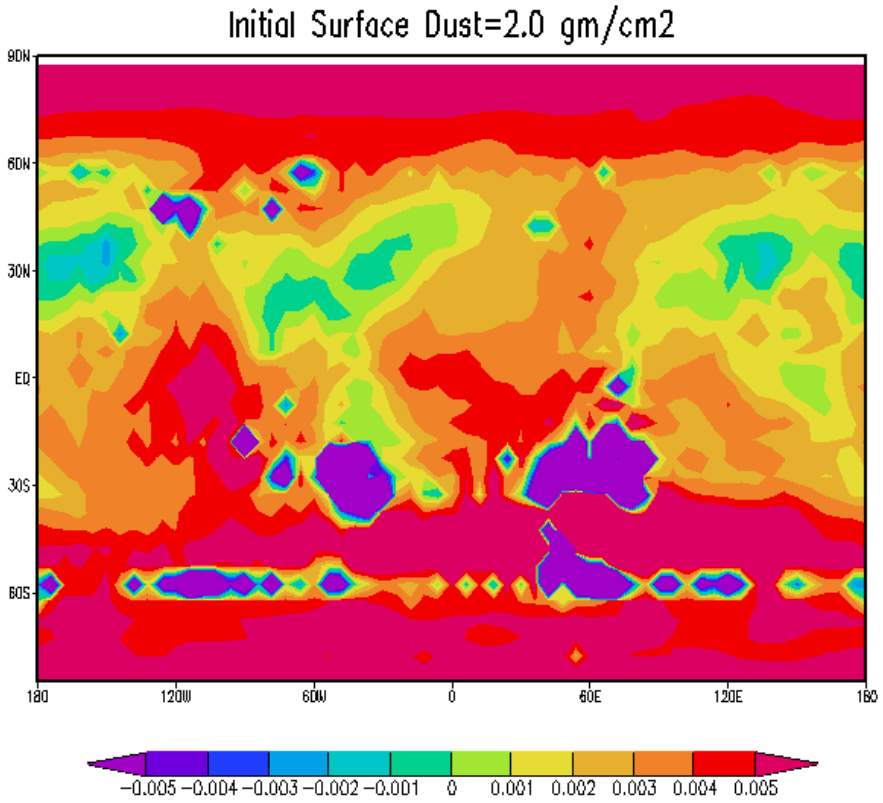


**Figure 4b-** shows the erosion potential (gm/cm$^2$/yr) for the simulation Figure 6. There is a lot of depletion from the active lifting centers. The polar cap edge storms also deplete a fair bit from the southern polar cap edges.

#### 4.3.2.3 A particularly significant simulation

The simulation described now is the first to show the effect of re-supply of primary source regions during the simulation. The left panel of Figure. 5 shows T-15 temperatures for a simulation begun with 3gm/cm$^2$ of dust on the surface. The simulation is important because of two characteristics: (1) it produces storms that decay prior to the end of the storm season, and (2) it demonstrates re-supply of exhausted regions between storm seasons.

Characteristic (1): the simulation produces a global storm in year 1 followed by a large regional storm in year 2, which ends well before the end of the storm season. This is distinctly different from the behavior observed in infinite dust simulations (even with large amounts of variability) in which all large dust storms during the storm season, regardless of their onset time or size, did not decay fully until the end of the storm season (when the seasonal forcing finally diminishes). Such results are shown in Basu et al. 2004. It is thus an indication – one which is confirmed by surface dust amounts at this time in the simulation – that some of the primary source regions have expired during the second storm season, and that this is capable of producing more rapid storm decay than we simulated previously, in line with observations.

Characteristic (2): the early decay of the regional storm in year 2 is due specifically to a lack of available dust in the Hellas region. There is another large (in fact planet-encircling) storm in year 3, however, and then two years with no storms are followed by a global storm in year 6 which is as large as the year 1 event. Without examining the changes in surface dust cover these results alone would not be sufficient to prove re-supply of regions exhausted during year 2 or other no storm years, as the later storms could be due to lifting from other source areas. It seems unlikely, however, that the year 6 storm would be so large [and in terms of its T-15 impact be so similar to the year 1 storm] if all [or the same] source regions were not again active. Figure 6 proves the case by showing plots of surface dust cover [for a grid point in the Hellas region which is an active lifting center] before and after a storm. It can be seen that as soon as the particular grid point is replenished with a certain amount of dust there is global dust storm that depletes the site completely yet again.

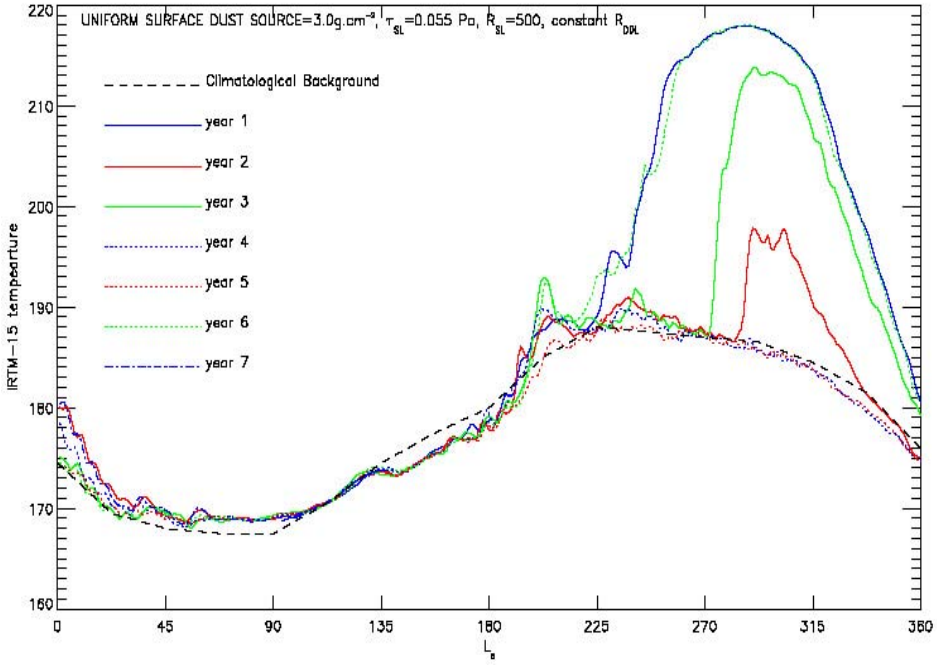


**Figure 5a.** Multiyear globally averaged T-15 temperatures for simulation with initial, uniform dust abundance of 3gm/cm$^2$. It can be seen in year 2 the storm is cut off as the active lifting center is stripped of dust. This plot shows good inter-annual variability with alternating 'global storm' and 'no storm' years. It is seen here that even though the initial surface dust amount if more than simulation in figure 6 yet there is faster dust removal in year 2 resulting in a smaller storm that looks cut off due to dust expiration. This is possibly due to a stronger circulation due to more lifting of greater amounts of available dust from the lifting centers, which removes a higher proportion of dust than in the 2gm/cm$^2$ run.

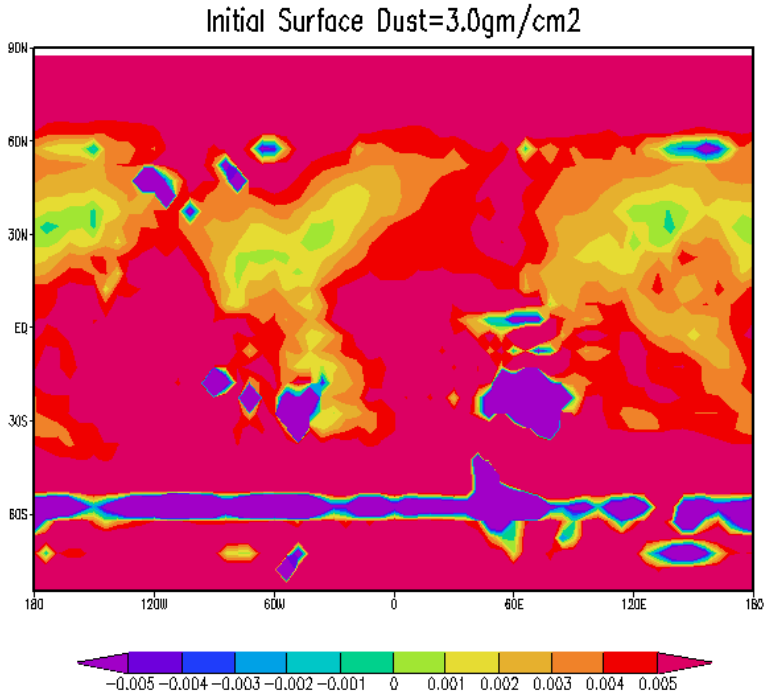


**Figure 5b-** Erosion potential (gm/cm$^2$/yr) for the simulation in Figure 5a.

It may seem confusing that the 2.0gm/cm$^2$ simulation shown in Figure. 4 has huge global storms in years 1-3 without showing noticeable effects of regions being exhausted, but the 3gm/cm$^2$ simulation shown in Figure. 5 has a much smaller storm in year 2 (following a global storm in year 1) and does show exhaustion effects despite a higher initial uniform dust cover. The reason is that there is also intrinsic inter-annual variability at work, which is combining with even subtle differences in surface dust availability to produce different effects. The simulations begin from the same initial state, and by the time the second storm season approaches there are perhaps only a few model grid points that differ due to the different amounts of dust on the surface initially. With all the feedbacks, however, this is apparently enough to suppress any global storm in year 2 of the 3gm/cm$^2$ simulation. Instead there is a smaller storm, which has a highly concentrated source. Added to the effect of transport away from here not being matched by transport in from elsewhere since nowhere else is lifting much, and we can see why the source regions for this storm are exhausted whilst the more

widespread sources for the global storms are not in the 2.0gm/cm$^2$ simulation. This is in fact an excellent demonstration of just how complex and non-linear the Martian system may be.

**Summary of finite dust runs**

We therefore find that an initially uniform dust cover of 1.5-3 gm/cm$^2$ provides enough dust in supply-limited areas such that, accounting for re-supply via transport and fallout, the simulation can run for 7 years without trapping so much dust in permanent sinks that global storms become impossible [not enough dust able to be sent aloft]. As before, after some time will inevitably trap some dust permanently – but again, is this over geologic timescales – e.g. what 'x' is needed on southern Hellas slopes to ensure never runs out there.

In these simulations by taking a uniform value for 'x' globally we may vastly underestimate the amount of dust in basins like Hellas or Argyre, with the dust there having built up during different epochs, in order to see the effect of having finite dust come in to play in other regions where there probably is only a small, easily depleted dust cover.

This has two significant implications with regard to storm variability. One is that inter-annual variability may be increased over that found in infinite dust runs, simply by 'resetting' the surface dust cover each year. The other is that we may be able to find a necessary condition for certain storm types – i.e., along the lines of 'if there isn't this much here, then we can't have a global storm this year'. This would allow us to predict that a global storm, say, should not be able to occur in the current year's storm season [or possibly beyond], which would be incredibly useful for mission design, etc.

When the finite dust sources are introduced in the system there is added variability apart from the weather noise. This arises from the fact that the active lifting centers now have a finite supply of dust, which may be partially or entirely depleted when there is a global dust storm. This may result in no global storms in one or more subsequent years, as time is required for them to be replenished (by dust devils and dust fallout from the atmosphere) with sufficient

dust to once again allow a global storm to develop. Thus the finite supply of dust gives added variability to the system.

In the simulations with an infinite supply of dust (Basu et al 2005), we saw that the storms that start later in the season ~Ls=270, are much bigger than the storms observed on Mars and have a purely seasonal decay i.e., decay only when the summer circulation, linked to seasonal solar forcing, diminishes sufficiently. In the case of infinite dust supply, the active lifting centers continue to inject dust into the atmosphere even after the peak opacities have been reached. This results in slower decay rates than is seen in the observations [Richardson and Wilson 2002, Liu et al. 2003].

Reducing the initial surface dust supply to 0.1gm/cm$^2$ (Figure 2) produces a global storm in the first year that has a much sharper peak, as observed [observations, TES, Viking]. The storm decays at a faster rate than in the infinite dust source simulations, as there is no further lifting after the dust supply is exhausted at the active lifting centers, and may represent what actually occurs on Mars. This simulation produces no further global storms in the 8 subsequent years of the simulation, however. This is because the required source regions are not replenished sufficiently - by the fallout of dust lifted by dust devil and smaller wind stress lifting events - within this amount of time. It is possible that after several more years dust may have accumulated sufficiently to produce another global storm, but even if this were to happen we know that on real Mars such events occur far more frequently (on average every 3 years [Cantor et al 2002]).

Thus while global storms can be produced if the source regions have 0.1g/cm$^2$ of dust at the surface, the rearrangement of dust during just one global storm event is enough to reduce the available dust in these regions to lower values and the amounts available at the various wind stress and dust devil lifting sites is not enough, when raised into the atmosphere, to provide sufficient fallout for the main source regions to be replenished above the levels required for global storms to occur.

When the surface dust is increased to 0.8gm/cm$^2$ there are big storms the first three years. The peak temperatures are higher than in the 0.1gm/cm$^2$ case, as expected. It can be seen that in the third year the storm has a sharper peak than in the previous two years. (Figure 4) This indicates that the dust supply has expired at the active lifting centers and there is no lifting once the peak opacities have been reached. The following year there is no storm, and there are no storms for the subsequent 10-15 years that the simulation was run out for.

This indicates that 0.8gm/cm$^2$ of uniform surface dust cover is still not enough for lifting rates (in non-global storm years) to provide enough atmospheric dust (hence fallout) such that the global storm source regions are sufficiently replenished for another global storm to occur. It might be possible that the main source regions for infinite dust are not the main ones for real Mars and the replenished regions are not able start up a global storm due to lack of high stresses. This would require a careful investigation with higher resolution model where secondary components of the circulation are captured. The lifting rates in the replenished regions were increased in this simulation so that it would be relatively easier to lift dust from these regions. However once the main lifting centers were depleted no new global started up anywhere else.

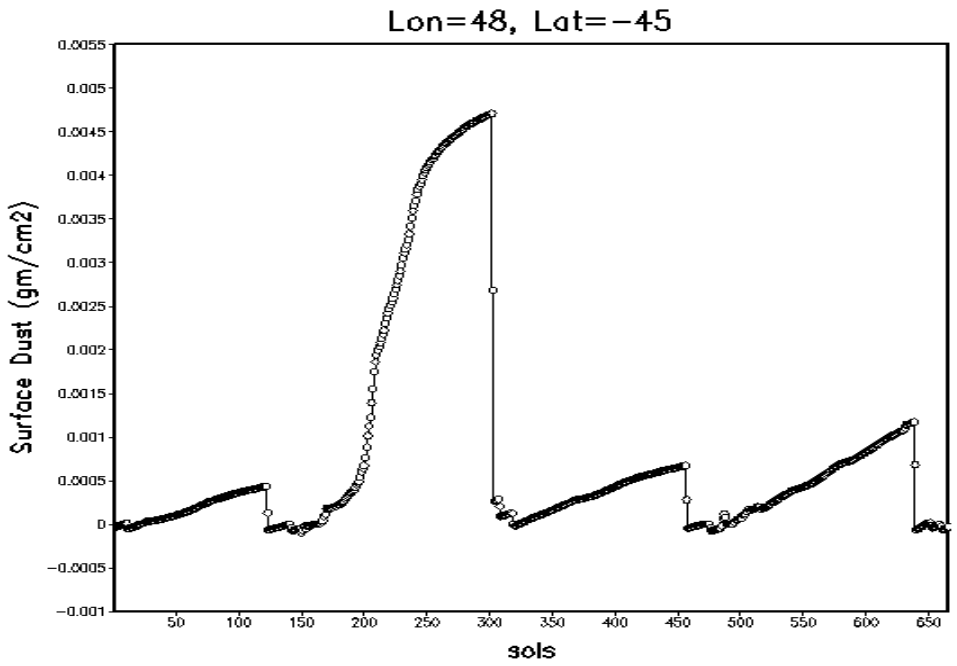


**Figure6:** shows the surface dust cover as a function of season for the specific grid point, which is a primary lifting center. This simulation was initially started with a dust cover of 2.0 gm/cm$^2$. It can be seen that once the completely depleted site (dust amount=0) is replenished, there is a big global storm, which again strips off the dust completely.

Experiments conducted with gradually increased surface dust established that, when the initial surface dust amount was greater than ~1.5 gm/cm$^2$, the rate of replenishing active lifting centers was fast enough for global storms to resume within a couple of years of the centers becoming exhausted following a global storm (Figure 6). This simulation was run out for ~30 years to see if it reached some sort of equilibrium on geologic timescales. It was found that unlike the 0.8gm/cm$^2$ initial dust case, in this simulation the active lifting centers were replenished after the big storms.

The dust amount goes down to 0 after a huge storm at some of these centers and it is replenished soon after (less than a year) by dust devils and dust fall out. However the next global storm does not start immediately after the replenishment – the intrinsic variability factor comes into play and even with the same amount of dust at the surface some years have global storms and some other years don't. Hence no dust at the active lifting centers results in no

global dust storms, however once these sites are replenished the development of a storm depends on the intrinsic variability of the system and is finely tuned [Basu et al. 2005]. Also the local circulation in the Hellas region reorganizes the dust in a way that net sink regions become source regions for some storms and vice versa (Figure 8 and Figure 10). Thus even after the main source grid points (e.g. Figure 6 and Figure 9) have been depleted, a global storm might start up as dust gets stripped off from neighboring grid points that were sink regions before. So the coupling of intrinsic variability, surface dust depletion and the re-distribution of dust around the rims of Hellas makes it a highly non-linear system where it is difficult to pinpoint a particular storm in a year as attributed to intrinsic variability or depletion/replenishment of particular grid points in the primary lifting regions. It can however be ascertained from our control run (with infinite dust) and Figure 4,6,9 that finite surface dust does introduce more variability in the system as the number of intermittent no storm years between global storms is much higher in the finite surface dust case.

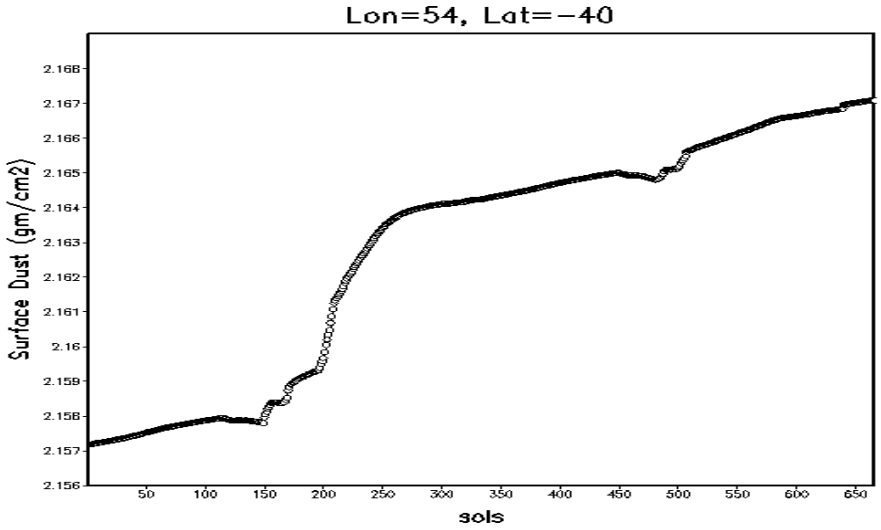

**Figure 7:** Shows an example from a simulation with initial dust cover of 2gm/cm$^2$. This particular grid point is a sink region as can be seen and is accumulating more and more dust with time.

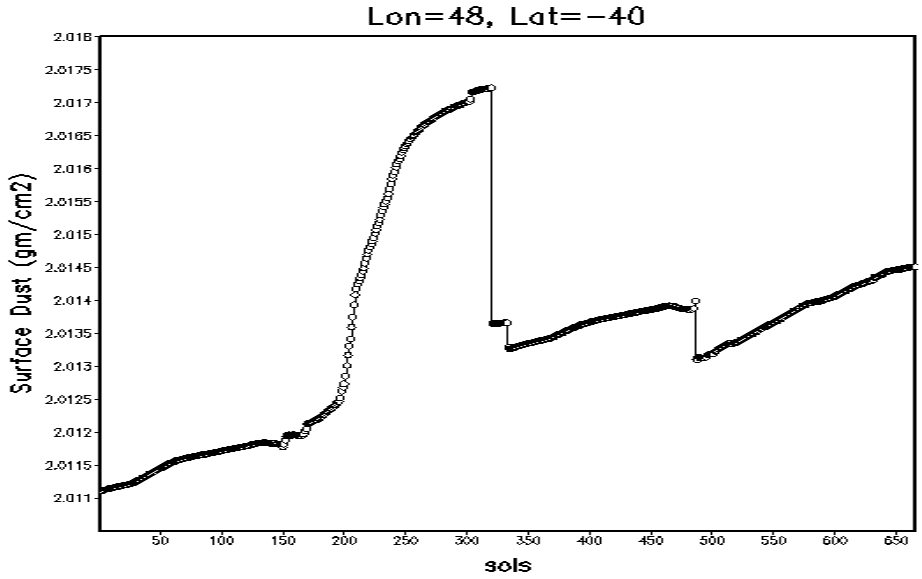


**Figure 8:** Shows an example from a simulation with initial dust cover of 2gm/cm$^2$. This particular grid point, which is a net sink region at the end of 15 years, becomes a source region (huge dip in dust amount during the storm) for the global storm.

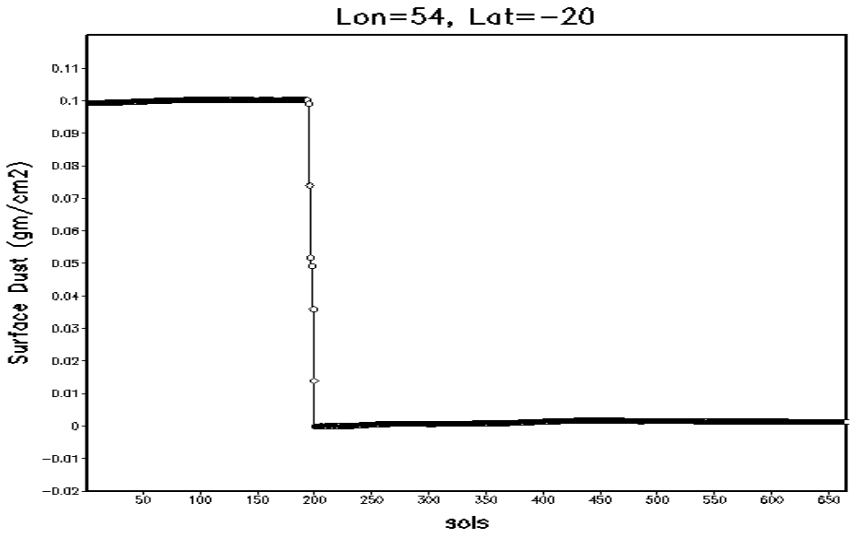


**Figure9:** Shows a grid point from the 2.0 gm/cm$^2$ uniform, initial dust simulation. This particular grid point is a source region where dust is completely depleted from a value of 0.1gm/cm$^2$ at the beginning of the storm.

For these simulations, the global storms are big when there is adequate supply of dust. As the lifting centers are stripped off of dust, the storms die out. Similar is the case

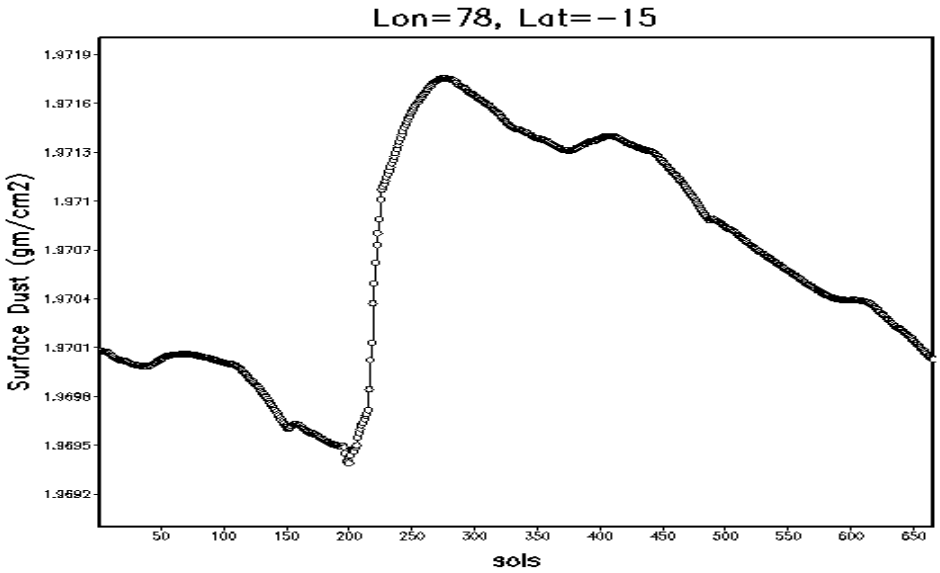


**Figure 10:** This shows the dust amount at a particular grid point varying with season. The initial uniform dust amount for this simulation was 2gm/cm$^2$. In this example we can see that a regular source region is actually becoming a sink region for this particular global storm.

When the surface dust amount is increased to 2gm/cm$^2$- there is greater inter-annual variability than the case with a similar lifting scheme but infinite amount of dust source.

In this case the dust devil lifting and the dust fall out balance out the dust removal from the active lifting sites in a couple of years so that the storms start up on their own. There are a greater number of no storm years in the limited surface case than in the infinite surface dust case. This suggests that there is additional variability due to the redistribution of finite dust sources. The dust distribution on the surface, in this case, acts as a long time memory element and induces greater inter-annual variability. The net depletion and erosion sites for the 2.0gm/cm2 uniform initial surface amount are shown in Figure4b. The figure indicates that there is net dust transport towards the polar-regions, and net deposition in regions including the floor of Hellas, areas surrounding the Tharsis peaks, with lesser increases in surface dust around Elysium Mons and in the Arabia region. These results are consistent with observations which indicate net transport from the southern to the northern hemisphere, and suggest net deposition in Tharsis, Arabia and Elysium regions, (Christensen 1986, Ruff and Christensen),

although work is ongoing to repeat these analyses of the surface particle size distribution using improved models and data, e.g. Bridges (1994). Figure (4b) also indicates that regions of net erosion include the slopes of Hellas, Argyre, Alba Patera and Elysium Mons. Other regions of net erosion are the Chryse region, Syrtis Major, Amazonis and Arcadia regions. These lie within strong Western boundary current flows along the eastern flanks of topography [Joshi et al] Where net deposition is enhanced in close proximity to erosion (e.g respectively the floor and slopes of Hellas) this indicates that not all of the dust lifted in the area of net erosion is lifted into the main circulation, but rather that some is almost immediately re-deposited close to its point of injection.

The dust lifting mechanism in our model can strip off up to 3gm/cm$^2$ (Figure 5) of initial dust supply in a couple of years. It can be seen from the figure that in the second year the storm is cut off due to unavailability of dust at the critical lifting regions. If the initial dust supply is considerably more than 3gm/cm$^2$, it was equivalent to having an infinite supply of dust on the surface. There were big storms and the lifting centers were never fully depleted.

In most of these cases of limited uniform surface dust, the storms are similar in behavior to the infinite surface dust simulations. This is because the stress threshold criterion is uniform throughout the planet and as such new centers of lifting are not activated when the primary centers are depleted of dust. The stress criterion sets the threshold conditions to be still high enough for inactivity at other centers where there is enough dust. Surely even with no variation in threshold, there will still be variations in (wind stress – threshold), and therefore secondary regions which one might expect to become more important and then less important as dust is exhausted there too, with eventually the dominant regions being those where there is an optimum balance between 1) proximity of local winds to the threshold and 2) replenishment efficiency. We don't see this in our experiments possibly because our dominant lifting regions are also quite efficiently replenished though, and/or dominate secondary regions (in terms of being near threshold) so completely that the secondary ones never show up. There might be some shift near the edge of such regions but it does not show in the large-scale dust storm behavior.

### 4.3.3 The impact of using non-uniform initial finite dust distributions based on observed albedo pattern

Thermal inertia is high in regions with low dust amounts and is low in regions where a lot of dust is present (e.g. Jakosky et al., 2000). It is used to assess current dust distribution by many research groups, e.g. Newman et al. (2005) use maps of thermal inertia derived from MGS TES spectra (Mellon et al. 2000 and Ruff and Christensen (2002). However small changes in dust do not change the thermal inertia noticeably (Szwast et al 2005) and hence it is not suitable for analyzing dust deposition and erosion on shorter timescales when lower amounts of dust are involved. Thermal inertia is more useful in identifying longer-term accumulation or thicker dust deposits (Newman et al 2005). Based on the most recent thermal inertia maps, there is a large section of high dust content over Arabia (~10W-60E, 10S-40N), and another broad region of high dust content stretching from Elysium through Amazonis and over Tharsis (~140-180E and 180-70W), covering most latitudes from 15S-40N). If the observed regions of high dust content formed recently and if local dust production (via erosion) is ignored, then such regions should coincide with MGCM predictions of peak dust accumulation for the current obliquity. If, however the observed regions formed over much longer timescales or were mostly formed at a time when higher obliquities dominated, then our simulations with current obliquity might not be able to simulate the dust distributions close to the thermal inertia maps [Newman et al. 2005].

Figure 11a compares the dust distribution (after 20 years ) of a simulation that began with a uniform, infinite cover of dust everywhere on the plane with the thermal inertia maps from TES data. Detailed descriptions of these runs can be found in [Basu et al 2004, 2005]. As discussed before, thermal inertia maps are representative of dust distribution over a longer timescale (20 years) that we are interested in instead of the shorter re-distribution of dust due to local, regional and global storms that are better compared to the albedo maps as we have done in section (4.3.3)

**Comparisons of dust distributions after a number of years for the simulations starting from a uniform dust distribution**

**uniform, infinite surface dust cover case:** On investigating the change in the surface dust cover after 20 years of simulations (Figure 11a) it can be seen the dust distributions agree with the thermal inertia maps from the 2001 TES year in some regions and in some other regions they don't. In the northern hemisphere there are alternate regions of high and low amount of dust. The high thermal inertia regions correspond to low dust amounts and vice versa (Claire 2005, Christensen 2001, Szwast 2005). The Arcadia and Alba Patera regions, Arabia region and the Cerberus regions have higher amounts of dust compared to the Acidalia-Chryse region and the Utopia region.

We see a similar pattern in our simulations (Figure 11a), however the Arcadia region is depleted in our simulations contrary to the observations where it shows up as relatively more abundant with dust. Starting from a uniform dust distribution, this pattern starts establishing itself a couple of years into the simulation, and later years just enhance the contrast between the high and low dust abundant regions, apart from the minor redistributions due to storms. The regions of low dust amount correspond to the lowland channels of eddy velocities [Basu et al . 2005].

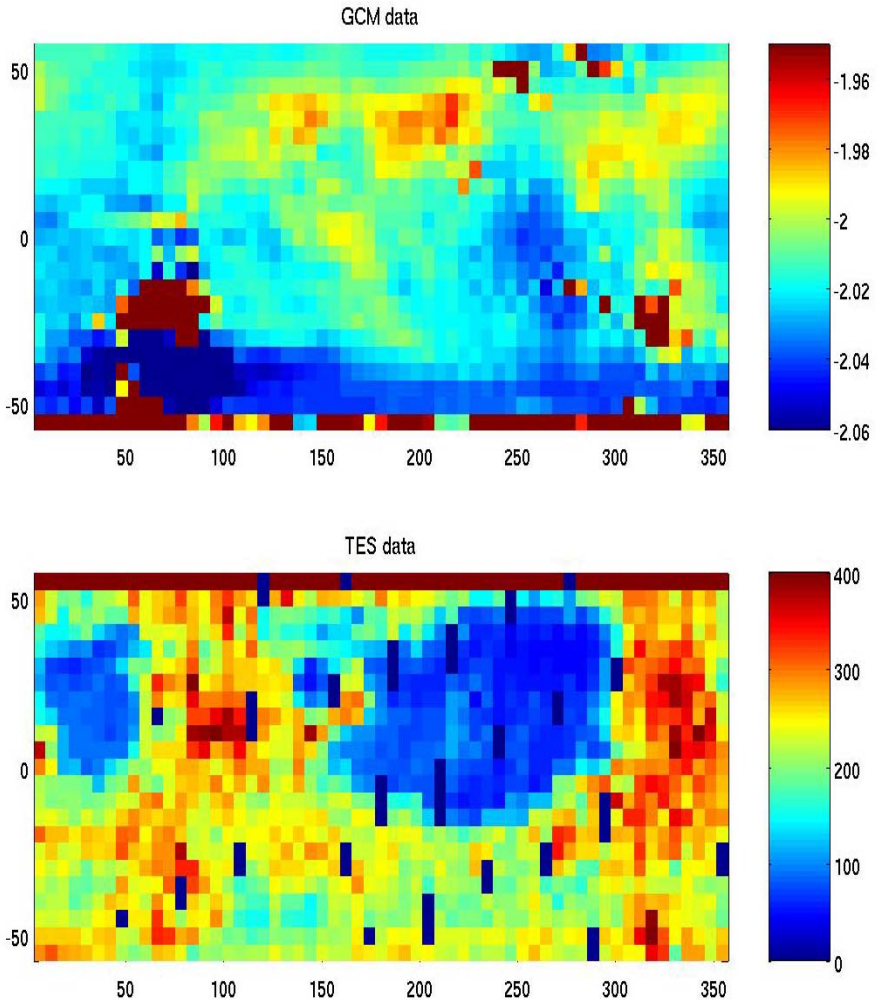


**Figure 11a: Comparison of spatial maps (Latitude vs Longitude) of GCM dust distributions (infinite, uniform dust supply) after 20 years vs. TES thermal inertia maps.**

In the southern hemisphere the southern rims of the Hellas and Argyre basin have relatively high thermal inertia or low dust deposits compared to the rest of the region. This agrees with our simulations, where the Hellas and Argyre northern and southern rims are the major sources of dust and are heavily depleted. However, the contrast between these lifting regions and the nearby areas is much greater than that observed. This shows that the Hellas and Argyre regions are getting replenished by some component of the circulation system may be other secondary lifting centers that our model fails to capture in the simulations. We concluded similar results from the albedo comparisons (sec 3.3). Figure 11b shows a similar comparison

for a case where the initial dust distribution was a function of the TES abedo. It can be seen from the figure that even after 5 years of the simulation there is good agreement in the thermal inertia maps/dust distribution maps as thermal. This says that despite the global storms, the large-scale dust distribution is similar to what it was in the beginning of the simulation.

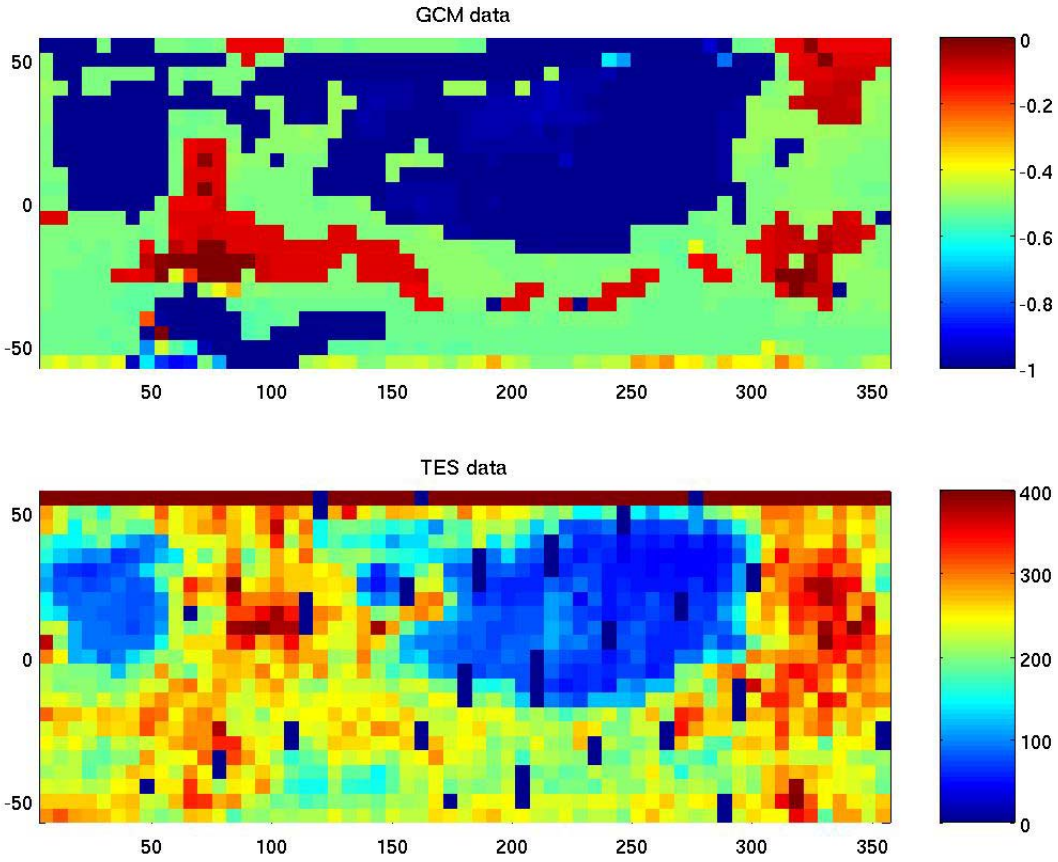


**Figure 11b:** Spatial maps (latitude vs longitude) of the dust distribution (after 5 years) vs. thermal inertia (TES) comparison for a simulation with initial prescribed dust distribution dependent on TES albedo

**Initializing dust distributions according to TES albedo maps and comparisons with observations**

However the albedo maps are better gauges of surface dust coverage over shorter timescales. [Szwast et al. 2005]. Ruff and Christensen (2001) developed the idea of the 'Dust Cover Index' (DCI) that takes advantage of a transparency feature associated with silicates of particle radii less than 100 microns, located at an area of the spectrum that does not show string aerosol/atmospheric effects as long as the surface emission temperature is higher than that of the atmosphere. The independent DCI and albedo measurements from the MGS mapping-orbit mission [Christensen 2001 and Szwast 2005] agree to a remarkable degree and suggest that both are providing a direct measure of the surface dust coverage. Due to much greater volume of the albedo data, we choose to use these to study and compare dust distributions.

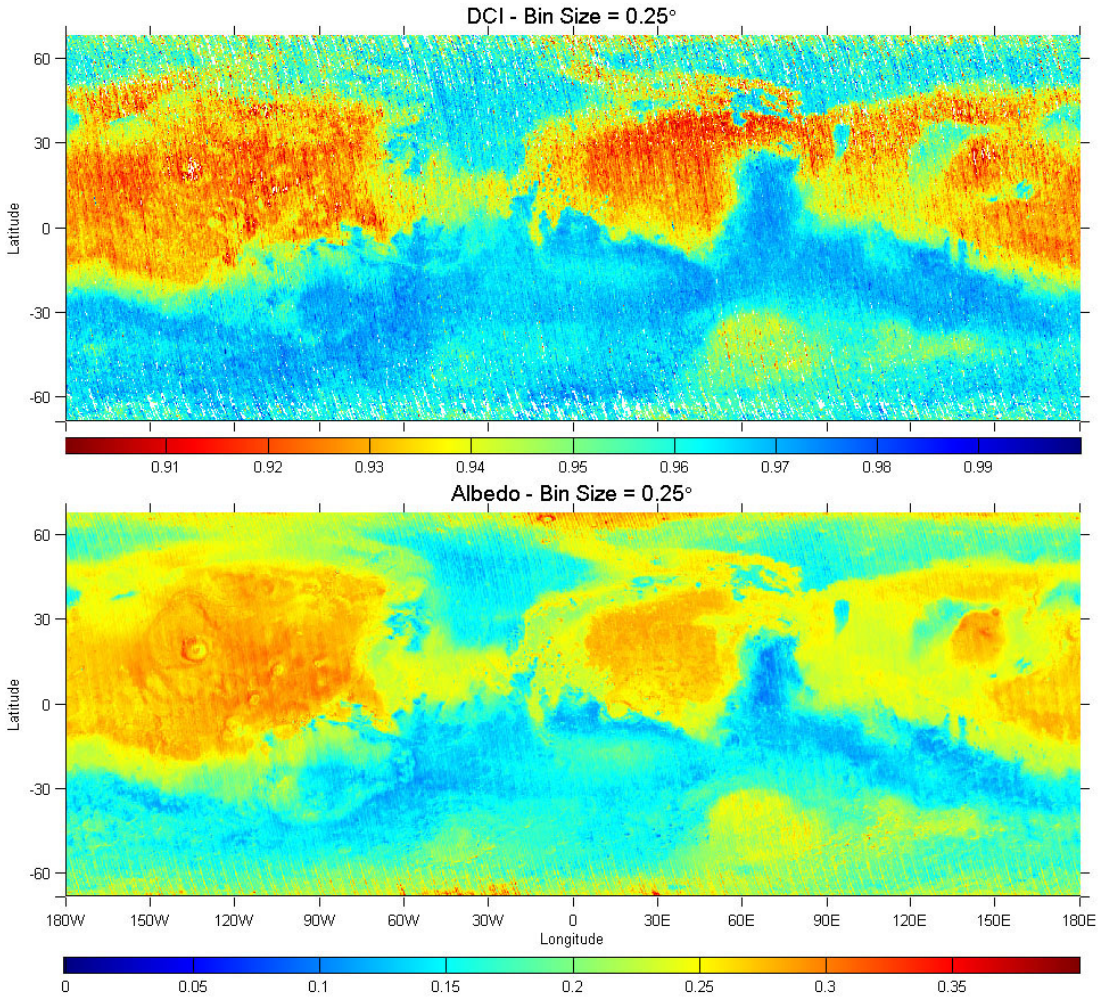

**Figure 11** Comparison of the dust cover index with the Albedo maps (Szwast et al. 2005)

So far in our simulations we have assumed that there is uniform distribution of dust on Mars. This however is not true as can be seen from the albedo maps and thermal inertia measurements. There are no strong observations to suggest the precise amounts of dust at the high albedo regions vs. the low albedo regions [ref]. The clouds and the surface ice also affect the albedo especially at the Polar Regions [Wilson et al. 2004]. The contribution of such unknown weather components and the uncertainty in the relative amounts of dust in the high albedo vs. low albedo region, prevented us from beginning with an initial surface dust distribution identical to that on Mars itself – this is simply not known at the present time. Instead we based the initial amount of surface dust on the TES albedo map (Richardson and Wilson, 2002) varying it from 0.1gm/cm$^2$ for the lowest albedo regions [below 0.11] to 3gm/cm$^2$ for the highest albedo regions [above 0.29]. The simulations were started from the northern summer season when the dust activity in the atmosphere is minimal.

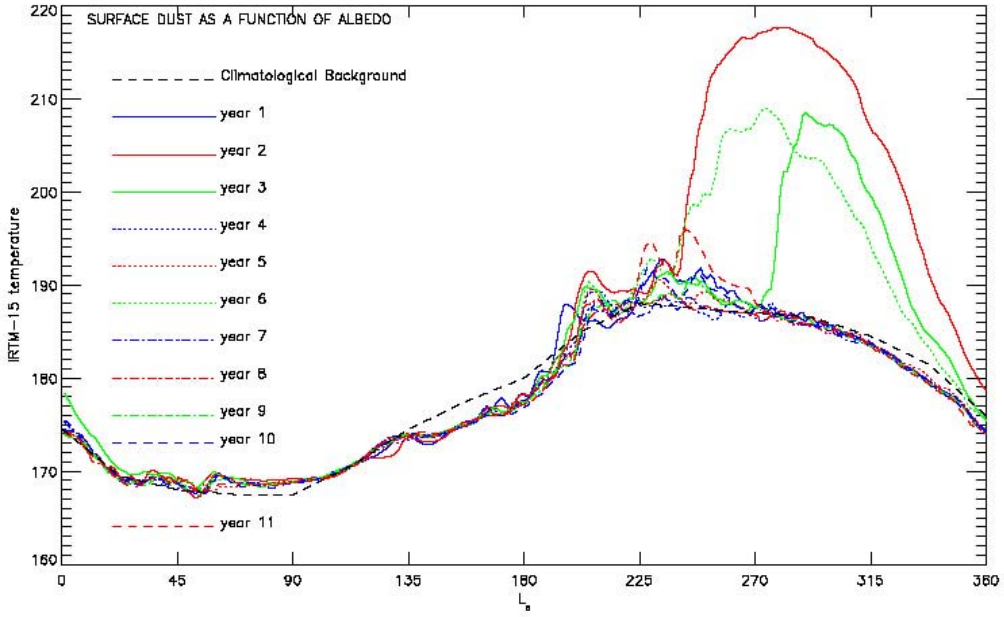


**Figure 12a** Globally averaged T-15 temperatures from a multiyear run for dust distribution dependent on albedo maps. High albedo corresponded to high dust regions and low albedo corresponded to the low dust region. Note the cross over storms and the inter-annual variability in the global dust storms simulated.

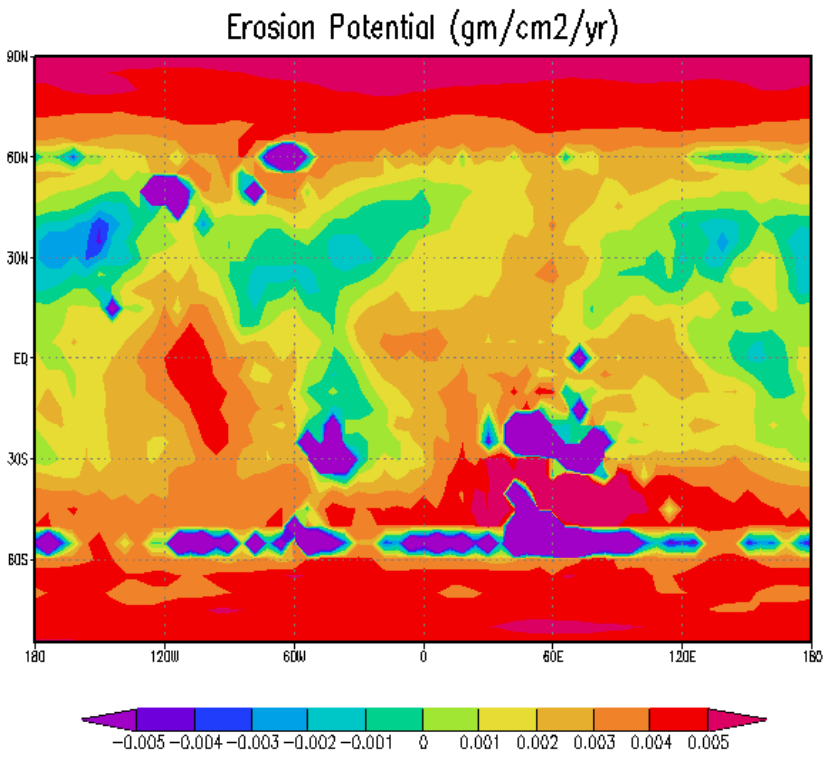


**Figure 12b** Erosion potential for same case.

This parameterization introduced added variability into the global storm behavior as can be seen from figure 12a. This scheme introduces added variability to the system compared to the case of uniform dust distribution everywhere on the planet (Figure 2,4,6,8). In this case even though the winds at some locations are strong enough to lift dust but the dust amount available is not enough to start a feedback mechanism for a strong storm. Thus it biases certain regions as the preferred lifting centers over others just because of the relative abundance of dust. After a number of years, the distribution is also determined by the model's rearrangement of dust in addition to the initial albedo based distribution.

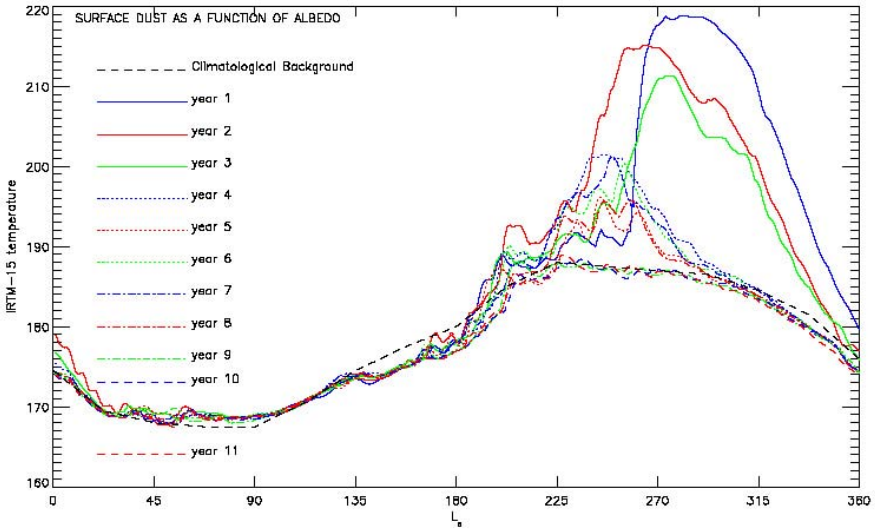


**Figure 13a**

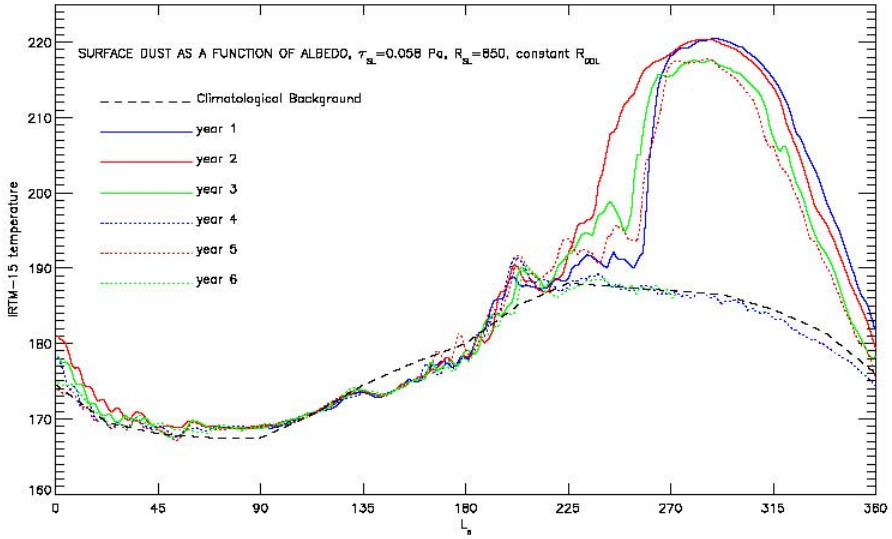


**Figure 13b**

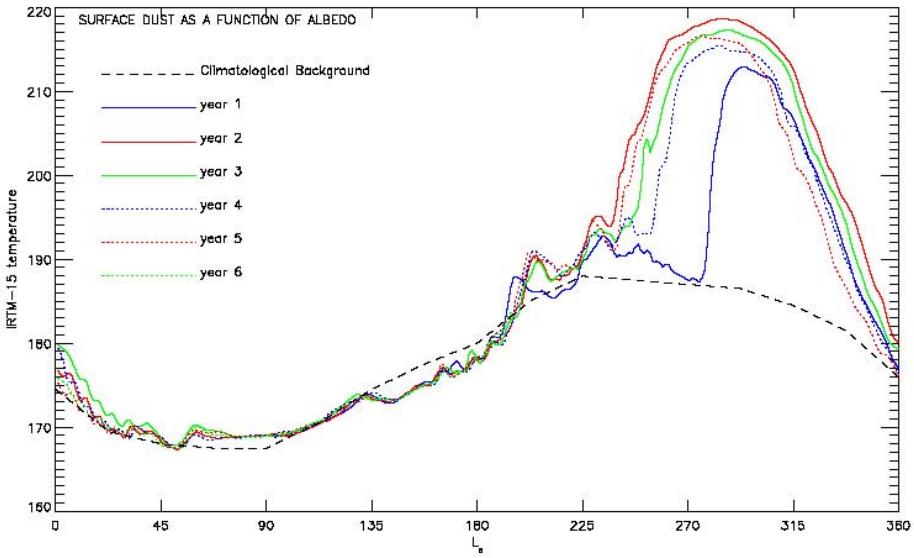


**Figure 13c**

**Figure 13**: Figure 13a is similar to Figure 12a simulation but the stress threshold is lower that gives rise to bigger storms, as there is more widespread lifting. Figure 13b is same as Figure 12a but the surface dust amounts are higher, hence the storms are bigger. Figure 13c- same as Figure 13a but surface dust amounts are higher and hence the storms are bigger.

Figure 13b shows a multiyear simulation from a run where the wind stress threshold was set at 0.058 Pa. The initial amount of dust on the surface was dependent on the albedo map. It varied from 0.1gm/cm$^2$ for the lowest albedo regions to 3gm/cm$^2$ for the highest albedo regions. It can be seen that the variability in terms of start times and intensity of the storms is greater than the simulation in Figure 4a where the finite dust on the surface is uniform all over the planet. There is crossing over of storms and they are not nested as in the uniform surface dust case. Thus the unequal distribution of dust dependent on surface albedo incorporates added variability to our storm system.

We see similar behavior for a set of simulations that had a lower wind stress threshold of 0.055 Pa (Figure 13c). The active lifting centers in both these cases are Hellas and Argyre. Since the stress threshold does not change with the albedo- there is not much variation in the storm behavior compared to the uniform dust supply case [Figure 4b]. However the variability arises from uneven distribution of dust, this changes the circulation thus giving rise to different growth rates of storms as can be seen from the globally averages T-15 temperatures [Figure 12, 13a, b, c].

In terms of the primary and secondary lifting centers there is much less variability than the changing stress threshold condition with dust depletion (see section 4.3.4).

Figure 12 and 13a,b,c simulations show a good variability in the multiyear simulations of storms. In all of these cases the range of surface dust supply dependent on albedo was different and the stress threshold was also different. There are a good number of cross over storms in terms of the initiation times of the global storms in these simulations.

**Starting with a dust distribution that is a function of TES albedo at Ls=170 just before the 2001 global storm.**

To see how the circulation systems on actual Mars are similar or different to our simulations, we started with an initial dust cover that was dependent on the TES albedo at $L_S$=170 just before the start of the 2001 global Mars dust storm [Smith et al 2005]. A global storm also occurred in our simulation. A comparison of the after storm scenarios in both cases would

give us a better understanding of the circulation system on Mars.

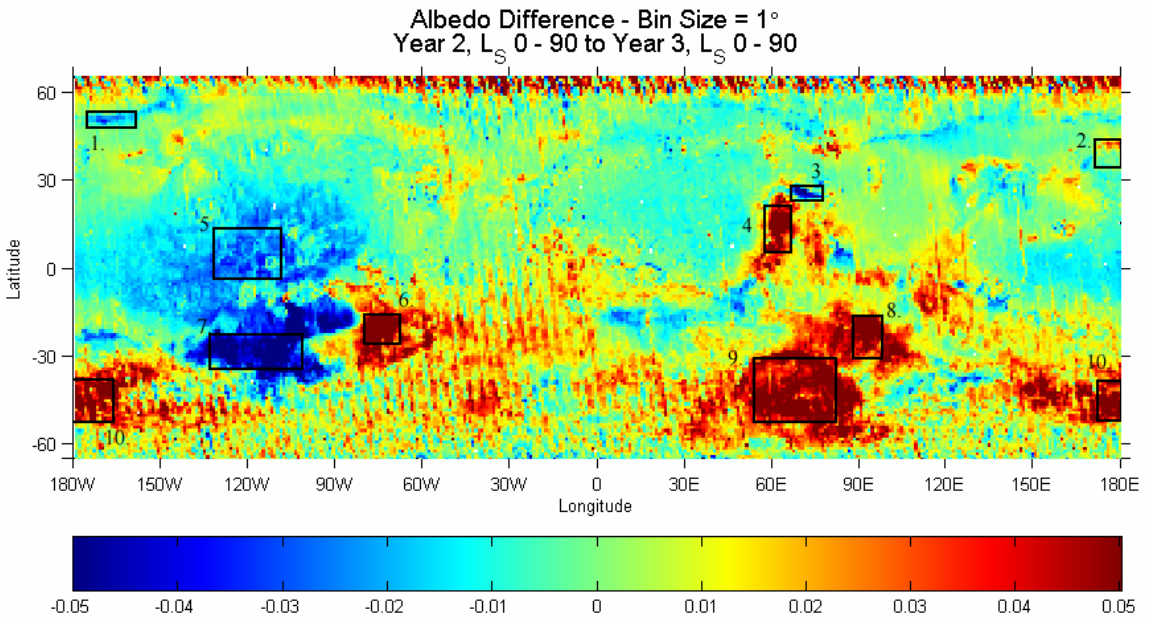


**Figure 14** – Szwast et al 2005 shows the changes in Albedo before and after the 2001 storm

The maps of change in the surface albedo (Szwast et al 2005) [Figure 14] show that after the occurrence of the 2001 global storms there were some changes in albedo that is representative of changes in surface dust cover [Figure14]. The surface dust coverage reduced in Daedalia and southern Tharsis region (Syria and Sinai). The surface dust cover however increased in Hellas, Hesperia, Solis, Sirenum and Argyre. There is also some hint of increased surface dust in southern Syrtis region.

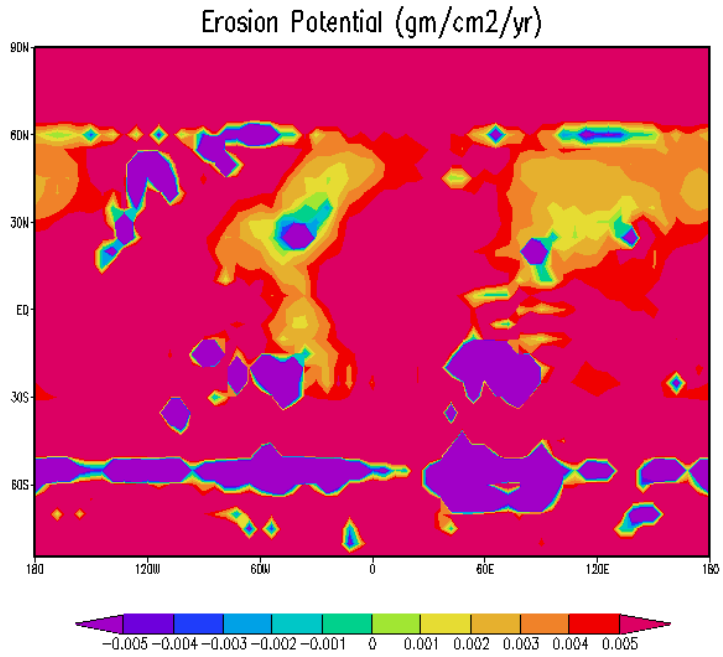


**Figure 15**: Difference in dust distribution before and after a simulated storm. The initial dust distribution was set according to the albedo map from the pre-2001 storm season Szwast et al 2005.

In our simulations (Figure 15) there was net erosion from the polar cap edges- both the northern polar caps and the southern polar caps. However the southern polar caps were more active as suppliers of dust than the northern polar cap edges. Other major dust sources were northern and southern rims of Hellas, southern rim of Argyre, southern Thaumasia, southern sirenum, Daedalia, Claritas, Sinai, east of Solis, northeast of Argyre, Olympus Mons, Alba Patera, Southern Acidalia, Elysium Mons, Isidia, western Libya and Mare cimmerium. Out of these locations Sinai, Daedalia and Claritas are the only regions of dust depletion in both observations [Szwast 2005, Christensen 2001] and simulations.

The dust increased in the floor of Hellas, Hesperia, Solis, Sirenum, floor and northern rims of Argyre, southern Syrtis region- and these match observations as well.

Other major dust sinks in simulations were Amazonis, Tharsis, Syria, Arabia, Noachis, Libya, Syrtis Major, Memnonia, Arcadia, Thaumasia, eridania, Cerberus.

The primary lifting center was the southern rim of Hellas, and the secondary lifting centers were Isidis, Claritas, Daedalia, Sinai and north east of Argyre. Thus Daedalia/Claritas region is the secondary lifting center that is activated both in observations (Szwast 2005, Christensen 2001) and simulations. The activation of Daedalia as a secondary center is purely as a result of the dust distribution we started with. In the simulations where we started with infinite surface dust cover, this region was not activated and lifting centers were limited to Hellas and Argyre, Hellas being the primary lifting region and Argyre being the secondary lifting center that is activated once the Hadley Cell circulation becomes strong enough and there are increased stresses along the subtropical convergence zone. These two lifting centers were overwhelming the other centers due to a uniform stress threshold-lifting criterion everywhere on the planet.

In the simulations with changing stress threshold conditions with decreasing amounts of dust on the surface (discussed in section 4.3.4), the Isidis region is active as an active lifting center but much later in the season and has no role in intensifying the main global storm that starts from the Hellas region. The Daedalia region however is not activated in these simulations. Thus it seems that the surface dust distribution plays an important role in activating the Daedalia and Sinai.

The Hellas region is surprisingly observed to be a net sink for dust integrated over the full course of the 2001 global storm. (Szwast et al. 2005). In our simulations, the floor of Hellas is a major sink, however the southern and northern rims of the Hellas basins are the biggest sources of dust and do not get replenished by other components of circulation in the course of the storm. The secondary lifting centers as Daedalia, Isidis and Sinai possibly return much of the dust lifted back to the Hellas region, but our simulations do not capture this component of the circulation.

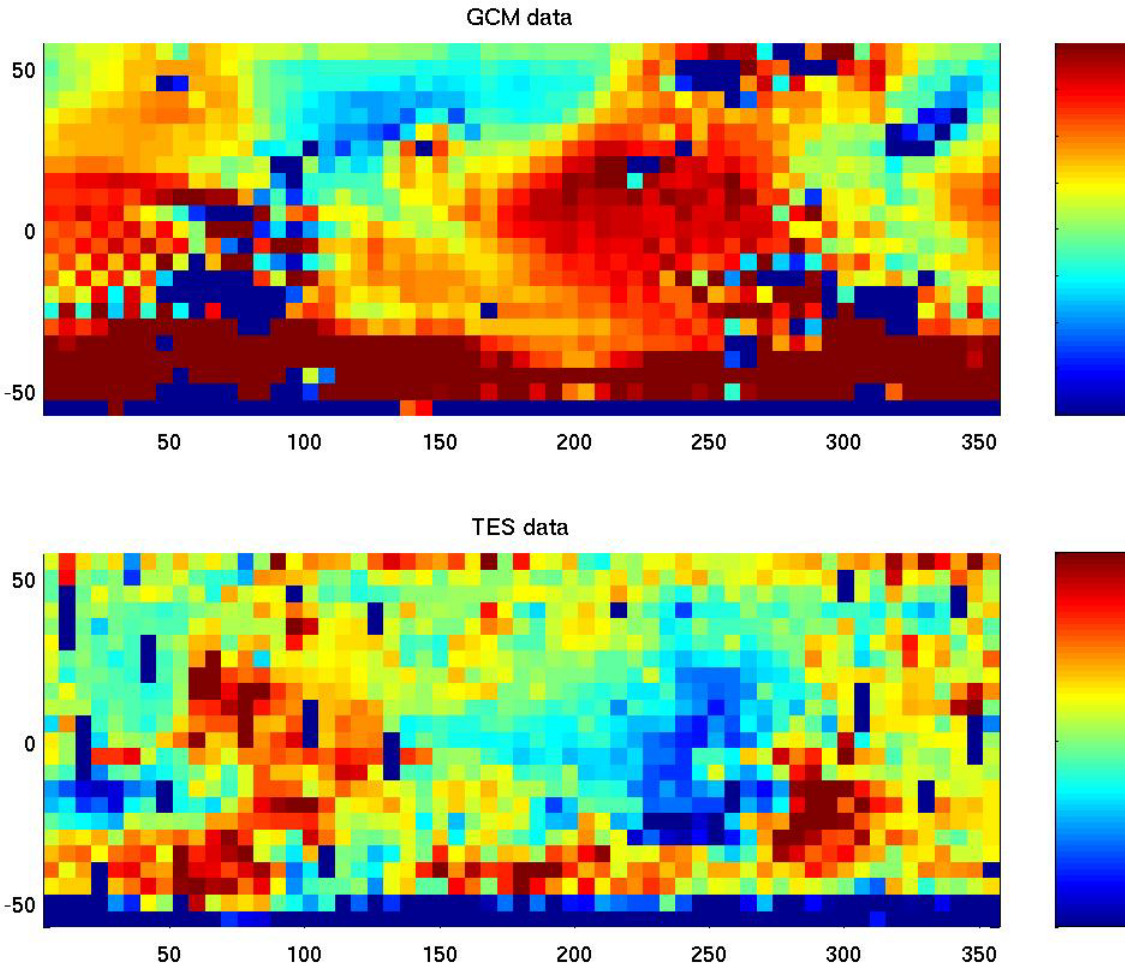


**Figure 15a**: Spatial maps (latitude vs. longitude) of changes in dust distribution (GCM) vs changes in albedo following the 2001 global storm (TES) when the initial dust distribution was prescribed similar to the pre 2001 storm albedo map (TES).

Hesperia brightens up in the observations due to net depositions of dust during the 2001 global dust storm (Szwast et al 2005). In our simulations also this region shows up as a net sink of dust. A large amount of dust lifted from the nearby Hellas is possibly re-deposited in the Hesperia region even before the global circulation picks it up.

In our simulations, the Argyre basin also has similar dust removal/deposition trends as the Hellas basin. They lie in the same zonal collar of the Hadley cell circulation. There is net deposition in the floor of Argyre and removal from the northern rim and southern rims of Argyre. It has however been observed (Szwast et al 2005) that the Argyre basin again acts as a

net sink of dust and is probably replenished by the dust lifted from other secondary lifting centers.

The Sirenum region has been observed to be a net sink of dust (Szwast et al 2005). However in our simulations, the southern Sirenum region is a source if dust- this coincides with the southern cap edge storms and hence is a depleted of dust that is not replenished during the course of the global storm.

The Tharsis region and the Solis Planum region that show up as a major source of dust in the 2001 global storm (Szwast et al 2005) however shows up as a net sink of dust except for the southern most part of Tharsis and Sinai regions that are secondary lifting centers in our simulations and are suppliers of dust that make the global storm stronger. The model is not capturing the local components of circulation that pick up more dust from this region.

It is clear from the other lifting regions in the simulations that topography is playing a major role in eroding regions such as Alba Patera, Olympus Mons, Elysium Mons and Isidis. These regions don't show up as dust sources in the 2001 dust storm albedo maps. Even though dust, which has been well mixed in the atmosphere, is deposited preferentially over high topography yet these regions show up as net sources. The high topography often gives rise to strong tidal waves that overwhelms the traveling wave signatures and the variability in the traveling waves is often not captured to a significant degree in the simulations.

The other dust sources were the northern polar cap edges and southern Acidalia that is a major lifting center due to traveling waves that are responsible for cross equatorial Chryse type of storms. This region however is active ~ Ls=180 which is when the early Hellas dust activity starts to show up for the first time.

### 4.3.4 The impact of finite dust sources when the stress threshold is varied with the amount of dust available on the surface

**Changing stress threshold conditions with changes in the surface dust**

More variability in the lifting centers can be obtained by calculating thresholds at each point using the semi-empirical formula used by [White, Lorenz, Newman et al 2002]. In our previous simulations we chose to employ a constant stress threshold criterion for simplicity. Here we explore an avenue of changing threshold conditions. One might expect more variable storms if secondary areas take over when the primaries are depleted. In our simulations, we employ both threshold increase and decrease with depleting dust sources on the surface. In the former case, because the main lifting centers are depleted most rapidly, so if thresholds increase they are effectively cut off before being completely exhausted, giving other regions more of a chance. In the latter case, a region where lifting previously occurred only during global storms (when winds were increased) can have a low enough threshold for lifting to occur here during storm onset, producing a different storm type. Threshold also fall in the main lifting centers, but these are then fully depleted so no lifting can occur anyway. It basically comes down to bringing the main lifting centers and other secondary lifting centers closer together, in terms of how close typical wind stresses in these regions are to the thresholds.

It can be seen from Figure [16] the dust is preferably transported to the Polar Regions and is depleted from the active lifting centers. The main active lifting centers are the northeastern and southwestern rims of the Hellas basin, the northern rim of the Argyre basin and to some extent the southern polar cap boundaries (where the cap edge storms occur in early southern summer). In the year with no large storm, the secondary lifting centers (such as rims of Argyre) are not activated, and although there is a broader region of dust depletion the amount of dust lifted is also much less compared to that during a global dust storm. It is probably unlikely on real Mars that the Hellas and Argyre basins are the only suppliers of dust for the global dust storms. In fact the 2001 global storm has been observed (TES ref) to have other active lifting centers such as Solis Planum. This region is not activated in our simulations. This is probably because for the infinite surface dust case, the Hellas basin dominates the circulation system with maximum number of storms starting from its northern or southern rim.

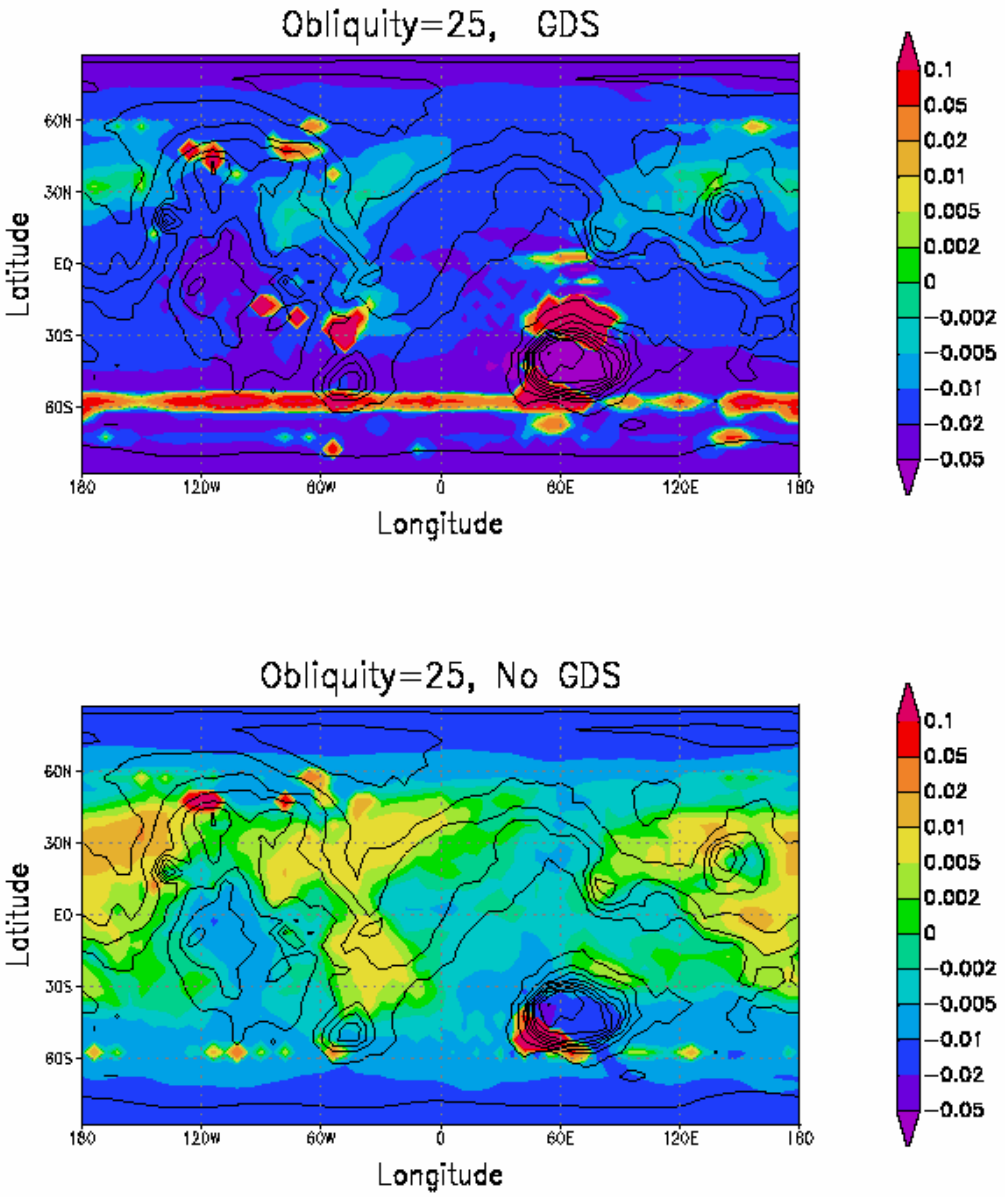


**Fig 16-** shows the erosion potential (cm/year) for the two cases of a dust storm year and a no dust storm year both with infinite, uniform initial supply of dust

Once the Hellas basin is shut off by dust exhaustion, it is expected that changing stress threshold conditions would activate lifting centers elsewhere on the planet. This would give much more variability in terms of the location of storms.

There are no supporting data to determine the how the stress threshold varies as a function of dust depletion. It would depend on the dust packing and other factors such as the inter-

particle cohesion between the dust particles and other particles, weather conditions, saltation conditions etc. Thus to implement a uniform decrease or increase in stress threshold for the entire planet would not accurately represent the microphysics on Mars. However to explore the idea of changing threshold conditions, we performed two simple experiments: one with an increase in the stress threshold, the other with a decrease in the stress threshold, when the surface dust abundance drops below a certain amount.

#### 4.3.3.1 Increasing stress threshold with dust depletion

The reasons for an increasing threshold condition for depleting dust amount would be exposure of new dust that is more tightly packed, or the inter-particle cohesion is higher because the dust is moist or simply that no erodible rock particles have been exposed in parts of the region.

From section 4.3.2 it is clear that even though the finite supply of dust introduces an added element for variation in the intensity of the storms, the quality and nature of the storms is quite similar to infinite surface dust case. To start new storms from a variety of locations as observed on Mars, the stress threshold has to be optimum and not too high for regions that have enough dust to start a storm. This is in line with the theory of negative feedback by Pankine and Ingersoll [2004]- where the stress threshold gets higher it is more difficult to lift dust from a depleted region due to aerodynamic shielding. To explore this theory we employ a new lifting scheme in this section.

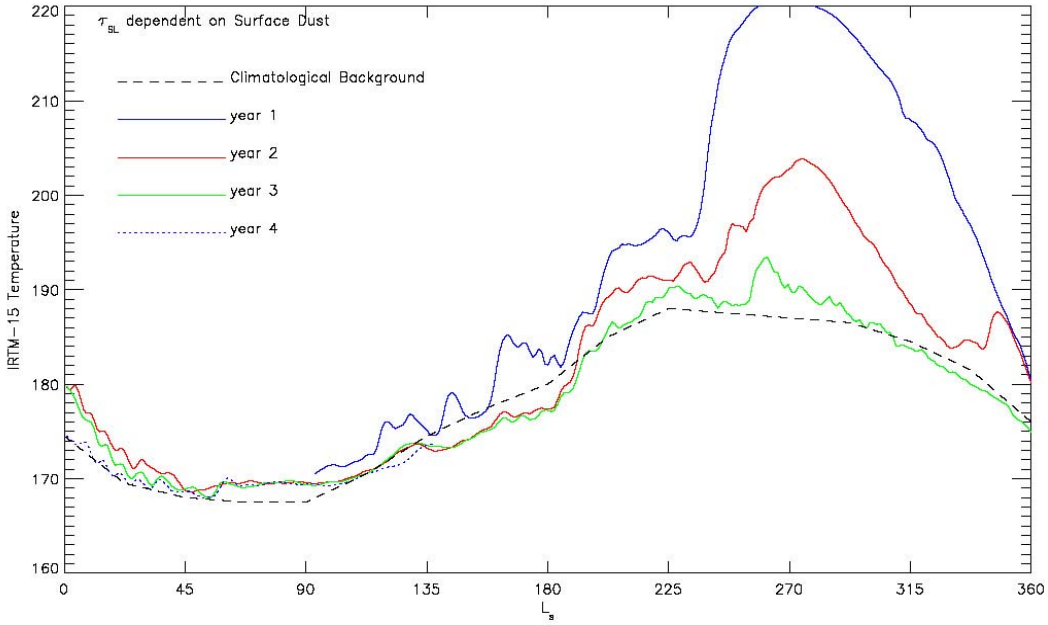


**Figure 17a-** Shows the multiyear simulations (globally averaged T-15 temperatures) which started with an initial dust amount of 0.1 gm/cm$^2$ but the threshold for depleted regions that have dust <0.06 gm/cm$^2$ was raised to 0.060 Pa compared to 0.040 for other regions. Comparing this to Figure 2 shows that even though there is same of amount of dust to begin with in both cases, Figure 2 had just 1 storm, but in this case there are two storms in the second year as now other lifting centers (e.g Isidis) are activated.

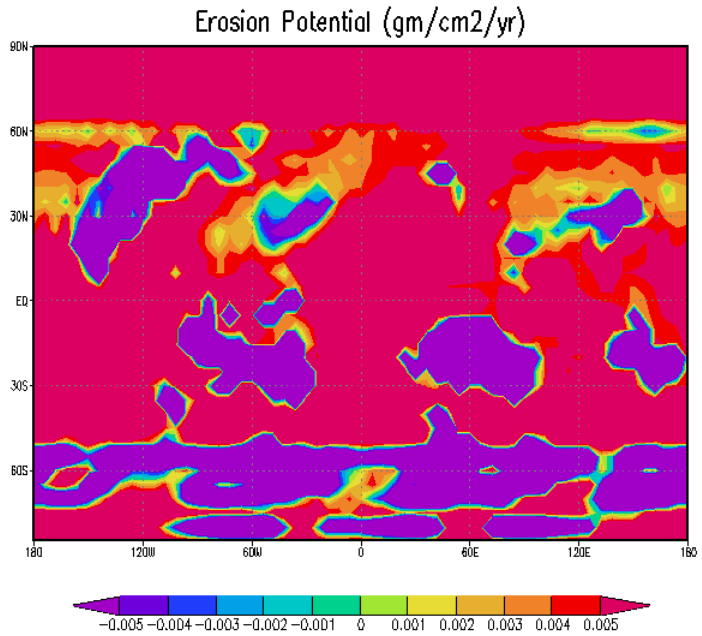


**Figure 17b** Erosion potential (gm/cm$^2$) for the Figure 17a simulation. Note the wide ranging of lifting centers that are enabled due to the relative lowering of threshold in regions others than the primary lifting centers that are depleted of dust

The stress threshold is increased when the surface dust goes below a certain value. Take Figure (17) for example. The first year there is a normal storm that starts in the Hellas region and becomes quite big and has a seasonal decay when the Hadley cell circulation becomes weaker.

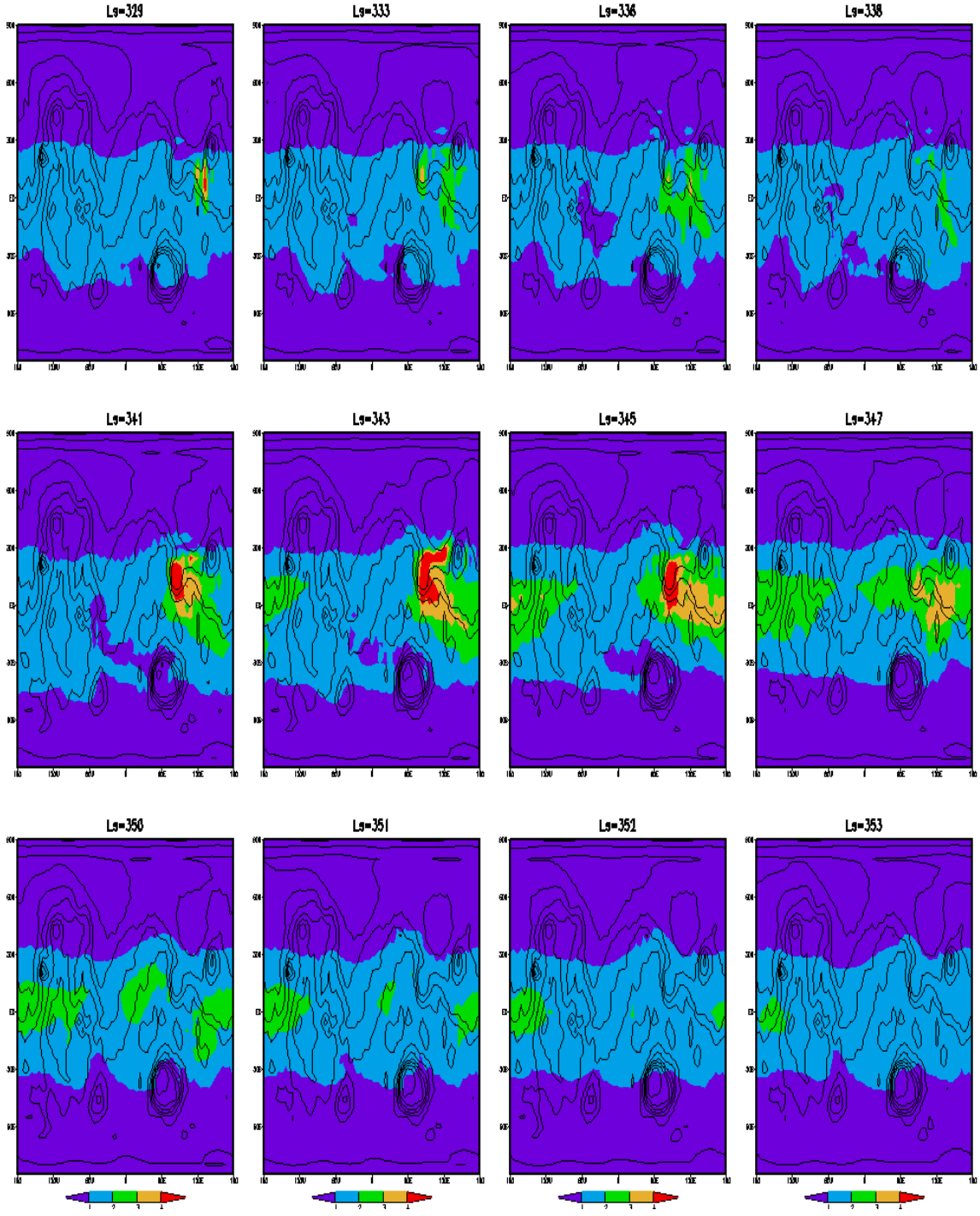
Ls=329
Ls=333
Ls=336
Ls=338
Ls=341
Ls=343
Ls=345
Ls=347
Ls=350
Ls=351
Ls=352
Ls=353

**Figure18-** shows the spatial maps of normalized opacities in the late southern summer season for increasing stress threshold with dust depletion experiments. Note the storm in the Isidis region.

However, in the second year, when the dust is depleted from the main centers of lifting in Hellas and Argyre, the storm decays earlier than usual around Ls=325, but a second smaller storm starts soon after near the Isidis region (120E, 10N) (Figure 18) where dust storms have been observed (MOC daily global images, June 29, 2003). Compare this case to the simulation, which had the same initial dust cover of 0.1 gm/cm$^2$ (Figure 2) but had uniform stress threshold condition for the entire run. It can be seen that dust expires in the first year in the 'Figure 2' case and there are no new lifting centers due to the high threshold of 0.055 Pa employed for the entire planet. The relative stress threshold in this case is not lowered for other regions of lifting and hence there are no storms after the year.

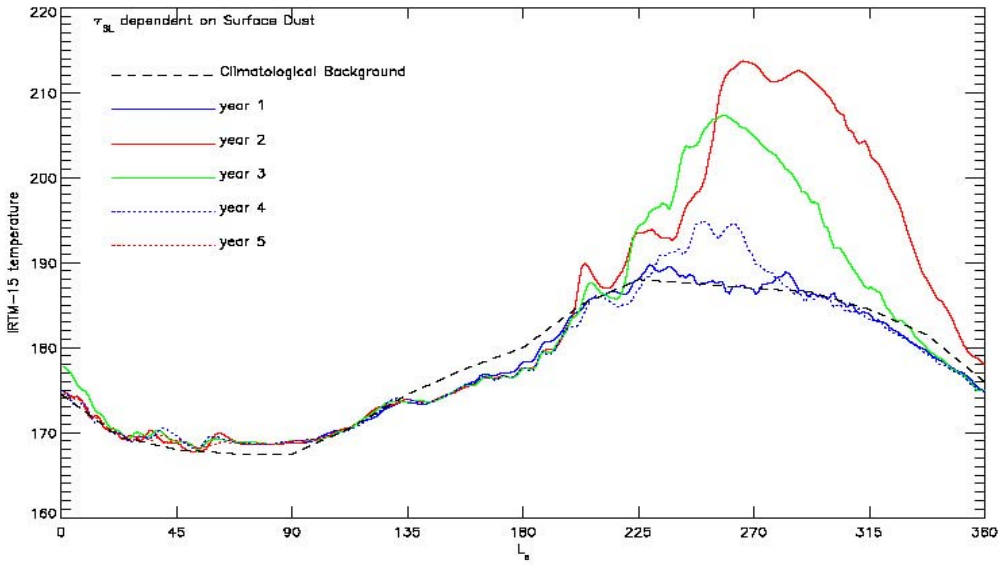


**Figure 19a**- Cross over storms (in terms of initial growth rates) in a simulation with an initial uniform dust cover of 0.1 gm/cm$^2$ but the threshold for depleted regions (<0.07 gm/cm$^2$ of dust) was increased to 0.055Pa compared to 0.045 for other regions.

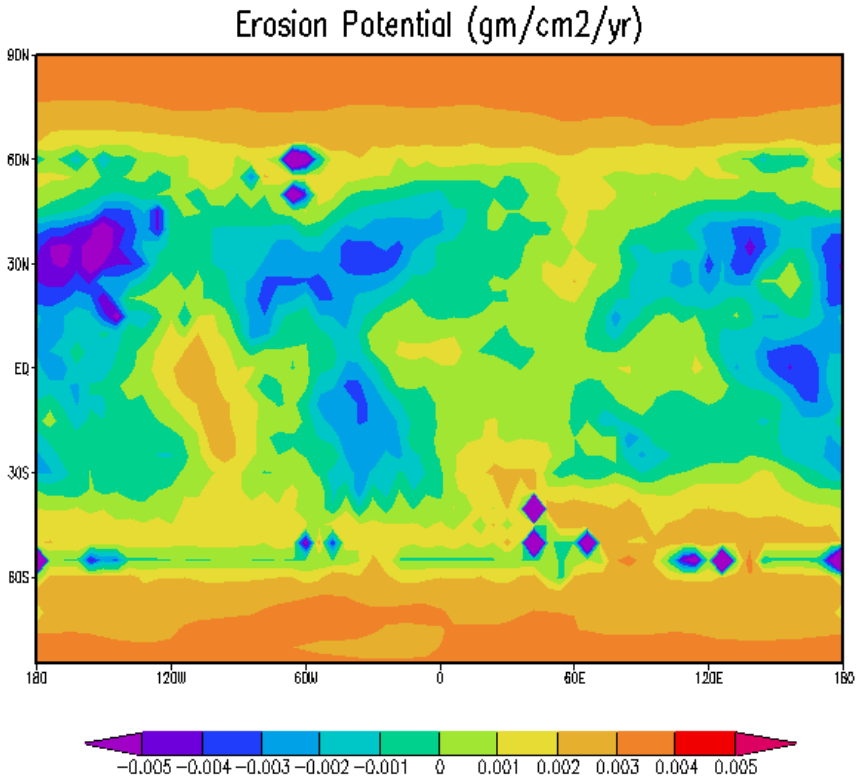


**Figure 19b**- Erosion potential for Figure 19a case (gm/cm$^2$/yr). Compared to Figure 17b the lifting centers are not that widespread as the threshold employed for the non-depleted regions is higher in this case and higher stress threshold automatically restricts lifting centers, as higher stresses are difficult to achieve.

In the global average T-15 temperatures (Figure 19) it can be seen that there were cross over storms in subsequent years in terms of starting times. This was an additional variability in our system since it can be seen with the uniform stress threshold condition that the storms in consecutive years are all nested in the globally average T-15 temperature plots. This shows that as long as the same stress threshold conditions apply, the same regions are responsible for dust-lifting each year for and the T-15 response is quite predictable in terms of growth rates.

The later the storm is, the smaller it is and the growth rates of these storms are similar thus resulting in nested T-15 plots (Figure 2,4,6,8). However when different regions are responsible

for dust lifting (Figure 12, 13, 19), the growth rates are different and the storm behavior is different as different circulation systems are influencing it. Even for the increasing threshold with depleting dust simulations (e.g. Figure 19a), the number of storm years depends on the thresholds and the lifting rates set.

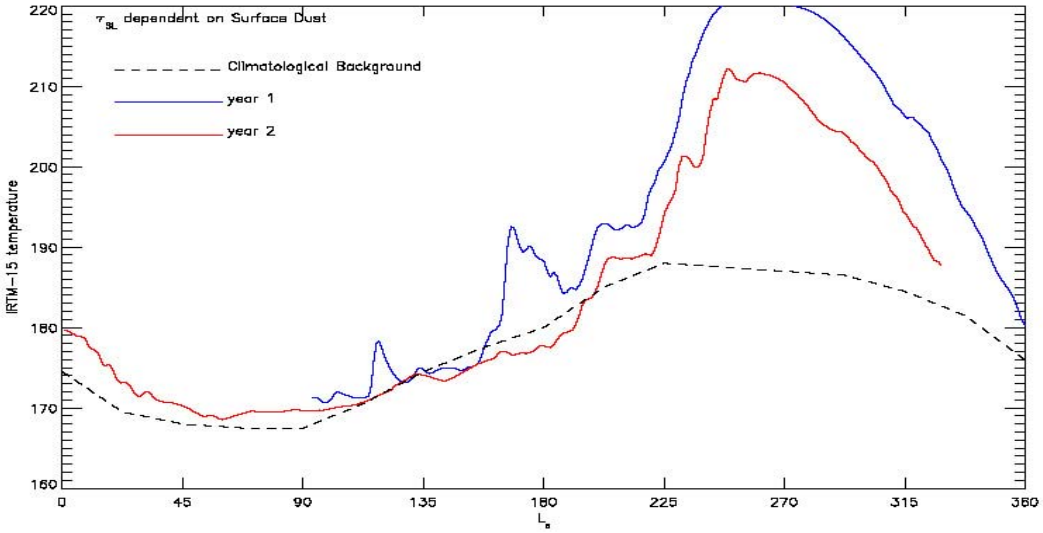


**Figure 20a**- Globally averaged T-15 temperatures for simulation similar to Figure 11, but in which the stress threshold for non-depleted regions was too low 0.030 Pa. The storms are too big as too much lifting is going from a variety of regions and there is unrealistic storm activity in northern summer season as well.

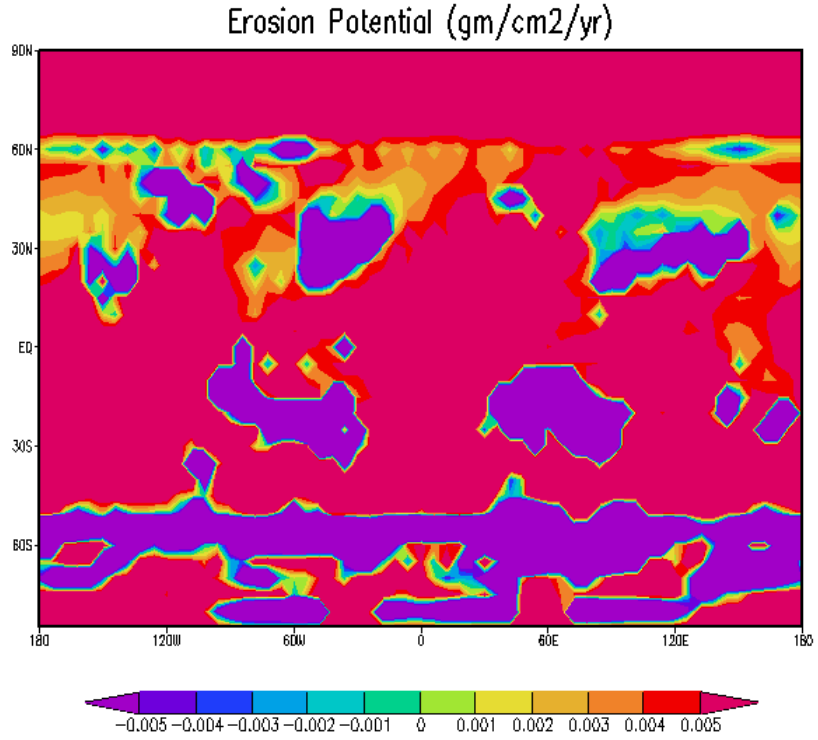


**Figure 20b**: Erosion potential (gm/cm$^2$/yr) for Figure 20a simulation. Note the wide range of lifting centers due to low threshold set. Such widespread lifting gives rise to unrealistically high opacities.

If the stress threshold is too low (less than 0.035 Pa) for non-depleted regions (e.g. Figure 20), this gives rise to abnormal and unrealistic storm activity in northern spring and summer seasons (Figure 20a).

Thus it is important for realistic simulations to maintain a minimum stress threshold value for any region on the planet, so that excessive lifting from unrealistic locations can be prevented. The idea is to relatively lower the thresholds for non-depleted regions, by increasing the stress threshold for depleted regions relative to the standard value of ~ 0.055 Pa (Basu et al. 2004). Thus shutting off the active lifting centers like the Hellas region by implementing a higher stress threshold on dust depletion prevents the Hellas storms from overwhelming dust activity in other regions. When the stress threshold is relatively lowered for regions with surplus dust, new storms start from these locations that were not active in the infinite dust supply case.

### 4.3.3.2 Decreasing stress threshold with dust depletion

The stress threshold might reduce with depleting dust due to exposure of dust that is loosely packed (or inter-particle cohesion might be lower) and easier to launch in the atmosphere. We employed this threshold criterion where the stress threshold was reduced when the surface dust was depleted below a certain value. These simulations (Figure 21) also gave greater variability than the simulations with uniform single stress threshold for the entire planet at all times (e.g. Figure 2). In general there were a larger number of storms than the previous case (section 4.3.3.1). The globally averaged T-15 plots showed cross over storms in terms of the starting times. The growth rates were different in different years as the storms started from new lifting centers once the primary lifting center was shut off.

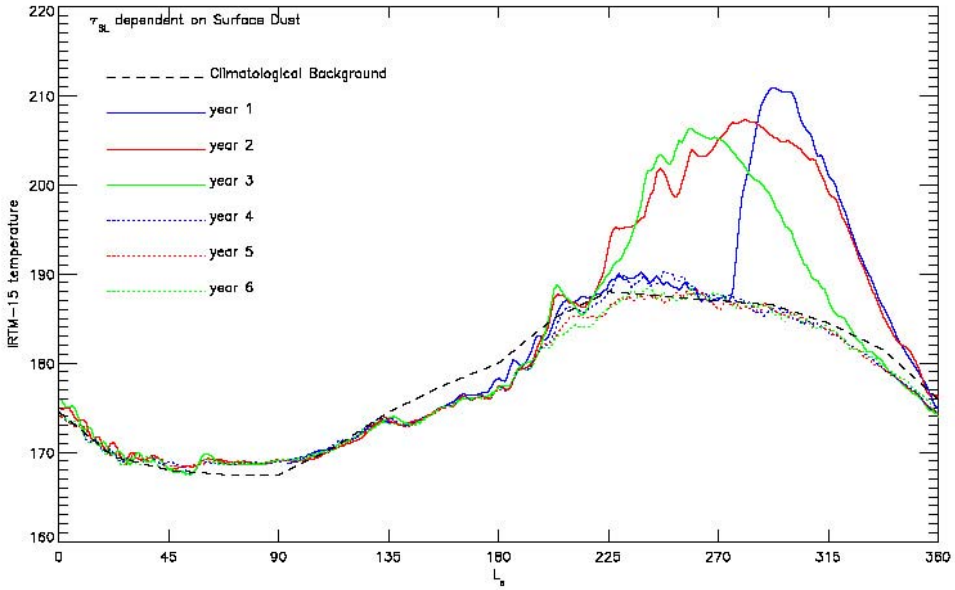


**Figure 21a:** Multiyear runs from a simulation that started with an initial dust amount of 0.1 gm/cm$^2$. In this case the stress threshold was lowered to 0.040 Pa when dust depleted below 0.07 gm/cm$^2$. The threshold for non-depleted regions was 0.055 Pa. Note this parameterization gives rise to 3 consecutive storm years with just 0.1 gm/cm$^2$ of dust to begin with.

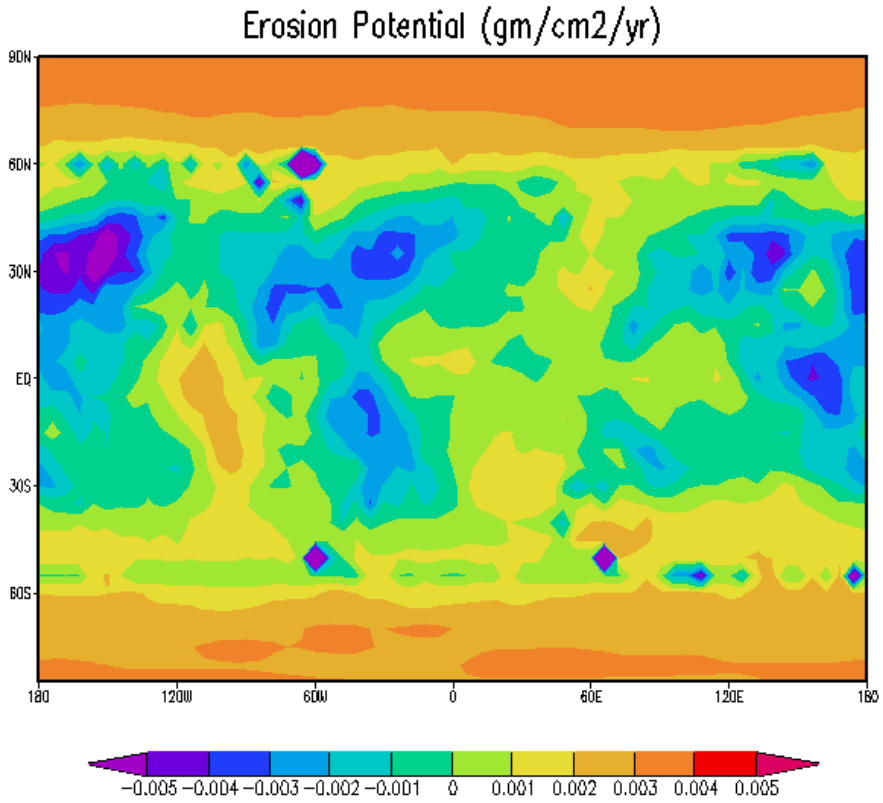


**Figure 21b**: Erosion Potential for Figure 21a case (gm/cm$^2$/yr). Note that the lifting centers are not that widespread (compared to Figure 20b) in this case as the threshold for no depleted region is higher compared to the depleted regions. Thus the active lifting centers are still concentrated around the main centers of lifting that have been depleted. Redistribution of dust around the active lifting centers makes these sites favorable for dust lifting for this particular parameterization.

There were 2-3 storms before the dust expired compared to the simulation with same initial dust amount of 0.1 gm/cm$^2$ which just gave a single year of storm with no storms in the subsequent years (Figure 2). There were no new lifting centers in the uniform, finite supply of dust case (Figure 2) as the stress threshold was held constant. In general the number of storms, before the dust expired from all active lifting centers was greater than the previous cases (Figure 17 and Figure 19) where the stress threshold was increased with depleting dust on the surface. When higher thresholds are set with dust depletion, there are fewer storms because the higher threshold active lifting sites expire sooner as the dust lifting is faster with higher

lifting rates. Also lifting sites are less widespread (Figure 19) due to the as higher stresses are less frequently reached.

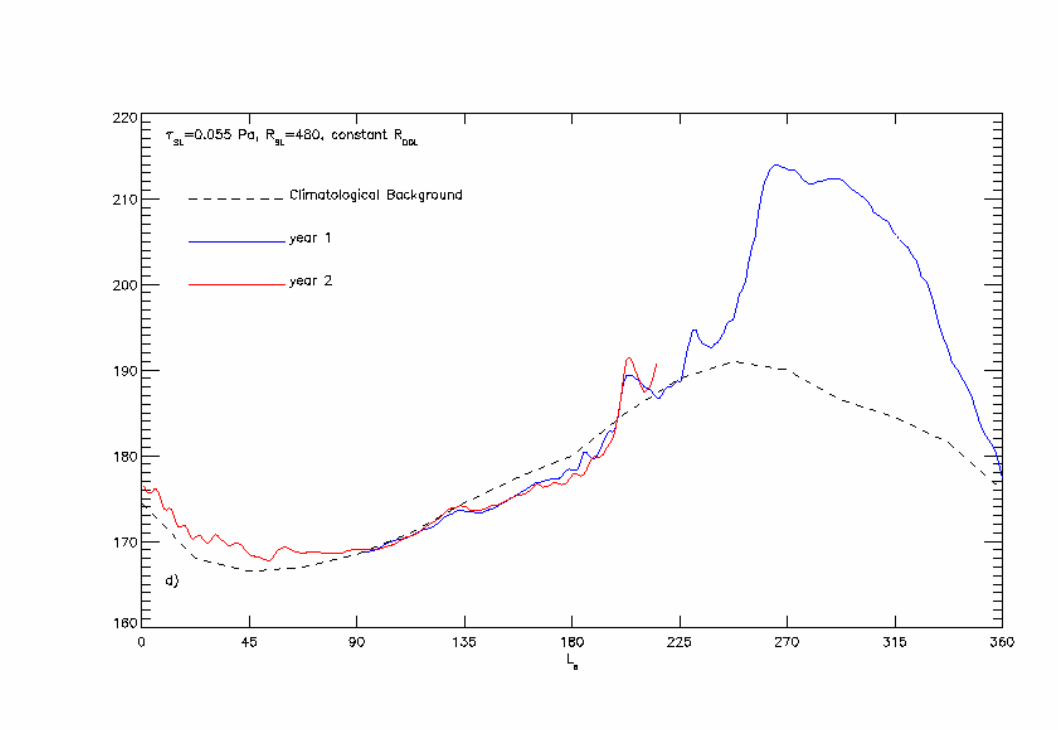


**Figure 22a**: Simulation with an initial surface dust of 0.1 gm/cm$^2$. Threshold for regions depleted below 0.07 gm/cm$^2$ is 0.030 Pa in this case. The low threshold gives rise to huge storms that give unrealistic opacities in year 2

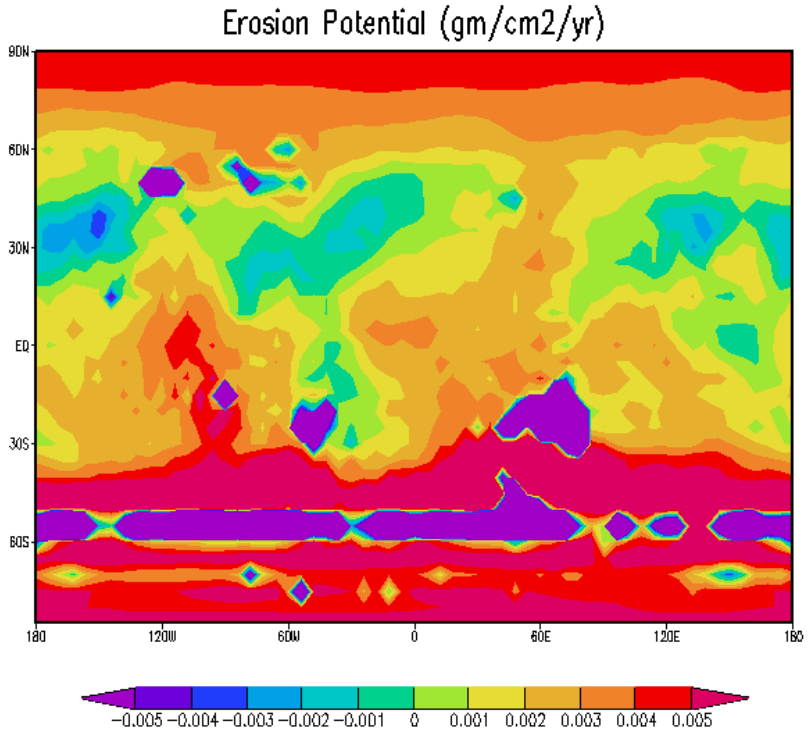


**Figure 22b**- Erosion potential (gm/cm$^2$/yr) for Figure 22a case. The lifting regions are concentrated around the main lifting centers and cannot be distinguished from them as such.

However lowering the threshold too much with dust depletion gives rise to huge storms (Figure 22) that give unrealistically high opacities. Even though the main lifting centers (rims of the Hellas and Argyre basin (Figure 22b)) might be stripped off of dust, but the re-distribution of dust in the nearby regions that can still get high stresses as they lie in the same zonal collar makes it easy to lift huge amounts of dust if the thresholds are too low. This again suggests that even with dust depletion, the range of stress threshold values in which we get realistic storm behavior does not change much. Due to this reason there is expansion of the main lifting regions, rather than the start of a whole bunch of new lifting centers.

The lowering or raising of the stress threshold with depleting surface dust might or might not be physically plausible as discussed before. However from the simulations it is not obvious that one gives more realistic storms compared to the other scheme. The final dust distributions after a 6-10 years look similar in both cases and they globally averaged T-15

temperatures are also well-behaved in both the cases. There is a possibility that these timescales are not long enough for the simulations to settle down. However, it has been established that as expected they increased variability.

### 4.4 Conclusions

The GFDL Mars GCM predicts that when finite surface dust abundances are used in the simulations added variability is introduced in the system. Due to the unavailability of dust in some regions, the circulation system is weakened in these regions. Even though the wind stresses are high, there is no dusted lifted and the positive feedback does not ensue resulting in weaker circulations and no dust storms. This added variability in the system gives rise to greater inter-annual variability in the simulated global dust storms. Changing the stress threshold with depleting dust also adds more variability than the uniform stress threshold condition that was applied to the entire planet in our previous simulations (Basu et al 2004, 2005). The net sources and sinks of dusts in the simulations are not completely in agreement with the TES thermal inertia and albedo maps. Our MGCM fails to capture some components of the circulation even when the initial dust distribution is prescribed according to the TES abedo maps e.g. circulation system involving the secondary lifting centers that replenish the primary lifting centers as Hellas. Dust fall out and dust devils do not replenish these sites fast enough. The high lifting rates set for wind stress lifting are much faster than the combined slow replenishment rate of dust fall out and dust devils.

### 4.5 **Future Work**

The topography and traveling waves play a major role in shaping the dust continents on Mars. High topographical regions like Alba Patera and other volcanoes like Olympus Mons, Elysium etc. play a significant role in shaping the frontal storm systems. If the tidal waves are strengthened by the topography too much then the traveling waves fail to produce dust storms through the frontal system and this gives less variability to the system as it does not capture the inter-annual variability in the traveling waves. Also the accurate simulation of circulation systems associated with the secondary lifting centers that have been observed such as Daedalia or Solis Planum is important. To achieve these goals, it is important to run the model with

higher resolution. This will resolve the topography and secondary circulation systems better giving rise to more realistic simulations.

# Chapter 5

## Conclusions

This thesis presents results from GCM simulations of an interactive dust cycle on Mars. The version of the GFDL Mars GCM used in this study differs from that described by Fenton and Richardson [2001], Richardson and Wilson [2002ab] and Mischna *et al.* [2003]. Instead of a dust injection scheme based only on the surface-air temperature contrast, the present model includes detailed, physically based parameterizations of dust lifting, similar to the approach of Newman *et al.* [2002a]. These schemes represent the injection of dust by convective motions, using thermodynamic theory of dust devils [Renno *et al.*, 1998; 2000], applied on the coarse resolution of the GCM grid, and by large-scale wind stresses, using a functional dependence on the frictional velocity [Shao, 2001]. As before, the model treats dust as a transportable trace species, the dust distribution being affected by the model-resolved winds, sub-grid scale diffusion, and particle-mass-dependent sedimentation. The dust is radiatively active in the GCM, influencing thermal infrared and visible radiative heating of the atmosphere.

The convective and resolved-wind dust injection schemes introduce three free parameters. A given simulation, extending for multiple Martian years, uses spatially and temporally fixed values for each of these free parameters. These parameters are the rate constants applied to the two injection schemes (simple multipliers) and the threshold lifting stress for the resolved-wind lifting scheme. Convective lifting is prescribed without a threshold. We chose to use the seasonal cycle of globally averaged air temperatures as our primary quantitative means of assessing the quality of the GCM simulations. The first question we address with the model is whether the injection schemes can generate a dust cycle in agreement with observations, and what combination(s) of parameters allow the best fit. We find that the shape of the seasonal air temperature curve in northern spring and summer, when air temperatures are observed to be highly repeatable [Liu *et al.*, 2003], can be fit either by the convective lifting scheme or by the stress-lifting scheme with low values of stress-threshold and lifting rate. The northern spring and summer temperatures cannot be fit if the dust opacity only results from the fall-out of dust from a global storm in the previous southern summer. Both the convective and low-

threshold stress-lifting schemes require steady and widespread dust lifting throughout northern spring and summer. Widespread convective (dust devil) lifting seems consistent with the widespread observation of dust devils and dust devil tracks, and indeed the model predicts injection rates that are in good agreement with analysis of Imager for Mars Pathfinder data [Ferri *et al.*, 2003]. Widespread wind stress lifting seems much less consistent with the relatively few and sporadic local dust storms observed in northern summer [Cantor *et al.*, 2001]. Specifically, cap edge storms, other local dust storms, and lifting associated with dust streak formation appear insufficiently frequent. Further work is needed to provide quantitative support for these qualitative arguments. However, on the basis of the model results and inferences from observations, we propose that dust devils are the primary dynamical system providing the dust injection necessary to sustain the background haze on Mars.

Regardless of the convective scheme rate parameter, dust storms cannot be generated in the model. From this we suggest that dust devils are not the precursors of dust storms, in agreement with imaging observations. It is also not possible to generate dust storms with the stress-lifting scheme set with parameter values necessary to sustain the background dust haze. Conversely, with stress values and injection rates high enough to initiate storm activity, lifting does not occur throughout much of northern spring and summer. Simulation of the dust cycle involving storms and the background haze requires two schemes: a combination of high rate, high threshold lifting, and either convective lifting or low threshold, low rate stress lifting. Justification for the use of two different sets of injection parameters in two parallel stress-lifting schemes is possible, but seems a more complex and observationally less-well supported solution than the convective plus high threshold injection scheme option. When run with a combination of convective and high threshold dust injection schemes, the model is able to generate both a realistic background dust cycle, and for the first time, spontaneous and inter- (and intra-) annually variable global dust storms. These storms are discussed in greater detail in B04.

Varying injection parameters, a multiyear "best fit" simulation can be produced with optimal air temperature and dust storm emulation. This simulation uses convective and high threshold

stress lifting. The model develops a range of local and regional storms, the variety and distribution of which compares reasonably well with observations [Cantor *et al.*, 2001]. Specifically, seasonal ice-cap edge dust storms are simulated, as are storms associated with various topographic features. Comparisons with air temperature cross-section data suggest that cap edge lifting is somewhat under-predicted. Several small dust storms are generated in the northern early autumn and later winter, associated with low-pressure frontal storms, as described by Wang *et al.* [2003] and also generated in the Oxford Mars GCM [Newman *et al.*, 2002b]. One such storm develops into a large regional event, resembling the 1999 storm and the dust storm that preceded the Mars Exploration Rover landings [B04]. The model also predicts the distribution and seasonal variation of dust devil activity (if the convective lifting is ascribed to dust devils). A distinct peak in activity is found in the model in Amazonis, a region of observed enhanced dust devil activity.

The rates of dust injection and the net removal/deposition of dust on the surface are predictions of the model. It has not been possible to predict annually integrated net dust deposition/erosion rates until this point as it requires a validated dust cycle that includes interactive lifting, transport, and deposition of dust. Previous estimates of dust erosion have had to rely on "lifting potential" derived from the model wind stresses to predict lifting and have ignored the other side of the cycle: deposition [Haberle *et al.,* 2003]. Our results suggest that net annually integrated erosion/deposition rates are roughly one to two-orders of magnitude lower when the full dust cycle is taken into account. Thus extreme caution must be taken when interpreting the previously generated "lifting potential" erosion values. Net annual erosion/deposition rates compare well with estimates from the Mars Pathfinder solar panel experiment [Landis and Jenkins, 2000] and from analysis of the darkening of slope streaks [Aharonson *et al.*, 2003]. Between 75°S and 75°N, the net annual erosion rate is 0.3μm/Martian year (0.1-1μm/Martian year, conservatively), which is balanced by net polar deposition at roughly 20μm/Martian year, consistent with estimates from Pollack *et al.* [1979]. Although these values are the best possible GCM estimate at this time, the model still neglects processes of potential importance, including dust-ice interactions. These must be assessed in future models.

The successful generation of global dust storms within a GCM that simultaneously provides a good simulation of the non-dust storm climate [Basu *et al.*, 2004] is a leap ahead from previous models that could not simulate both aspects of the dust cycle simultaneously [Newman et al. 2002ab]. However realistic looking dust cycles with inter-annual variability of dust storms are simulated only for a narrow range of the free parameters. Similar results have been obtained by lower order models (Pankine and Ingersoll, 2002) where the system was critically balanced close to a threshold. The question that then arises is 'Is Mars critically balanced and if yes- what keeps the system so finely tuned'. The answer to that can partly answered within the scope of the models used. The dust lifting parameterizations are very simplistic in our models with a uniform dust cover and uniform stress threshold criterion everywhere on the planet. Also the model resolution is relatively low so that it is unable to capture many small-scale circulations associated with unresolved topography and winds. As a result of this, similar weather is simulated every year and hence to capture whatever little transience there is in the system one has to really fine-tune the system. Similar is the case with simplistic lower order models. The actual Martian weather system may or may not be finely tuned. Pankine and Ingersoll argue that a negative feedback mechanism between the surface dust and stress threshold might be instrumental in keeping the system finely tuned. The dust storms develop spontaneously within the GCM, without *ad hoc* forcing, during southern spring and summer, consistent with observations. Simulated global storms are seeded by spontaneously generated local events, and grow by a radiative-dynamical feedback involving increased radiative heating associated with the lofted dust, increased Hadley cell vigor, and increased wind stresses and dust lifting. Growth from regional to global scales involves the activation of secondary lifting centers. During the simulated global storms, dust is lifting from a relatively small number of sites where wind stresses are maximized. Common areas are the rim of the Hellas basin, the southern seasonal cap edge, Syria/Solis, and Acidalia.

Model-resolved wind stresses are responsible for the generation of simulated storms. Only when the threshold stress for lifting is set low enough, and the injection rate parameter (linking the stress function to the injection rate) is set high enough, do global storms develop. In a limited area of this phase-space, the GCM develops inter-annually-variable global storms. Within a given, continuous simulation, the model will generate years without any major storm

activity, interspersed with years with global storms of various size and specific timing of initiation. This variability is internal to the atmosphere and the $CO_2$ cycle, as the surface dust deposits do not deplete, and the surface albedo and thermal inertia are not modified by the presence of dust. It is possible that additional richness in the complexity of the dust cycle will emerge in a model with an interactive surface dust distribution, but this work suggests that such interplay with a surface memory site is not required for inter-annually-variable storms. Instead, they are an emergent property of the smoothly and periodically (annually and seasonally) forced system.

The simulated storms remain unrealistic in a number of ways. The most important being the inability of the storms to shut-down in the observed manner. For example, the 2001 global storm began its decay phase around $L_s$=214° [Smith *et al.*, 2002], about 35° of $L_s$ after initiation. However, the simulated storms do not spin-down until the Hadley cell begins to spin-down in mid-southern summer. Storm switch-off must result from either an internal feedback mechanism that kicks in once opacities reach a specific level, or from depletion of the active surface dust source (supply). The physical processes that would have to be involved in the former are inherently included in the model, but do not generate such a feedback. While it is possible that the fidelity of their representation needs to be improved, the model shows no tendency towards spin-down at high opacity, but the reverse. The latter mechanism is not included in the standard model, initial work with exhaustible sources suggest (not surprisingly) that realistic storm evolution, including switch-off can be simulated. More work is clearly warranted on storm spin-down. While the inability of the model to generate two global storms in a given year (such as the 1977a and 1977b events) might seem like a distinct, additional model problem, it is actually a trivial consequence of the spin-down problem. In order for there to be two storms in a year, the first must happen in early-to-mid southern spring, yet we know that when a GDS forms in the model, it persists until mid southern summer. A second storm can never begin. Given that the model is quite capable of generating early- and late-season global storms, it seems likely that once the spin-down or switch-off problem is solved, dual storm years will emerge. Finally, the range of locations on the surface at which storms initiate and at which secondary dust lifting centers are generated is in pleasing agreement with observations (the western and northern rim of Hellas, the

Syria/Solis in the southern part of Tharsis, and in the northern mid-latitudes in the Acidalia/Chryse "flushing storms" channel [Wang *et al.*, 2003]), the range of behavior seems a little stilted compared to observations. After a while, one recognizes similar types of storms being generated, albeit in a continuously randomized sequence.

Additional variability may require interaction with depletable surface dust deposits and one in which the surface albedo and thermal properties depend on the amount of dust present. Such feedback with the surface may also be necessary to explain the occurrence of variable global storms, despite the fact that a very limited area of model domain space permits these kinds of storms. We speculate, as do Pankine and Ingersoll [2004], that a negative feedback system may pull the Martian climate towards a state with variable storms.

The GFDL Mars GCM predicts that when finite surface dust abundances are used in the simulations added variability is introduced in the system. Due to the unavailability of dust in some regions, the circulation system is weakened in these regions. Even though the wind stresses are high, there is no dusted lifted and the positive feedback does not ensue resulting in weaker circulations and no dust storms. This added variability in the system gives rise to greater inter-annual variability in the simulated global dust storms. Changing the stress threshold with depleting dust also adds more variability than the uniform stress threshold condition that was applied to the entire planet in our previous simulations (Basu et al 2004, 2005). The net sources and sinks of dusts in the simulations are not completely in agreement with the TES thermal inertia and albedo maps. Our MGCM fails to capture some components of the circulation e.g. circulation system involving the secondary lifting centers (Isidis, Solis Planum, Sinai Planum etc.) that replenish the primary lifting centers as rims of Hellas and Argyre basin. Dust fall out and dust devils do not replenish these sites fast enough. The high lifting rates set for wind stress lifting are much faster than the combined slow replenishment rate of dust fall out and dust devils.

# Chapter 6

## Future Work

So far we have examined the behavior of dust in a Martian General Circulation Model (GCM) with a self-consistent realistic dust cycle. There are many aspects of the Martian dust cycle that still need to be explored with model simulations.

The following models will be used:

**Model 1**: The Geophysical Fluid Dynamics Laboratory (GFDL) Mars GCM was used to examine the dust cycle on Mars. This model has been extensively used and validated against available spacecraft data [Wilson and Hamilton, 1996; Wilson and Richardson, 2000; Richardson et al. 2002; Wang et al., 2003]. The model integrates the primitive equations on a discretized grid and includes a significant number of Mars-specific physical parameterizations. These include a $CO_2$ cycle with prognostic variations in surface pressure and seasonal ice caps [Mischna et al. 2003], a water cycle, which includes atmospheric transport, simple cloud microphysics, dust physics and water ice seasonal caps [Richardson and Wilson, 2002; Basu et al., 2004]; and radiative heating due to solar and thermal infrared interactions with dust and $CO_2$ gas [Wilson and Hamilton, 1996]. The dust cycle components are included in the model. Dust is transported in the atmosphere by the model-resolved winds and sub-grid scale diffusion and falls under the influence of gravity (we currently carry two particle sizes). Dust is injected using a scheme that represents the net effect of dust devils and one that represents resolved wind stress driven lifting.

**Model 2**: This is an adapted version of the Weather Research and Forecast model which has been developed by representatives from major institutions like NOAA/NCEP, NOAA/FSL, NCAR and AFWA. We have been working towards incorporating the Martian physics into this model. This is computationally superior to the previous model due to its scaling nature and flexibility with regards to limited or global domain size. The high-fidelity semi-lagrangian transport scheme has also been incorporated into the model. This model is similar to the

GFDL model in many ways and will also be available for running simulations in addition to the GFDL model in a couple of months time.

Following are the broad categories under which the proposed research can be divided:

**6.1 High resolution simulations of the Martian dust cycle and global dust storms-**

This is a natural extension of the work done so far. The low resolution simulations predict the general storm behavior correctly but accurate simulations of storms such as the observed 2001 Hellas storm are only possible with a high resolution model by incorporating components of local circulation, stress thresholds specific to the region of interest, interaction with the polar caps, clouds and other fine tunings. The topography and traveling waves play a major role in shaping the dust continents on Mars. High topographical regions like Alba Patera and other volcanoes like Olympus Mons, Elysium etc. play a significant role in shaping the frontal storm systems. If the tidal waves are strengthened by the topography too much then the traveling waves fail to produce dust storms through the frontal system and this gives less variability to the system as it does not capture the inter-annual variability in the traveling waves. Also the accurate simulation of circulation systems associated with the secondary lifting centers that have been observed such as Daedalia or Solis Planum is important. To achieve these goals, it is important to run the model with higher resolution. This will resolve the topography and secondary circulation systems better giving rise to more realistic simulations. We would also like to test the sensitivity of the parameterizations for the high-resolution cases. The quality and accuracy of the storms can be assessed in greater detail by comparing cross sections (latitude and height) and latitude vs. local time plots of temperature for different seasons.

**6.2 Interaction of the water cycle and the clouds with the dust**

In our current research, the water cycle has been switched off. It would be interesting to see how the seasonal dust cycle and storm evolution changes by including the water cycle and clouds. The inter-particle cohesion between the water molecules and the dust would affect the dust dynamics in terms of the fall-out rates, ease of lifting and stress threshold values. It would be interesting to see how these modify the dust activity and dust storms. The inclusion of

radiatively active clouds would also give us a clearer picture of the role of dust in shaping the mid-level atmospheric temperatures. Preliminary results show that the clouds may have an important role to play in shaping these temperatures.

### 6.3 Interaction of the polar caps with the dust cycle

In our current simulations there is a dearth of cap edge storm activity. Employing uniform stress threshold conditions for the entire planet is clearly not capturing the dust dynamics at the cap edges. The interaction of the polar caps with the dust cycle, the local circulation and local stress threshold conditions have to be incorporated into the model. Additionally the polar-layered deposits that are stacked layers of dust and water ice contain records of the Martian climate and also act as memory elements for dust activity. When the polar layer melts and the dust is exposed, it acts as an additional source of variability in the dust cycle in terms of the total reservoir of dust. Thus it is important to capture these components into our model. This would give us a better understanding of the mechanisms of deposition and dependence of layer dust content upon the behavior of dust in the climate system.

### 6.4 Incorporating variable stress threshold scheme for Mars

In our current dust-lifting scheme, we employ a simplified version of the wind stress-lifting scheme and thus the model is not able to capture all the different kinds of storms. In some of our future simulations we plan to incorporate variable stress threshold schemes that are dependent on surface properties like atmospheric density, inter-particle cohesion, roughness length, local circulations, etc. This would produce a greater variety of storms as have been observed.

### 6.5 Improving the current Mars GCM with better schemes

We have plans to improve the radiation scheme, the vertical resolution of the planetary boundary layer and to incorporate a better boundary layer scheme. This would be a part of the regular upgrade of the Mars General Circulation Model that we will be using for our simulations.

We hope that the work proposed in this document will move us towards greater understanding of the Martian dust cycle. This cycle is a critical component of the Martian Climate System, and one that in many ways is least well understood. Significant improvement in understanding would not only have direct impact on the quality and accuracy of current models for Mars, but also on the representation of dust processes in models that seek to understand conditions on Mars in the past.

# BIBLIOGRAPHY

Aharonson, O., N. Schorghofer and M. F. Gerstell, *Slope streak formation and dust deposition rates on Mars*, J. Geophys. Res*., 108*, art no: 5138, 2003.

Basu Shabari, M. I. Richardson, R. J. Wilson, "*Simulations of the Martian Dust Cycle with the GFDL Mars GCM"*, VOL. 109, E11006, doi:10.1029/2004JE002243, Journal of Geophysical Research, 2004.

Balme, M. R., P. L. Whelley and R. Greeley, *Mars: Dust devil track survey in Argyre Planitia and Hellas Basin*, J. Geophys. Res., 108, art. no: 5086, 2003.

Banfield, D., B. J. Conrath, M. D. Smith et al., *Forced waves in the Martian Atmosphere from MGS TES nadir data*, Icarus, 161, 319-345, 2003.

Briggs, G. A., Baum, W. A. and Barnes, J., *Viking Orbiter imaging observations of dust in the Martian atmosphere*, J. Geophys. Res., 84, 2795-2820, 1979.

Cantor, B. A. *et al., Martian dust storms: 1999 Mars Orbiter Camera observations*, J. Geophys. Res. 106*,* 23653-23687, 2001.

Cantor, B.A., P.B. James, M. Caplinger, and M.J. Wolff, *Martian dust storms: 1999 Mars Orbiter Camera observations*, J. Geophys. Res., 106(E10), 23653-23687, 2001.

Cantor, B.A., M.C. Malin, and K.S. Edgett, *Multiyear Mars Orbiter Camera (MOC) observations of repeated Martian weather phenomena during the northern summer season,* J. Geophys. Res., 107, (E3), 1029/2001JE001588, 2002.

Cantor, B. A., and K. S. Edgett, *AGU*, 2002.

Christensen, P. R., *Regional dust deposits on Mars- Physical properties, age and history*, J. Geophys. Res., 91, 3533-3545, 1986.

Clancy, R. T., D. O. Muhleman and G. L. Berge, *Global changes in the 0-70 km thermal structure of the Mars atmosphere derived from 1975 to 1989 microwave CO spectra*, J. Geophys. Res., 95, 14543-14554, 1990.

Clancy, R. T., A. W. Grossman, M. J. Wolff, P. B. James, D. J. Rudy, Y. N. Billawala, B. J. Sandor, S. W. Lee, and D. O. Muhleman, *Water vapor saturation at low altitudes around Mars aphelion: A key to Mars climate?*, Icarus, 122, 36-62, 1996.

Clancy, R. T., B. J. Sandor, M. J. Wolff, P. R. Christensen, M. D. Smith, J. C. Pearl, B. J. Conrath and R. J. Wilson, *An inter-comparison of ground based millimeter, MGS TES, and Viking atmospheric temperature measurements: Seasonal and inter-annual variability of temperatures and dust loading in the global Mars atmosphere*, J. Geophys. Res., 105, 9553-9571, 2000.

Colburn, D. S., Pollack, J. B. and Haberle, R. M., *Diurnal-variations in optical depth at Mars,* Icarus 79, 159-189, 1989.

Conrath, B. J., J. C. Pearl, M. D. Smith, W.C. Maguire, P. R. Christensen, S. Dason and M. S. Kaelberer, *Mars Global Surveyor Thermal Emission Spectrometer (TES) observations: Atmospheric temperatures during aerobraking and science phasing*, J. Geophys. Res., 105, 9509-9519, 2000.

Fenton, L. K. and Richardson, M. I., *Martian surface winds: Insensitivity to orbital changes and implications for aeolian processes*, J. Geophys. Res., 106, 32885-32902, 2001.

Fenton, L. K., Pearl, J. C. and Martin, T. Z., *Mapping Mariner 9 dust opacities*, Icarus, 130, 115-124, 1997.

Ferri, F., P. H. Smith, M. Lemmon and N. O. Renno, *Dust devils as observed by Mars Pathfinder*, J. Geophys. Res., 108, art no: 5133, 2003.

Fisher, J. et al., *A survey of Martian dust devil activity using Mars Global Surveyor Mars Orbiter camera images*, AGU fall meeting, section: P, session: P01, ref no: 5742, 2002.

Forget, F., F. Hourdin, R. Fournier, C. Hourdin, O. Talagrand, M. Collins, S.R. Lewis, P.L. Read, and J.-P. Huot, *Improved general circulation models of the Martian atmosphere from the surface to above 80 km*, J. Geophys. Res., 104, 24155-24175, 1999a.

Gierasch, P. J. and R. M. Goody, *A study of the thermal and dynamical structure of the Martian lower atmosphere*, Planet. Space. Sci., 16, 615-646, 1968.

Gierasch, P. J. and Goody, R. M., *Model of a Martian great dust storm*, J. Atmos. Sci., 30, 169-179, 1973.

Greeley, R., Lancaster, N., Lee, S. and Thomas, P. *in Mars* ((Univ. of Arizona Press, Tucson, AZ, 1992), pp. 730-776.

Haberle, R.M., C.B. Leovy, and J.B. Pollack, *Some effects of global dust storms on the atmospheric circulation of Mars,* Icarus, 50, 322-367, 1982.

Haberle*,* R. M*., Inter-annual variability of global dust storms on Mars*, Science*, 234*, 459-461, 1986.

Haberle, R.M., J.B. Pollack, J.R. Barnes, R.W. Zurek, C.B. Leovy, J.R. Murphy, H. Lee, and J. Schaeffer*, Mars atmospheric dynamics as simulated by the NASA Ames General Circulation Model 1. The zonal mean circulation*, J. Geophys. Res., 98, 3093-3123, 1993.

Haberle, R. M., J. R. Murphy and J. Schaeffer, *Orbital change experiments with a Mars general circulation model*, Icarus*, 161*, 66-89, 2003.

Hamilton, K., *Inter-annual variability in the northern-hemisphere winter middle atmosphere in control and perturbed experiments with GFDL Skyhi general circulation model*, J. Atmos. Sci., 52, 44-66, 1995.

Hanel, R. C., V. Kunde, B. Schlachm, P. Straat, T. Burke, J. Pearl, J. Pirragli, W. Maguire, P. Lowman, G. Levin, C. Prabhakara, B. Conrath and W. Hovis., *Investigation of Martian environment by Infrared spectroscopy on Mariner 9*, Icarus*, 17*, 423-442, 1972.

Hinson, D. P. and R. J. Wilson, *Transient eddies in the southern hemisphere of Mars*, Geophys. Res. Lett., 29, art. no. 1154, 2002.

Hinson, D.P. and R. J. Wilson, *Temperature inversions, thermal tides, and water ice clouds in the Martian tropics*, J. Geophys. Res., 109, art. no. E01002, 2004.

Hollingsworth, J. L., R. M. Haberle, J. R. Barnes, A. F. C. Brider, J. B. Pollack, H. Lee and J. Schaeffer*, Orographic control of storm zones on Mars*, Nature, 380, 413-416, 1996.

Joshi, M.M., S.R. Lewis, P.L. Read, and D.C. Catling, 1995: *Western boundary currents in the martian atmosphere: Numerical simulations and observational evidence*. J. Geophys. Res., 100, 5485-5500.

Kahn, R. A., T. Z. Martin, R. W. Zurek, and S. W. Lee, *The Martian dust cycle, in Mars* (Univ. of Arizona Press, Tucson, AZ, 1992), pp. 1017-1053.

Kieffer, H. H., A. P. Zent*, Quasi-periodic climate change on Mars*, in *Mars* (Univ. of Arizona Press, Tucson, AZ, 1992), pp. 1180-1220.

Landis, G. A. and P. P. Jenkins, *Measurement of the settling rate of atmospheric dust on Mars by the MAE instrument on Mars Pathfinder*, J. Geophys. Res., 105, 1855-1857, 2000.

Leovy, C. B. *et al*., *Mariner 9 television experiment progress report*, Icarus, 17, 373-&, 1972.

Leovy, C. B., J. B. Pollack, B. A. Smith, E. N. Shipley, R. L. Wildey, A. T. Young and G. A. Briggs, *Mariner 9 television experiment progress report*, Icarus, 17, 373-&, 1972.

Leovy, C. B., Zurek, R. W. and J. B. Pollack, *Mechanisms for Mars dust storms*, J. Atmos. Sci., 30, 749-762, 1973.

Liu, J., Richardson, M. I. and Wilson, R. J., *An assessment of the global, seasonal and inter-annual spacecraft record on Martian climate in the thermal infrared*, J. Geophys. Res., 108, art. no. 5089, 2003.

Lorenz, R. D., J. I. Lunine, J. A. Grier and M. A. Fisher, *Martian surface wind speeds described by the Weibull distribution*, J. Spacecr., 33, 754-756, 1996.

Magalhaes, J. A., R. E. Young, *Downslope windstorms in the lee of ridges on Mars*, Icarus, 113, 277-294, 1995.

Malin, M. and K. S. Edgett, *Mars Global Surveyor Mars Orbiter Camera: Interplanetary cruise through primary mission*, J. Geophys. Res., 106, 23429-23570, 2001.

Martin, T. Z. and H. H. Kieffer, *Thermal infrared properties of the Martian atmosphere .2. 15-MU-M band measurements*, J. Geophys. Res., 84, 2843-2852, 1979.

Martin, T. Z., *Mean thermal and albedo behavior of the Mars surface and atmosphere over a Martian Year*, Icarus*, 45*, 427-446, 1981.

Martin, T. Z., *Thermal Infrared opacity of the Mars atmosphere*, Icarus, 66, 2-21, 1986.

Martin, L. J. and Zurek, R. W., *An analysis of the history of dust activity on Mars*, J. Geophys. Res., 98, 3221, 1993.

Martin, T. Z. and M. I. Richardson, *New dust opacity mapping from Viking infrared thermal mapper data*, J. Geophys. Res., 98, 10941-10949, 1993.

Metzger, S. M., J. R. Carr, J. R. Johnson, T. J. Parker and M. T. Lemmon, *Dust devil vortices seen by Mars Pathfinder Camera,* Geophys. Res. Lett., 26, 2781-2784, 1999.

Mischna, M.A., M. I. Richardson, R. J. Wilson, and D. J. McCleese, *On the orbital forcing of Martian water and $CO_2$ cycles: A general circulation model study with simplified volatile schemes,* J. Geophys. Res., 108, art. no. 5062, 2003.

Moore, H. J., *The Martian dust storm of Sol-1742*, J. Geophys. Res., 90, D163-D174, 1985.

Murphy, J. R., O. B. Toon, R. M. Haberle and J. B. Pollack, *Numerical simulations of the decay of Martian global dust storms*, J. Geophys. Res., 95, 14629-14648, 1990.

Murphy, J.R., O.B. Toon, R.M. Haberle, and J.B. Pollack, (1995), *Numerical simulations of the decay of Martian global dust storms*, J. Geophys. Res*., 104*, 24177-24194, 1995.

Murphy, J. R. and S. Nelli, *Mars Pathfinder convective vortices: Frequency of occurrence*, J. Geophys. Res., 29, art. no. 2103, 2002.

Newman, C. E., S. R. Lewis, P. L. Read, and F. Forget, *Modeling the Martian dust cycle, 1: Representations of dust transport processes*, J. Geophys. Res., 107, art. no. 5123, 2002.

Newman, C. E., S. R. Lewis, P. L. Read, *The atmospheric circulation and dust activity in different orbital epochs on Mars,* submitted to Icarus, Feb. 2004.

Newman, C. E., S. R. Lewis, P. L. Read, and F. Forget, *Modeling the Martian dust cycle, 2: Multi-annual radiatively active dust transport simulations*, J. Geophys. Res., 107, art. no. 5124, 2002.

Newman, C.E., P.L. Read, and S.R. Lewis, *Investigation atmospheric predictability on Mars using breeding vectors in a general circulation model*, Q. J. R. Meteorol. Soc, 130, 2971-2989, doi:10.1256/qj.03.209, 2005.

Pankine, A. A. and Ingersoll, A. P., *Inter-annual variability of Martian global dust storms: simulations with a low order model of the general circulation*, Icarus, 155, 299-323, *2002.*

Pollack, J. B., D. Colburn, F. M. Flasar, R. Kahn, C. E. Carlston and D. Pidek, *Properties and Effects of dust particles suspended in the Martian atmosphere*, J. Geophys. Res, 84, 2929-2945, 1979.

Read, P. L., M. Collins, F. Forget, R. Fournier, F. Hourdin, S. R. Lewis, O. Talagrand, F. W. Taylor and N. P. J. Thomas, *A GCM climate database for Mars: For mission planning and scientific studies*, Adv. Space Res., 19, 1213-1222, 1997.

Renno, N. O., M. L. Burket and M. P. Larkin, *A simple thermodynamic theory for Dust Devils*, J. Atmos. Sci., 55, 3244-3252, 1998.

Renno, N. O., A. A. Nash, J. Lunine and J. Murphy, *Martian and terrestrial dust devils: Test of a scaling theory using Pathfinder data*, J. Geophys. Res., 105, 1859-1865, 2000.

Renno, N. O. *et al*., *Martian and terrestrial dust devils: Test of a scaling theory using Pathfinder data*, J. Geophys. Res., 105*,* 1859, 2000.

Richardson, M. I., *Comparison of microwave and infrared measurements of Martian atmosphere temperatures: Implications for short term climate variability,* J. Geophys. Res., 103, 5911-5918, 1998.

Richardson, M. I. and R. J. Wilson, *Investigation of the nature and stability of the Martian seasonal water cycle with a general circulation model*, J. Geophys. Res., 107, art. no.5031, 2002.

Richardson, M. I., R. J. Wilson and A. V. Rodin, *Water ice clouds in the Martian atmosphere: General Circulation Model experiments with a simple cloud scheme*, J. Geophys. Res.,107, art no*: 5064, 2002.*

*Richardson and Wilson, Comparison of Mars GCM with Viking mission observations*, 5th international conference on Mars, Abstract no. 6234 (1999)

Schneider, E. K., *Martian great dust storms- interpretive axially symmetric models*, Icarus, 55, 302-331, 1983.

Seguro, J. V. and T. W. Lambert*, Modern estimation of the parameters of the Weibull wind speed distribution for wind energy analysis*, J. Wind Eng Ind Aerod., 85, 75-84, 2000.

Smith, M.D., J.C. Pearl, B.J. Conrath, and P.R. Christensen, *Mars Global Surveyor Thermal Emission Spectrometer (TES) observations of dust opacity during aerobraking and science phasing*, J. Geophys. Res., 105(E4) 9539-9552, 2000a.

Smith, M.D., J.C. Pearl, B.J. Conrath, and P.R. Christensen, *Thermal Emission Spectrometer results: Atmospheric thermal structure and aerosol distribution*, J. Geophys. Res., 106 (E10), 23929-23945, 2001a.

Smith, M.D., B.J. Conrath, J.C. Pearl, and P.R. Christensen, *Thermal Emission Spectrometer observations of martian planet-encircling dust storm 2001A*, Icarus, 157, 259-263, 2002.

Smith, M. D., J. C. Pearl, B. J. Conrath and P. R. Christensen, *Thermal Emission Spectrometer results: Mars atmospheric thermal structure and aerosol distribution*, J. Geophys. Res., 106, 23929-23945, 2001.

Smith, M. D., R. J. Conrath, J. C. Pearl and P. R. Christensen, *Thermal Emission Spectrometer observations of Martian planet encircling dust storm 2001A*, Icarus, 157, 259-263, 2002.

Smith, M.D., *Interannual variability in TES Atmospheric observations of Mars during 1999-2003*, Icarus, 108, 148-165, 2004.

Smith, P. H. and M. Lemmon, *Opacity of the Martian atmosphere measured by the images from Mars Pathfinder*, J. Geophys. Res., 104, 8975-8985, 1999.

Strausberg, M.J., H. Wang, M.I. Richardson, S.P. Ewald, and A.D. Toigo (2005), *Observations of the initiation and evolution of the 2001 Mars global dust Storm*, J. Geophys. Res., 110, E02006, doi:10.1029/2004JE002361.

Shao, Y., in *Physics and Modeling of Wind Erosion* (Kluwer Academic Publishers, MA 2001), pp. 113-316. Smith, D.E. *et al*. *The global topography of Mars and implications for surface evolution*. Science. 284, 1495- 1503, 1999.

Shao, Y., in *Physics and Modeling of Wind Erosion* (Kluwer Academic Publishers, MA 2001), pp. 113-316. 8.

Thomas, P., J. Veverka, S. Lee and A. Bloom, *Classification of wind streaks on Mars*, Icarus, 45, 124-153, 1981.

Thomas, P., J. Veverka, D. Gineris and L. Wong, *Dust streaks on Mars,* Icarus, 60, 161-179, 1984.

Thomas, P. and P. J. Gierasch, *Dust devils on Mars*, Science, 230, 175-177, 1985.

Thomas, P., S. W. Squyres, K. Herkenhoff, A. Howard and B. Murray, *Polar deposits of Mars, in Mars* (Univ. of Arizona Press, Tucson, AZ, 1992), 767-798.

Thomas, P. C., P. Gierasch, R. Sullivan, D. S. Miller, E. A. del Castillo, B. Cantor and M. T. Mellon, *Meso-scale linear streaks on Mars: environments of dust entrainment,* Icarus, 162, 242-258, 2003.

Tillman, J. E., Mars *global atmospheric oscillations- annually synchronized, transient-normal mode oscillations and the triggering of global dust storms*, J. Geophys. Res., 93, 9433-9451, 1988.

Toigo, A. D. and M. I. Richardson, *Seasonal variation of aerosols in the Martian* atmosphere, J. Geophys. Res., 105, 4109-4121, 2000.

Toigo, A. D., M. I. Richardson, S. P. Ewald and P. J. Gierasch, *Numerical simulation of Martian dust devils*, J. Geophys. Res., 108, art. no. 5047, 2003.

Wang, H. Q., M. I. Richardson, R. J. Wilson, A. P. Ingersoll, A. D. Toigo and R. W. Zurek., *Cyclones, tides and the origin of a cross-equatorial dust storm on Mars*, Geophys. Res. Lett., 30, art. no.1488, 2003.

Wang, H., R.W. Zurek, and M.I. Richardson, *The relationship between frontal dust storms and transient eddy activity in the northern hemisphere of Mars as observed by Mars Global Surveyor,* J. Geophys. Res., 110, E07005, doi:10.1029/2005JE002423, 2005.

White, B. R., *Soil transport by winds on Mars*, J. Geophys. Res., 84, 4643-4651, 1979.

Wilson, R. J. and K. Hamilton, *Comprehensive model simulations of thermal tides in the Martian atmosphere*, J. Atmos. Sci., 53, 1290-1326, 1996.

Wilson, R.J., *A general circulation model simulation of the Martian polar warming*, Geophys. Res. Lett., 24, 123-127, 1997.

Wilson, R.J., and M. I. Richardson, *Comparison of Mars GCM dust storm simulations with Viking mission observations*, In The Fifth International Conference on Mars, Abstract #6234, LPI contribution No. 972, Lunar and Planetary Institute, Houston (CD-ROM), 1999.

Wilson, R. J., *Evidence for diurnal period Kelvin waves in the Martian atmosphere from Mars Global Surveyor TES data,* Geophys. Res. Lett., 27, 3889-3892, 2000.

Wilson, R. J. and M. I. Richardson, *The Martian atmosphere during the Viking mission 1, infrared measurements of atmospheric temperatures revisited*, Icarus, 145, 555-579, 2000.

Wilson, R.J., D. Banfield, B.J. Conrath, and M.D. Smith, *Traveling waves in the northern hemisphere of Mars*, Geophys. Res. Lett., 29(14), 10.1029/2002GL014866, 2002.

Zurek, R.W., J.R. Barnes, R.M. Haberle, J.B. Pollack, J.E. Tillman, and C.B. Leovy, *Dynamics of the atmosphere of Mars*, in *Mars*, edited by H.H. Kieffer, B.M. Jakosky, C.W. Snyder, and M.S. Matthews, pp. 835-933, Univ. of Ariz. Press, 1992

Zurek, R. W. and Leovy, C. B., *Thermal tides in the dusty Martian atmosphere: a verification of theory*, Science, 213, 437-439, 1981.